Alma Mater Studiorum - Università di Bologna

DOTTORATO DI RICERCA IN

INGEGNERIA ELETTRONICA, TELECOMUNICAZIONI E TECNOLOGIE DELL'INFORMAZIONE

Ciclo 33

Settore Concorsuale: 09/F2 - TELECOMUNICAZIONI

Settore Scientifico Disciplinare: ING-INF/03 - TELECOMUNICAZIONI

SATELLITE SYSTEMS IN THE ERA OF 5G INTERNET OF THINGS

Presentata da: Matteo Conti

Coordinatore Dottorato

Alessandra Costanzo

Supervisore

Alessandro Vanelli-Coralli

Co-Supervisore

Alessandro Guidotti

Esame finale anno 2021

"Remember to look up at the stars and now down at your feet. Try to make sense of what you see and wonder about what makes the universe exist. Be curious. And however difficult life may seem, there is always something you can do and succeed at. It matters that you don't just give up"

Stephen Hawking

Contents

List of Figures

List of Tables

List of Acronyms

3GPP	Third Generation Partnership Project
5G	5th generation of communication systems
ACK	Acknowledgment
ACM	Adaptive Coding and Modulation
AESM	Average Effective SINR Mapping
AWGN	Additive White Gaussian Noise
BDS	BeiDou Navigation Satellite System
BER	Bit Error Rate
BFN	Beam Forming Network
BS	Base Station
BSS	Broadcasting Satellite Service
CDF	Cumulative Distribution Function
CDMA	Code Division Multiple Access
CESM	Capacity Effective SINR Mapping
CFO	Carrier Frequency Offset
CINR	Carrier-to-Interference plus Noise Ratio
CIR	Carrier-to-Interference Ratio
CML	Coded Modulation Library
CNR	Carrier-to-Noise Ratio
CP	Control Plane
CP	Cyclic Prefix
CRDSA	Contention Resolution Diversity Slotted ALOHA
CRF	Celestial Reference Frame
CRS	Celestial Reference System
CSI	Channel State Information
CTP	Conventional Terrestrial Pole
DAMA	Demand Assignment Multiple Access
DCI	Downlink Control Indicator
DFT	Discrete Fourier Transform
DgNB	Donor gNB
DL	Downlink
DS-SS	Direct Sequence Spread Spectrum

DVB Digital Video Broadcasting
DVB-S2X Digital Video Broadcasting - Satellite Second Generation Extension

ECEF Earth Centered Eart Fixed
ECI Earth Centered Inertial
ECR Earth Centered Rotational
eDRX extend Discontinuous Reception
EESM Exponential Effective SINR Mapping
EIRP Equivalent Isotropically Radiated Power
eMTC enhanced Machine Type Communication
ENU East North Up
ESM Effective SINR Mapping
E-SSA Enhanced Spread Spectrum ALOHA
EES Earth Exploration Satellite Service
eMBB enhanced Mobile Broadband
EPC Evolved Packet Core network
ESA European Space Agency
ESiM2M ESA M2M Simulator
ESTEC European Space Research and Technology Centre

FBMC Filter Bank Multicarrier
FCC U.S. Federal Communications Commission
FEC Forward Error Correction
FFR Full Frequency Reuse
FOV Field Of View
FR Frequency Reuse
FR3 Frequency Reuse 3
FSL Free Space Loss
FSS Fixed Satellite Service

G2G Galileo Second Generation
GEO Geostationary Orbit
GLONASS GLObal NAvigation Satellite System
gNB-DU Distributed Unit
gNB-CU Centralised Unit
GNSS Global Navigation Satellite Systems
GPS Global Positioning System
GS Ground Station
GSO Geosynchronous Orbit
GW Gateway

HAPS High Altitude Platform Systems
HARQ Hybrid Automatic Repeat reQuest
HEO Highly Elliptical Orbit

HPBW Half Power Beam Width
HTS High Throughput Satellite

IAB Integrated Access and Backhaul
ICO Intermediate Circular Orbits
IoT Internet of Things
iSIC Iterative Successive Interference Cancelation
ISL Inter Satellite Links
ISM Industrial, Scientific and Medical
IU Intermediate Unit

KPI Key Performance Indicator

L2S Link-to-System
LAN Longitude of the Ascending Node
LB Link Budget
LEO Low Earth Orbit
LESM Logarithmic Effective SINR Mapping
LLA Latitude-Longitude-Altitude
LLR Log-Likelihood Ratio
LLS Link-Level Simulation
LO Local Oscillator
LoS Line of Sight
LPWAN Low Power Wide Area Network
LTE Long Term Evolution
LTP Local Tangent Plane
LUT Look Up Table

M-S Multi-Satellite
M2M Machine to Machine
MAC Media Access Control
MCL Maximum Coupling Loss
MCS Modulation and Coding Scheme
MEO Medium Earth Orbit
MI Mutual Information
MIB Mutual Information per Coded Bit
MIESM Mutual Information Effective SINR Mapping
MIMO Multiple Input Multiple Output
ML Maximum Likelihood
MMIB Mean Mutual Information per Coded Bit
mMTC massive Machine Type Communications
MSE Mean Square Error
MSS Mobile Satellite Service
MTC Machine Type Communications

NACK Non-Acknowledgment
NB-IoT Narrowband IoT
NED North East Down
NFV Network Function Virtualisation
NGC Next Generation Core network
NN Neural Network
NOMA Non Orthogonal Multiple Access
NPDCCH Narrowband Physical Downlink Control Channel
NPDSCH Narrowband Physical Downlink Shared Channel
NPRACH Narrowband Physical Random Access Channel
NPUSCH Narrowband Physical Uplink Shared Channel
NR New Radio
NTN Non-Terrestrial Network

OBC On-Board Computer
OFDM Orthogonal Frequency Division Multiplexing
OSI Open Systems Interconnection

PDCP Packet Data Convergence Protocol
pdf probability density function
PER Packet Error Rate
PHY Physical Layer
PLR Packet Loss Ratio
pmf probability mass function
PRB Physical Resource Block
PSM Power Saving Mode

QoS Quality of Service

RA Random Access
RAAN Right Ascension of the Ascending Node
RAR Random Access Response
RBIR Received Bit Mutual Information Rate
RF Radio Frequency
RLC Radio Link Control
RN Relay Node
RPY Roll-Pitch-Yaw
RRC Radio Resource Control
RTD Round Trip Delay
RTT Round Trip Time
RV Random Variable

S-S Single-Satellite
S-ALOHA Slotted ALOHA

SAR Satellite–based Search and Rescue
SC-FDMA Single-Carrier Frequency Division Multiple Access
SCS Sub-Carrier Spacing
SDAP Service Data Application Layer
SDN Software Defined Networking
SDR Software Defined Radio
SF Spreading Factor
SI Study Item
SIC Successive Interference Cancelation
SINR Signal-to-Interference plus Noise Ratio
S-IoT Satellite-Internet of Things
SatCom Satellite Communication
SIR Signal-to-Interference Ratio
SISO Single Input Single Output
SLS System-Level Simulation
SMS Short Message Service
SNR Signal-to-Noise Ratio
SoA State-of-the-Art
SRI Satellite Radio Interface
SSA Spread Spectrum ALOHA
SSP Sub-Satellite Point

TA Timing Advance
TB Transport Block
TLE Two-Line Element
TOA Time of Arrival
TRF Terrestrial Reference Frame
TRS Conventional Terrestrial Reference System
TTI Transmission Time Interval

UAS Unmanned Aircraft System
UE User Equipment
UL Uplink
UP User Plane
UT User Terminal

VHTS Very High Throughput Satellite
VLEO Very LEO
VSAT Very Small Aperture Terminal

W-CDMA Wideband Code Division Multiple Access
WI Work Items

XPD Cross Polarisation Discrimination

Introduction

This thesis is the outcome of a three-year work done during the PhD course in "Electronics, Telecommunications and Information Technologies Engineering". The main research topic is focused on Satellite-Internet of Things (S-IoT) applications, specifically related to the design and analysis of specific solutions for Non-Terrestrial Network (NTN), and on the Third Generation Partnership Project (3GPP) standardisation process.

In recent years, Internet of Things (IoT) applications have drawn a great deal of attention, both in academia and industry. It is, in fact, expected that IoT devices will be half of the global connected devices within the next few years, with billions of Machine to Machine (M2M) connections. A crucial requirement of any infrastructure serving the IoT market will be to guarantee ubiquitous connectivity to the low-cost, low-powered devices distributed all over the globe. It is widely accepted that this requirement will not be met by the terrestrial network alone. There will be, in fact, vast areas of the globe where the terrestrial infrastructure deployment will be unfeasible or not economically viable, thus leaving those areas un- or underserved. For this reason, several studies and projects are addressing the use of a NTN component to seamlessly complement and extend the terrestrial network coverage in future systems.

The design of these extremely complex systems requires manifold analyses at different levels of abstraction, from satellite constellation and ground segment architecture aspects, to the evaluation of the air interface behaviour, in order to evaluate the system performance. The aim of this work is to perform a detailed analysis of the Satellite Communication (SatCom) system aspects, trying to be as accurate as possible but without getting lost in unnecessary details, in order to provide a comprehensive set of tools, organised in a simulation platform, to support the design and performance evaluation of the system. Notably, simulation softwares play an important role in this framework; however, a full-featured simulation tool does not yet exist for the evaluation of the described emerging technologies. ESA M2M Simulator (ESiM2M) is a System-Level Simulator, developed in collaboration with the European Space Agency (ESA), which is intended for closing this gap, as a tool for the design and analysis, from a system-level point of view, of S-IoT systems. The following discussion is primarily based on S-IoT systems, presenting the simulation tool and the results derived with the latter.

This work is organised as follows. Chapter 1 describes all the main aspects regarding the SatCom systems architecture, with particular emphasis on NTN architectures as proposed in the 3GPP standardisation process and on the requirements for S-IoT. Chapter 2 illustrates the main aspects characterizing the ESiM2M simulation tool. Chapter 3 gives the mathematical framework for the geometrical computations, fundamental for the analyses performed with the simulator. Chapter 4 characterizes the satellite constellations and describes the main steps for the constellation design process. Chapter 5 describes the theoretical background behind the Physical Layer (PHY) abstraction methodologies adopted for System-Level Simulations (SLSs) and details the results achieved in the simulator testing phase, justifying the choice of a specific Received Bit Mutual Information Rate (RBIR) abstraction method. Chapter 6 details the mathematical characterization for delay and Doppler, describes the main impairments and contributions to the path loss, and gives the mathematical framework for the link budget analyses performed by the tool, providing the baseline for the results presented. Chapter 7 describes applications and results obtained by means of the ESiM2M tool. Finally, Chapter 8 contains the conclusions.

List of Publications

[P1] A. Guidotti, A. Vanelli Coralli, M. Conti, S. Andrenacci, S. Chatzinotas, N. Maturo, B. Evans, A. Awoseyila, A. Ugolini, T. Foggi, L. Gaudio, N. Alagha, S. Cioni, "Architectures and Key Technical Challenges for 5G Systems Incorporating Satellites", *IEEE Transactions on Vehicular Technology*, 2019

[P2] A. Guidotti, S. Cioni, G. Colavolpe, M. Conti, T. Foggi, A. Mengali, G. Montorsi, A. Piemontese and A. Vanelli Coralli, "Architectures, standardisation, and procedures for 5G Satellite Communications: A Survey", *Computer Networks*, 2020

[P3] M. Conti, S. Andrenacci, N. Maturo, S. Chatzinotas, A. Vanelli Coralli, "Doppler Impact Analysis for NB-IoT and Satellite Systems Integration", *IEEE International Conference on Communications*, 2020

[P4] M. Conti, A. Guidotti, C. Amatetti, A. Vanelli Coralli, "NB-IoT over Non Terrestrial Networks: Link Budget Analysis", *IEEE Global Communications Conference*, 2020

[P5] M. Conti, A. Vanelli Coralli, "Galileo Second Generation: Two-Way Messaging for IoT", *IEEE International Conference on Communications Workshops*, 2021

[P6] C. Amatetti, M. Conti, A. Guidotti, A. Vanelli Coralli, "Wavelet based preamble detection in NB-IoT via Satellite", *IEEE Global Communications Conference*, 2021 [submitted]

[P7] A. Guidotti, M. Conti, A. Vanelli Coralli, "Beamforming in LEO Constellations for NB-IoT Services in 6G Communications", *IEEE Global Communications Conference*, 2021 [submitted]

Chapter 1

Satellite Communication Systems

SatComs are the product of communications and space technology research with the goal of achieving ever-increasing ranges and capability at the lowest possible cost. In this chapter, the main aspects of SatCom systems will be described.

1.1 SatCom Systems Architecture

The main entities composing a SatCom system, as shown in Figure 1.1, can be categorized into: i) the *space segment*, containing one or several active and spare satellites organised into a constellation; ii) the *control segment*, consisting of all ground facilities for the control and monitoring of the satellites, also named Tracking, Telemetry, and Command (TTC) stations, and for the management of the traffic and the associated resources on board the satellite; and iii) the *ground segment*, consisting of all the traffic earth stations.

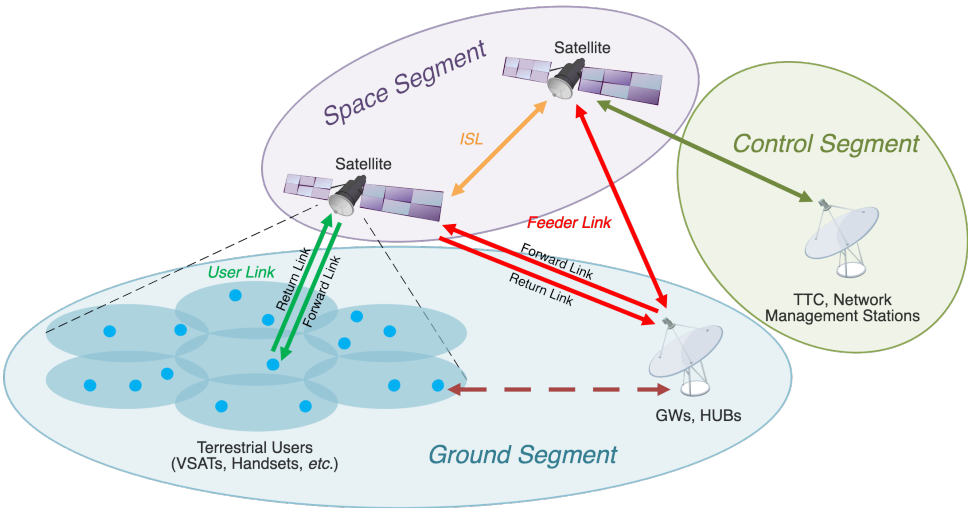

FIGURE 1.1: SatCom System high-level architecture.

Satellite networks are characterized by their topology, the types of links they support, and the connectivity they offer among earth stations. SatCom network configurations are: *meshed*, *star*, or *multi-star*. i) In a meshed network, every node[1] is able to

[1]A node is either a redistribution point or a communication endpoint. A satellite, as well as a Ground Station (GS) or a ground terminal can act as network nodes.

communicate with every other node. A meshed satellite network consists of a set of earth stations that can communicate with one another using satellite links consisting of radio-frequency carriers. ii) In a star network, each node can communicate only with a single central node, often called the hub. A star satellite network consists of earth stations that can communicate only with a central earth station called the hub. The star configuration is the most widely used because of its cost-effectiveness. iii) In a multi-star topology, several central nodes (hubs) are identified. The other nodes can communicate only with those central nodes.

1.1.1 Space Segment

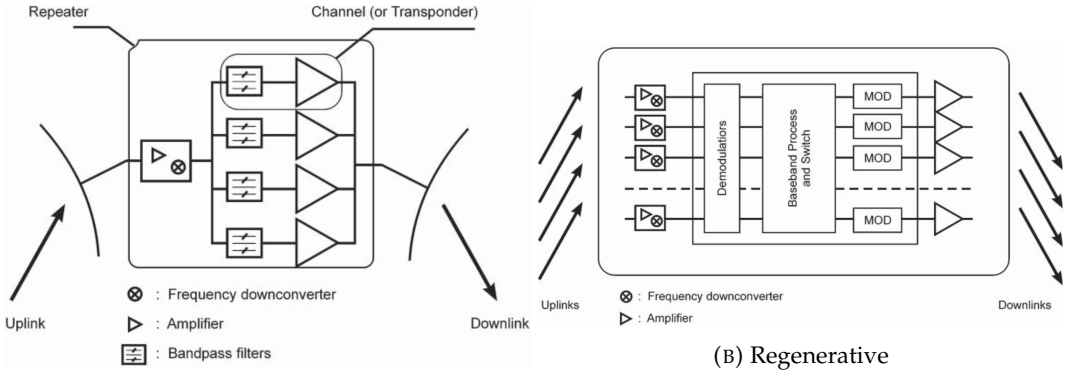

(A) Transparent

(B) Regenerative

FIGURE 1.2: Payload organisation, [1].

The space segment consists of one or several active and spare satellites, which are composed of the *payload* and the *platform*. The payload consists of the receiving and transmitting antennas and all the electronic equipment supporting the carriers' transmissions. Figure 1.2 describes the two possible types of payload organisation: *transparent* and *regenerative*.

A transparent payload (sometimes referred to as bent pipe) in which the carrier power is amplified and the frequency is down-converted, is shown in Figure 1.2a. In order to boost the power level of the received carrier from a few tens of picowatts to the power level of the carrier fed to the transmitting antenna (a few watts to a few tens of watts), the power gain is 100-130 dB. To improve the separation between the receiving input and the transmitting output, frequency conversion is required. Due to technology power limitations, the overall satellite payload bandwidth is split into several sub-bands, and the carriers in each sub-band are amplified by a dedicated power amplifier. The amplifying chain associated with each sub-band is called a satellite channel, or *transponder*. The bandwidth separation is accomplished using a series of filters called the *input multiplexer* (IMUX). The amplified carriers in the output are then recombined in the *output multiplexer* (OMUX). The transparent payload depicted in Figure 1.2a could be used on a single-beam satellite where each transmitting and receiving antenna generates one beam only. Considering multiple-beam antennas, the payload would then have as many inputs/outputs

as upbeams/downbeams. The routing of carriers from one upbeam to a given downbeam implies either routing through different satellite channels, *transponder hopping*, depending on the selected uplink frequency, or *on-board switching with transparent on-board processing*.

Figure 1.2b shows a multiple-beam regenerative payload. Here the uplink carriers are demodulated, instead of being directly amplified and re-routed to the output. The availability of the baseband signals allows *on-board processing* and routing of information from upbeam to downbeam through *on-board switching at baseband*. The frequency conversion is achieved by modulating on-board-generated carriers at downlink frequency. The modulated carriers are then amplified and delivered to the destination downbeam.

Each beam defines a beam coverage area, also called a *footprint*, on the Earth's surface. The aggregate beam coverage areas define the multibeam antenna coverage area. A given satellite may have several multiple-beam antennas, and their combined coverage defines the satellite access area, which is directly related to the Field Of View (FOV) of the satellite, as detailed in Chapter 3.

It is possible to define an *instantaneous* and *long-term* system coverage. The former consists of the aggregation at a given time of the coverage areas of the individual satellites participating in the constellation, while the latter is the area on the earth scanned over time by the antennas of the satellites in the constellation. For real-time services, the instantaneous system coverage should at any time have a footprint covering a *service zone*, *i.e.*, a geographical region where at least a GS is installed. For what concerns store-and-forward services, this condition is not necessary, but a long-term coverage of the service zone is required. In order to achieve continuous global coverage, a large number of satellites is needed for Low Earth Orbit (LEO) and Medium Earth Orbit (MEO) satellite constellations (*e.g.*, Iridium Next has 66 satellites, Starlink phase 1 first orbital shell will contain 1600 satellites). With Geostationary Orbit (GEO) systems, three satellites are sufficient in order to achieve global coverage (except for the polar areas).

A key technology for SatCom systems, in particular to achieve high capacity for High Throughput Satellite (HTS) reducing the cost per bit for information delivery, is *frequency reuse*. The available bandwidth can be divided into three or four sub-bands (also called three- or four-color techniques, according to the arrangement of the spot beams) so that different sub-bands (*colors*) can be allocated to different spot beams, similar to the frequency reuse in terrestrial networks. Different colors could share the same frequency but using opposite polarisations. Then, adjacent spot beams use different colors to reduce the interference. Furthermore, it is worth mentioning that *active antennas* payloads are expected to become always more predominant in future Very HTS (VHTS). These payloads exploit a more advanced phase array antenna in which each antenna element has its own transmit and receive units, all controlled by the On-Board Computer (OBC) by means of a Beam Forming Network (BFN). As a result, the antenna is fully reconfigurable enabling the satellite to adapt to new

demands in coverage, bandwidth, power and frequency as well as providing interference mitigation and beam-hopping.

The platform consists of all the subsystems that permit the payload to operate, like: i) the fuel system that is responsible for making the satellite run for years; ii) the solar panels that provide the required energy for the satellite's operation; iii) the satellite and telemetry control system, used to transmit commands to the satellite as well as to send the status of the onboard systems to the ground stations. In order to ensure service with a specified availability, a satellite communication system must make use of several satellites to provide redundancy. A satellite can in fact cease to be available due to a failure or because it has reached the end of its lifetime. In this respect, it is necessary to distinguish between the reliability and the lifetime of a satellite. *Reliability* is a measure of the probability of a breakdown and depends on the reliability of the equipment and any schemes to provide redundancy. The *lifetime* is conditioned by the ability to maintain the satellite on station in the nominal attitude and depends on the quantity of fuel available for the propulsion system and attitude and orbit control system. In a system, provision is generally made for an operational satellite, a backup satellite in orbit, and a backup satellite on the ground. The reliability of the system involves not only the reliability of each of the satellites but also the reliability of launching, [1].

1.1.2 Ground Segment

Earth stations come in three classes: i) *user stations*, such as handsets, portables, mobile stations, and Very Small Aperture Terminals (VSATs), which allow the customer to directly access the space segment; ii) *interface stations*, known as gateways, which interconnect the space segment to a terrestrial network; and iii) *service stations*, such as hub or feeder stations, which collect or distribute information from and to user stations via the space segment. Communications among users are set up through *user terminals*, which consist of equipment such as telephone sets, computers, smartphones, and in general devices that are connected to the terrestrial network or to the user station, or that are part of the user station (*e.g.*, if the terminal is mobile).

The ground segment consists of all the earth stations which are most often connected to the end user's terminal by a terrestrial network or, in the case of small station VSATs, directly connected to the end user's terminal. Stations are distinguished by their size, which varies according to the volume of traffic to be carried on the satellite link and the type of traffic. In the past, the largest were equipped with antennas having a 30 m diameter and the smallest had 0.6 m antennas, or even smaller (mobile stations, portable stations, or handsets). Along with the antenna, there is an Outdoor Unit (ODU), which contains the radio hardware to receive the signal and amplify it. The radio signal is sent to an Indoor Unit (IDU), which demodulates the signal and carries out the necessary baseband processing. Some stations can both transmit and receive, while others, like the ones used for a broadcasting satellite system, can only receive, [1].

1.1.3 Communication Links

The characteristic links in a SatCom system can be categorized in:

- *Downlinks (DLs)* from the satellites to the GSs and User Terminals (UTs);
- *Uplinks (ULs)* from GSs and UTs to the satellites; and
- *Inter Satellite Links (ISL)* between the satellites.

ULs and DLs consist of radio-frequency modulated carriers, while ISL can be either radio frequency or optical. Some large-capacity data-relay satellites also use optical links with their ground stations. Carriers are modulated by baseband signals conveying information for communications purposes. Connections among end users entail an UL and a DL, and possibly one or several ISLs.

Two types of links can be established through a satellite network: *unidirectional links*, where one or several stations only transmit and other earth stations only receive; and *bidirectional links*, where earth stations both transmit and receive. Unidirectional links are usually associated with a star topology in satellite broadcast-oriented networks, while bidirectional links can be associated with a star or meshed topology and are required to transport any two-way telecommunication service. Furthermore, in a SatCom network different types of connectivity can be defined depending on the type of service (*e.g.*, point-to-point for unicast, point-to-multipoint for multicast/broadcast, multipoint-to-point for multiplexing and concentration, and multipoint-to-multipoint).

For what concerns the nomenclature accounting for the link direction, we can distinguish *forward* and *return* links, as shown in Figure 1.1. A connection between a service provider and a user goes through a hub (for collecting services) or a feeder station (*e.g.* for broadcasting services). A connection from a gateway, hub, or feeder station to a user terminal is called a forward connection. The reverse connection is the return connection. Both forward and return connections entail an UL and a DL, and possibly one or more ISL. As for the ISL, three classes of these links link can be distinguished: i) links between GEO and LEO satellites (GEO-LEO), also called Inter-Orbital Links (IOL); ii) links between GEO satellites (GEO-GEO); and iii) links between LEO (LEO-LEO).

The Radio Regulations published by ITU subdivide the available bandwidth among the numerous SatCom specific applications (*e.g.*, Fixed Satellite Service (FSS), Mobile Satellite Service (MSS), Broadcasting Satellite Service (BSS), Earth Exploration Satellite Service (EES), *etc.*). Furthermore, frequency bands are allocated to the various radio communications services to allow compatible use. The allocated bands can be either exclusive for a given service or shared among several services. In order to simplify the frequencies allocation process worldwide, the globe is subdivided into three different geographical regions, each one characterized by certain frequency allocation rules for the plethora of available services, [1].

1.2 Technological Trends in SatCom

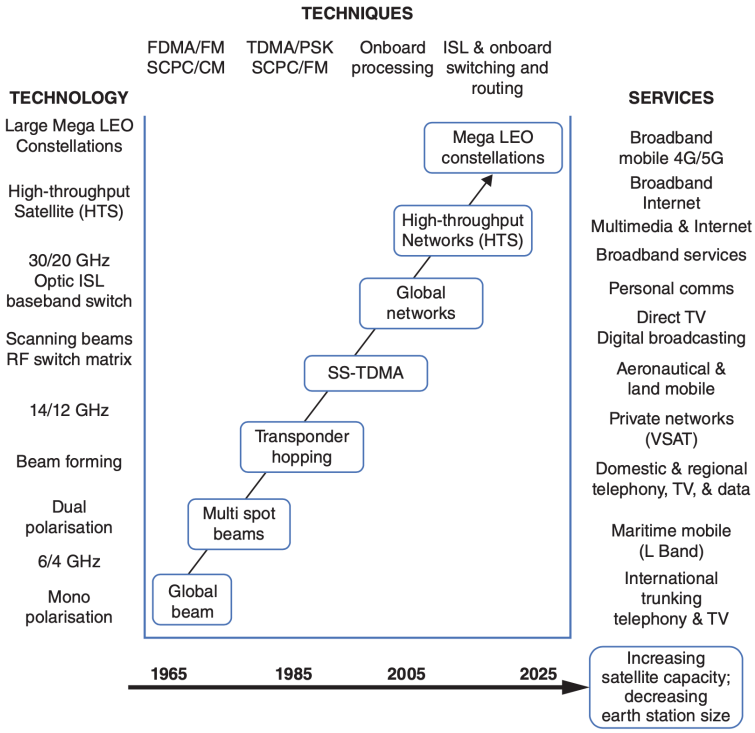

FIGURE 1.3: The evolution of SatCom technologies [1].

SatComs have grown continuously since the '70s. In the beginning, satellites were designed to complement submarine cables and played essentially the role of telephone trunk connections. Then communication techniques have changed from analog to digital, enabling the development of many novel technologies up to the current pinnacle of Digital Video Broadcasting - Satellite Second Generation Extension (DVB-S2X). Efficient modulation and coding schemes, powerful Forward Error Correction (FEC), Adaptive Coding and Modulation (ACM) provide performance close to the Shannon limit. New Multiple Access techniques have been developed to meet the diverse requirements of the continuously growing plethora of new services, from high-capacity links for internet and TV services, to low-capacity ones for supporting the ever growing IoT/Machine Type Communications (MTC) markets.

Simultaneously, the progress of antenna technology enabled the beams to conform to the coverage of the service area, improving the performance of the link while reducing interference among systems. Multi-beam satellites emerged, with the capability of producing hundreds of beams, implementing beam-hopping and precoding techniques exploiting either on-board or on-ground processing capabilities. This provides manifold advantages: i) the link budget is improved to small user terminals, thanks to the high satellite antenna gain obtained with very narrow beams; ii) the capacity is increased by reusing the frequency band allocated to the system many times; and iii) the interference is reduced thanks to the implementation of precoding techniques. Finally, ISLs were developed for civilian applications

in the framework of multi-satellite constellations and the use of higher frequencies (Ka band) enables the emergence of broadband services and the development of HTS, thanks to the large amount of bandwidth currently available.

1.2.1 New Space

SatComs have recently entered a period of renewed interest motivated by technological advances and nurtured through private investment and ventures. Following the evolution of Internet-based applications, SatComs are going through a transformation phase refocusing the system design on data services, namely broadband SatComs. The main motivations are the rapid adoption of media streaming instead of linear media broadcasting and the urgent need to extend broadband coverage to underserved areas (*e.g.*, developing countries, aero/maritime, rural, *etc.*).

Furthermore, the fusion and convergence of various wired and wireless technologies is a crucial achievement of the 5th generation of communication systems (5G), or New Radio (NR) in 3GPP terminology. Besides that, the exploding market of massive MTC (mMTC) is a key driver for telecommunications in the last few years. In this framework, SatCom creates the opportunity for streamlined integration targeting particular use cases that can take advantage of their unique capabilities. Concurrently, private investments have contributed to the growth of a multitude of production and launching alternatives, formerly reserved exclusively to governments and a handful of big multinational companies. This initiative, named *New Space*, has spawned a large number of innovative broadband and earth observation missions all of which require advances in SatCom systems.

As part of New Space initiatives, new more ambitious constellation types are currently being designed, besides the more traditional GEO satellite ones. In this direction, there has recently been a tremendous interest in developing LEO megaconstellations, made viable from: i) a sufficiently mature manufacturing, which enabled mass production of miniaturized satellites (CubeSat); ii) advancement in communication technologies; and iii) cheap launching costs. Multiple companies, such as SpaceX, Amazon, OneWeb, TeleSAT, have already announced large LEO plans including thousands of satellites that can deliver high-throughput broadband services with low latency. As of October 2020, SpaceX Starlink is composed of 895 active satellites and the company recently filed paperwork to the U.S. Federal Communications Commission (FCC) to arrange spectrum for 30 000 additional satellites, on top of the already approved 12 000 for the 1^{st} Starlink generation [2]. LEO orbits are particularly attractive also for small ventures like: OQ Technology, Sateliot, Hiber, Kepler, Lacuna Space, which are investing in the attractive S-IoT market.

Additionally to LEO orbits, there is interest also in MEO, where the SES O3b constellation of 20 satellites has been placed in a circular orbit along the equator at an altitude of 8063 km. Each satellite is equipped with twelve mechanically steerable antennas to allow tracking and handover of terminals and the next generation of O3b satellites is planned to use active antennas capable of generating thousands of beams

along with an on-board digital processor. This constellation type is unique since it manages to hit a trade-off between constellation size and latency.

The proliferation of various types of constellations has led to hybrid constellations integrating assets in multiple orbits. The MEO and GEO networking combination is one example where terminals will seamlessly handover between the two orbits, [3]. The backhauling of LEO satellite data by higher orbit satellites is another example, [4].

Besides the new methodologies and approaches for satellite constellations design, recent advances in the efficiency of power generation as well as the energy efficiency of radio frequency and digital processing components have allowed an evolution of the payload architecture. Enhanced on-board processing can enable innovative communication technologies, such as flexible routing/channelization, beam-forming, free-space optics, and even signal regeneration. Furthermore, space-hardened Software Defined Radio (SDR) can enable on-board waveform-specific processing which can be upgraded during the satellite lifetime, as opposed to the past years, where the on-board processing capabilities have been the limiting factor for advanced SatCom strategies.

It is worth highlighting that New Space does not refer to a specific technology, but it rather implies a new mentality towards space. It originated from three main aspects: i) space privatization; ii) satellite miniaturization; iii) and novel services based on space data, [5]. As opposed to the conventional institutional approach, privatization refers to the development and, particularly, the launching of satellites by private enterprises, such as SpaceX and Rocket Lab. In parallel, satellite and component miniaturization allowed easy access to space by multiplexing multiple micro/nano/pico-satellites into a single launcher. The combination of the two first aspects has lead to the third one, by allowing quick and relatively inexpensive access to space.

A wealth of data collection constellations have made it into orbit in this direction, covering a wide variety of services (*e.g.*, earth observation, Radio Frequency (RF) monitoring, asset tracking, sensor data collection *etc.*). New Space has inspired new opportunities in terms of collecting data from ground sensors directly via satellites, *i.e.* S-IoT. Currently, tens of private companies are building demonstrators and competing to launch viable commercial services, relying on LEO satellites. Cloud-based services (*e.g.*, Amazon Web Services) have rolled out ground station networks that can be shared among the various constellations, while providing easy access to high-performance computing for the data processing, eliminating the need for New Space ventures of deploying ad-hoc GS networks for collecting data on the ground, thus reducing costs and allowing fast services deployment.

1.3 3GPP 5G Non-Terrestrial Networks Integration

Drawing from the work reported in *"Architectures and Key Technical Challenges for 5G Systems Incorporating Satellites"* [6] and *"Architectures, standardisation, and procedures for 5G Satellite Communications: A survey"* [7], this section gives an overview on the standardisation process for the integration of NTN in 5G terrestrial network and on the related industrial and scientific endeavours.

An ever growing demand for broadband high-speed, low latency, and ultra-reliable, heterogeneous secure services recently started being experienced in wireless communications. These drivers require enhancements to devices, services, and technologies that are currently well established in the global market, as for instance the 3GPP Long Term Evolution (LTE) standard. Thus, the definition of new standards and technologies, known as 5G, has become of outmost importance in order to introduce novel techniques and technologies that can support the fulfillment of the significantly demanding requirements as well as to support novel market segments. The massive scientific and industrial interest in 5G communications is in particular motivated by the key role that these future systems will play in the global economic and societal processes to support the next generation vertical services, *e.g.*, Internet of Things, automotive and transportation sectors, e-Health, Industry 4.0, *etc.*, [8], [9].

Unlike previous standards, which can be seen as general purpose technologies to which the different services were adjusted, the next 5G standard is expected to be able to provide tailored and optimised support for a plethora of services, traffic loads, and end-user communities. Such a technology revolution can only be achieved through a radical shift in the way both the access and the core network are designed. This heterogeneous and optimised framework is reflected in the challenging requirements that 5G systems are expected to meet, *e.g.*, large throughput increase (the target peak data rate should be 20 Gbps in the downlink and 10 Gbps in the uplink), global and seamless connectivity, reliability (99.999% of successful packet reception), and connection density (1 million devices per square km), amongst others, [10]. In this context, the integration of satellite and terrestrial networks can be a cornerstone to the realisation of the foreseen heterogeneous global system. Thanks to their inherently large footprint, satellites can efficiently complement and extend dense terrestrial networks, both in densely populated areas and in rural zones, as well as provide reliable Mission Critical services. The definition of the new 5G paradigm provides a unique opportunity for the terrestrial and satellite communities to define a harmonised and fully-fledged architecture, differently from the past when terrestrial and satellite networks evolved almost independently from each other, leading to a difficult a posteriori integration.

In this context, 3GPP recognised the added value of SatCom and initiated several Study Item (SI) and succeeding Work Items (WI) related to NTN for NR, [11], [12]. It is expected that the integration of both satellite and aerial access networks in the 5G ecosystem can bring manifold benefits, among which: i) supporting 5G service

provision in both un-served areas that cannot be covered by terrestrial 5G networks (isolated/remote areas, on board aircrafts or vessels) and underserved areas (e.g., sub-urban/rural areas); ii) improving the 5G service reliability thanks to a better service continuity, in particular for mission critical communications or MTC and IoT devices, M2M/IoT devices or for passengers on board moving platforms; and iii) enabling the 5G network scalability by providing efficient multicast/broadcast resources for data delivery.

In addition to the 3GPP standardisation effort, also funded projects are currently addressing SatCom-based 5G systems, as, for instance: i) Sat5G, related to the development and validation of key technologies for enhanced Mobile Broadband (eMBB) scenarios, [13]; ii) SATis5G, in which a testbed has been developed to demonstrate the benefits of SatCom components in NR systems has been developed, including both GEO and LEO systems, [14]; iii) 5G-VINNI, focused on developing an end–to-end 5G facility to be used to demonstrate implementation of the 5G infrastructure so as to support key 5G performance indicators, [15]; iv) 5GENESIS, a project aimed at providing an open set of tools to facilitate 5G experimentations, [16]; v) CloudSat, focused on the review and analyses of virtualisation and softwarisation technologies and the definition of their applicability in the SatCom context, [17]; vi) VITAL, considering the combination of terrestrial and satellite systems by bringing Network Function Virtualisation (NFV) into SatCom and by enabling Software Defined Networking (SDN) based resources management in hybrid satellite–terrestrial networks, [18]; and vii) SANSA, aimed at enhancing the performance of mobile wireless backhaul net- works, both in terms of capacity and resilience, while assuring an efficient use of the spectrum, [19].

In addition to the above effort in terms of funded projects, also the scientific literature has provided a valuable addition to the global 5G knowledge. In [6], [7], the authors provide an overview of the possible 5G-based SatCom architectures and identify some of the most critical issues in terms of PHY and Media Access Control (MAC) layer procedures, as well as for the waveforms. In [20]–[22], the authors focused on resource allocation algorithms for multicast transmissions, in particular analysing the performance of the TCP protocol in a LTE-based GEOsystem. In [23], [24], LEO mega-constellations in Ku-band were proposed to provide LTE broadband services, also taking into account the impact of typical satellite channel impairments as large Doppler shifts and delays on the PHY and MAC layer procedures. Moving to the introduction of 5G in SatCom systems, preliminary analyses have been addressed by the authors in [25], [26], in which the focus was on the PHY and MAC layer techniques that shall cope with satellite channel impairments; these works were based on several assumptions since the 3GPP standardisation for SatCom-based 5G was still in its infancy, which brought to a more detailed analysis in [6]. In [27], an interesting analysis of the adaptability of frequency-localised waveforms based on Orthogonal Frequency Division Multiplexing (OFDM) is provided in the context of non-linear satellite channels. The authors of [28] provide a valuable

evaluation of the performance of live 4K video streaming over a 5G core network supported by a live GEO backhaul. Multimedia content delivery is also addressed in [29], in which a novel radio resource management algorithm for efficiently managing multicast multimedia content transmissions over satellite networks is designed, providing robust performance with respect to State-of-the-Art (SoA) solutions. In [30], the authors focus on Narrowband IoT (NB-IoT) and propose an interesting uplink scheduling technique to be used in LEO constellations, which aims at mitigating the level of the differential Doppler down to a value tolerable by the IoT devices. The authors of [31] addressed energy efficient communications in satellite-based 5G systems, in particular investigating the fundamental relationship between spectral efficiency and energy efficiency. The authors of [32] provide an interesting feasibility analysis on the utilisation of C-band (3.4-3.8 GHz) spectrum for mobile 5G services, in particular taking into account the impact on existing FSS systems. In [33], a top-down network architecture for the integration of nanosatellites in 5G systems in the millimeter wave domain is described; the system performance is evaluated in terms of Signal-to-Interference plus Noise Ratio (SINR) in the presence of fading, shadowing, and interference, and both random access and routing aspects are discussed. The work in [34] is focused on the application of Non Orthogonal Multiple Access (NOMA) solutions to different satellite architectures, aiming at satisfying the demanding 5G requirements in terms of availability, coverage, and efficiency. Aspects related to spectrum assignment and sharing have been addressed in [35] and [36], respectively. In the former paper, an intelligent spectrum assignment algorithm is proposed based on dynamic cooperation between primary and secondary spectrum users for 5G-based SatCom systems. In the latter, the authors introduce an advanced technique for spectrum sharing between satellite and terrestrial systems; in particular, the satellite spectrum is shared with terrestrial in-building small cells and the discussion is more focused on the terrestrial link performance assessment in the presence of a supporting satellite system. The authors of [37] and [38] focus on the design of the Random Access (RA) preamble. As for the former paper, a long preamble sequence is built by concatenating multiple Zadoff-Chu sequences and, to improve the detection performance, a joint correlation scheme is exploited based on power delay profiles. In the latter publication, the authors propose a RA preamble based on a pruned Discrete Fourier Transform (DFT) spread Filter Bank Multicarrier (FBMC) waveform. In [39], the authors provide a detailed overview of the NTN system-level assumptions, together with a description of the methodology to be used for link budget calibration and the corresponding results. Finally, in [40], an interesting overview of 3GPP activities for NTN is provided; in particular, the authors first provide a quick introduction on the NTN scenarios and system characteristics and then focus on idle and connected mode User Equipments (UEs), providing an overview of the related mobility challenges.

1.3.1 NTN System Architecture

Based on the Radio Access architecture and interfaces described in 3GPP TR 38.801, [41], a set of architecture options has been defined within the NTN Study Item, as for TR 38.811, [12]. The impact of the NTN environment on the technologies developed for terrestrial NR systems is strictly linked to the scenarios and architectures under consideration: the type of "flying" element and its capabilities, the constellation, and the use cases shall be identified. Moreover, this impact does not only depend on the specific implementation of the *SatCom user*, *space*, and *ground segments*, but also on how these are interconnected and mapped to the NR network elements. In terms of the space segment, two macro-categories have been identified: the space-borne, *i.e.*, satellite-based communication platforms, and the air-borne, *i.e.*, High Altitude Platform Systems (HAPS), devices.

In the 3GPP framework, six macro-scenarios have been identified as outlined in Table 1.1. In all of the proposed scenarios, the user service link can be either in S-band (*e.g.*, 2 GHz) or in Ka-band (*e.g.*, 20 GHz in the downlink and 30 GHz in the uplink). For the LEO constellations, a further distinction is based on the type of on-ground coverage that is provided. In particular, on the one hand, the payload can be equipped to be able to steer the on-board antenna in order to always cover the same on-ground area, which means that the on-ground beams are not moving (as in the GEO scenarios). On the other hand, when no such capability is present, the area covered by each satellite will move accordingly with the satellite movement on its orbit, *i.e.*, the on-ground beams are moving with the satellite since the coverage centre is always located at the sub-satellite point. Another important aspect to be highlighted is that scenarios D1 and D2 are the only ones in which it is possible to implement an ISL, if needed for the chosen system architecture. These scenarios, which are classified based on the payload type and the presence or absence of an ISL, can then be mapped to different system architectures, as outlined below. From the beginning of NTN standardisation activities, scenarios A, C2, and D2 have been considered with higher priority; however, recently, the possibility to implement steerable beams (scenarios C1 and D1) is receiving an increasing attention. Finally, scenario B is not of interest, for the moment being.

TABLE 1.1: NTN reference scenarios per system type, [11].

System	Transparent	Regenerative
GEO	A	B
LEO steerable beams	C1	D1
LEO fixed beams	C2	D2

The different architectural options can be broadly categorised based on: i) the type of satellite payload, either transparent or regenerative, in which the satellite can contain a full gNB(s) (next generation NodeB), part of it in case functional split solutions are implemented, or a Relay Node (RN); and ii) the type of user access link,

either direct or relay-based, in which the UE is connected to a RN and not directly to the satellite. Before detailing the architectures, it is worth highlighting that, in Figures 1.4, 1.5, and 1.6, a single system Gateway (GW) is represented for the sake of clarity; however, it shall be noticed that multiple GWs can be deployed to provide connectivity to the data network(s). In this context, it is also worth mentioning that, for GEO systems, an on-ground beam is associated with a specific GW, while for non-GEO solutions specific requirements for service continuity shall be met to ensure that the successive serving GWs can manage the handover due to the satellites' movement.

1.3.1.1 Direct access

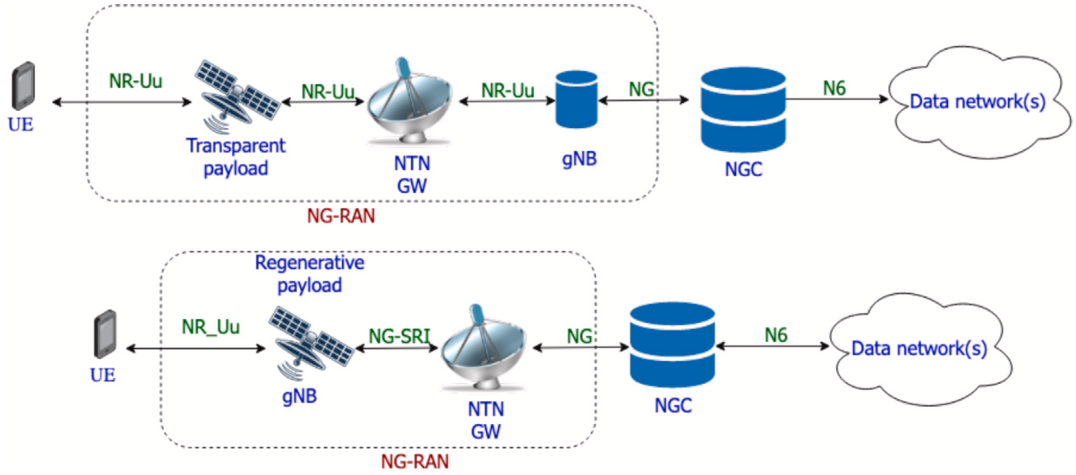

FIGURE 1.4: Architectural options with direct user access with transparent (top) and regenerative (bottom) payload. Applicable to: A, C1, and C2 (transparent); B, D1, and D2 (regenerative), [7].

Figure 1.4 shows the architectures with direct access. In particular, the top diagram refers to a transparent payload and the bottom one to a solution with regenerative payload. The difference between the two architecture options, is related to the location of the gNB. With a transparent satellite, the gNB is conceptually located at the GW, while with regenerative payloads it is implemented on-board. In both cases, the user access link between the satellite and the on-ground UE is implemented utilizing the traditional NR-Uu air interface; this air interface is specifically designed for terrestrial systems and, thus, it is of paramount importance to properly assess the impact of the satellite channel impairments on the PHY and MAC procedures. As for the feeder link between the satellite and the GW, the solution to be adopted depends on where the NR-Uu interface protocols are terminated, *i.e.*, on the position of the gNB: i) a transparent payload only acts as a radio-frequency repeater, thus not terminating the protocols, which requires the feeder link to be implemented with a NR-Uu solution; ii) in the regenerative payload case, the gNB is located on the satellite and, thus, the feeder link is implemented employing the NG air interface, *i.e.*, the air interface between a gNB and the Next Generation Core network (NGC). This

architecture is more expensive and complex; however, this solution also allows to significantly reduce the propagation delays for NR PHY and MAC procedures and, thus, to ease the adaptations that might be needed for NTN (for a detailed discussion, refer to the following sections). Moreover, the NG air interface on the feeder link is a logical interface, *i.e.*, can be implemented with any existing Satellite Radio Interface (SRI), as long as specific signalling operations are guaranteed, [42]. Thus, it can be implemented with a modified version of the terrestrial air interface, or even by means of SoA solutions for SatCom, as the DVB-S2, [43], DVB-S2X, [44], or DVB-RCS, [45], air interfaces.

1.3.1.2 Relay-based access

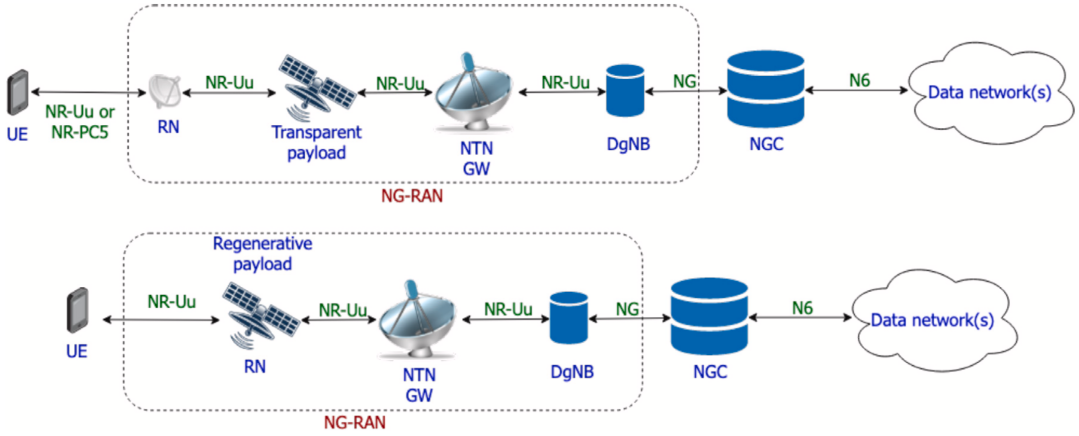

FIGURE 1.5: Architectural options with relay-based user access with transparent (top) and regenerative (bottom) payload. Applicable to: A, C1, and C2 (transparent); B, D1, and D2 (regenerative), [7].

Solutions based on RN, also known as Integrated Access and Backhaul (IAB) in 3GPP terminology, are currently considered for further study, [11]; however, they are worth being introduced for the sake of completeness. In this architecture, shown in Figure 1.5, the UE is connected to a RN, which is a network entity quite similar to its LTE equivalent. In particular, it is worth to be highlighting the following aspects for relay RNs: i) the RN is connected to a Donor gNB (DgNB), which is the entity providing connectivity towards the NGC; ii) the RN can terminate the procedures up to Layer 3; iii) the air interface on the user access link (RN-UE) can be implemented either as the traditional NR-Uu as for direct access or as a NR-PC5 interface, which is a device-to-device (or sidelink) air interface for NR, used, *e.g.*, in enhanced Vehicular-to-Everything (eV2X) applications; and iv) the air interface on the backhaul link (RN-DgNB) is a modified version of the NR-Uu air interface, in which only Radio Frequency characteristics and minimum performance requirements are different. Based on these operational aspects, the RN basically acts as a traditional gNB from the users' perspective, while it is seen as a UE from the DgNB, which motivates the implementation of the NR-Uu interface on both links and is also reflected in the RN attach procedure. The architecture with RNs and transparent payloads

(top diagram in Figure 1.5) is more complex with respect to the direct access scenarios due to the introduction of a potentially large number of on-ground relays, acting as gNBs; these entities must be managed by several DgNBs and, thus, the overall system cost might increase. However, since the RNs can terminate the protocols up to Layer 3, no modification is needed on the user service link. In this case, the impact of typical satellite channel impairments thus has to be assessed on the backhaul link only. When an on-board RN is implemented, *i.e.*, the regenerative solution, the payload cost increases but we also have the advantage of terminating the protocols up to Layer 3 on-board the satellite, as in the regenerative direct access architecture. In terms of feeder link, the connection between the RN and the DgNB must be implemented with a NR-Uu air interface, [44]. Finally, it shall be noticed that the NR-PC5 air interface can be implemented only when the RNs are on-ground.

1.3.1.3 Functional split

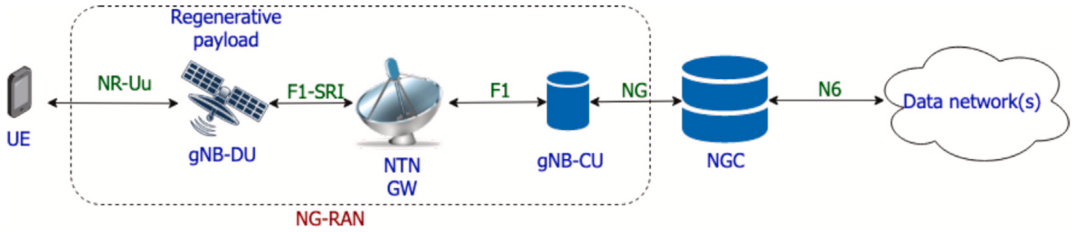

FIGURE 1.6: Architectural option with direct user access, regenerative payload and functional split. Applicable to B, D1, and D2, [7].

Figure 1.6 shows an architecture option with direct access and regenerative payload, in which functional split concepts are applied. The functional split allows scalable solutions, a significant adaptability to the different use cases and vertical services, and enhanced performance in terms of load and network management; moreover, it is at the basis of NFV and Software Defined Networking (SDN). Clearly, this solution also increases the overall system cost. As provided in TS 38.401, [42]: i) a gNB can be split into a Centralised Unit (gNB-CU) and one or more Distributed Unit (gNB-DU); ii) a gNB-DU can be connected to only one gNB-CU; iii) the air interface to be used between the gNB-CU and its gNB-DUs is the F1 air interface; iv) the F1 air interface is logical as the NG, *i.e.*, as long as specific signalling operations are ensured, it can be implemented by means of any existing standard, [46]. The split between gNB-CU and gNB-DUs can be implemented at different layers, and even within a given layer, as detailed in [41]; however, the most considered option in NR, which is also that considered for NTN for the moment being, is as follows: i) PHY, MAC, and Radio Link Control (RLC) (RLC) are implemented in the gNB-DU; and ii) the Packet Data Convergence Protocol (PDCP) and Service Data Application Layer (SDAP) for the User Plane (UP) or the Radio Resource Control (RRC) for the Control Plane (CP) are implemented in the gNB-CU. Finally, it is worth highlighting that intermediate solutions can also be envisaged: apart from a gNB-CU and the

controlled gNB-DU, there can be an Intermediate Unit (IU) that further splits the gNB in 3 entities and controls several gNB-DUs. This option is not yet considered in the current status of NTN systems.

1.3.1.4 Multi-connectivity

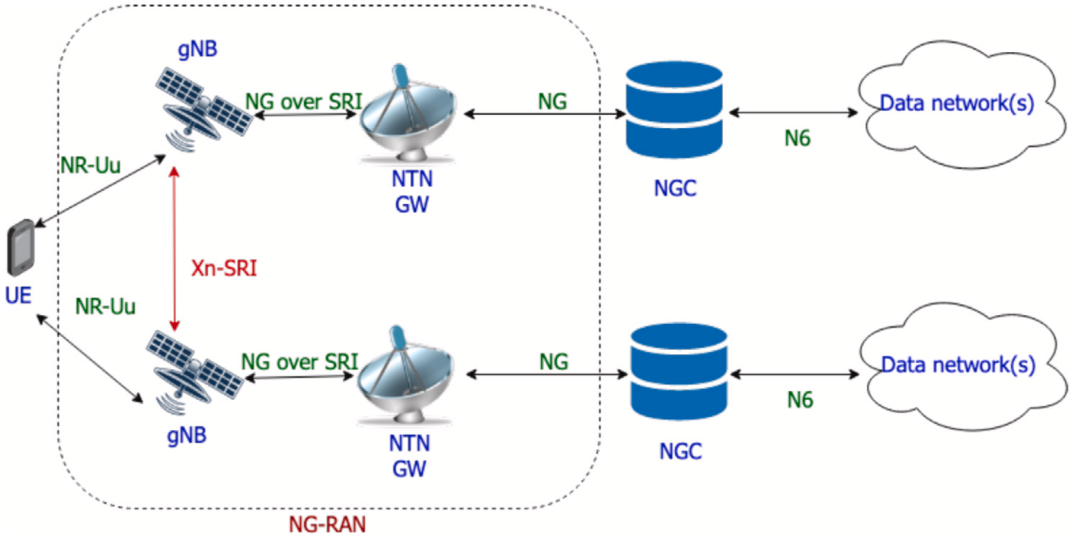

FIGURE 1.7: Architectural option with direct user access, regenerative payload and ISL. Applicable to B, D1, and D2, [7].

Figure 1.7, shows an architecture in which the UE can be simultaneously connected to more than one satellite. The satellites are assumed to be regenerative, but it shall be noticed that also solutions with transparent satellites (and, thus, no ISL) are considered for NTN. In addition, the possibility to have multi-connectivity with one NTN satellite and a terrestrial gNB are also foreseen. In the solution represented in Figure 1.7, the regenerative satellites are connected using the Xn air interface, which is a logical interface as the NG and F1, [47].

1.4 Satellite IoT

In the last few years, IoT applications have drawn a great deal of attention, both in academia and industry. It is, in fact, expected that IoT devices will be half of the global connected devices within the next few years, with 14.7 billion M2M connections by 2023, as shown in Figure 1.8, [48]. Connected IoT devices include connected cars, machines, meters (water, gas, electric, or parking), sensors, point-of-sales terminals, consumer electronics, wearables and so on. IoT applications can be divided into *short-range* and *wide-area* segments: in the former, the devices are connected to the network by means of unlicensed radio technologies, such as Wi-Fi, Bluetooth and ZigBee; in the latter, for which a massive growth is foreseen, mostly rely on 3GPP compliant standards (*e.g.*, 2G, 3G, 4G, and 5G) or alternatives like Sigfox and

LoRa, for connectivity. Furthermore within the wide-area segment, two distinct sub-segments with different requirements have emerged: *massive* and *critical* applications.

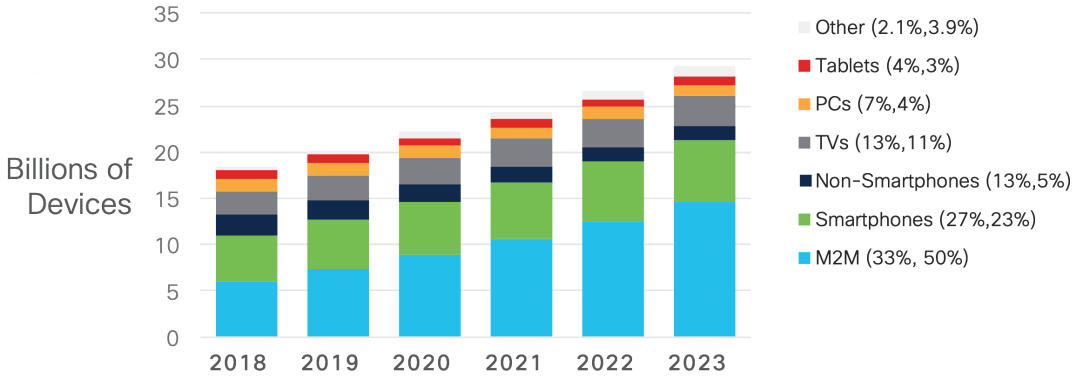

FIGURE 1.8: Global device and connection growth, [48].

A crucial requirement for any infrastructure serving the IoT market will be to guarantee ubiquitous connectivity to the low-cost, low-powered devices distributed all over the globe. It is widely accepted that this requirement will not be met by the terrestrial network alone. There will be, in fact, vast areas of the globe where the terrestrial infrastructure deployment will be unfeasible or not economically viable, thus leaving those areas un- or under-served. For this reason, several studies are addressing the use of a NTN component to seamlessly complement and extend the terrestrial network coverage in future systems [6], [24], [25].

Undoubtedly, IoT communication via satellite represents a great opportunity for the satellite market, and many funded projects are currently addressing SatCom-based IoT systems, as, for instance: i) E2UT, with the objective of designing and demonstrating solutions for compact and energy efficient M2M user terminals for direct, massive uncoordinated access via satellite, [49]; ii) NB-IoT4Space, which aims at developing a demonstrator to functionally verify the communication between a NB-IoT user and the eNB on-board the satellite, [50]; iii) LacunaSat-1, which has proven and continues to prove the concept of receiving LoRa messages in space successfully and from locations all around the world, [51]; iv) IOT SATBACK, with the aim of designing and developing a prototype backhauling solution for future NB-IoT networks, [52]; v) R3-IoT, for providing industrial IoT via smart satellite backhaul sustaining mass-manufacture, [53], [54]; and vi) M2MSAT, with the objective of reviewing and proposing improvements for the prominent light-weight application and transport protocols for M2M/IoT communications, [55].

In addition to the above efforts in terms of funded projects, also the scientific literature has provided a valuable addition to the study and development of the S-IoT use case. In [56], an overview of the IoT scenarios and use cases in which satellite systems can play a key role is provided, focusing on the concept of "Internet of Remote Things". In [57], the authors focus on the LEO satellite constellation-based IoT services, analysing the possible use cases and proposing some possible constellation

design to fullfil their requirements. The author in [58] gives an interesting overview of the evolution of the satellite air interfaces evolution for serving the IoT scenarios. In [59], the authors study the LoRa adaptability in the IoT use case for LEO satellites. In [60], the authors explore the potential of SatCom systems in 5G MTC.

Besides air interfaces like SigFox and LoRa solutions, also the 3GPP showed an ever growing interest towards the IoT market introducing a number of key features for supporting the IoT use case since Release 13. Furthermore, besides the NTN standardisation process, the 3GPP decided to study the feasibility of using the NB-IoT air-interface over the NTN in its Release 17 [61]. The study phase, starting in 2021, will identify the needed adaptations and assess the performance of NB-IoT over NTN. In this framework, several scientific works have been published on the subject. In [62] the authors give a preliminary analysis on the key system aspects for NB-IoT air interface implementation over NTN. In [63] the authors review the fundamentals of NB-IoT and NTN and explain how NB-IoT can be adapted to support satellite communication through a minimal set of modifications. An interesting study for the NB-IoT feasibility over GEO satellite is done in [64], where the authors consider the necessary mechanisms for adapting NB-IoT to the satellite context, providing a study of the delay of a communication as function of gNB parameters, cell specification (*e.g.*, size, link budget, satellite altitude), and payload size. An overview of the possible challenges of NB-IoT over NTN is reported in [65]. The effects of the high *Doppler* and *delay* induced by non-geostationary satellites and the possible countermeasures are detailed in [30], [66], [67]. The design of a NB-IoT receiver in the presence of Doppler effects, at the GW side, is addressed in [68]. An initial interesting analysis of the *link budget* is presented in [69], where the case of a single LEO satellite, at a given elevation angle is addressed to shed light on the trade-offs between the link parameters and the payload characteristics. The authors in [70] propose a link budget analysis thoroughly following the simulation parameters and requirements of 3GPP standardisation process.

As an alternative to SatCom systems, Global Navigation Satellite Systems (GNSS), *i.e.*, Galileo, Global Positioning System (GPS), GLObal NAvigation Satellite System (GLONASS), and BeiDou Navigation Satellite System (BDS) BDS, constellations are already providing an ubiquitous, continuous, and highly reliable coverage; thus, they can represent an efficient integration to the forthcoming satellite mega constellations in serving the IoT use cases. Among these systems, BDS stands out for its two-way communication function, providing a bidirectional Short Message Service (SMS). This feature can be used to provide emergency communications in harsh environments, *e.g.*, after natural disasters, and can open the way for other applications like, for instance, power-grid on-line monitoring systems [71]; satellite distance education systems to serve remote areas [72]; voice services based on ultra low bit rate vocoders [73], [74]. Similarly, through the Galileo infrastructure, several services, beyond the positioning ones, are already enabled with the current satellite generation. Among these, Satellite–based Search and Rescue (SAR) is the most important one,

allowing for the localizations of distress beacons. An extension of the SAR feature has been proposed in [75] through the introduction of a Galileo-based SMS service. On the basis of those considerations, the authors in [76], proposed a Two-Way Messaging feature for the Galileo Second Generation (G2G) satellite constellation.

1.4.1 IoT Technical Requirements and Impacts for SatCom Integration

Considering the vast number of IoT verticals, *e.g.*, industrial IoT, transportation and logistics, smart cities, smart agriculture, smart buildings, smart oil and gas, connected healthcare, the requirements are manifold and diversified. Based on the nature of the deployed application, IoT can be segmented into two main categories with very distinguishable network requirements: Massive and Critical IoT, as previously mentioned. The former is characterized by billions of low-cost and low-energy devices spread throughout the globe, able to generate small traffic volumes reporting information to the core network on a regular basis (*e.g.*, sensors in a smart home, smart metering, environmental sensor etc.). The latter has to cope with ultra-high reliability, availability, and extremely low latency communications (*e.g.*, remote surgery, health care, tactile Internet, traffic safety *etc.*). Despite the profoundly different nature of the applications, the requirements can be summarized in few categories as follows.

1.4.1.1 Low Cost and Complexity

Lowering the device complexity and using low cost hardware components (targeting a total cost of few tens of euros) are key enabler for massive-volume, mass-market applications. Design characteristics, such as using single receive RF chain, restricting supported peak data rates to the maximum required by IoT applications, reducing supported data bandwidth, help cutting down the production and deployment costs.

However, these key requirements for IoT applications could result in some limitations for the integration with satellite systems and the terminal design should be developed according to the target SatCom scenario to serve. For example, in order to achieve these goals, the use of integrated circuits for signal processing, digital/analog conversion, and possibly RF functions is critical. The UE local oscillator must be economical while still providing acceptable performance in terms of phase noise and frequency stability. The power amplifier range typically varies from a few milliwatts to less than 1 W of radio frequency peak power depending on the frequency band and type of service. Finally, omni-directional patch antennas are used whenever possible to reduce manufacturing and installation costs, [60]; however this could lead to some difficulties in closing the link budget due to the lower gain. Another possible source of price increase could be the presence of a GNSS

receiver for delay and Doppler pre-compensation. SDR can help improve functionalities and performance of devices extending their life through over-the-air updates, thus reducing their cost.

1.4.1.2 Energy Efficiency

Since most IoT devices are battery powered and are expected to be operational for a very long period without human intervention, achieving a high-level of energy efficiency for IoT UEs is of paramount importance, in particular when they are deployed in remote areas. The main sources of battery drain in the IoT UE can be identified in: i) power consumption during the activity period, *i.e.*, transmission and reception phases; ii) Idle/Sleep mode power consumption. While the latter is strictly related to the hardware characteristics, for the former different optimisation solutions could be followed. Ideally, the device should only be activated for the minimum time required to send the information bits, minimizing packet retransmissions. This implies that signalling information during idle/sleep status is minimized. When switched to active status, the UE should have a fast (re-)acquisition time and exploit a protocol that minimizes the energy required for transmitting the information bits.

However, keeping the device cost low, thus using low quality oscillators, and reducing the battery drain through minimizing the signal processing, makes fast synchronization acquisition harder. To overcome these issues and adapt to the satellite scenarios, further information, (*e.g.*, GNSS information, like satellite constellation ephemeris, to compute satellite visibility windows) should be made available for the UE. Besides that, the adoption of an energy efficient air-interface could lead to reduction in terms of battery consumption, as in the case of the optimisations that will be suggested in Chapter 7 for the NB-IoT air-interface. Despite the optimisations, the required transmission power for closing the link could lead to an increased energy consumption, which must be considered. This is particularly true for GEO scenarios, which would require UEs equipped with specific outdoor units to aggregate and transmit sensors' data.

1.4.1.3 Support for Massive Number of Devices

It has been envisaged that in the next few years, there will be several billion of mMTC devices connected by means of cellular technologies, with IoT connectivity growing faster with respect to legacy mobile broadband connections. For what concerns the UE density, depending on the location and on the type of application, some cells will be more densely populated than others (*e.g.*, up to thousands of devices per square kilometer) and, therefore, IoT connectivity solutions should be able to simultaneously handle most of these connected smart devices, [77]. As for the network resource allocation, due to the sporadic traffic characteristics (*e.g.*, small daily monitoring data exchange as opposed to massive data burst after a natural disaster from environmental sensors) and IoT terminals distribution, fixed frequency and power

allocation could result in a waste of resources. For this reason, flexible payload with dynamic resource allocation, or the utilization of SDR, could result in overall better system performance and optimisation.

In order to cope with this massive number of connections, efficient air-interfaces are needed. The 3GPP NB-IoT technology previously mentioned meets this requirement and could be adopted in the satellite scenario through some adaptations, which will be better discussed in Chapter 7 (*e.g.*, RA procedure and timers to cope with larger propagation delays and discontinuous connection to the NGC/Evolved Packet Core network (EPC), in case of store and forward satellite architectures and LEO satellites). Considering the S-IoT requirement for signalling overhead and the UE energy consumption minimization, an appealing Multiple Access solution could also be the Enhanced Spread Spectrum ALOHA (E-SSA). Because of the large propagation delay, terrestrial RA protocols are inefficient, then the introduction of efficient NOMA RA schemes minimizing signalling overhead and packet retransmissions solved the problem. Furthermore, Successive Interference Cancelation (SIC) allows resolving packet collisions reducing the need of retransmissions [8], [9].

1.4.1.4 Extreme Coverage

The extension of the coverage is a major design requirement for Massive IoT connectivity when considering applications in remote areas and in general in areas characterized by a very poor coverage (*e.g.*, assets tracking, solar, oil&gas harvesting, environment monitoring, mining, *etc.*). Satellites can provide worldwide coverage for IoT devices, in densely populated areas as well as in remote ones, providing especially in the latter a cost-efficient solution with respect to other terrestrial technologies for UEs interconnection and communication with the rest of the network. According to the scenario and the satellite constellation parameters (*e.g.*, GEO with regional/global coverage, LEO mega-constellation with global coverage or LEO constellations with discontinuous coverage), different type of IoT services could be enabled.

1.4.1.5 Latency

Although most of the IoT applications, falling into the Massive IoT category do not require stringent latency requirements (*e.g.*, smart-cities/home, smart power systems, agriculture/environment monitoring, *etc.*), there are some applications, falling into the Critical IoT applications (*e.g.*, remote healthcare, traffic/industrial control, tactile Internet, *etc.*) for which low latency is of paramount importance. For the latter, the delay constraints of GEO could make it impossible to meet the requirements.

Regarding Non-GEO scenarios, it could be possible to meet stringent latency requirements if the satellite constellation and ground segment are properly designed, such to allow a continuous connection among the UEs and the GWs, either directly or through ISLs. For what concerns these scenarios, it is worth highlighting that

the short satellite visibility windows (*e.g.*, few minutes depending on the satellite altitude) and the fast handover (*e.g.*, from few seconds up to few minutes according to the satellite altitude and antenna pattern design) among different cells, in the case of moving beam reference scenario, should be taken into account. This happens in particular when a continuous satellite coverage cannot be ensured and the UE connection to the network must be guaranteed within a few opportunity windows throughout the day. Moreover, it is worth highlighting that, according to the chosen air interface and architecture, a proper evaluation of the impact of the propagation delay on protocol procedures and timers should be performed.

1.4.1.6 Security and Privacy

Aspects regarding security and privacy are also design requirements to be considered in IoT applications. Indeed, the IoT UE real identity should be protected from the public, but at the same time it shall be traceable by authorities if the need arises. As an example, location privacy is of utmost importance as this can reveal the physical location of the IoT device. Additionally, forward and backward security should be supported for effective deployment of IoT use cases, [77]. With IoT, the diversity of devices and the usage models will largely vary. Moreover, during their life cycle these IoT devices go through different stages, involving the change in ownership among different operators, change of subscription, *etc.* A method of dynamic subscription generation and management is needed, and must be managed securely and efficiently by the UE authentication in the network, avoiding security leakage, [78]. Finally, the satellite visibility window duration and handover must be taken into account also for security purposes.

Chapter 2

The ESiM2M System Level Simulator

As discussed in the previous chapters, the New Space trends and the escalating demand for small satellites for services in various industries (*e.g.*, oil and gas, energy, agriculture), for earth observation, and defense across the globe, are the primary factors driving the satellite market growth. Besides, the emergence of IoT and the vision of Billions of objects being connected to the Internet have drawn a great deal of attention, both in academia and industry, becoming a key driver for telecommunication markets for the next years. The natural synergy between these two sectors has contributed to the birth of several private and governative initiatives in the last period. Furthermore, the thrust coming from the 3GPP standardisation process, with its Study Items on NB-IoT/enhanced Machine Type Communication (eMTC) support for NTN [79], is leading to a deeper symbiosis between these two worlds.

The design of these extremely complex systems, as described in Chapter 1, requires manifold analyses at different levels of abstraction, from satellite constellation and ground segment architecture aspects to the evaluation of the air interface behaviour, in order to understand the system performance. From direct measurements in a real environment to analytical mathematical derivation, there are many approaches for analysing wireless mobile networks. However it should be taken into account, when learning about emerging technologies, that full-featured systems do not yet exist; moreover, due to the extremely complex and multi-factor design, complete analytical methods could hardly be applicable. That is why computer simulation is a fundamental tool for the design of modern telecommunication systems. A broad variety of modelling software are available on the market to satisfy the specifications for design processes in any area of the system (*e.g.*, AGI STK for constellation design, TICRA SATSOFT for satellite antenna pattern design, *etc.*). However, in this wide panorama of instruments, there was a lack of one that could take into account all the key aspects of a complex SatCom system, being still versatile and properly optimised to allow rapid system analyses to be carried out effectively in order to analyse various aspects of the system. In particular, a simulation tool was needed for carrying out research in the field of S-IoT.

To meet this need, I developed, in collaboration with ESA, a System-Level Simulator, ESiM2M, during my period abroad in the Telecommunication Systems & Techniques Section of European Space Research and Technology Centre (ESTEC), in the Netherlands, [80]. The tool has been fully developed in MATLAB®, taking as an example another simulation tool, LEOSIM, developed in the same section in ESTEC, [81].

The main objective of this tool is the modelling of the user UL of a satellite system, for the reference use case of mMTC applications performing direct access to the satellite network. In this chapter, the tool will be introduced with all its basic components; then, the mathematical framework behind the main building blocks of the simulator will be analysed in detail in the following chapters.

2.1 Simulator Scope

The simulator foresees a massive number of simple IoT devices that may be deployed at arbitrary locations on earth, accessing the network through single- and multi-plane, full or partial satellite constellations at LEO, MEO, GEO, and hybrid orbits (*e.g.*, LEO+MEO or LEO+GEO). The outputs of the simulator are manifold (*e.g.*, Packet Loss Ratio (PLR), throughput, latency, *etc.*) and can be derived for different air interfaces already implemented in the simulator (*e.g.*, E-SSA, Contention Resolution Diversity Slotted ALOHA (CRDSA), ALOHA, Slotted ALOHA (S-ALOHA), NB-IoT) for different scenarios (*e.g.*, satellite constellation, UT and GS deployment, *etc.*). It is thus possible to design and test new system-level solutions.

2.2 Space and Ground Segment Simulation Models

It is possible to identify three main entities in the simulator: i) the Satellite; ii) the UT; and iii) the GS. Each one with its specific features and functions. The main characteristics of their simulation models are described in the following.

2.2.1 Satellite

The satellite payload, for the purpose of this simulator, has to be intended as transparent or regenerative, according to the simulation parameters. The main characteristics defining the satellite model are:

Antenna: according to the type of chosen payload, the antenna is modelled either with a generic antenna pattern file (*e.g.*, GRASP files, θ-ϕ vs Gain) or with an analytical antenna pattern (*e.g.*, Bessel, IsoFlux). Both single- and multi-beam antennas are supported.

Links: carrier frequency and bandwidth on both user and feeder links can be configured according to the scenario and the air interface to be simulated (*e.g.*,

S-band with 180 kHz of bandwidth for NB-IoT). As a further improvement of the tool, ISLs are under development.

Access Paradigm: for what concern the unslotted RA paradigms, all the satellites visible from a UT will try to decode its packets (*i.e.*, if the packet SINR is above the capture SINR threshold, the satellite will try the decoding). Once a packet has been decoded from a satellite, it is stored in the satellite buffer. In the first available visibility window with a GS, the buffer will be emptied according to the maximum allowed throughput for the feeder link and the duration of the visibility window. As for the slotted RA paradigms, a further simplification has been done: the UT is considered synchronous only with the best serving satellite, *i.e.*, the satellite in visibility with the best link budget for that UT in that snapshot. Then, only this selected satellite will try to decode the packets of that UT, while all the other visible satellites will consider them as interference.

Constellation: ESiM2M allows to handle swarms of LEO, MEO, GEO satellites and also hybrid constellations, either complete or partial. The statistics computed based on the simulator outputs are meant for each satellite in the constellation, which can be seen as a separate entity with its own characteristics, and for the whole swarm.

2.2.2 User Terminal

A UT, for the purpose of this simulator, has to be intended as a simple IoT device deployed at a fixed geographical position. A feature encompassing UT mobility, with the UTs changing their geographical positions during the evolution of the simulation, could be considered for further enhancements. The main characteristics defining the UT model are:

Antenna: the UT antenna is omnidirectional as default. Furthermore the simulator is capable of handling tracking antennas and taking as input a generic antenna pattern file (*e.g.*, θ-ϕ vs Gain, GRASP files, analytical, omnidirectional).

UT Distribution: UTs can be either uniformly distributed, according to a specific UT density, or deployed on specific positions over latitude-longitude (*lat-lon*) coordinates, based on input UT distribution files.

Data Traffic: the traffic generation per UT follows a Poisson distribution, with reconfigurable parameter λ, according to the traffic intensity associated with the UT at the beginning of the simulation. Data traffic is considered per individual UT, with no traffic aggregation. According to the simulated protocol and the associated rules, a packet may be transmitted only when the UT has at least one satellite in visibility. If this does not apply, all the packets generated at timestamps with no satellites in visibility will be stored in the UT buffer. In the first available satellite visibility window, the buffer will be emptied according

to the maximum allowed throughput and duration of the visibility window. The packet will be delayed by a random back-off, according to the simulated air-interface, in order to simulate an UL channel congestion avoidance technique.

Access Paradigm: ESiM2M is mainly focused on the user UL channel and in RA procedures. In particular, the target air interfaces, simulated by their specific PHY abstraction, are: E-SSA, CRDSA, ALOHA, S-ALOHA, and NB-IoT; other air interfaces are being considered for further enhancement.

Signaling: in general, forward link signalling for Channel State Information (CSI) and grant procedures is not required and will not be simulated. For example, Acknowledgment (ACK)/Non-ACK (NACK) messages are not actually generated; an ACK will be considered received if the packet has been decoded by the PHY abstraction, otherwise a NACK will be assumed and the packet will be scheduled for a retransmission, if foreseen by the simulated protocol.

Power: the UTs have to be intended as powered by battery. A fixed power class for the UTs is chosen as an input parameter of the simulator. Moreover, power randomization in transmission is supported. Further enhancements should include battery consumption statistics according to the activation time.

2.2.3 Ground Station

The feeder link is assumed to be ideal, and the GS antenna is always perfectly tracking the satellite seen at the highest elevation angle in its FOV; then, except for the Free Space Loss (FSL), there is no other impairment affecting the transmission between the satellite and the GS. At the current stage of the simulator, the deployment of the GSs allows to properly analyse and design the system architecture in order to meet the latency requirements of the system. Indeed, it is possible to account for the actual latency experienced by a packet from its generation to its reception at the core network.

Since the feeder link is ideal, signalling is not required. It is assumed that the connection between the satellite and the GS is established when the elevation angle is higher than a threshold (*e.g.*, $\varepsilon > 10°$). Then, the link will be established at the maximum achievable throughput for the whole duration of the satellite visibility window and it will be used to empty the satellite buffer.

2.3 System Level Simulator architecture

A Monte Carlo simulation approach has been adopted in ESiM2M in order to compute the Key Performance Indicator (KPI) and analyse them. In particular, a time-driven simulator has been realized, where the satellite constellation geometry, the Link Budget (LB), the stochastic shadow fading, as well as the interference due to

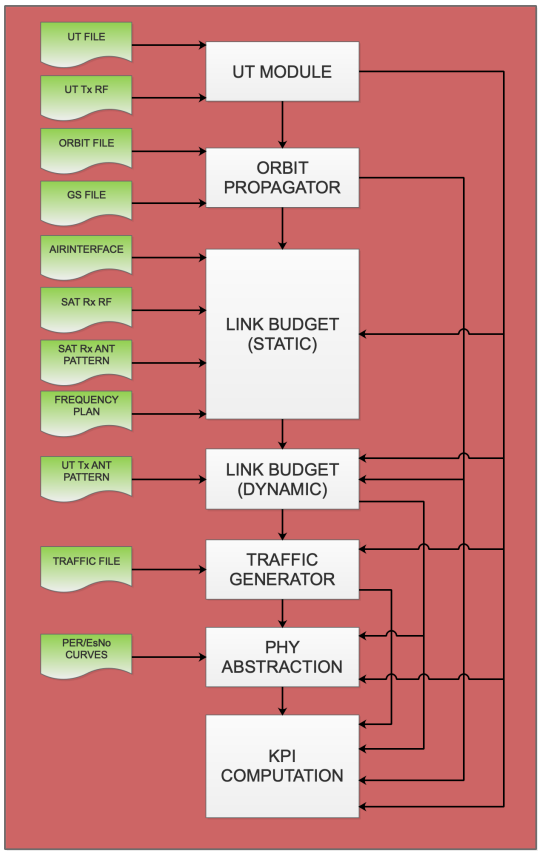

FIGURE 2.1: High-level system-level Simulator architecture.

the generated traffic conditions, vary at each simulation step. The simulation step width must be properly chosen according to the simulated scenario, in order to make the stationarity condition valid, *i.e.*, the hypothesis of fixed satellites positions, fixed UTs positions, and stationary channel conditions. The ESiM2M can be seen as composed of two main simulation parts, each one characterized by specific modules and functions:

Offline Simulation: in this part of the simulation the UTs are deployed and the state vectors describing the constellation evolution are pre-computed. A partial computation of the link budget and the Signal-to-Noise Ratio (SNR) is performed, without taking into account the actual interference generated by the UTs, in order to reduce the computational complexity of the Online simulation.

Online Simulation: in this part, the actual time-driven simulation runs for the whole time duration chosen for the analyses to be performed. The time step granularity is a parameter that can be tuned according to the precision needed for the analyses. It is possible to start with longer snapshot durations such as to test some specific constellation geometries, and then increase the simulation resolution to achieve statistical convergence.

The high-level architecture of the simulator, with its main modules, is shown in Figure 2.1; in the following, the basic behaviour and functions will be described.

2.3.1 Offline Simulation Modules

2.3.1.1 User Terminal distribution

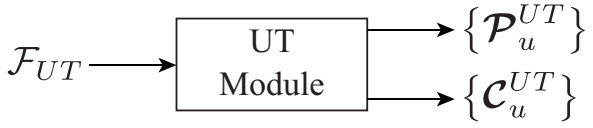

FIGURE 2.2: UT module, high-level Architecture.

UTs objects are defined with their attributes (*e.g.*, position, antenna type, power class, *etc.*). In order to properly assess the performance for different satellite constellations, coverages, and GSs distributions, the tool is capable of handling flexible UTs deployment by adopting custom input files. As it is shown in Figure 2.2, the input file $\mathcal{F}_{UT}$ contains all the informations regarding the UTs geographical locations, $\{\mathcal{P}_u^{UT}\}$, and device characteristics (*e.g.*, RF, amplifier, *ets.*), $\{\mathcal{C}_u^{UT}\}$[1]. It is also possible to generate $\mathcal{F}_{UT}$ for randomly distributed users populations on ground and/or to generate UTs populations based on public available data sets on the user density per geographical area. Different UTs distributions, as well as a variable number of UTs in the system, can be chosen according to the scenario characteristics.

2.3.1.2 Orbit Propagator

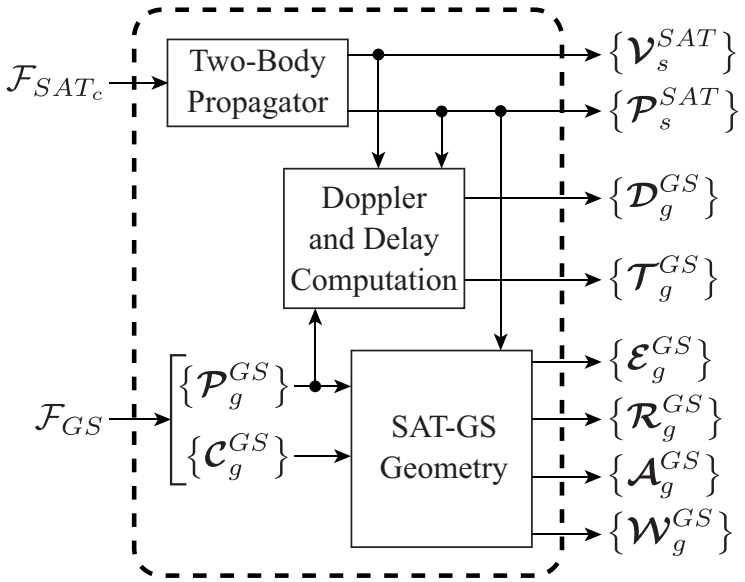

FIGURE 2.3: Orbit Propagator module, high-level Architecture.

[1]In the remainings of the chapter: i) the {curly braces}, will define a set of values; ii) the boldface will define an array list of values; and iii) the overline will define a grid of value (*e.g.*, u-v coordinates grid). For example $\{\mathcal{P}_u^{UT}\}$ contains the position vector of all the u users, and $\{\overline{\mathbf{SNR}}_{s,h}\}$ is the set of grids containing the SNR values for all the satellites s and all the spacecraft orientations h.

As depicted in Figure 2.3, a user-defined constellation can be modelled through a constellation input file, $\mathcal{F}_{SAT_c}$, containing the classic orbit elements, *i.e.*, semi-major axis, eccentricity, inclination, Longitude of the ascending node, argument of the periapsis, and true anomaly. The orbit propagator is based on the Two-Body model. Starting from a reference epoch and given the Keplerian orbital elements, the state vectors, *i.e.*, position, $\{\boldsymbol{\mathcal{P}}_s^{SAT}\}$, and velocity, $\{\boldsymbol{\mathcal{V}}_s^{SAT}\}$, for all satellites are computed at each simulation step. Knowing the successive spacecraft positions at each simulation step, *i.e.*, ephemerides (thus, its trajectory), it is possible to compute the geometrical relationship of each satellite with respect to the GSs on ground, which characteristics are contained in a user defined file $\mathcal{F}_{GS}$. Then the GSs slant range, $\{\boldsymbol{\mathcal{R}}_g^{GS}\}$, elevation, $\{\boldsymbol{\mathcal{E}}_g^{GS}\}$, azimuth, $\{\boldsymbol{\mathcal{A}}_g^{GS}\}$, propagation delay, $\{\boldsymbol{\mathcal{T}}_g^{GS}\}$, visibility windows, $\{\boldsymbol{\mathcal{W}}_g^{GS}\}$, Doppler shift, and Doppler rate, $\{\boldsymbol{\mathcal{D}}_g^{GS}\}$, are computed for the whole simulation duration. Finally, an ordered list of best tracking GSs per satellite is extracted at each time step of the simulation, based on the elevation angle at which the satellite is seen from the GS. Furthermore, it is possible to generate a simple ad-hoc satellite constellation file, $\mathcal{F}_{SAT_c}$, by choosing only the number of satellites and orbital planes as input parameters. A detailed description of the satellite orbit design and geometry is given in Chapter 4.

2.3.1.3 Link Budget (static)

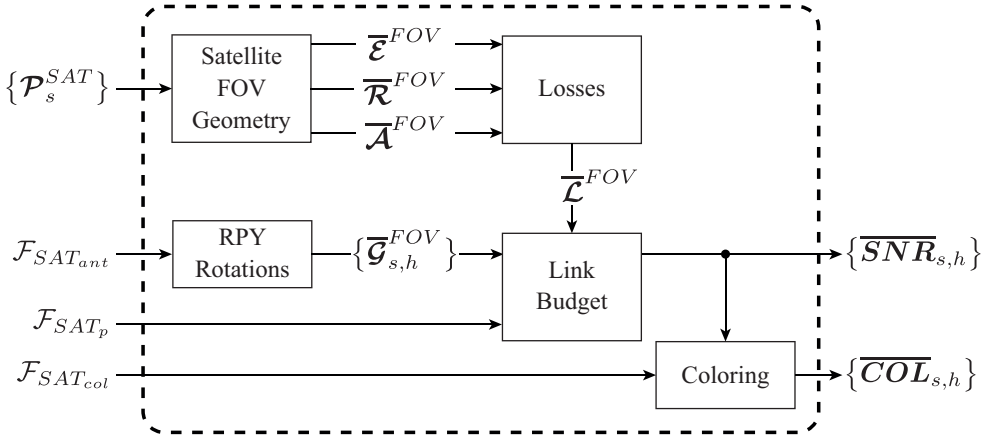

FIGURE 2.4: Link Budget (static) module, high-level Architecture.

This module allows to pre-compute a partial value for the SNR values with respect to the FOV of the satellite, represented by a grid in *u-v* coordinates[2]. The satellite FOV, thus the *u-v* grid size, depends only on the altitude, heading, and tilt of the satellite. Then a different grid is computed for each unique combination of those parameters.

[2]The *u-v* coordinates system is described in Chapter 3.

The main operations, depicted in Figure 2.4, can be summarized as follows[3]: i) The file describing the antenna pattern, $\mathcal{F}_{SAT_{ant}}$, the one describing the satellite payload characteristics, $\mathcal{F}_{SAT_p}$, the file containing the frequency reuse scheme, $\mathcal{F}_{SAT_{col}}$, and the satellite position computed by the previous module, $\{\boldsymbol{\mathcal{P}}_s^{SAT}\}$, are taken as input. ii) Firstly, the slant range, $\overline{\boldsymbol{\mathcal{R}}}^{FOV}$, elevation, $\overline{\boldsymbol{\mathcal{E}}}^{FOV}$, and azimuth, $\overline{\boldsymbol{\mathcal{A}}}^{FOV}$, grids are computed, based on the geometrical relations among the satellite and the points in its FOV. iii) Then, exploiting these geometrical outputs, the FSL and the characteristic losses, $\overline{\boldsymbol{\mathcal{L}}}^{FOV}$, of a satellite channel (*e.g.*, tropospheric/ionospheric scintillation losses, atmospheric losses, *etc.*) are computed. iv) After that the RF parameters for the satellite are taken as input (*e.g.*, satellite antenna pattern, input losses, *etc.*). Different types of payload are supported by means of user defined input files, containing the receiving chain parameters. v) The satellite antenna pattern is extrapolated from a GRASP file or it is defined by an analytical function (*e.g.*, Bessel antenna) and is transformed by means of Roll-Pitch-Yaw (RPY) rotations (as explained in Chapter 3) in order to take into account the actual heading, h, of the satellite, s, obtaining a grid, $\{\overline{\boldsymbol{\mathcal{G}}}_{s,h}^{FOV}\}$, with the values for the satellite antenna gains. vi) The noise value is computed according to the receiver characteristics of the satellite payload and the bandwidth chosen for the simulated air interface. vii) Once the fixed gains, powers, noise and losses are known, it is possible to pre-compute the grid containing a partial value for the SNR, $\{\overline{\boldsymbol{SNR}}_{s,h}\}$, which does not account for the statistical terms of the LB, which will be considered in the online simulation modules. viii) Furthermore, a grid containing the coloring scheme adopted in the beam pattern, $\{\overline{\boldsymbol{COL}}_{s,h}\}$, is computed according to the coloring scheme and frequency reuse files defined by the user.

Notably, considering an antenna pattern in a fixed position with respect to the Sub-Satellite Point (SSP) and referring to satellites moving on circular orbits, the relationships among the satellite antenna (*e.g.* the antenna gain) and the access area does not change, regardless the spacecraft position on its orbit. For the ESiM2M it is then possible to pre-compute some of the LB components previously described, and store them on u-v grids which are independent from the position of the SSP. Furthermore, the transformations between θ-ϕ and u-v coordinates is immediate, as described in Chapter 3, so the values can be represented and stored with respect to the satellite FOV. Only when the final LB, taking into account also for the interference is computed, these values are projected onto *lat-lon* coordinates grid for each specific SSP of the satellite constellation. This technique for reducing memory occupancy has been inherited from LEOSIM tool [81].

Although this concept of storing data on a grid with fixed resolution can be used to speedup simulations, with ESiM2M is also possible to compute dynamically the LB, without the need of any pre-computation. This alternative is suitable for being

[3]The complete mathematical formulation for the link budget analyses, with the computation of all the fixed and statistical parameters, is thoroughly described in Section 6.2.

used in the Highly Elliptical Orbit (HEO) applications and in the steerable beam use case, which are under development.

2.3.2 Online Simulation Modules

2.3.2.1 Link Budget (dynamic)

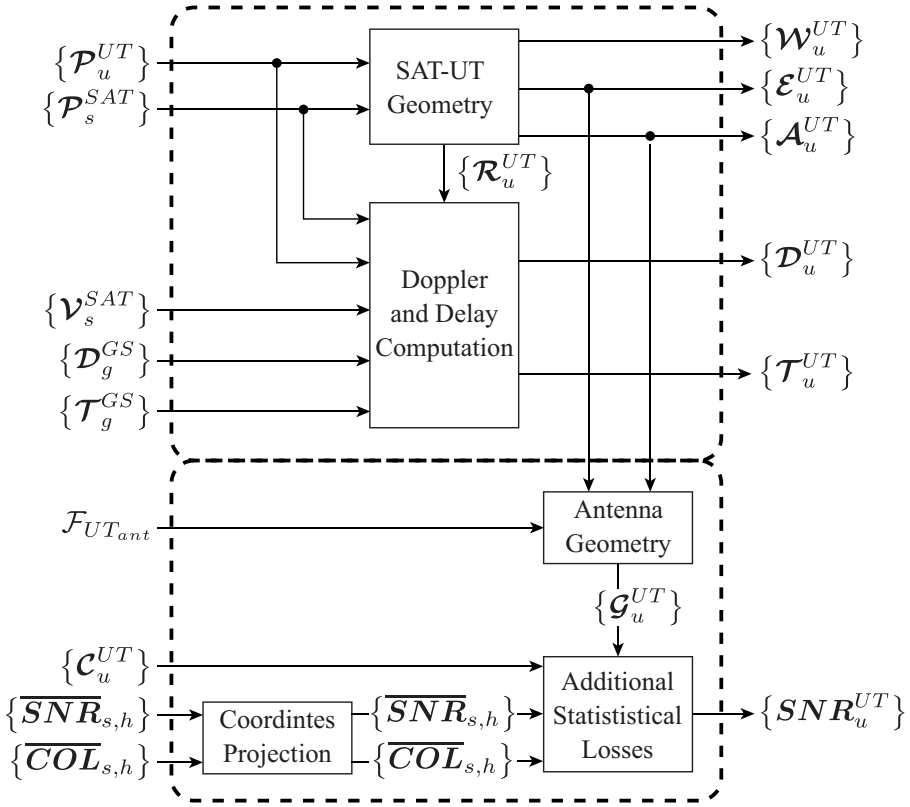

FIGURE 2.5: Link Budget (dynamic) module, high-level Architecture.

As it is shown in Figure 2.5, this module takes as input the outcomes of all the offline simulation modules, and the antenna files of the UTs. At each simulation step, the grids with the partial value for the SNR values are projected onto the actual coverage in *lat-lon* coordinates for each satellite, for that time step. According to the actual constellation geometry for the current orbital step, the UT-to-satellite geometry is computed, the slant range, $\{\mathcal{R}_u^{UT}\}$, the elevation, $\{\mathcal{E}_u^{UT}\}$, and the azimuth, $\{\mathcal{A}_u^{UT}\}$, are evaluated from each UT. Then the UTs visibility analysis is performed, evaluating which are the visible satellites for each UT, $\{\mathcal{W}_u^{UT}\}$.

Based on the visibility assessment and the geometry of the system, the actual antenna transmitting gain is computed for the UTs, $\{\mathcal{G}_u^{UT}\}$, taking into account the UT antenna pattern file, $\mathcal{F}_{UT_{ant}}$, de-pointing loss, and polarisation mismatch loss. Known the actual transmitting gain and the transmitting power (*e.g.*, if power control or multiple power class are used, any UT could have a different transmission power) the Equivalent Isotropically Radiated Power (EIRP) is computed for each

UT. The statistical shadow fading loss, modelled as a Log-Normal Random Variable (RV) is added to the overall losses. Eventually the partial value SNR, precomputed as previously described, can be completed with all the aforementioned parameters. According to the SNR value so computed, $\{\boldsymbol{SNR}_u^{UT}\}$, it is possible to determine which are the best serving satellite-beam pairs, by picking the highest value of SNR for each UT, for that specific simulation step. The detailed Link Budget computation for a satellite channel is thoroughly described in Section 6.2. Furthermore, the Doppler shift and Doppler rate, $\{\boldsymbol{\mathcal{D}}_u^{UT}\}$, are computed for every UT with respect to each satellite in visibility for the latter. In order to find the actual Time of Arrival (TOA) of the packets at the receiving satellite, the propagation delays between UTs and satellites are evaluated, $\{\boldsymbol{\mathcal{T}}_u^{UT}\}$, exploiting the geometrical computations previously performed.

2.3.2.2 Traffic Generator

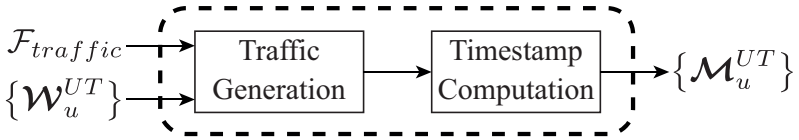

FIGURE 2.6: Traffic Generator module, high-level Architecture.

The traffic module, depicted in Figure 2.6, handles the traffic generation according to the average daily traffic of the users. An example of packets generation is given in Section 7.5, following the Poisson distribution. The packets are generated at the beginning of each snapshot for the UT in visibility with at least one satellite. It is also possible to generate packets for the whole population, considering the packets generated from the UTs out of visibility as lost for the statistics. In order to reduce the simulation duration, the approach adopted for the traffic generation consists in generating a considerable amount of packets to produce a reliable statistic for the interference for a specific constellation geometry. With this method, it is possible to simulate each snapshot, *i.e.*, each constellation geometry, just once, collecting reliable statistics for the interference. In such a way, a Monte Carlo simulation over the interference, is performed for each constellation geometry, and another one is performed over the satellite constellation evolution, collecting the statistics along the whole simulation duration. The drawback of this approach is that the actual generation time, *i.e.*, generation horizon, is much longer than the actual duration of a single snapshot. For this reason, the statistics collected at each snapshot are "wrapped" around the actual duration of the snapshot, in order to obtain a value coherent with the duration of the simulation step.

For what concerns the traffic generation, a user defined traffic file is taken as input, $\mathcal{F}_{traffic}$, in order to define the average daily traffic per UT. The satellite visibility for each UT, $\{\boldsymbol{\mathcal{W}}_u^{UT}\}$, is taken into account as a further option that allows

a UT to transmit only if in visibility with at least one satellite. The average daily traffic can be the same for the whole simulation or varying along the simulation duration (*e.g.*, in order to simulate peaks of traffic in specific moments of the day). Each packet is characterized by a timestamp, $\{\mathcal{M}_u^{UT}\}$, and associated to an UT. Variable packet sizes and durations are supported and, subject to packet duration, the packets for each UT are rearranged to avoid overlaps, *i.e.*, simultaneous transmissions from the same UT. According to the simulated air interface, retransmissions may be supported. During the packet generation, power randomization can be used to assign a specific power to each packet, but, according to the UT characteristics, the power cannot exceed the maximum transmit power allowed by its power class.

2.3.2.3 PHY Abstraction

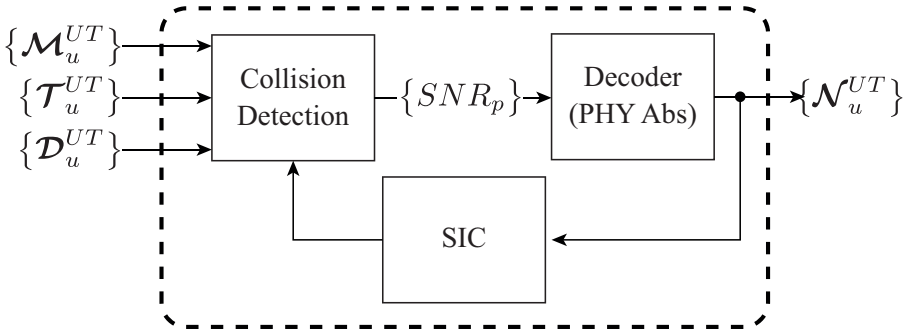

FIGURE 2.7: PHY Abstraction module, high-level Architecture.

The PHY Abstraction module, depicted in Figure 2.7, takes as input the generated traffic, $\{\mathcal{M}_u^{UT}\}$, the propagation delays between UT and satellite, $\{\mathcal{T}_u^{UT}\}$, and the value of Doppler shift, $\{\mathcal{D}_u^{UT}\}$. According to the values of $\{\mathcal{T}_u^{UT}\}$ and $\{\mathcal{D}_u^{UT}\}$ it is possible to evaluate the actual overlap in time and frequency among the packets. Then the collision detection, interference assessment, and decoding emulation are performed. An independent decoder is modelled for each beam of each satellite. For each packet at the decoder input, the collision with other packets is detected and the SINR value is computed, according to the interference power level. Then the decoding process is emulated by means of a PHY abstraction.

The objective of the PHY abstraction is to accurately predict the link layer performance in a computationally simple way. The requirement for an abstraction stems from the fact that simulating the PHY layer links among multiple satellites and UTs in a SLS can be computationally prohibitive. In system-level simulations, the effect of the channel impulse response selectivity, causes a variation of the SINR distribution along the packet. This produces, especially with long packets durations, portion of the packet experiencing different values of SINR. There are many different types of PHY abstraction, which are thoroughly explained in Chapter 5; the simulator currently uses a typical PHY abstraction methodology called Effective SINR Mapping (ESM), which allows to average, in a non-linear way, the instantaneous values of

SINR, along the received packet, $\{SINR_p\}$, extracting an equivalent value of SINR, the *effective SINR*, $SNIR_{eff}$, used to predict the Packet Error Rate (PER) for a specific packet. After the SINR for the single packet is computed according to the ESM method chosen, a random threshold, *i.e.*, a threshold $T \sim \mathcal{U}(0,1)$, is chosen for all the received packets. The packet is considered as decoded if its threshold T is above the uncoded PER, *i.e.*, the PER with respect to the Additive White Gaussian Noise (AWGN) channel curve, corresponding to the $SNIR_{eff}$ associated to the packet.

An additional feature of this module is the SIC implementation. According to the simulated air interface, if SIC is active, once a packet is decoded its power contribution is canceled. It is also possible to set a residual power after cancellation, depending on the SIC performance. If a packet is captured and decoded by more then one satellite-beam pair, the packet is considered decoded only by the one for which the decoding happens first. According to the type of satellite payload (*e.g.*, transparent or regenerative), a store-and-forward policy can be chosen by the user, then the decoded packets fill up a virtual buffer associated to the satellite. Decoded packets and their decoding timestamp are stored for KPI post processing. According to the simulated air interface, if the packet is not correctly decoded, it can be scheduled for a re-transmission by adding a random back-off time and the Round Trip Time (RTT) duration to its timestamp in order to simulate the reception of a NACK. The traffic after the aforementioned analysis is stored in $\{\boldsymbol{\mathcal{N}}_u^{UT}\}$ for further data processing.

2.3.2.4 KPI Computation

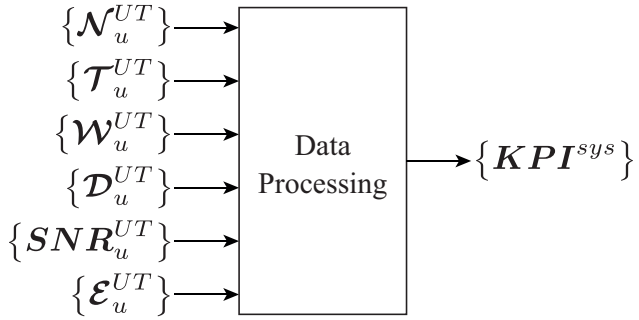

FIGURE 2.8: KPI Computation module high-level Architecture.

This module handles the interpretation of the outputs from the previous modules, as shown in Figure 2.8, and performs the KPI computation. Notably, the following values are taken as input of this module: i) the traffic after the PHY abstraction processing, $\{\boldsymbol{\mathcal{N}}_u^{UT}\}$; ii) the propagation delays between UTs and satellites, $\{\boldsymbol{\mathcal{T}}_u^{UT}\}$; iii) the output of the visibility analysis, $\{\boldsymbol{\mathcal{W}}_u^{UT}\}$; iv) the Doppler shift and Doppler rate, $\{\boldsymbol{\mathcal{D}}_u^{UT}\}$; v) the SNR values, $\{\boldsymbol{SNR}_u^{UT}\}$; and vi) the elevation angles, $\{\boldsymbol{\mathcal{E}}_u^{UT}\}$. It is worth highlighting that the satellite constellation geometry, the link budget, the stochastic shadow fading, as well as the interference due to the generated traffic,

vary through Monte Carlo iterations. The statistics are gathered from all the points of the UT grid. Then, the performance analysis is computed for the whole evolution in time of the satellite constellation and averaged over the entire UT population. The main KPIs taken into account for the scope of this simulator can be divided into two categories: UT and Satellite/Constellation KPIs. The UT KPIs are: i) the PLR per geographical location; ii) the throughput per geographical location; iii) the latency distribution per geographical location; iv) the retransmission ratio per geographical location; and v) the handover rate. The single satellite and constellation KPIs are: i) the buffer occupancy, according to the visibility with the GS; ii) the user link average throughput; and iii) the feeder link required capacity.

Chapter 3

Reference Systems and Frames

A reference system is a set of coordinates used at a given instant to identify the position of a body in space. When considering a system in which each point-like particle, subtracted from all external forces, stays at rest or travels with uniform rectilinear motion, it is possible to talk about an inertial reference system. The nature of this reference system is established by the first basic law of dynamics, according to which:

In an inertial frame of reference, an object either remains at rest or continues to move at a constant velocity, unless acted upon by a force.

Stars, and in particular fixed stars, have been used since ancient times as a reference. They can be considered as point-like particles considering their very small size compared to large relative distances. In addition, they can be seen as a system of isolated points, provided that the gravitational interaction between the latter is very weak. By selecting a frame of reference related to them properly, it is possible to observe that the first law of dynamics is perfectly satisfied. In fact, accounting for a local estimate of a component of the universe which is somewhat disturbed from the gravitational point of view, the presence of an inertial relation is conceivable.

For what concerns the realization of ESiM2M, the need arose to compare quantities of different types and measured with respect to different reference systems. For example local coordinate systems centered on the UTs on ground and on the center of mass of the spacecraft have been used in order to compute the attitude of the bodies, their state vectors, as well as to perform antenna measurements. In order to simultaneously utilize those independent local reference systems, a common reference frame must be adopted and the geometrical relationships among them must be defined. In this way it would be possible to express all the measurements on a common reference frame. This chapter is not meant to be an in-depth discussion of all the reference systems and related geometric transformations, but the key aspects outlined during the PhD activity and the ESiM2M development will be emphasized. In particular all the geometrical relationships described are fundamental for understanding the link budget and orbital geometry computations.

3.1 Cartesian Earth Centered Reference Systems

Satellite coordinates and earth user receivers must be identified in a well defined reference system. Hence, an accurate definition and determination of such systems is essential to guarantee a precise positioning. The two main cartesian reference systems, with the Earth's center of mass in their origin, are introduced below.

3.1.1 Earth Centered Inertial (ECI)

Earth Centered Inertial (ECI) coordinate frames, also referred to as Celestial Reference System (CRS), are quasi-inertial[1], thus not accelerating, in contrast to the Earth Centered Eart Fixed (ECEF) frames, which rotate with respect to stars and then remain fixed with respect to the Earth's surface in its rotation. The ECI reference system has its origin at the center of mass of the Earth and is fixed with respect to the stars. For objects in space, the equations of motion that describe orbital motion are simpler in a non-rotating frame such as ECI. Thus, the ECI frame is useful for specifying the direction towards celestial bodies, their motion, as well as the motion of spacecrafts, and for these reasons it is one of the most used inertial-coordinates systems. For representing the positions and velocities of terrestrial objects, it is more convenient to use ECEF coordinates or latitude, longitude, and altitude.

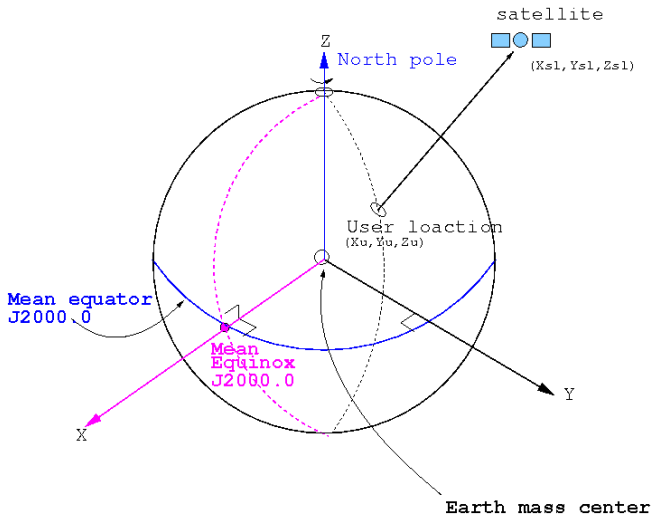

FIGURE 3.1: ECI Reference System

The direction of the axis of the ECI reference system, showed in Figure 3.1, are defined as follows:

[1]It is not an inertial system in a strict way, because it is affected by the accelerated motion of the earth around the sun (annual revolution).

- X_{ECI}: it points in the direction of the mean equinox at J2000 epoch[2], where equatorial and ecliptic plane[3] intersect.
- Z_{ECI}: it is orthogonal to the plane defined by the mean equator at J2000 epoch (fundamental plane) and corresponds to the Earth rotation axis at Epoch J2000 (near the pole star).
- Y_{ECI}: it is orthogonal to the former ones, so the system is directly (right-handed) oriented.

Thus, the X_{ECI}-Y_{ECI} fundamental plane is colocated with the equatorial plane, but the Earth itself is rotating relative to the vernal equinox at its sidereal rotation rate of about $7\,292\,115\,167 \cdot 10^{-14}$ rad/s, or 15.04109 deg/h. The practical implementation is called (conventional) Celestial Reference Frame (CRF)[4] and it is determined from a set of precise coordinates of extragalactic radio sources, *i.e.*, it is fixed with respect to distant objects of the universe. The mean equator and equinox J2000 were defined by International Astronomical Union (IAU) agreements in 1976, with 1980 nutation series (Seildelmann, 1982 and Kaplan, 1981), which are valid analytic expressions for long time intervals (the former reference epoch was 1950.0) [83], [84].

3.1.2 Earth Centered Earth Fixed (ECEF)

ECEF, also known as Earth Centered Rotational (ECR), is a geographic and Cartesian coordinate system and it is sometimes known as Conventional Terrestrial Reference System (TRS) [85]. It represents positions in meters as X_{ECEF}, Y_{ECEF}, and Z_{ECEF} coordinates. The origin of the reference system is defined as the center of mass of Earth, hence the term *geocentric coordinates*. ECEF is a non-inertial reference system because it is fixed with Earth and rotates with the latter.

The axes orientations for this reference system, depicted in Figure 3.2, are:

- Z_{ECEF}: it is identical to the direction of the Earth's rotation axis defined by the Conventional Terrestrial Pole (CTP).
- X_{ECEF}: it is defined as the intersection between the equatorial plane and the mean Greenwich meridian. The equatorial plane is orthogonal to the CTP and in the Mean Greenwich meridian direction. This meridian was established by the Bureau International de l'Heure (BIE) observatory.

[2] In astronomy, an epoch is a moment in time used as a reference point for some time-varying astronomical quantity (*e.g.*, the celestial coordinates or elliptical orbital elements of a celestial body) because these are subject to perturbations and vary with time. The currently-used standard epoch J2000 is defined by international agreement to be equivalent to the Julian date 2451545.0 TT (Terrestrial Time) [82].

[3] The ecliptic plane is the plane of Earth's orbit around the Sun.

[4] Notice that *Reference System* and *Reference Frame* are different concepts. The former is considered as a theoretical definition, including models and standards for its implementation. The latter is its practical implementation through observations and a set of reference coordinates (*e.g.*, set of fundamental stars for a CRF or fiducial stations for a Terrestrial Reference Frame (TRF)).

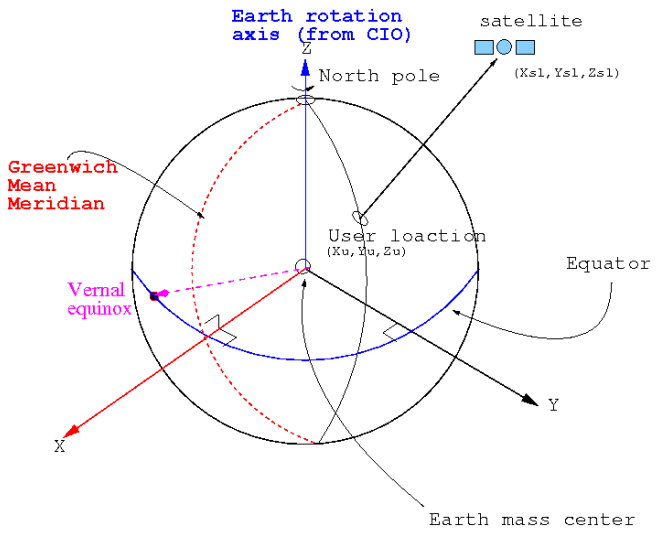

FIGURE 3.2: ECEF Reference System

- Y_{ECEF}: it is orthogonal to the formers ones, so the system is right-handed.

Thus the X_{ECEF}-Y_{ECEF} plane is colocated with the equatorial plane. The distance from a given point of interest to the center of the Earth is called the *geocentric radius* or *geocentric distance*. This reference system is fundamental in the areas related to positioning and satellite navigation; in fact, in these fields the need arises to be able to express both the status of the satellites and that of the receivers in a single reference system. The definition of this reference system involves a mathematical model for a physical earth in which positions are expressed and have small temporal variations due to geophysical effects (plate motion, earth tides, *etc.*). The practical implementation of this system is named (conventional) TRF and it is carried out through the coordinates of a set of points on the earth serving as reference points[5], as better explained in the next section [84], [85].

3.2 Geodetic Reference Systems

A geodetic reference system, also called *Geodetic Datum* or more simply *Datum*, is a reference system that allows to define in mathematical terms the position of points on the surface of the Earth. The datum therefore allows the geo-referencing of places and objects. The Earth is not a perfect spheroid, thus the reference datum cannot be unique. It is therefore always necessary associating the coordinates of a point with its reference datum, as the same point could have different coordinates depending on the datum used.

These reference systems can be classified according to various criteria. As previously discussed with ECI and ECEF reference systems, they could be identified as

[5] A conventional TRF is defined as a set of physical points with precisely determined coordinates in a specific coordinate system that is the realization of an ideal TRS [86].

inertial (*e.g.*, fixed with respect to the Sun or fixed stars, which are used in astronomy) and non-inertial (*e.g.*, Earth-fixed which are those typically used in geodesics and topography) systems. A second differentiation concerns the number of dimensions used to define the datum. It is therefore possible to speak of:

- *Horizontal Datum*: they are the models used to measure positions on the Earth; they are used in classical geodesy[6] and they are based on measurements performed on the ground.
- *Vertical Datum:* they are a reference surface for vertical positions, such as the elevations of Earth features including terrain, bathymetry, water level, and man-made structures.
- *Three-dimensional Datum*: these models take into account both horizontal and vertical positioning and are used in modern geodesy based on measurements made with satellites.

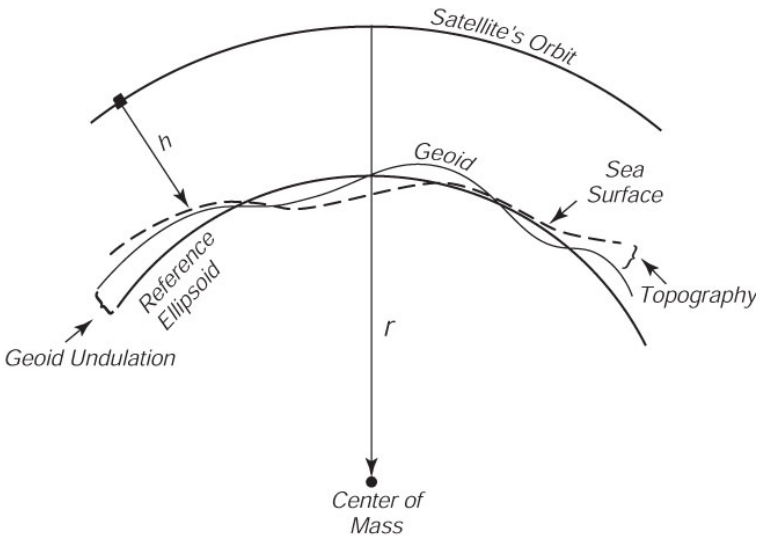

FIGURE 3.3: Reference Geoid and Ellipsoid

In classical geodesy, *i.e.*, the one before satellite availability, the only way to quantify the point coordinates was to carry out field measurements by means of triangulations. Therefore it is important to have a reference surface, or rather a known mathematical formulation representing the latter, on which geodetic calculations could be created. The Earth is not actually a sphere, as previously mentioned, but can be approximated with a surface called a *geoid*, with complex mathematical derivation. A further approximation of the Earth is an *ellipsoid* which can be easily represented analytically. This surface is called a reference ellipsoid and it is described by the following equation:

$$\frac{x^2 + y^2}{a^2} + \frac{z^2}{b^2} = 1 \tag{3.1}$$

[6]Geodesy is a discipline belonging to the Earth sciences that deals with the measurement and of the representation of the Earth, of its gravitational field and of geo-dynamic phenomena such as pole shift, earth tides and crustal movements.

Where a is the semi-major axis (or equatorial radius), b is the semi-minor axis (or polar radius) with $a > b$. In geodesy publications, however, it is common to specify the characteristics of the ellipsoid using the semi-major axis, a, and the flattening, f, defined as:

$$f = \frac{a - b}{a} \tag{3.2}$$

As it is shown in Figure 3.3, after the ellipsoid's parameters have been defined, it is also necessary to uniquely connect them to the actual Earth's surface. This operation is called *orientation* and can be distinguished into two main categories:

Local Orientation is used for limited areas (*e.g.*, typically at a national level). The connection between the reference surface and the surface of the Earth is limited to a single point, *i.e.* the emanation point, with known geographical coordinates expressed in terms of latitude, longitude, and altitude. After the reference ellipsoid with known parameters is chosen, this is oriented to the emanation point, imposing certain geometric conditions. In particular the reference ellipsoid is locked on a fixed position with respect to the Earth, *i.e.*, with respect to the geoid. Using this model it is possible to relate the measurements made on the actual Earth's surface to the reference ellipsoid, with a good approximation. The ellipsoid is then used for further mathematical analyses.

Average Orientation is on the other hand used for larger areas such as continents or the whole globe. In this case, the connection between the reference surface and the Earth's surface occurs through several points. The position of the ellipsoid is determined in such a way as to minimize the mean square error between the geoid and the ellipsoid in those points.

When the altitude of a point on the Earth's surface becomes of interest, the indication of height provided by a *Horizontal Datum* is no longer sufficient. In the latter, in fact, the height of the point is related to the reference ellipsoid which does not take into account the actual altitude with respect to the sea level. For these measurements it is therefore necessary to define a specific *Vertical Datum* which is called vertical or altimetric datum. Once defined the origin for the altitudes, the zero level, at the sea level, it is possible to define an altimetric matrix covering the entire territory of interest. The latter is composed of points located at regular distance for which the absolute altitude with respect the sea level must be measured. Finally, a local or global geoid model is associated to this matrix. Modern geodesy is mainly based on satellite geodesy, thus on services provided by satellite navigation systems allowing the computation of the geographic coordinates of any point on the Earth's surface or atmosphere with an error of a few meters. In satellite geodesy it is necessary to adopt *Three-dimensional Datum* with global orientation, that is valid for the whole Earth.

While for a local datum each nation chooses a reference ellipsoid and its orientation, in order to best approximate the characteristics of the geoid for that particular

area, for global datum the average characteristics of the geoid must be taken into account. For example, Italy, after the Second World War, adopted the datum with a medium orientation ED50 (European Datum 1950), to conform to other European countries. For what concern global datum, it is worth mentioning: the International Terrestrial Reference Frame (ITRF) introduced by the International Earth Rotation and Reference Systems Service (IERS), which is updated every year (ITRF98, ITRF99, etc.); the World Geodetic System 84 (WGS-84), which is applied for GPS; the Parametry Zemli 1990 (Parameters of the Earth 1990) (PZ-90) for GLONASS, or the Galileo Terrestrial Reference Frame (GTRF) for Galileo system. All these reference frames are called TRF. Furthermore it is possible to convert the coordinates of a point from one datum system to another. Datum conversion may frequently be accompanied by a change of grid projection [83], [85], [87].

3.2.1 Latitude-Longitude-Altitude

As previously said, in geodetic coordinates, the Earth's surface is approximated by an ellipsoid, and locations near the surface are described in terms of latitude, ϕ, longitude, λ, and height, h, as shown in Figure 3.4a.

Two different definitions for the latitude, ϕ, can be given: the *geodetic latitude* and *geocentric latitude*. Geodetic latitude is defined as the angle between the equatorial plane and the surface normal at a point on the ellipsoid, whereas geocentric latitude is defined as the angle between the equatorial plane and a radial line connecting the centre of the ellipsoid to a point on the surface, as it is shown in Figure 3.4b. When used without qualification, the term latitude refers to geodetic one. Lines joining points of the same latitude trace circles on the surface of Earth called parallels, as they are parallel to the Equator and to each other. The North Pole is considered 90° N while the South Pole is considered 90° S. The 0° parallel of latitude is designated the Equator, the fundamental plane of all geographic coordinate systems. The Equator divides the globe into Northern and Southern Hemispheres.

The longitude, λ, of a point on Earth's surface is the angle east or west of a reference meridian to another meridian that passes through that point. All meridians are halves of great ellipses, often called great circles, which converge at the North and South Poles. The meridian of the British Royal Observatory in Greenwich, in southeast London, England, is the international reference meridian, although some organisations continue to use other meridians for internal purposes. The prime meridian determines the proper Eastern and Western Hemispheres, the antipodal meridian of Greenwich is both 180° W and 180° E. The combination of these two components specifies the position of any location on the surface of Earth, without consideration of altitude or depth, on a grid formed by lines of latitude and longitude.

The geodetic altitude, h is defined as the height above the ellipsoid surface, normal to the ellipsoid, whereas geocentric altitude is defined as the height above the ellipsoid surface along a line to the center of the ellipsoid. As it is for the latitude, when used without qualification, the term altitude refers to geodetic one[83], [85].

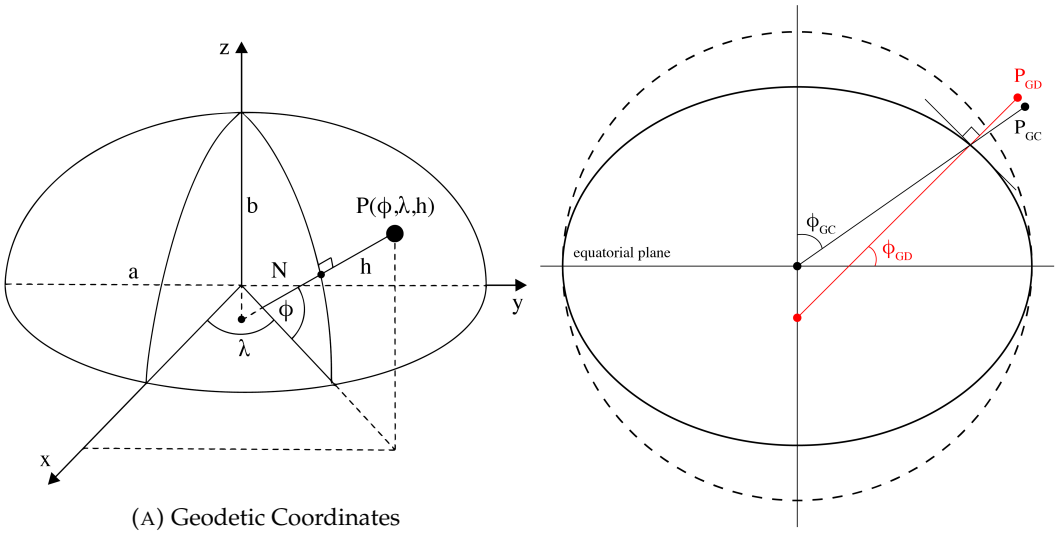

(A) Geodetic Coordinates

(B) Geodetic and Geocentric Latitude

FIGURE 3.4: Geodetic and Geocentric Coordinates.

3.3 Local Reference Systems

In this section, the main local reference systems as well the *body* reference systems, thus the ones fixed with the terminal or spacecraft body, will be described. It is of paramount importance to understand the geometrical relationships among these reference system such to properly translate measurements performed with respect to different reference systems into a common one.

3.3.1 ENU and NED Reference Systems

Local Tangent Plane (LTP) coordinates, also called locally level coordinates, are a return to the first-order model of the earth as being flat, where they serve as local reference directions for representing vehicle attitude and velocity for operation on or near the surface of the earth (*e.g.*, aviation and marine cybernetics). It consists of three coordinates: i) one represents the position along the northern axis; ii) one along the local eastern axis; and iii) one represents the vertical position. East North Up (ENU) and North East Down (NED) are two common right-handed LTP coordinate systems. The axis of these two coordinate systems are directed as follows:

- the X_{ENU} axis, colocated with the Y_{NED} axis, is facing the East direction;
- the Y_{ENU} axis, colocated with the X_{NED} axis, is directed towards the geodetic north and lies with X_{ENU} (Y_{NED}) on a plane tangent to the surface of Earth;
- the Z_{ENU} axis is orthogonal to the reference ellipsoid and directed in the opposite direction with respect to the center of the Earth, while the Z_{NED} axis points in the opposite direction, towards the center of the Earth.

Figure 3.5 shows the ENU local tangent plane, which is similar to NED, except for swapping *Down* for *Up* and x for y. ENU coordinates may be preferred to NED

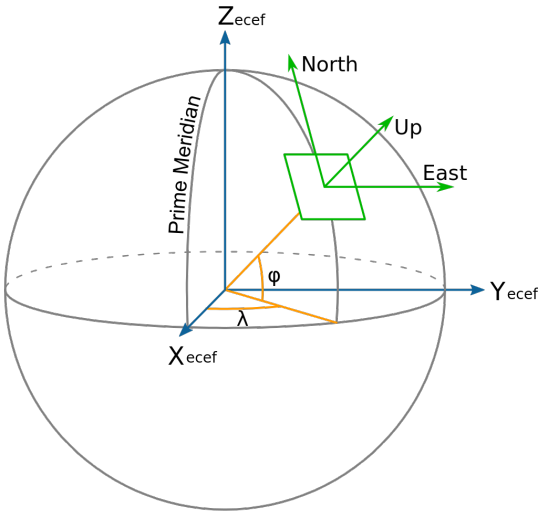

FIGURE 3.5: The ENU local tangent plane.

coordinates because altitude increases in the upward direction. However NED coordinates may also be preferred over ENU coordinates because the direction of a right (clockwise) turn is in the positive direction with respect to a downward axis, and moreover NED coordinate axis coincide with vehicle-fixed RPY coordinates when the vehicle is level and headed north [83]. A problem that could arise using these ENU and NED coordinate systems is the following: if by chance the vehicle is exactly to the geodetic north, the axis orientations would no longer be definable, as it would not be possible to orient the northern-axis.

3.3.2 RPY Reference Systems

The RPY coordinates are vehicle fixed, with the *roll* axis in the nominal direction of motion of the vehicle, the *pitch* axis out the right-hand side, and the *yaw* axis such that turning to the right is positive. The same orientations of vehicle-fixed coordinates are used for surface ships and ground vehicles. They are also called SAE coordinates, because they are the standard body-fixed coordinates used by the Society of Automotive Engineers. For rocket boosters with their roll axes vertical at lift-off, the pitch axis is typically defined to be orthogonal to the plane of the boost trajectory, also called the pitch plane or ascent plane. The spacecraft fixed coordinates frame is typically used for satellite in order to express measures with respect to the body of the satellite payload (*e.g.*, viewing angles and satellite antenna measures). As it is shown in Figure 3.6, it has the x or roll axis directed towards the satellite nominal velocity, the y or pitch axis directed towards the nominal negative orbit normal, and the z or yaw axis orthogonal to the first two and directed towards the nominal nadir[7] of the satellite.

[7]The *nadir* is a straight line virtually connecting the satellite (origin of the local reference system) to the Earth's center.

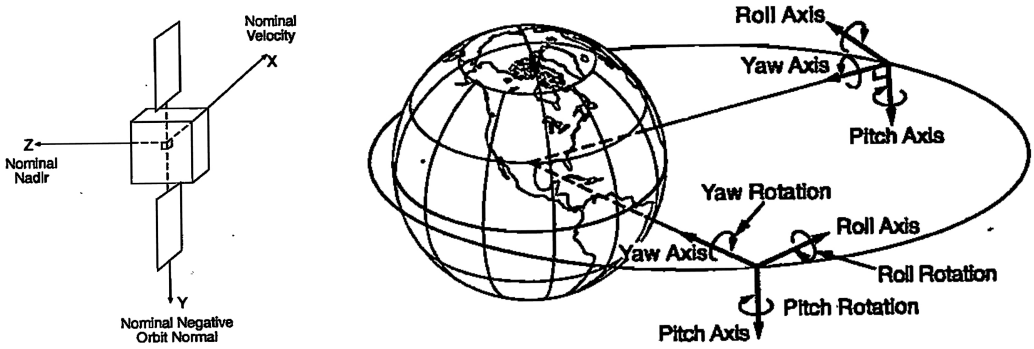

(A) Spacecraft fixed Coordinates

(B) Roll, Pitch, and Yaw (RPY) Coordinates

FIGURE 3.6: Body fixed Coordinates [88].

Therefore the attitude of the vehicle body with respect to local coordinates can be specified in terms of rotations about the vehicle roll, pitch, and yaw axis, starting with these axes aligned with NED coordinates. The angles of rotation about each of these axes are called *Euler angles*, which will be further explained in the following. A fairly common convention for vehicle attitude Euler angles is illustrated in Figure 3.7a, where, starting with the vehicle level with roll axis pointed north. This right-handed reference system can be described as [83], [88]:

- *Yaw/Heading*, referred also as z axis, rotates through the yaw angle (Y) about the vehicle yaw axis to the intended azimuth, *i.e.*, heading, of the vehicle roll axis. Azimuth is measured clockwise, from North towards East.
- *Pitch*, referred also as y axis, rotates through the pitch angle (P) about the vehicle pitch axis to bring the vehicle roll axis to its intended elevation. Elevation is measured positive upward from the local horizontal plane.
- *Roll*, referred also as x axis, rotates through the roll angle (R) about the vehicle roll axis to bring the vehicle attitude to the specified orientation.

3.4 Orbits Reference System

The natural frame for an orbit is called *perifocal frame*. As illustrated in Figure 3.8, the perifocal plane is centered at the focus of the orbit. Its $\overline{x}$ $\overline{y}$ plane is the plane of the orbit itself, and its $\overline{x}$ axis is directed from the focus through periapse. The unit vector along the $\overline{x}$ axis (the apse line) is denoted by $\hat{\mathbf{p}}$. The $\overline{y}$ axis, with unit vector $\hat{\mathbf{q}}$, lies at 90° true anomaly[8] to the $\overline{x}$ axis. Finally the $\overline{z}$ axis is normal to the plane of the orbit, with unit vector $\hat{\mathbf{w}}$, in the direction of the *specific orbital angular momentum*[9]

[8] All the orbital parameters mentioned in the following (*e.g.*, true anomaly, angular momentum, eccentricity, *etc.*) will be thoroughly described in Chapter 4.

[9] The specific orbital angular momentum plays a pivotal role in the analyses of the two-body problem. It is a vector quantity (more precisely, a pseudovector) that represents the product of a body's rotational inertia and rotational velocity (in rad/s) about the axis perpendicular to the orbital plane, with origin in the focus of the orbit.

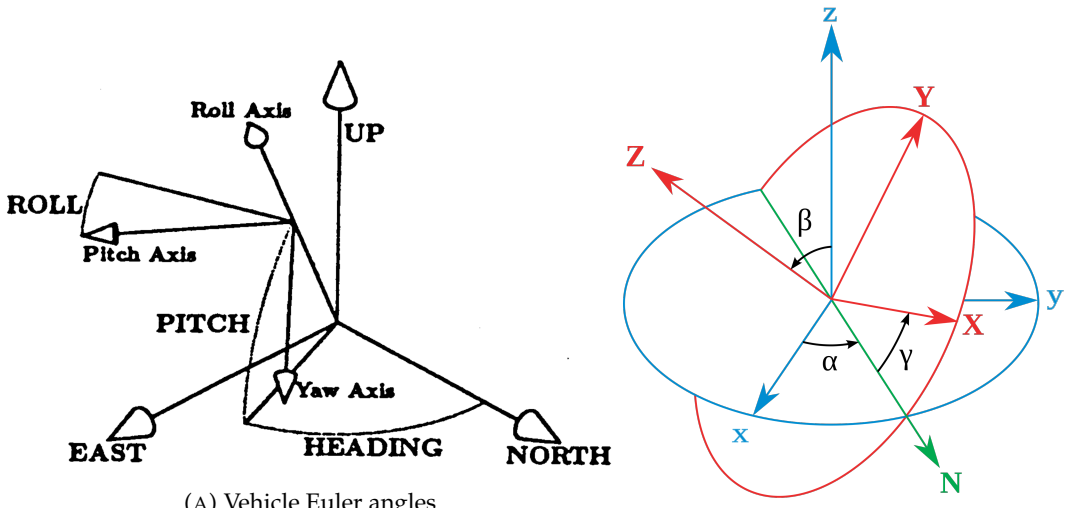

(A) Vehicle Euler angles

(B) Classic Euler angles geometrical definition

FIGURE 3.7: Euler Angles representation [83].

vector $\mathbf{h}$. Thus the $\overline{z}$ unit vector $\hat{\mathbf{w}}$ is:

$$\hat{\mathbf{w}} = \frac{\mathbf{h}}{h} \tag{3.3}$$

where $\mathbf{h}$ is the *specific orbital angular momentum* vector, and h its absolute value. The latter can be defined as, [89]:

$$h = \sqrt{a\mu(1-e^2)} \tag{3.4}$$

where a is the semi-major axis of the orbit, μ is the standard gravitational parameter of Earth, and e is the orbit eccentricity.

In the perifocal frame, the *position vector* $\mathbf{r}$, depicted in Figure 3.9a is written as:

$$\mathbf{r} = \overline{x}\hat{\mathbf{p}} + \overline{y}\hat{\mathbf{q}} \tag{3.5}$$

where

$$\begin{aligned} \overline{x} &= r\cos\nu \\ \overline{y} &= r\sin\nu \end{aligned} \tag{3.6}$$

with r the magnitude of $\mathbf{r}$, and ν being the true anomaly of the body in the orbit, defined in Equation 4.3. The magnitude, r, referred as the *orbit radius*, can be written as, [89], [90]:

$$r = \frac{h^2}{\mu}\frac{1}{1+e\cos\nu} = \frac{a(1-e^2)}{1+e\cos\nu} = a\Big(1-e\cos\big(E(t_k)\big)\Big) \tag{3.7}$$

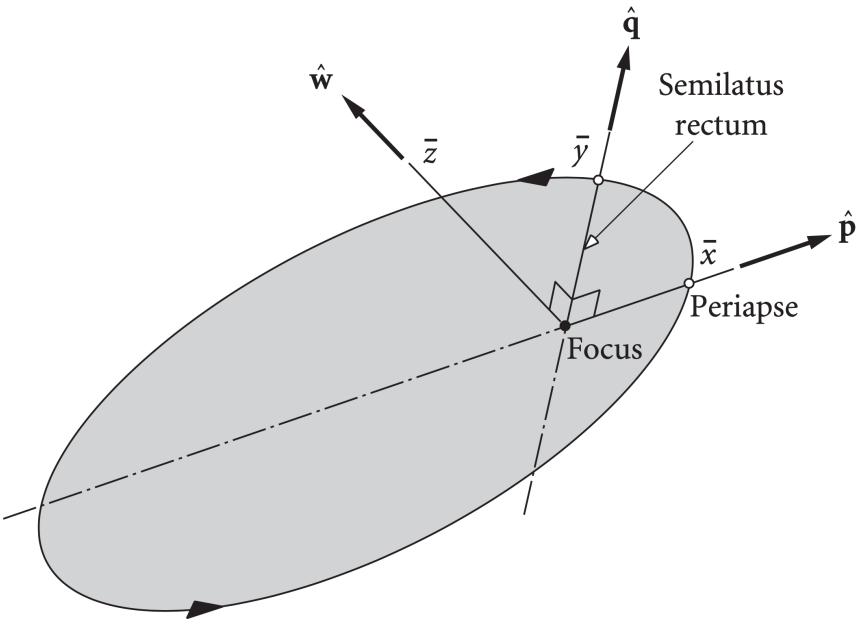

FIGURE 3.8: Perifocal reference system, [89].

where $E(t_k)$ is the eccentricity anomaly, defined in Chapter 4. Plugging Equation 3.7 in Equation 3.6, the *position vector* $\mathbf{r}$ can then be written in matrix form as:

$$\mathbf{r} = \begin{bmatrix} \frac{a(1-e^2)}{1+e\cos\nu}\cos\nu \\ \frac{a(1-e^2)}{1+e\cos\nu}\sin\nu \\ 0 \end{bmatrix} \tag{3.8}$$

As for the *velocity vector*, $\mathbf{v}$, represented in Figure 3.9a, it can be defined in the perifocal frame by taking the time derivative of $\mathbf{r}$ in Equation 3.5:

$$\mathbf{v} = \dot{\mathbf{r}} = \dot{\bar{x}}\hat{\mathbf{p}} + \dot{\bar{y}}\hat{\mathbf{q}} \tag{3.9}$$

Then from Equation 3.6:

$$\begin{aligned} \dot{\bar{x}} &= \dot{r}\cos\nu - r\dot{\nu}\sin\nu \\ \dot{\bar{y}} &= \dot{r}\sin\nu + r\dot{\nu}\cos\nu \end{aligned} \tag{3.10}$$

where $\dot{r}$ is the radial component of the velocity, v_r, depicted in Figure 3.9b and defined as, [89]:

$$\dot{r} = v_r = \frac{\mu}{h}e\sin\nu \tag{3.11}$$

and $r\dot{\nu}$, being the azimuthal component of velocity, $v_\perp$, depicted in Figure 3.9b and defined as, [89]:

$$r\dot{\nu} = v_\perp = \frac{\mu}{h}(1 + e\cos\nu) \tag{3.12}$$

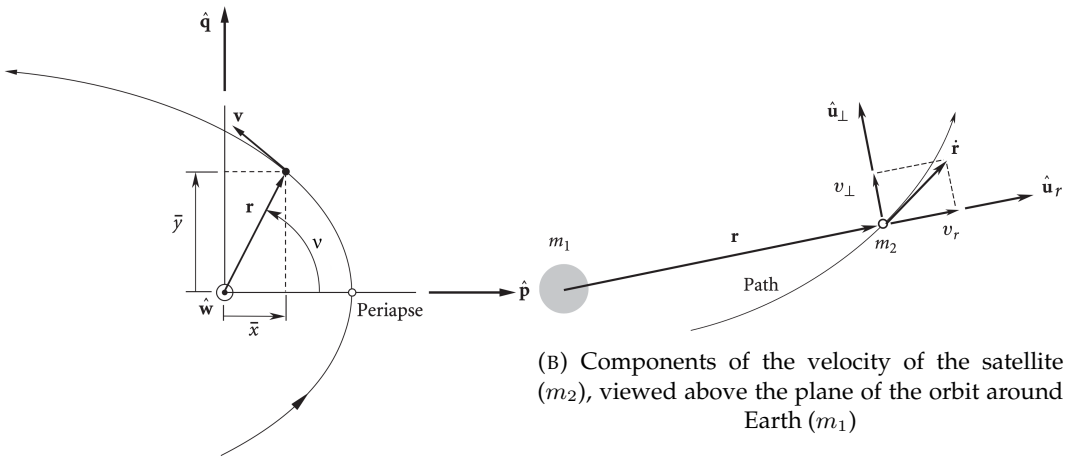

(A) Position and velocity relative to the Perifocal Frame

(B) Components of the velocity of the satellite (m_2), viewed above the plane of the orbit around Earth (m_1)

FIGURE 3.9: Perifocal frame, [89].

Substituting Equations 3.11 and 3.12 in Equation 3.10 it is possible to obtain:

$$\begin{aligned} \dot{\bar{x}} &= -\frac{\mu}{h}\sin\nu \\ \dot{\bar{y}} &= \frac{\mu}{h}(e+\cos\nu) \end{aligned} \tag{3.13}$$

hence the velocity vector can be written in matrix form as:

$$\mathbf{v} = \begin{bmatrix} -\frac{\mu}{h}\sin\nu \\ \frac{\mu}{h}(e+\cos\nu) \\ 0 \end{bmatrix} \tag{3.14}$$

The mathematical formulation for position and velocity vectors in the perifocal frame is then complete. It is now possible to define the set of transformations needed for the conversion on the ECI frame as it will be shown in Section 3.7.6.

3.5 Antenna Reference Systems

An antenna radiation pattern is defined as a mathematical function or a graphical representation of the radiation properties of the antenna as a function of space coordinates. In most cases, the radiation pattern is determined in the far-field region and it is represented as a function of the directional coordinates. Radiation properties include power flux density, radiation intensity, field strength, directivity, phase, or polarisation. The radiation property of most concern is the two- or three-dimensional spatial distribution of radiated energy as a function of the observer's position along a path or surface of constant radius. The most convenient reference systems, also adopted by many antenna design softwares (*e.g.*, TICRA SATSOFT) are described in the following.

3.5.1 Spherical Coordinate System

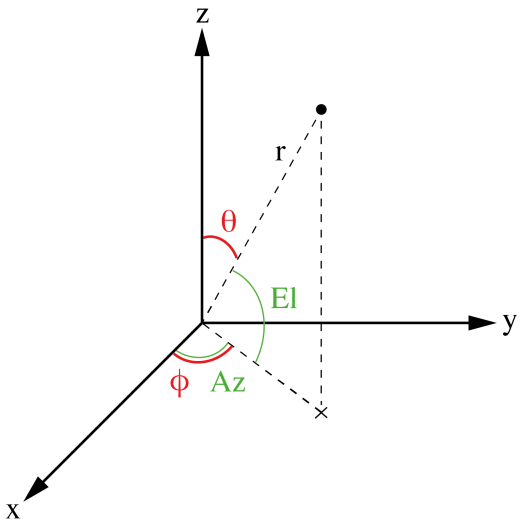

(A) Spherical Coordinates

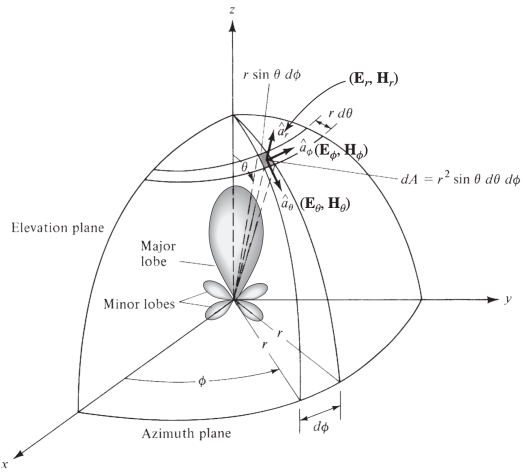

(B) Coordinate system for antenna analyses

FIGURE 3.10: Antenna Reference System [91].

A spherical coordinate system is a coordinate system for the three dimensional space where the position of a point is specified by three numbers: the *radial distance* of that point from a fixed origin, its *polar angle* measured from a fixed zenith direction, and the *azimuthal angle* of its orthogonal projection on a reference plane that passes through the origin and is orthogonal to the zenith, measured from a fixed reference direction on that plane. It can be seen as the three dimensional version of the polar coordinate system. The use of symbols and the order of the coordinates differs among sources and disciplines.

A commonly used coordinates convention, which is also the one adopted for ESiM2M, is the physics convention shown in Figure 3.10 where:

- r is the radial distance, so the distance to origin,
- θ is the polar angle from the z axis to the vector itself, the angle is positive towards the x-y plane, and
- ϕ is the azimuthal angle from the positive x axis to the vector's orthogonal projection onto the x-y plane, the angle is positive towards the positive y axis

Any spherical coordinate triplet (r, θ, ϕ) specifies a single point of the three dimensional space, however every point has infinitely many equivalent spherical coordinates multiple of 2π. It is worth highlighting that $0 < \phi < 2\pi$ and $0 < \theta < \pi$. An alternative to this nomenclature is based on *Azimuth* and *Elevation* angles shown in Figure 3.10a, which is particularly useful when handling satellite to earth geometry. In particular the $Az = \phi$ and $El = 90 - \theta$.

Usually the boresight of the antenna is assumed to be aligned with z axis as shown in Figure 3.10. The Cartesian triplet is furthermore usually assumed fixed

with the vehicle reference system, *e.g.*, for a satellite the z axis of the antenna is aligned to the nadir, for an on-ground user with the Yaw/Up axis. Therefore it is possible to compute the antenna positions according to the motion of the body reference system by means of rotations, as previously explained. Equivalently it would be possible to compute antenna rotations with respect to the body reference frame.

3.5.2 U-V Coordinate System

Spherical coordinate systems allow to represent antenna measurements over a unitary sphere (*e.g.*, normalized by the maximum gain), centered in the origin of the antenna plane. However, it is useful to define another coordinates system allowing to express antenna parameters on a two dimensional space. u-v mapping is a modelling process of projecting a two dimensional image to a three-dimensional model, and viceversa. The letters u and v denote the axis of the two dimensional coordinate systems. This reference system is particularly useful for representing satellite antenna patterns and it is adopted by design softwares like TICRA SATSOFT.

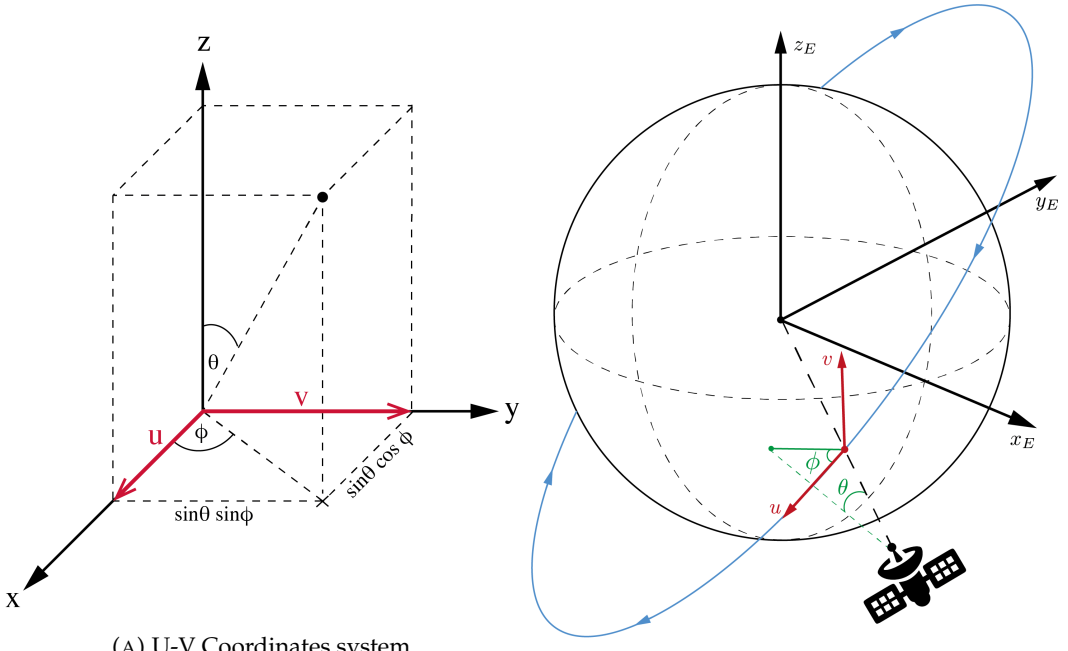

(A) U-V Coordinates system

(B) Satellite FOV in U-V

FIGURE 3.11: U-V Coordinates.

As shown in Figure 3.11a, the u-v coordinates are two unit vectors intended as the direction cosines corresponding to the angles θ and ϕ of the antenna. Using this reference system, it is then possible to project the values on a unitary sphere around the antenna, onto two dimensional u-v coordinates. It is important to highlight that the relationship between θ-ϕ and u-v coordinates systems is not linear and a regularly spaced grid of points on the θ-ϕ plane will not result on a regularly spaced grid

on the u-v plane, and viceversa. The values of u and v satisfy the inequalities:

$$\begin{aligned} -1 \leq u \leq 1 \\ -1 \leq v \leq 1 \\ u^2 + v^2 \leq 1 \end{aligned} \tag{3.15}$$

The u-v axis orientations, being local coordinates, can be chosen such as to best adapt to the specific use case. For example, as depicted in Figure 3.11b, the satellite FOV is described by means of u-v coordinates aligned with the spacecraft cartesian reference system. Specifically, u is aligned with the direction of the satellite on its orbit (x-axis), while v is aligned with the y axis. Considering then the z axis is pointing towards the center of the Earth, the correspondence between u-v and spacecraft fixed coordinates depicted in Figure 3.6, is obtained.

3.6 Earth-Satellite Geometry

The most common problem in space mission geometry is to transform back and forth between Earth coordinates and the view as seen from the spacecraft. An example of problems of this type is to use the given coordinates of a target on the Earth to determine its coordinates in the spacecraft FOV. Another is to determine the intercept point on the surface of the Earth corresponding to a given direction in spacecraft coordinates or a given location in the FOV of a spacecraft camera.

Figure 3.12a shows the relationship between the geometry on the Earth's surface and that as seen from the spacecraft. A vector from the spacecraft will be tangent to the surface of the Earth at the true or *geometric horizon*. The area inside the horizon is called *access area* and it represents the portion of the Earth's surface that the spacecraft can communicate with or look at, at this time. For a spherical Earth model, the true horizon will be a small circle[10]. The angular radius of this circle is called the *maximum Earth Central Angle*, λ_0, when measured from the center of the Earth, and the *angular radius of the Earth*, ρ, when measured from the space craft. The axis of the two cones formed by the horizon and either the Earth's center or the spacecraft is the *spacecraft position vector* when it goes from the center of the Earth to the spacecraft, and the *nadir vector* when it goes from the spacecraft to the center of the Earth. This line intersects the surface of the Earth at the SSP. Finally, the direction toward the center of the Earth is called nadir, and the opposite direction is called zenith. Thus, for an observer standing at the SSP, the center of the Earth is in the nadir direction and the spacecraft is at the zenith.

It is convenient to define an access area coordinate frame on the Earth's surface corresponding to the nadir coordinate frame on the spacecraft. As shown in Figure 3.12b, the Earth Central Angle, λ, is measured from the SSP, and the azimuthal

[10] A circle on a sphere whose plane passes through the center of the sphere is called a great circle, otherwise it is a small circle.

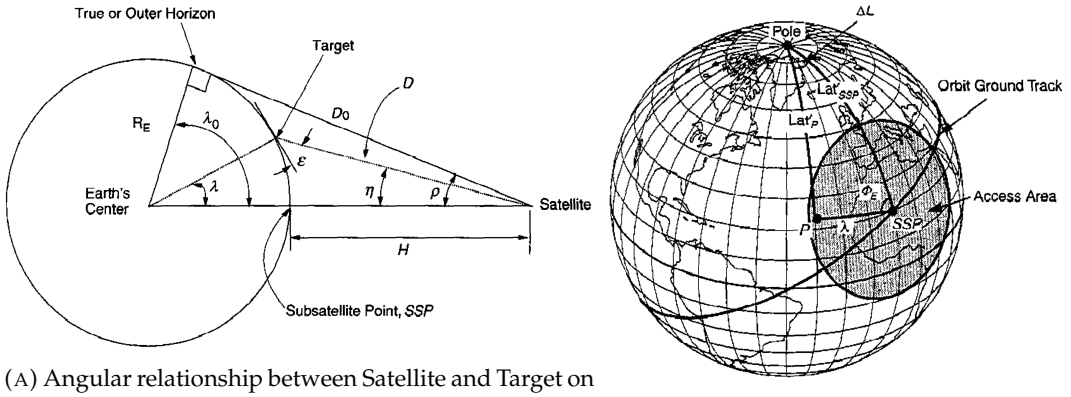

(A) Angular relationship between Satellite and Target on Earth

(B) Access Area Coordinate Frame

FIGURE 3.12: Relationship between geometry as Viewed from the Spacecraft and from the Center of the Earth. [88].

angle,Φ_E, is the rotation angle measured at the SSP from a reference direction to the point in question. Depending upon the particular problem, the reference direction may be either North or the projection of the velocity vector down onto the Earth's surface. The transformation between latitude and longitude and access area coordinates, by means of spherical geometry rules, can be written as follows, [88]:

$$\lambda = \cos^{-1}\left(\cos Lat'_P \cos Lat'_{SSP} + \sin Lat'_P \sin Lat'_{SSP} \cos \Delta L\right) \tag{3.16}$$

$$\Phi_E = \left[h_{sat}(\Delta L) \cdot \cos^{-1}\left(\frac{\cos Lat'_P - \cos Lat'_{SSP} \cos \lambda}{\sin Lat'_{SSP} \sin \lambda}\right)\right] \bmod 2\pi \tag{3.17}$$

where:

$$h_{sat}(\varphi) = \begin{cases} 1, & \text{if } 0 \leq \varphi \bmod 2\pi \leq \pi \\ -1, & \text{if } 180 \leq \varphi \bmod 2\pi \leq 2\pi \end{cases} \tag{3.18}$$

$$Lat'_P = \cos^{-1}\left(\cos \lambda \cos Lat'_{SSP} + \sin \lambda \sin Lat'_{SSP} \cos \Phi_E\right) \tag{3.19}$$

$$\Delta L = \left|Lon_{SSP} - Lon_P\right| = \cos^{-1}\left[\frac{\cos \lambda - \cos Lat'_P \cos Lat'_{SSP}}{h_{sat}(Lat'_{SSP}) \sin Lat'_{SSP} \sin Lat'_P}\right] \tag{3.20}$$

In the previous equations Lat_P and Lon_P represent the latitude and longitude coordinates of the target point on the Earth's surface, while Lat_{SSP} and Lon_{SSP} the coordinates for the SSP. The azimuthal angle, Φ_E, is about the SSP from the reference direction to the target point and it is measured on the surface of the Earth.

Eventually the fundamental geometry problem has been reduced to transforming back and forth between access area coordinates on the surface of the Earth and spacecraft coordinates centered at the nadir. This is particularly easy to do for the azimuthal component, since it is the same azimuth angle measured in either frame of reference, Φ_E.The remaining problem is to transform the radial component. Depending on the problem at hand, it is convenient to measure this radial component

either in terms of angles at the satellite, at the Earth's center, or at the target point on the surface of the Earth. As shown in Figure 3.12a, the nadir angle, η, is measured at the spacecraft from the SSP to the target point. The Earth central angle, λ, is measured at the center of the Earth from the SSP to the target, and the spacecraft *elevation angle*, ε, is the angle measured at the target between the spacecraft and the local horizontal. First, the angular radius of the Earth, ρ, and the maximum Earth Central Angle, λ_0, are computed from:

$$\begin{aligned} \rho &= \sin^{-1}\left(\frac{R_E}{R_E + h_{sat}}\right) \\ \lambda_0 &= \cos^{-1}\left(\frac{R_E}{R_E + h_{sat}}\right) \end{aligned} \tag{3.21}$$

where R_E is the Earth radius, thus approximately 6371 km and h_{sat} is the satellite altitude. Next, if λ is known it is possible to compute η as:

$$\eta = \tan^{-1}\left(\frac{\sin\rho\sin\lambda}{1 - \sin\rho\cos\lambda}\right) \tag{3.22}$$

Or if η is known it is possible to compute ε as:

$$\cos\varepsilon = \cos^{-1}\left(\frac{\sin\eta}{\sin\rho}\right) \tag{3.23}$$

Or if ε is known it is possible to compute η as:

$$\eta = \sin^{-1}(\cos\varepsilon\sin\rho) \tag{3.24}$$

Finally, the remaining angle is determined from:

$$\eta + \lambda + \varepsilon = 90\text{deg} \tag{3.25}$$

The *slant range*, D, to the target, is:

$$D = R_E\frac{\sin\lambda}{\sin\eta} \tag{3.26}$$

and the distance to the true horizon, D_0 is given by:

$$D_0 = \frac{R_E}{\tan\eta} \tag{3.27}$$

The spherical Earth approximation adopted for this mathematical computations, is adequate for most mission geometry applications. It is also the hypothesis on which ESiM2M is based. However, for precise work, a correction for oblateness, must be applied. Taking into account the satellite to Earth geometry depicted in Figure 3.12, under the spherical Earth approximation hypothesis, the relationship

between θ-ϕ coordinates and the spacecraft coordinates centered on nadir is straightforward. Recalling the concepts for θ-ϕ coordinates previously described, it is indeed trivial to proof that θ is equivalent to η, and that ϕ can be easily obtained knowing Φ_E [83], [85], [88], [92].

3.7 Reference Systems Transformations

In this section the main coordinate transformations among different reference systems will be showed. For the sake of synthesis only the main rotations and coordinate changes adopted in the framework of ESiM2M will be considered. Other use-case specific transformations could be derived from the main ones and from the references.

3.7.1 Basic Concepts for Cartesian reference systems Transformations

Spatial transformations in the three dimensional Euclidean space $\mathbb{R}^3$ can be distinguished into *active* (or alibi) transformations and *passive* (or alias) transformations. The former is a transformation that actually changes the physical location of a point or rigid body, that can be specified in the absence of a coordinate system. The latter is a change in the coordinate system in which the object is represented (*e.g.*, change of coordinate map, or change of basis). A passive transformation refers then to a description of the same object in two different coordinate systems while an active transformation corresponds to changing the position of one or more objects with respect to the same coordinate system [93].

These transformations can be performed by means of *rotations*, *shifts*, and *scaling*. It is possible to define three basic (elemental) rotation matrices in $\mathbb{R}^3$, each one applying a rotation around one of the three cartesian axis (x, y, z). These rotation matrices, for values of $\theta > 0$, refer to active rotations of vectors counterclockwise in a right-handed coordinate system by left-multiplication. Since matrix multiplication has no effect on the zero vector, *i.e.*, the coordinates of the origin, rotation matrices describe rotations about the origin. Rotation matrices are square matrices, with real entries. More specifically, they can be characterized as orthogonal matrices with $\det = 1$, thus a square matrix $\mathbf{R}$ is a rotation matrix if and only if $\mathbf{R}^T = \mathbf{R}^{-1}$ and

$\det \mathbf{R} = 1$. The three basic rotation matrices can be written as follow [94]:

$$\mathbf{R}_x(\theta) = \begin{bmatrix} 1 & 0 & 0 \\ 0 & \cos(\theta) & -\sin(\theta) \\ 0 & \sin(\theta) & \cos(\theta) \end{bmatrix} \tag{3.28}$$

$$\mathbf{R}_y(\theta) = \begin{bmatrix} \cos(\theta) & 0 & \sin(\theta) \\ 0 & 1 & 0 \\ -\sin(\theta) & 0 & \cos(\theta) \end{bmatrix} \tag{3.29}$$

$$\mathbf{R}_z(\theta) = \begin{bmatrix} \cos(\theta) & -\sin(\theta) & 0 \\ \sin(\theta) & \cos(\theta) & 0 \\ 0 & 0 & 1 \end{bmatrix} \tag{3.30}$$

These rotation matrices can be applied for rotations of vectors in every cartesian reference system, and can be composed in order to achieve any general rotation. As previously mentioned, it is also possible to apply a passive rotation in order to convert the coordinates of a column vector, $\mathbf{v}$, to another cartesian reference system, with a different orientation, θ. For this purpose, it is sufficient to left-multiply $\mathbf{v}$ by $\mathbf{R}^T$, or equivalently right-multiply $\mathbf{v}^T$ by $\mathbf{R}$. The elemental rotations could be also concatenated; thus, from elemental linear algebra, all transformations between two Cartesian coordinate systems, $CRS1$ and $CRS2$, can be generalized as:

$$\mathbf{X}_{CRS2} = \Delta\mathbf{X} + \alpha \cdot \mathbf{R}_x^T(\theta_1)\mathbf{R}_y^T(\theta_2)\mathbf{R}_z^T(\theta_3) \cdot \mathbf{X}_{CRS1} \tag{3.31}$$

which is a composition of a shift vector $\Delta\mathbf{X} = [\Delta x, \Delta y, \Delta z]$, three consecutive rotations around the coordinate axes by an angle $\theta_1, \theta_2, \theta_3$, and a scale factor, α. It is worth highlighting that there are 6 different possible sequences for the axis rotation and it is of primary importance to choose the right sequence for each use case as highlighted in the following.

As a further extension to the aforementioned concept of basic rotations showed in Equations 3.28, 3.29, and 3.30, it is important to introduce the concept of *Euler angles*. These angles are used for defining vehicle attitude representation, by describing the orientation of a rigid body with respect to a fixed coordinate system. Euler angles are used to define a coordinate transformation in terms of a set of three angular rotations, performed in a specified sequence about three specified orthogonal axes, to bring one coordinate frame to coincide with another and are commonly used in navigation. Figure 3.7 shows the classical Euler angle representation for a vehicle attitude description. In particular Figure 3.7b shows the fixed reference system x, y, z in blue and the rotated one, X, Y, Z in red, with N representing the line of nodes where the fundamental planes of the two reference systems intersect.

Euler angles can be defined by elemental rotations or by a composition of rotations. The geometrical definition demonstrates that three composed elemental rotations are always sufficient to reach any target frame. These elemental rotations may

be *extrinsic* or *intrinsic*. Extrinsic rotations are about the axes x, y, z of the original coordinate system, which is assumed to remain motionless. Intrinsic rotations are about the axes of the rotating coordinate system X, Y, Z, fixed with the moving body, which changes its orientation after each elemental rotation. Furthermore, these rotation sequences can be defined by means of: i) *proper Euler angles*, when the first and third rotations happen to be about the same axis; and ii) *Tait–Bryan angles*, which represent successive rotations about three distinct axis. The latter are commonly used in aviation and is the convention adopted in the following, if not otherwise specified. A common rotation sequence is the so called RPY, which corresponds to the sequence of rotations around axis $z - y' - z''$. This represents the intrinsic rotation sequence with y' being the new y axis fixed with the body of the vehicle after the first rotation, and z'' being the z axis after the second elemental rotation. This sequence correspond to the extrinsic one $x - y - z$.

It is worth highlighting that rotation matrices do not commute. Euler angles suffer by a discontinuity issue analogous to the *gimbal lock*. For example, when the vehicle roll axis is pointed upward, as it is for launch of many rockets. In that orientation, tiny changes in the vehicle pitch or yaw cause $\pm 180°$ changes in heading angle. For aircraft, this creates a slewing rate problem for electromechanical compass card displays. In order to overcome the gimbal lock problem it is possible to use alternative mathematical models for computing vehicle attitude angle, like the *quaternions*, but this is outside the scope of this work [83], [92].

3.7.2 Ellipsoidal and Cartesian Coordinates Conversion

The Cartesian coordinates of a point $P(X_{ECEF}, Y_{ECEF}, Z_{ECEF})$ can be obtained from the ellipsoidal coordinates $P(\phi, \lambda, h)$ as follows [82]:

$$X_{ECEF} = (N(\phi) + h) \cos\phi \cos\lambda \tag{3.32}$$

$$Y_{ECEF} = (N(\phi) + h) \cos\phi \sin\lambda \tag{3.33}$$

$$Z_{ECEF} = ((1 - e^2)N(\phi) + h) \sin\phi \tag{3.34}$$

where $N(\phi)$ is the radius of curvature in the prime vertical:

$$N(\phi) = \frac{a}{\sqrt{1 - e^2 \sin^2\phi}} \tag{3.35}$$

and e is the ellipsoid eccentricity, related with the semi-major axis a, the semi-minor axis b and the flattening factor f previously shown:

$$e^2 = \frac{a^2 - b^2}{a^2} = 2f - f^2 \tag{3.36}$$

The ellipsoidal coordinates of a point $P(\phi, \lambda, h)$ can be obtained from the cartesian coordinates $P(X_{ECEF}, Y_{ECEF}, Z_{ECEF})$ as follows:

$$\lambda = \tan^{-1}\left(\frac{Y_{ECEF}}{X_{ECEF}}\right) \tag{3.37}$$

$$\phi_{(0)} = \tan^{-1}\left[\frac{Z_{ECEF}}{\left(1-e^2\right)\left(\sqrt{X_{ECEF}^2 + Y_{ECEF}^2}\right)}\right] \tag{3.38}$$

where $\phi_{(0)}$ is the initial value for the latitude to be used in the following iterative approach, until the change between two successive values of $\phi(i)$ and $h_{(i)}$ are smaller than the precision required:

$$N_{(i)} = \frac{a}{\sqrt{a - e^2 \sin^2 \phi_{(i-1)}}} \tag{3.39}$$

$$h_{(i)} = \frac{\sqrt{X_{ECEF}^2 + Y_{ECEF}^2}}{\cos \phi_{(i-1)}} - N_{(i)} \tag{3.40}$$

$$\phi_{(i)} = \tan^{-1}\left[\frac{Z_{ECEF}}{\left(1 - e^2 \frac{N_{(i)}}{N_{(i)}+h_{(i)}}\right)\left(\sqrt{X_{ECEF}^2 + Y_{ECEF}^2}\right)}\right] \tag{3.41}$$

It is worth highlighting that here only the geodetic Latitude-Longitude-Altitude (LLA) coordinates have been considered. In the case of spheroid approximation, *i.e.*, approximating the geoid to a perfect sphere, these relations remain valid.

3.7.3 ECI and ECEF Conversion

ECEF coordinates have the same origin (Earth's center) but the two reference system axis are not aligned. In general four steps would be required to convert coordinates from ECI to ECEF and viceversa: i) calculate Earth's precession[11]; ii) calculate Earth's nutation[12]; iii) account for Earth's rotation including the offset with respect to J2000 epoch; and iv) account for polar motion[13]. The difference in axis orientation

[11] In astronomy, axial precession is a gravity-induced, slow, and continuous change in the orientation of an astronomical body's rotational axis. For what concern the Earth this gradual shift in the orientation of Earth's axis of rotation follow a periodic cycle of approximately 26 000 years [82].

[12] The short-period motion of the Earth's rotation axis with respect to a space-fixed coordinates system is called nutation. As for the precession, astronomical nutation is a phenomenon which causes the orientation of the axis of rotation of a spinning astronomical object to vary over time. It is caused by the gravitational forces of other nearby bodies acting upon the spinning object and it is intimately connected with polar motion [82].

[13] Polar motion of the Earth is the motion of the Earth's rotational axis relative to its crust. Can be defined with respect to the rotation axis position at J2000 epoch. It is then the movement of the Earth's rotation axis with respect to an Earth-fixed coordinate system [82].

between ECI and ECEF reference systems is measured with respect to the reference epoch. These rotations can be represented by a composition of basic rotations. Due to the fact that for analyses over a short time-span, as for the system simulations for a satellite communication system, the effect of precession, nutation, and polar rotation is negligible, the third (polar) axis of ECI and ECEF systems, are considered colocated. As a consequence, ECI and ECEF longitudes differ only by a linear function of time. It is possible to compute the Earth Rotation Angle, θ_{ERA}, with respect to the inertial frame as [95]:

$$\theta_{ERA}(t_U) = 2\pi(0.7790572732640 + 1.00273781191135448 \cdot t_U) \tag{3.42}$$

Where 0.7790572732640 is the Earth Rotation Angle at the standard epoch J2000, $t_U = JD - 2451545.0$ is the Julian Date at the time of measurement minus 2451545.0 which is the Julian Date of the standard epoch J2000, and 1.00273781191135448 is the sidereal day. Then, in order to apply the reference system transformation is sufficient to consider a rotation about the $Z_{ECI-ECEF}$ axis. The transformation from a reference system to a new one, being a passive rotation, requires the transposition of the rotation matrix. Then referring to Equations 3.28, 3.29, and 3.30, the transformations from ECI to ECEF coordinate vectors, and viceversa can be computed as:

$$\begin{bmatrix} X_{ECEF} \\ Y_{ECEF} \\ Z_{ECEF} \end{bmatrix} = \mathbf{R}_z^T(\theta_{ERA}) \cdot \begin{bmatrix} X_{ECI} \\ Y_{ECI} \\ Z_{ECI} \end{bmatrix} \tag{3.43}$$

$$\begin{bmatrix} X_{ECI} \\ Y_{ECI} \\ Z_{ECI} \end{bmatrix} = \mathbf{R}_z(\theta_{ERA}) \cdot \begin{bmatrix} X_{ECEF} \\ Y_{ECEF} \\ Z_{ECEF} \end{bmatrix} \tag{3.44}$$

3.7.4 ENU/NED and ECEF Conversion

First of all, it is worth highlighting that the coordinate transformation matrix $\mathbf{C}_{ENU}$ from ENU to NED coordinates and the transformation matrix $\mathbf{C}_{NED}$ from NED to ENU coordinates are one and the same [83]:

$$\mathbf{C}_{NED}^{ENU} = \mathbf{C}_{ENU}^{NED} = \begin{bmatrix} 0 & 1 & 0 \\ 1 & 0 & 0 \\ 0 & 0 & -1 \end{bmatrix} \tag{3.45}$$

The relation between the local ENU coordinates and the ECEF coordinates is illustrated in Figure 3.13. Referring to the geodetic coordinates It is obvious that ENU coordinates can be transformed to ECEF ones by means of two rotations: i) a clockwise rotation about X_{ENU} (east-axis) by an angle $(90 - \phi)$ to align the Z_{ENU} axis with the Z_{ECEF} axis; and ii) a clockwise rotation about the Z_{ENU} axis by and angle $(90+\lambda)$ to align the X_{ENU} axis with the X_{ECEF}-axis. Recalling Equations 3.28,

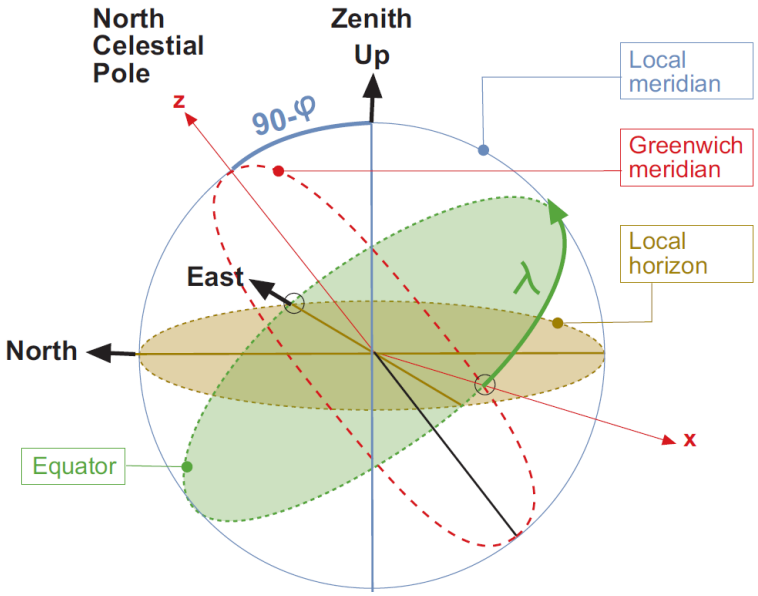

FIGURE 3.13: ENU and ECEF coordinates transformation [96].

3.29, and 3.30, and remembering that a coordinates change corresponds to a passive transformation, the transformation from ENU to ECEF coordinates can be written as [83], [96]:

$$\begin{bmatrix} X_{ECEF} \\ Y_{ECEF} \\ Z_{ECEF} \end{bmatrix} = \underbrace{\mathbf{R}_z^T\left(-\frac{\pi}{2}-\lambda\right)\mathbf{R}_x^T\left(-\frac{\pi}{2}+\phi\right)}_{R_{ECEF}^{ENU}} \begin{bmatrix} X_{ENU} \\ Y_{ENU} \\ Z_{ENU} \end{bmatrix} \tag{3.46}$$

$$\mathbf{R}_{ECEF}^{ENU} = \begin{bmatrix} -\sin\lambda & -\cos\lambda\sin\phi & \cos\lambda\cos\phi \\ \cos\lambda & -\sin\lambda\sin\phi & \sin\lambda\cos\phi \\ 0 & \cos\phi & \sin\phi \end{bmatrix} \tag{3.47}$$

It is worth noting that the order of rotations is *not commutative*, then the rotations could be applied separately in the aforementioned order (*e.g.*, left-multiplication by $\mathbf{R}_x^T$ then by $\mathbf{R}_z^T$) or by composing the rotations but in the reverse order, being a left-multiplication (*e.g.*, left-multiplication by $\mathbf{R}_z^T \cdot \mathbf{R}_x^T$).

As of the inverse transformation, from ECEF to ENU coordinates, requires: i) a counter-clockwise rotation about the Z_{ECEF} axis by and angle $(90+\lambda)$ to align the X_{ECEF} axis with the X_{ENU} axis; and ii) a counter-clockwise rotation about X_{ECEF} axis by an angle $(90-\phi)$ to align the Z_{ECEF} axis with the Z_{ENU} axis. It can be

written as [83], [96]:

$$\begin{bmatrix} X_{ENU} \\ Y_{ENU} \\ Z_{ENU} \end{bmatrix} = \underbrace{\mathbf{R}_x^T\left(\frac{\pi}{2}-\phi\right)\mathbf{R}_z^T\left(\frac{\pi}{2}+\lambda\right)}_{R_{ENU}^{ECEF}} \begin{bmatrix} X_{ECEF} \\ Y_{ECEF} \\ Z_{ECEF} \end{bmatrix} \tag{3.48}$$

$$\mathbf{R}_{ENU}^{ECEF} = \begin{bmatrix} -\sin\lambda & \cos\lambda & 0 \\ -\cos\lambda\sin\phi & -\sin\lambda\sin\phi & \cos\phi \\ \cos\lambda\cos\phi & \sin\lambda\cos\phi & \sin\phi \end{bmatrix} = \left(\mathbf{R}_{ECEF}^{ENU}\right)^T \tag{3.49}$$

For what concern the transformation from NED to ECEF and viceversa, it is possible to follow a similar approach. For the sake of synthesis in the following only the transformation matrices $\mathbf{R}_{ECEF}^{NED}$ and $\mathbf{R}_{NED}^{ECEF}$ will be showed [83]:

$$\mathbf{R}_{ECEF}^{NED} = \begin{bmatrix} -\cos\lambda\sin\phi & -\sin\lambda & -\cos\lambda\cos\phi \\ -\sin\lambda\sin\phi & \cos\lambda & -\sin\lambda\cos\phi \\ \cos\phi & 0 & -\sin\phi \end{bmatrix} \tag{3.50}$$

$$\mathbf{R}_{NED}^{ECEF} = \begin{bmatrix} -\cos\lambda\sin\phi & -\sin\lambda\sin\phi & \cos\phi \\ -\sin\lambda & \cos\lambda & 0 \\ -\cos\lambda\cos\phi & -\sin\lambda\cos\phi & -\sin\phi \end{bmatrix} = \left(\mathbf{R}_{ECEF}^{NED}\right)^T \tag{3.51}$$

3.7.5 RPY and ENU/NED Conversion

Due to the fact that the relationship between LTP reference systems and ECEF coordinates has been already explained, it is important to highlight the necessary transformations between RPY and LTP reference systems, such to have a complete chain of transformations to pass from one coordinate system to another. It is important to highlight that the sequence of intrinsic rotations to be computed is: i) a right-handed rotation about Roll, X_{RPY}, axis by an angle R; ii) a right-handed rotation about Pitch, Y_{RPY}, axis by an angle P; and iii) a right-handed rotation about Yaw, Z_{RPY}, axis by an angle Y. Recalling Equations 3.28, 3.29, and 3.30, and the fact that RPY reference system is aligned with the NED one at the starting point, it is possible to consider the transformation from RPY to NED as an active rotation performed in the NED reference system itself. The transformation matrix can be then written as a composition of the three basic rotations as [83], [92]:

$$\begin{bmatrix} X_{NED} \\ Y_{NED} \\ Z_{NED} \end{bmatrix} = \underbrace{\mathbf{R}_z(Y)\mathbf{R}_y(P)\mathbf{R}_x(R)}_{R_{NED}^{RPY}} \begin{bmatrix} X_{RPY} \\ Y_{RPY} \\ Z_{RPY} \end{bmatrix} \tag{3.52}$$

$$\mathbf{R}_{NED}^{RPY} = \begin{bmatrix} C_Y C_P & -S_Y C_R + C_Y S_P S_R & S_Y S_R + C_Y S_P C_R \\ S_Y C_P & C_Y C_R + S_Y S_P S_R & -C_Y S_R + S_Y S_P C_R \\ -S_P & C_P S_R & C_P C_R \end{bmatrix} \tag{3.53}$$

where S_R, S_P, S_Y corresponds to $\sin(R), \sin(P), \sin(Y)$, and where C_R, C_P, C_Y corresponds to $\cos(R), \cos(P), \cos(Y)$. As previously mentioned, the rotations order is not commutative, then the rotations could be applied separately in Roll, Pitch, Yaw order, or by composing the rotations but in the reverse order.

As of the inverse transformation, from NED to RPY coordinates, recalling that the inverse transformation corresponds to a passive rotation follows[83], [92]:

$$\begin{bmatrix} X_{RPY} \\ Y_{RPY} \\ Z_{RPY} \end{bmatrix} = \mathbf{R}_{RPY}^{NED} \begin{bmatrix} X_{NED} \\ Y_{NED} \\ Z_{NED} \end{bmatrix} \tag{3.54}$$

$$\mathbf{R}_{RPY}^{NED} = \begin{bmatrix} C_Y C_P & S_Y C_P & -S_P \\ -S_Y C_R + C_Y S_P S_R & C_Y C_R + S_Y S_P S_R & C_P S_R \\ S_Y S_R + C_Y S_P C_R & -C_Y S_R + S_Y S_P C_R & C_P C_R \end{bmatrix} = \left(\mathbf{R}_{NED}^{RPY}\right)^T \tag{3.55}$$

where S_R, S_P, S_Y, and C_R, C_P, C_Y have been already defined.

For what concern the transformation from RPY to ENU and viceversa, it is possible to follow a similar approach. For the sake of synthesis in the following only the transformation matrices $\mathbf{R}_{ENU}^{RPY}$ and $\mathbf{R}_{RPY}^{ENU}$ will be showed [83]:

$$\mathbf{R}_{ENU}^{RPY} = \begin{bmatrix} S_Y C_P & C_R C_Y + S_R S_Y S_P & -S_R C_Y + C_R S_Y S_P \\ C_Y C_P & -C_R S_Y + S_R C_Y S_P & S_R S_Y + C_R C_Y S_P \\ S_P & -S_R C_P & -C_R C_P \end{bmatrix} \tag{3.56}$$

$$\mathbf{R}_{RPY}^{ENU} = \begin{bmatrix} S_Y C_P & C_Y C_P & S_P \\ C_R C_Y + S_R S_Y S_P & -C_R S_Y + S_R C_Y S_P & -S_R C_P \\ -S_R C_Y + C_R S_Y S_P & S_R S_Y + C_R C_Y S_P & -C_R C_P \end{bmatrix} = \left(\mathbf{R}_{ENU}^{RPY}\right)^T \tag{3.57}$$

where S_R, S_P, S_Y, and C_R, C_P, C_Y have been already defined.

It is worth highlighting that for reference systems fixed with the vehicle body, it could be useful to associate the RPY to ENU coordinates system at the body initial state, instead of associating it to the NED reference system as previously described (*e.g.*, when the antenna reference system is fixed with the vehicle and at its initial state is aligned with ENU). For the sake of synthesis, only the transformations with respect to the standard RPY reference system orientation have been shown, but other use-case axis orientations could be adopted. To summarize, it is also possible to chose a different order and position for RPY with respect to the fixed LTP reference system. Thus other conventions for axis alignment between the two reference systems could be chosen. However it is of paramount importance maintaining a correct rotation order, compliant with the body attitude variations with respect to the fixed reference frame (*e.g.*, in order to avoid improper rotations and gimbal-lock issues).

3.7.6 Perifocal and ECI coordinates Conversion

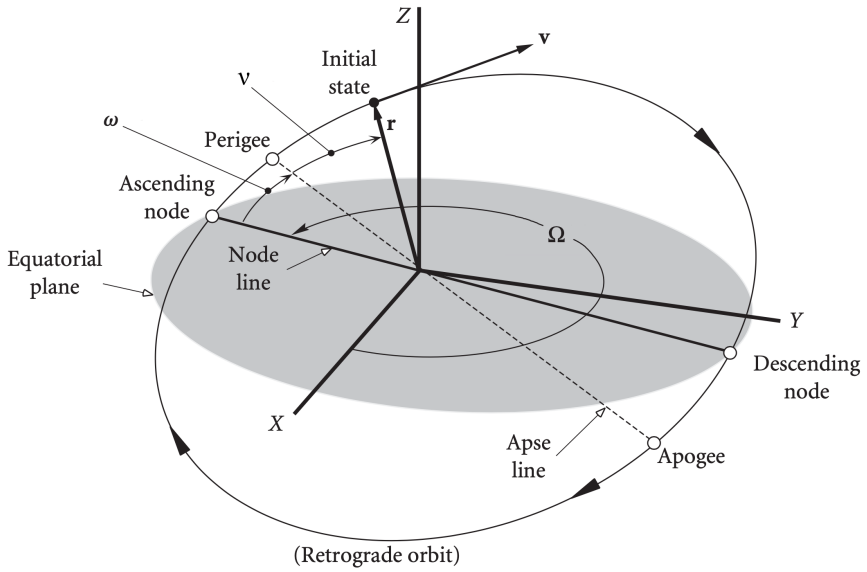

FIGURE 3.14: Perifocal-ECI frames transformation, [89].

Referring to Figure 3.14 and recalling the basic rotation matrices in Equations 3.28, 3.29, and 3.30, the ECI coordinates can be easily obtained from the perifocal one, by this composition of intrinsic rotations: i) a rotation of Ω, the orbit Right Ascension of the Ascending Node (RAAN), about the z axis; ii) a rotation of i, the orbit inclination, about the x axis; iii) a rotation of $\lambda = (\omega + \nu)$, the angle from the ascending node to the body on the orbit, about the z axis. Then the transformation is, [89], [90]:

$$\begin{bmatrix} X_{ECI} \\ Y_{ECI} \\ Z_{ECI} \end{bmatrix} = \underbrace{\mathbf{R}_z(\Omega)\mathbf{R}_x(i)\mathbf{R}_z(\omega+\nu)}_{R_{ECI}^{PQW}} \begin{bmatrix} P \\ Q \\ W \end{bmatrix} \tag{3.58}$$

$$\mathbf{R}_{ECI}^{PQW} = \begin{bmatrix} C_\Omega C_\lambda - S_\Omega S_\lambda C_i & -C_\Omega S_\lambda - S_\Omega C_\lambda C_i & S_\Omega S_i \\ S_\Omega C_\lambda + C_\Omega S_\lambda C_i & -S_\Omega S_\lambda + C_\Omega C_\lambda C_i & -C_\Omega S_i \\ S_i S_\lambda & S_i C_\lambda & C_i \end{bmatrix} \tag{3.59}$$

where S_Ω, S_λ, S_i corresponds to $\sin(\Omega), \sin(\lambda), \sin(i)$, and where C_Ω, C_λ, C_i corresponds to $\cos(\Omega), \cos(\lambda), \cos(i)$. Recalling Equations 3.8 and 3.14, the position vector,

r, and velocity vector, **v**, can be then written in ECI coordinates as:

$$\mathbf{r} = \begin{bmatrix} \frac{a(1-e^2)}{1+e\cos\nu}\big(\cos\Omega\cos(\omega+\nu) - \sin\Omega\sin(\omega+\nu)\cos i\big) \\ \frac{a(1-e^2)}{1+e\cos\nu}\big(\sin\Omega\cos(\omega+\nu) - \cos\Omega\sin(\omega+\nu)\cos i\big) \\ \frac{a(1-e^2)}{1+e\cos\nu}\sin(\omega+\nu)\sin i \end{bmatrix} \tag{3.60}$$

$$\mathbf{v} = \begin{bmatrix} -\frac{\mu}{h}\big[\cos\Omega\big(\sin(\omega+\nu) + e\sin\omega\big) + \sin\Omega\big(\cos(\omega+\nu) + e\cos\omega\big)\cos i\big] \\ -\frac{\mu}{h}\big[\sin\Omega\big(\sin(\omega+\nu) + e\sin\omega\big) - \cos\Omega\big(\cos(\omega+\nu) + e\cos\omega\big)\cos i\big] \\ -\frac{\mu}{h}\big(\cos(\omega+\nu) + e\cos\omega\big)\sin i \end{bmatrix} \tag{3.61}$$

As of the inverse transformation, from ECI to the perifocal frame, recalling that the inverse transformation corresponds to a passive rotation follows:

$$\begin{bmatrix} P \\ Q \\ W \end{bmatrix} = \mathbf{R}_{PQW}^{ECI} \begin{bmatrix} X_{ECI} \\ Y_{ECI} \\ Z_{ECI} \end{bmatrix} \tag{3.62}$$

$$\mathbf{R}_{PQW}^{ECI} = \begin{bmatrix} C_\Omega C_\lambda - S_\Omega S_\lambda C_i & S_\Omega C_\lambda + C_\Omega S_\lambda C_i & S_i S_\lambda \\ -C_\Omega S_\lambda - S_\Omega C_\lambda C_i & -S_\Omega S_\lambda + C_\Omega C_\lambda C_i & S_i C_\lambda \\ S_\Omega S_i & -C_\Omega S_i & C_i \end{bmatrix} = \big(\mathbf{R}_{ECI}^{PQW}\big)^T \tag{3.63}$$

3.7.7 Spherical and Cartesian coordinates Conversion

Referring to Figure 3.10a, (r, θ, ϕ) coordinates can be defined in terms of (x, y, z) Cartesian coordinates as:

$$r = \sqrt{x^2 + y^2 + z^2} \tag{3.64}$$

$$\phi = \left(\tan^{-1}\frac{y}{x}\right) \tag{3.65}$$

$$\theta = \left(\cos^{-1}\frac{z}{r}\right) = \tan^{-1}\left(\frac{\sqrt{x^2+y^2}}{z}\right) \tag{3.66}$$

Conversely, the Cartesian coordinates may be retrieved from the spherical coordinates as follows:

$$x = r\sin\theta\cos\phi \tag{3.67}$$

$$y = r\sin\theta\sin\phi \tag{3.68}$$

$$z = r\cos\theta \tag{3.69}$$

3.7.8 U-V and Spherical coordinates Conversion

Referring to Figure 3.11a, *u-v* coordinates can be defined in terms of θ and ϕ angles as:

$$u = \sin\theta\cos\phi \tag{3.70}$$

$$v = \sin\theta\sin\phi \tag{3.71}$$

Conversely, the θ-ϕ coordinates may be retrieved from *u-v* coordinates as follows:

$$\phi = \tan^{-1}\left(\frac{u}{v}\right) \tag{3.72}$$

$$\theta = \sin^{-1}\left(\sqrt{u^2+v^2}\right) \tag{3.73}$$

It is also possible to define *u-v* coordinates in terms of azimuth and elevation angles as:

$$u = \cos El \sin Az \tag{3.74}$$

$$v = \sin El \tag{3.75}$$

Conversely, the *Al-El* coordinates may be retrieved from *u-v* coordinates as follows:

$$El = \sin^{-1}(v) \tag{3.76}$$

$$Az = \tan^{-1}\left(\frac{u}{\sqrt{1-u^2-v^2}}\right) \tag{3.77}$$

Chapter 4

Satellite Orbits and Constellations

The *orbit* or *trajectory* is the path of a spacecraft or natural body through space. The trajectory is within a plane and shaped like an ellipse with a maximum extension at the apogee and a minimum at the perigee. The satellite moves more slowly in its trajectory as the distance from the earth increases, according to the laws of physics. An orbit is ordinarily specified by a *state vector* which can be the position and velocity of the spacecraft at some specified time or *epoch*. In principle, the state vector at any one time allows us to predict the position and velocity of the spacecraft at all future times. The list of successive positions of a satellite or planet is known as its *ephemerides*. In order to perform system-level analyses, and test the performance for specific satellite constellation designs, a proper orbit propagator for the ephemerides computation is needed in ESiM2M. In the remainings of the chapter, the mathematical framework necessary for this purpose is described.

4.1 Keplerian Orbits

The problem arising in astronomy for predicting the orbits (or escapes from orbit) of objects such as satellites, planets, and stars, is solved by means of orbits modelling. One of the most commonly used models is the unperturbed *Keplerian orbit*, where the hypothetical motion that the body follows under the gravitational effect of one other body only is typically a *conic section*, and can be readily modelled with the methods of geometry. This orbit is the model derived for the so called *Keplerian problem*, which is a special case of the *two-body problem*. In classical mechanics, the two-body problem is to predict the motion of two massive objects which are abstractly viewed as point particles. The problem assumes that the two objects interact only with one another, subordinately to the three Kepler's laws. The only force affecting each object arises from the other one, and all other objects are ignored. A Keplerian orbit is one in which: i) gravity is the only force; ii) the central body is spherically symmetric; iii) the central body's mass is much greater than that of the satellite; and iv) the central body and satellite are the only two objects in the system. Although this appears to be a large number of constraints, Keplerian orbits provide a remarkably good approximation for most spacecraft motion, in particular for those orbiting close to a celestial body of massive dimensions (*e.g.*, artificial satellites around the Earth).

4.1.1 Orbit Parameters

The position and velocity at any instant is convenient for computer applications but provide relatively little insight into the fundamental characteristics of the orbit. A convenient set for conceptualization is given by the *classical* or *Keplerian elements*, six elements characterizing the orbit shape in different ways. The information needed to fully specify an orbit are, [88]:

Orbit Size and Shape: for elliptical orbits, size and shape are completely defined by two Keplerian elements: *eccentricity*, and the *semimajor axis*. The eccentricity, e, which defines the shape of the ellipse, describing how much it is elongated compared to a circle. A value of 0 represents a circular orbit, while values between 0 and 1 form an elliptic orbit. As for the semimajor axis, a, it is defined as the sum of the perigee and apogee[1] distances, depicted in Figure 4.1, divided by two. The semimajor axis is one half of the major axis of the ellipse, and, thus, it runs from the centre, through a focus, and to the perimeter.

Orientation of the Orbit Plane: two elements completely define the orientation of the orbital plane in which the ellipse is embedded, the *inclination* and the *RAAN*. The *inclination* is the angle between the orbit plane and a reference plane which also contains the center of mass, *i.e.*, the equatorial plane. The intersection of the orbit plane and the equatorial plane through the center of mass is the line of nodes. For an Earth satellite the *ascending node* is the point in its orbit where the satellite crosses the equator going from south to north while the *descending node* is the point where it crosses the equator going from north to south. The inclination is measured at the ascending node, as represented in Figure 4.1. Most satellites travel on the same direction of Earth's rotation and are said to be in a *prograde orbit* which has an inclination between 0 and 90 deg; while satellites traveling in the opposite direction are in a *retrograde orbit* and have inclinations between 90 and 180 deg. To fully define the orbit plane, also the orientation of the line of nodes around the equator must be specified, with respect to an inertial space. The reference point that is ordinarily used for inertial space is the vernal equinox[2]. Consequently, the orientation of the ascending node on the sky is defined by the RAAN, Ω, which is the angle in the equatorial plane measured east ward from the vernal equinox to the ascending node of the orbit. For some applications it is also convenient to specify instead the Longitude of the Ascending Node (LAN), measured on the surface of the Earth from the Greenwich meridian to the ascending node.

Orientation of the Orbit within the Plane: knowing the orientation of the orbital plane, the rotational orientation of the major axis must be specified, *i.e.*, the

[1] Perigee and apogee denote the two extreme points, the nearest and the farthest respectively, in the orbit of the satellite about the Earth.

[2] The vernal equinox or first point of arise, is the reference point that is ordinarily used for inertial space, and corresponds to the ascending node of the Earth's orbit about the Sun. This is the location of the Sun in the sky on the first day of spring.

line connecting apogee and perigee, within that plane. This is done by defining the *argument of perigee*, ω, which is the angle at the center of mass of the Earth, measured in the orbital plane in the direction of the satellite's motion, from the ascending node to the perigee, as depicted in Figure 4.1.

Position of the Satellite within the Orbit: finally it is possible to specify the position of the satellite on its orbit, at any specific epoch by means of the *true anomaly*, ν, which is the angle measured at the center of mass of the Earth between the perigee and the satellite, as depicted in Figure 4.1. The computation of ν is quite complex, being the main parameter to be computed for the orbit propagation of position and velocity of the satellite, as it will be explained in Section 4.1.3.

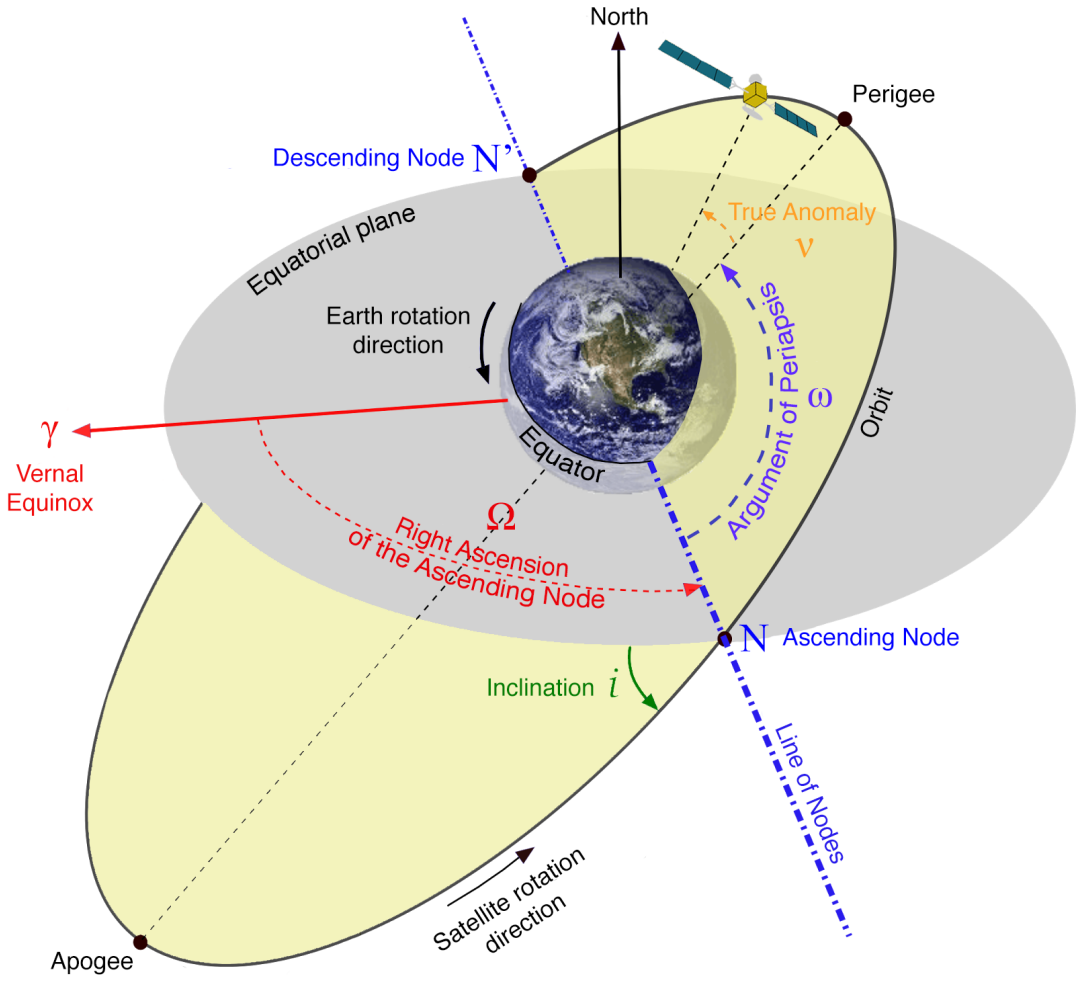

FIGURE 4.1: Kepler Orbit parameters.

4.1.2 Orbit Perturbations

The differences between the Keplerian orbit and the actual motion of the body are caused by *perturbations*. These perturbations are caused by forces other than the

gravitational effect between the primary and secondary body and must be modelled to create an accurate orbit simulation. It is possible to identify two types of perturbations: i) *secular perturbations* for which the effects build up over time; and ii) *cyclic perturbations* which are periodic, such that the effects cancel out after one cycle or orbit, [88].

The main perturbing forces may include, [1], [88]: i) *third body interactions*, so to the gravitational forces of the Sun and the Moon; ii) *magnetic fields* of the Earth can be a source of orbital perturbations, like gravity; iii) *solar radiation pressure*, which causes periodic variations in all of the orbit elements, particularly in low-mass, large-section satellites such as balloons or spacecraft with a large solar sail; iv) *non-spherical gravity* due to the non-perfect spherical shape of Earth, thus to an uneven mass distribution within the latter; and v) *atmospheric drag* which slows down the satellite removing energy from the orbit and causing the latter to get smaller, leading to increases in the drag until eventually the satellite reenters the atmosphere. The last two sources of perturbations are particularly strong on LEO satellites which, in fact, have a shorter lifespan with respect to MEO/GEO satellites.

As a consequence of perturbations, the orbit parameters of satellites differ from the nominal ones. The effect of the perturbations on the position of the satellite is first analysed in order to determine the magnitude of changes on the orbital elements. Then, controlled perturbations are generated on the satellites by means of motor thrusts such to fullfil the *orbital station-keeping* requirements[3].

If the application requires precise state vectors, taking into account the perturbations, orbit models are typically propagated in time and space using *special perturbation methods*. This is performed by first modelling the orbit as Keplerian; then, perturbations are added to the model to account for the various perturbations that affect the orbit. Typical perturbation methods for propagating the position of spacecrafts and celestial body over time, accounting for the perturbations are, [97], [98]: Cowell's method, Encke's method, and Sperling-Burdet method[4].

4.1.3 Mathematical Formulation

For a purely Keplerian orbit, knowing the position and velocity at any given instant, it is possible to integrate the equations of motion in order to determine the position

[3] In particular for GEO satellites, the orbit control of the satellite defines a station-keeping box whose typical dimensions are 0.1° in longitude and latitude. Furthermore, the eccentricity of the orbit is limited to a maximum value on the order of 4×10^{-4}. Thus the satellite is moving on a "small box in the sky" with respect to the GS, [1].

[4] Special perturbation methods are the basis of the most accurate machine-generated planetary ephemerides, like the Jet Propulsion Laboratory Development Ephemeris (JPL DE) model, consisting in the numeric representations of state vectors of major Solar System bodies, tabulated at equally spaced intervals of time. Furthermore also simplified perturbations models (SGP, SGP4, SDP4, SGP8 and SDP8) can be used to calculate orbital state vectors of satellites and space debris relative to the Earth-centered inertial coordinate system: for near earth objects with an orbital period of less than 225 minutes (SGP); and for objects with an orbital period greater than 225 minutes (SDP). Those models for orbital elements are usually encoded as Two-Line Element (TLE) format, which need to be frequently updated.

and velocity at all future times. Consequently, a Keplerian orbit can be fully specified by giving the three components of the position and the three components of the velocity at any instant. For most SatCom applications, it is sufficient to propagate the spacecrafts' positions over time using a simplified model like the unperturbed Keplerian orbit, even when LEO satellite are considered. Thus, in the following, the mathematical formulation for this propagation model, which has been used also for ESiM2M, is given. In particular, in order to determine the spacecraft positions and velocity at different time instants on its orbit, the derivation for a generic Keplerian elliptical orbit, is considered. Knowing all the six Keplerian elements, introduced in the previous section, it is firstly necessary to compute the mean anomaly as, [90]:

$$M(t_k) = M(t_{oe}) + t_k \sqrt{\frac{\mu}{a^3}} \tag{4.1}$$

where: i) $t_k = t - t_{oe}$, is the k-th orbit step, computed as the difference between the current time instant, t, and the reference orbit epoch, t_{oe}; ii) $M(t_{oe})$ is the mean anomaly at the orbit reference epoch; iii) $\mu = G \cdot M$, is the *standard gravitational parameter* of Earth computed as the product between Earth's mass, M, and gravitational constant, G; and iv) a is the semi-major axis of the orbit, previously described. Then the Kepler equation for the eccentricity anomaly, $E(t_k)$, can be computed by iteratively solving this equation, [90]:

$$M(t_k) = E(t_k) - e \cdot \sin\big(E(t_k)\big) \tag{4.2}$$

where e is the orbit eccentricity previously described. It is then possible to compute the true anomaly using the Kepler's equation as, [90]:

$$\nu(t_k) = \arctan\left(\frac{\sqrt{1-e^2}\sin\big(E(t_k)\big)}{\cos\big(E(t_k)\big) - e}\right) \tag{4.3}$$

Finally, it is possible to derive the values of the position and velocity vectors in the perifocal frame, defined in Section 3.4.

1. Firstly, h is determined by plugging the values of the gravitational parameter, μ, the semi-major axis, a, and the eccentricity, e, in Equation 3.4.

2. Then, r can be found by plugging the values of a, e, and the true anomaly, ν in Equation 3.7, or alternatively by plugging h in the very same equation.

3. Plugging the values obtained for r and h in Equations 3.8 and 3.13, it is then possible to obtain the position and velocity vectors respectively.

4. Finally, the corresponding vectors in the ECI coordinates can be determined by means of the rotations composition described in Equation 3.59, thus obtaining the position vector, $\mathbf{r}$, as in Equation 3.60, and the velocity vector, $\mathbf{v}$, as in

Equation 3.61. For this purpose, it is worth highlighting that the current position along the orbit, as the angle from the ascending node, can be determined by knowing the argument of the periapsis, ω, and ν. It is then possible to find the ECEF coordinates by means of Equation 3.43, [1], [88], [89].

4.2 Orbits for Satellite Communications

In principle, the plane of the orbit can have any orientation, and the orbit can have any form. The orbital parameters are determined by the initial conditions as the satellite is injected into orbit and with the Keplerian assumptions, these orbital parameters, and hence the shape and orientation of the orbit in space, remain constant with time. In the remainings of this section, the most common orbits for SatCom purposes will be described.

4.2.1 Circular Orbits

Circular orbits are the most common for satellite communications services because they allow a simpler design with respect to HEO and also allow to serve the vast majority of the Earth's surface. It is possible to distinguish three different types of circular orbit by their altitudes: GEO, MEO, and LEO.

4.2.1.1 Geosynchronous Orbits

Geosynchronous Orbit (GSO) are both the simplest and most used satellite orbits, where the satellite orbits at an altitude of 35 786 km with an orbital period corresponding to the *sideral day*[5], thus equal to the Earth's rotation period about its polar axis.

A particular case of GSO are the GEO, where the satellite orbits around the Earth in the equatorial plane, so with inclination, i, equal to zero, according to the Earth's rotation. Consequently, the satellite in GEO will remain indefinitely fixed over a point on the Earth's equator, appearing as a point fixed in the sky and ensuring continuous operation for the area of visibility of the satellite, which corresponds to about the 43% of the Earth's surface. Due to orbit perturbations the inclination of the orbit is not perfectly zero, resulting in the apparent movement of the satellite in an eight shape, crossing the equator line. However this movement must be contained into the station-keeping box, [1], [88].

4.2.1.2 Medium Earth Orbits

MEO, also called Intermediate Circular Orbits (ICO), orbit in a region of space around Earth above an altitude of 2000 km and below GSO altitude. The most common altitude for these orbits is around 20 000 km, which implies an orbital period of 12

[5] A sidereal day is approximately 86164.0905 seconds so 23h 56min 4.0905s or 23.9344696 h.

hours. These orbits are the most common for the GNSS satellite constellations like: Galileo, GPS, GLONASS, and BDS. SES is also using these orbits (in particular at 8063 km altitude) for its O3b constellation for SatCom purposes, [1].

4.2.1.3 Low Earth Orbits

The altitude of the satellites in LEO is constant and between a few hundreds of kilometres (Very LEO (VLEO)), up to a maximum of 2000 km, with an orbital period in the order of one and a half hours.

Nowadays, these are the most sought orbits for the New Space companies: SpaceX, Amazon, OneWeb, and many others are designing their satellite mega-constellations on LEO orbits. Moreover other constellations, like Iridium, are already established on LEO. Both polar orbits, with an inclination of $90°$, and Non-polar orbits, using orbits with an inclination lower than $90°$, can be envisaged for these applications.

As for SatCom services, these orbits are useful for Earth observation satellites (*e.g.*, weather satellites, environmental monitoring satellites), which exploit in particular near $90°$ inclination orbits. This type of orbit guarantees in fact a worldwide long-term coverage as a result of the combined motion of the satellite and earth rotation. At this purpose, particularly useful are the sun-synchronous orbits which ensure that a satellite passes over any given point on the Earth's surface at the same local mean solar time, [1].

4.2.2 Elliptical Orbits

The velocity of the satellite is not constant in the elliptical orbit; in fact, it is the highest at the perigee and the lowest at the apogee. Thus, the satellite stays in the vicinity of the apogee for a longer period of time than in the vicinity of the perigee, and this difference increases as the eccentricity of the orbit increases, *i.e.*, in HEO orbits. Thus, the satellite is visible to stations situated below the apogee for a significant part of the orbital duration, and this permits communication links of long duration to be established. It is useful for the satellite to return systematically to an apogee above the same area in order to establish repetitive satellite communication links, thus the period of orbits of this kind is a submultiple of the time taken by the Earth to perform one rotation with respect to the line of nodes of the orbit.

These orbits are particularly useful for mobile satellite communication services, where the masking effects caused by surrounding obstacles such as buildings and trees and multi-path effects are pronounced at low elevation angles. In fact, inclined elliptic orbits can provide the possibility of links at medium latitudes when the satellite is close to the apogee with elevation angles close to $90°$; these favourable conditions cannot be provided at the same latitudes by geostationary satellites, [1]. The most famous HEO orbits are Molniya and Tundra.

4.2.2.1 Molniya

This type of orbit is particularly stable with respect to irregularities in the terrestrial gravitational potential and, owing to its inclination, it enables the satellite to cover regions of high latitude for a large fraction of the orbital period as it passes to the apogee. This type of orbit has been adopted by Russia for the satellites of the Molniya system with a period of 12 hours. Molniya orbits are inclined at an angle of almost 64° with respect to the equatorial plane, the eccentricity ranges from 0.6 to 0.75, and the semimajor axis is 26 556 km. The system needs at least three satellites to guarantee a continuous coverage of the area of interest, each one active for about eight hours around its apogee, [1].

4.2.2.2 Tundra

Also a satellite in Tundra orbits remains above the regions located under the apogee for a time interval in the order of eight hours, and the continuous coverage can be ensured with three phased satellites in different orbits. Tundra orbits are inclined at an angle of almost 64° with respect to the equatorial plane, the eccentricity range from 0.25 to 0.4, and the semimajor axis is 42 164 km. As Molniya orbits, also the Tundra ones are well suited for serving high latitude regions, [1].

4.2.3 Constellation Design

Orbit and constellation selection and design is a process rather than a set of specific computations. Many different aspects are involved and historically different solutions have been adopted; Table 13.3 in [88] gives an insight on the most famous constellation design. There has been no single universal constellation pattern; instead, there are multiple issues that tend to drive the constellation design, each leading to somewhat different characteristics. Some of the aspects to be considered when designing a SatCom satellite constellation are, [1]:

Coverage Area: for example, complete global coverage could be a requirement, besides concentrating a higher fraction of our resources on high northern latitudes where most of the world's population resides. In most constellations, the number of satellites should be minimized, but also using lower altitudes constellations, in order to reduce the cost and complexity of each satellite, could be a requirement. On the one hand a satellite in LEO provides only a limited coverage at a given time and a limited time over a given location. Unless low-gain antennas that provide low directivity and hence almost omnidirectional radiation are installed, earth stations must be equipped with satellite-tracking devices, which increases the cost. A GEO satellite, on the other hand, appears to be particularly useful for continuous coverage of extensive regions. However, it does not permit coverage of the polar regions, which are however accessible by satellites in HEO or polar orbits. Furthermore, a satellite in an

inclined or polar elliptical orbit can appear overhead at certain times, which enables communication to be established in urban areas without encountering the obstacles that large buildings constitute for elevation angles between $0°$ and approximately $70°$. With a geostationary satellite, the angle of elevation decreases as the difference in latitude or longitude between the earth station and the satellite SSP increases. Related to the altitude and elevation angle, the link budget for the specific application must be taken into account, such that the satellite payload and ground terminal characteristics can compensate the losses and close the link budget.

Transmission duration and delay: depending on the type of application different constraints on latency are required. On the one hand a GEO satellite provides a continuous service for stations within visibility, but the propagation time is in the order of 250 ms. On the other hand a LEO satellite moving in a low orbit confers a reduced propagation time. The transmission time is thus low between stations that are close and simultaneously visible to the satellite, but it can become long (several hours) for distant stations if only store-and-forward transmission is considered; thus, a careful design of GSs positions is needed. For large LEO mega-constellations, the latency could be reduced by means of ISL at the price of a much more complex constellation management.

Interference: on the one hand, GEO satellites occupy fixed positions in the sky with respect to the stations with which they communicate and protection against interference between systems is ensured by planning the frequency bands and orbital positions. On the other hand, with LEO satellites the small orbital spacing between adjacent satellites operating at the same frequencies leads to an increase in the level of interference, making the installation of new satellites more difficult. Thus, a careful design of the constellation accounting for interference maps must be done in order for the satellite service to be compliant with other telecommunications services on ground.

There are different parameters to be optimised in the satellite constellation design process but the principal parameters to be considered can be summarized as, [88]: i) the *swath width*, which is the track on ground representing the actual coverage of the satellite; ii) the *altitude* of the orbit; iii) the *inclination* of the orbit; and iv) the *node spacing* among the different orbital planes of the constellation, so the spacing of their intersections with the equatorial plane. The Earth central angle, λ, depends on both the minimum elevation and the maximum Earth central angle λ_0, as shown in Equation 3.25, which depend on the payload performance and the satellite altitude. Once the value of λ is defined, depending on the application, the coverage circles of two consecutive satellites in the same orbital plane, and the swath of two adjacent orbital planes should overlap such to avoid gaps in coverage among the orbit planes, as shown in Figure 4.2. For this purpose, the spacing of the orbital nodes must be carefully chosen. Generally, all the orbits are at the same altitude, inclination, and

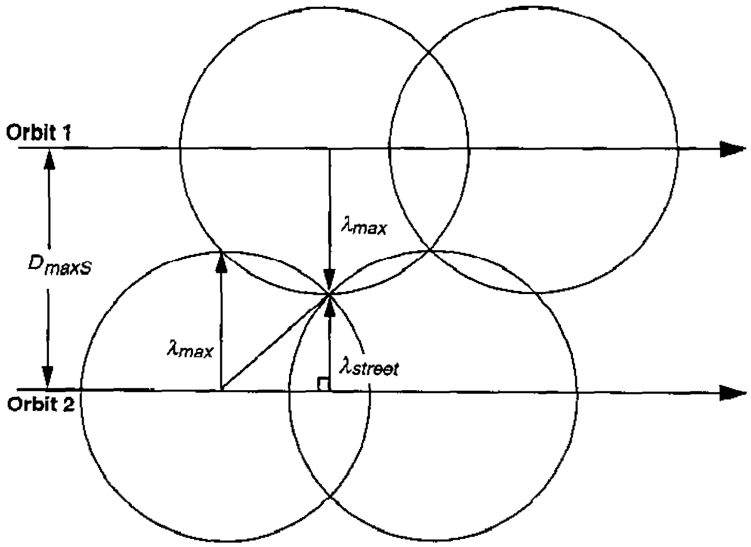

FIGURE 4.2: Coverage in Adjacent Planes, [88].

eccentricity. Having the same altitude, the satellites will have the same period and this is important in order to maintain a uniform relationship among the satellites over time. If all of the orbit periods in the constellation are the same, then the pattern will repeat every orbit.

Among the constellation patterns, the simplest one is a *set of geosynchronous satellites* that work together to perform a common function. With three satellites these constellations cover equatorial and mid-latitude regions extremely well, but perform poorly over high latitude region. *Street of coverage* constellations adopt n satellites in each of the m polar orbital planes in order to provide global coverage. The spacing among satellites in the same orbit, and the spacing among orbital planes, are related to the swath width as previously described. The most symmetric of the satellite patterns is the *Walker constellation* and the most common of these constellations is the Walker Delta Pattern, containing a total of T satellites with S satellites evenly distributed in each of P orbit planes. All of the orbit planes are assumed to be at the same inclination relative to the equator. Unlike the streets of coverage pattern, the ascending nodes of the P orbit planes in Walker patterns are uniformly distributed around the equator at intervals of $2\pi/P$. Among elliptical orbits constellation patterns, the previously described *Molniya* and *Tundra* are the most common. Furthermore, *hybrid constellations* including combinations of circular and elliptical orbits can be adopted in order to achieve determined communication and network objectives. It is worth highlighting that, in general, when constellations with multiple orbit planes are designed, it is important to properly design the *phasing* among the satellites in adjacent orbits such to avoid collisions at the line of nodes, [88].

4.2.3.1 Constellation Design in NTN 5G

In the framework of NTN integration in 5G networks, the design of satellite constellations is definitely a key aspect. As a matter of facts, according to the type of

scenario and service that should be provided, and the related requirements to be met, different satellite constellations can be used. For instance, a constellation with global coverage would be required for a use case in which latency constraints are particularly stringent, while a constellation with a long revisit period could fit an IoT scenario where the device does not need to be constantly connected to the network. Then, the orbital parameters, such as the orbit inclination and altitude, the number of orbital planes, and the number of satellites per orbital plane, must be designed accordingly. As for the possible orbits, a first distinction can be made between elliptical and circular; in terms of NTN standardisation, the current analyses described in Chapter 7 are focusing on the latter, [11]. In particular, aiming at assessing the network performance with different satellite constellations design, two main simulation methodologies have been proposed in TR 38.821, [11]:

Constellation-Based (Option-1): this approach is based on the definition of a reference constellation, in which all of the orbital parameters, the antenna pattern, and RF characteristics shall be defined, [99]–[101]. Notably, for a system aiming at achieving global coverage, the satellite altitude, the minimum elevation angle and inclination, as well as the Half Power Beam Width (HPBW) must be carefully chosen. According to the definitions in [11], a set of preliminary constellation parameters has been proposed in the past months in order to define an initial framework for performance evaluation. In particular, both GEO and LEO systems, at an altitude of 600 and 1200 km, are being addressed. As for the latter, a Walker star constellation layout with an inclination of 87.5° has been proposed, in which the reference parameters to compute the antenna patterns are defined in TR 38.821, [11], for both S-band and Ka-band. According to the constellation altitude and carrier frequency, the number of satellites per orbit and the number of beams per satellite change, such to ensure global coverage. The list of detailed parameters can be found in [99]. Another solution has been proposed in [100] based on a Walker Delta constellation, with similar parameters to the Galileo constellation, but at LEO altitude; since the constellation coverage depends on where the users are located, the coverage area to be simulated must be defined.

Regional-Based (Option-2): the second approach is based on the definition of a regional beam layout for multiple satellites. Instead of simulating the whole satellite constellation, as for the constellation-based methodology, a regional coverage for a specific geographical area is defined; then, the performance assessment is performed on this area to reduce simulation complexity while achieving accurate results, [102], [103].

Chapter 5

Physical Layer Abstraction

There are several approaches to study wireless mobile networks, from direct measurements in a real environment, to analytical mathematical derivation. However, when talking about new technologies, it should be taken into consideration that full-featured devices might not even exist. Furthermore, completely analytical approaches could be hardly applicable for the study of complete system performance, due to the highly dynamic and multi-factor nature of modern wireless networks. Computer simulation becomes then an essential part in the development process of new telecommunication systems and it is crucial in order to understand the system and user performance in reasonable operating conditions, in various deployment scenarios [104].

Considering a complex telecommunications system like the one described in Chapter 1, many aspects must be taken into account in the simulations' design. Focusing in particular on the ESiM2M tool depicted in Chapter 2, the simulations try to model and study the performance of a system with several elements, *e.g.*, satellites GSs, and UTs, taking into account both PHY related aspects and higher Open Systems Interconnection (OSI) protocol stack, and system aspects. As a matter of fact, in order to determine the system performance, PHY aspects must be properly taken into account, considering the signal propagation characteristics, the interference characterization due to the traffic conditions in the different scenarios, as well as the actual signal processing techniques adopted at transmitter and receiver side. Besides that, the effect of the different users distributions and configurations should be considered, as well as the multiple access techniques specific characteristics adopted. Furthermore, many solutions used to optimise the performance, such as ACM and dynamic resource allocation, exploit the dynamic phenomena affecting the communication channel, like the statistical fading, which must therefore be included in the model developed [105], [106].

The exact simulation of all these aspects involves a high computational load, making the system-level analyses performed by ESiM2M extremely complex and cumbersome to be executed. Therefore, for complexity reasons, system evaluations have to rely on simplified PHY models that still must be accurate enough to capture all these essential behaviours. In order to achieve this result, the PHY is usually modelled with some abstractions that simplify the simulations. Therefore, a widely

adopted approach is to divide the simulation process in two phases: i) Link-Level Simulation (LLS); and ii) SLS. By means of LLS, the single link between two network nodes is characterized. Using this result, a PHY abstraction model is elaborated and included in the SLS by means of a suitable Link-to-System (L2S) interface.

Traditionally, the performance of radio links has been evaluated in terms of PER as a function of SINR, averaged over all channel realizations of one specific channel model. PER vs SINR performance has therefore been widely used as the interface between the link- and system-level simulators. This may be adequate as long as every transmitted packet encounters similar channel statistics, which implies very small packet sizes/coding blocks with respect to the channel coherence time. However, this is generally not the case, and the specific channel realization encountered may result in a performance that is significantly different compared to the one predicted from the average curve. Consequently, the performance assessment of fast resource scheduling and fast link adaptation in system-level simulations requires a more accurate link performance model accounting for the instantaneous channel and interference conditions. Notably, this includes the effect of multiple antennas at the transmitter and/or at the receiver in combination with the applied spatial processing technique, such as beam-forming or spatial multiplexing [107].

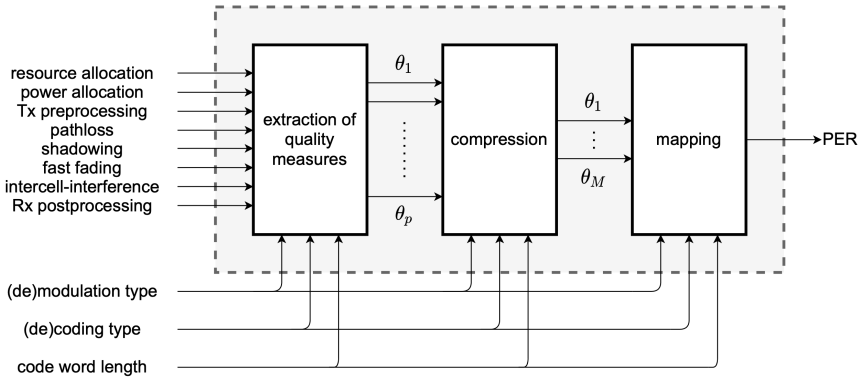

FIGURE 5.1: Generic link performance model [107].

A generic modelling approach that takes the instantaneous channel and interference characteristics into account is depicted in Figure 5.1. In a first step, a set of *quality measures*, *i.e.*, scalars $\theta_1 \dots \theta_P$, that could be obtained from SLSs, is extracted for the encoded packet of interest. Since the number of these quality indexes can be very large, some compression must be applied to reduce their number to typically one or two characteristic, *i.e.*, scalars $\theta_1 \dots \theta_M$. The main result of LLSs are tables or curves mapping these scalars (*e.g.*, SINRs, raw bit error probabilities, or SISO and MIMO channel capacities for Gaussian signalling) to PERs, for that link. Afterwards, when a quality measure is calculated in a SLS, its value is compared to the LLS results to get the realistic probability of successful frame or packet transmission. This mechanism refers to error probability modelling. A similar approach is utilized for link adaptation, where Modulation and Coding Scheme (MCS) is selected so that resulting PER is less than a predefined threshold [104].

It is thus possible to simulate the entire system, by means of SLSs, obtaining the performances of the manifold links with lower computational cost, since it is not necessary to carry out the entire processing at the PHY level for each of them [108]. Although this model has to guarantee accurate results for the specific system under analysis, it is desirable to have a performance model that is general enough (*e.g.*, such to cover different multiple access strategies and transceiver types, including different multiple antenna techniques), in order to allow the comparison among different types of systems.

5.1 Effective SINR Mapping

A typical PHY abstraction methodology is the so called ESM [104], [105]. It allows to average, in a non-linear way, the vector of instantaneous values of SINR, $\mathbf{SINR} = \{SINR_p\}$, extracting an equivalent value of SINR, the *effective SINR* ($SINR_{eff}$), [107]:

$$SINR_{eff} = \alpha_1 I^{-1}\left(\frac{1}{N}\sum_{n=1}^{N} I\left(\frac{SINR_n}{\alpha_2}\right)\right) \tag{5.1}$$

where N is the number of portions of the received encoded packet, experiencing different channel conditions. The main aspects to be taken into account for the extraction of this metric are the choice of a suitable *mapping function*, I, which is specific for the chosen abstraction method and proper tuning of model parameters α_1 and α_2. If $\alpha_1 = \alpha_2$, the values of instantaneous SINR, $\{SINR_p\}$, are constant over all resource units and equal to $SINR_{eff}$. That is exactly what has been observed in AWGN channels.

Starting from the aforementioned PHY abstraction general concepts, it is possible to describe in details the ESM methodology. The performance curves or tables, output of the LLSs that describe the PHY channel performance in AWGN conditions, are generated assuming a frequency flat channel response at a given SINR. Then, the obtained function maps a single scalar into an error probability, $PER_{AWGN} : \mathbb{R} \rightarrow [0, 1]$. The vector $SINR_p$, resulting from the SLS, is composed of heterogeneous elements due to the intrinsic characteristic of a selective channel, and must consequently be compressed into an effective value $SINR_{eff}$ [108].

The mapping function I, thus the PHY abstraction model, is considered efficient and sufficiently general if the performance of every other type of channel can be extracted from the general AWGN case, *i.e.*, the defined ESM should give the same error performance in AWGN channel that is given for the case in which SINRs are equal to $SINR_p$, and vary between different packet portions [109]:

$$PER(\{SINR_p\}) \simeq PER_{AWGN}(SINR_{eff}) \tag{5.2}$$

The tuning of parameters α_1, α_2 for a particular MCS and packet size, is done by

means of LLS, for all the different channel realizations, D. The following minimization problem should be solved [104], [110]:

$$(\alpha_1^*, \alpha_2^*) = \arg\min_{\alpha_1,\alpha_2} \left[\sum_{d=1}^{D} \left(PER^d - PER_{AWGN}\left(SINR_{eff}^d(\alpha_1, \alpha_2)\right) \right)^2 \right] \tag{5.3}$$

where PER^d is the measured PER for each of the D simulated channel realizations using LLS numerical methods. While PER_{AWGN} is the reference PER curve for AWGN channel, then $PER_{AWGN}\left(SINR_{eff}^d(\alpha_1, \alpha_2)\right)$ is the estimated PER. In order to obtain the optimal parameters α_1^* and α_2^*, the squared error between the estimated and the measured PERs for the set of simulations must be minimized.

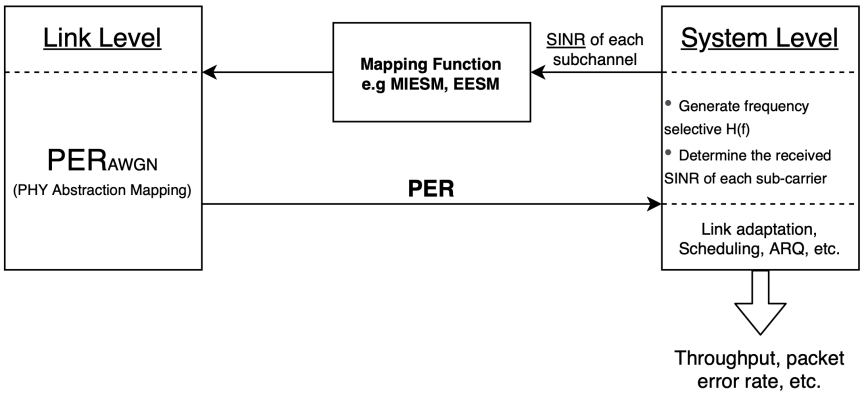

FIGURE 5.2: Effective SINR Mapping [106].

Equations 5.1 and 5.3 form the core of the ESM approach. In this case, the packet error modelling at system-level, shown in Figure 5.2, consists of the following steps:

1. Calculate the $SINR_{eff}$ based on $I(\mathbf{SINR})$ mapping.
2. Reference the AWGN link performance curves to obtain the mapping between SINR and PER.
3. Use the $SINR_{eff}$ obtained in *Step 1* and the mapping obtained in *Step 2* to derive the mapping between $SINR_{eff}$ and PER.

5.2 Effective SINR Mapping Methods

Particular methods only differ in how the mapping function is selected. Popular methods of PHY abstraction for wireless systems can be classified as shown in Figure 5.3. In the following subsections, these approaches are considered in more details.

5.2.1 Average Effective SINR Mapping (AESM)

In order to map instantaneous SINR per packets portions to a single $SINR_{eff}$, a simple approach could be to compute the average SINR. Then the mapping function

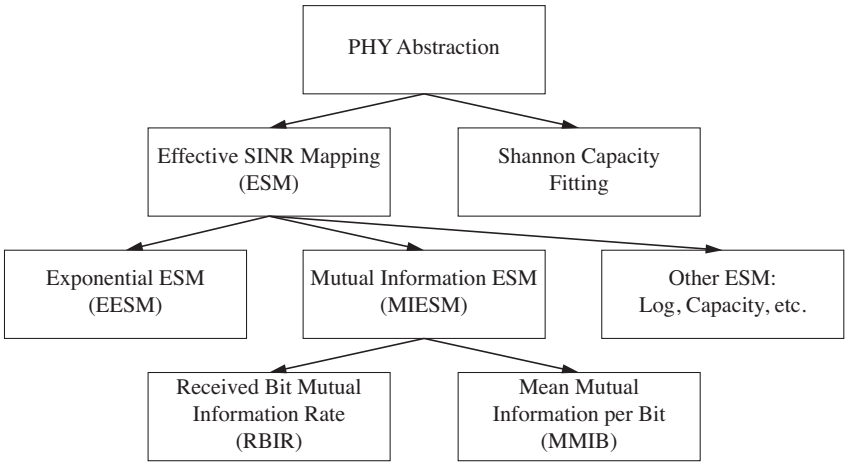

FIGURE 5.3: Effective SINR Mapping methods.

I will be as simple as:

$$I(x) = x \tag{5.4}$$

It follows that the $SINR_{eff}$ can be expressed as [108], [111]:

$$SINR_{eff} = \frac{1}{N}\sum_{n=1}^{N} SINR_n \tag{5.5}$$

However, it cannot provide accurate results under frequency selective fading [112]. A similar method which ensure slightly better performance, consist of averaging over the interference. In this case the mapping function I becomes:

$$I(x) = \frac{1}{x} \tag{5.6}$$

Thus the equation for the $SINR_{eff}$ using Average Effective SINR Mapping (AESM) can be written as:

$$SINR_{eff} = \left(\frac{1}{N}\sum_{n=1}^{N} \frac{1}{SINR_n}\right)^{-1} \tag{5.7}$$

For both these models the tuning of the parameters can be simplified considering only one of them, *i.e.*, $\alpha_1 = \beta$ and $\alpha_2 = 1$. The parameter β is optimised by means of Eq. 5.3

5.2.2 Exponential Effective SINR Mapping (EESM)

This ESM method is based on the Chernoff bound. In particular, assuming large enough SINRs, the error probability can be upper bounded as $P_e(SINR) \leq e^{-SINR}$ [113]. The expression for the mapping function I, derived from the Chernoff bound is then:

$$I(x) = e^{-x} \tag{5.8}$$

The generalized expression for effective $SINR_{eff}$ using Exponential Effective SINR Mapping (EESM) is:

$$SINR_{eff} = -\beta \ln \left[\frac{1}{N} \sum_{n=1}^{N} e^{-\frac{SINR_n}{\beta}} \right] \tag{5.9}$$

For this ESM model the tuning of the parameters can be simplified considering $\alpha_1 = \alpha_2 = \beta$ [107]. The parameter β is optimised by means of Eq. 5.3.

5.2.3 Logarithmic Effective SINR Mapping (LESM)

Another ESM model, referred to as Logarithmic Effective SINR Mapping (LESM), is based on the following equation for the mapping function I:

$$I(x) = \log_{10}(x) \tag{5.10}$$

Then, the generalized expression for effective $SINR_{eff}$ using LESM is:

$$SINR_{eff} = \beta \cdot 10^{\left(\frac{1}{N} \sum_{n=1}^{N} \log_{10}(SINR_n)\right)} \tag{5.11}$$

In this case $\alpha_2 = 1$ and $\alpha_1 = 10^{-\beta\sigma^2}$. Here, $\sigma^2 = \text{var}(\log_{10}(\mathbf{SINR}))$ reflects the variance of the considered $SINR_n$ values per encoded packet in the log domain [107], [109]. Note that in any case a single parameter β remains to be optimised by means of Eq. 5.3, in order to fit the LLS results.

5.2.4 Capacity Effective SINR Mapping (CESM)

This ESM model is related to the spectral efficiency concept. The mapping function I for the Capacity Effective SINR Mapping (CESM) method can be written as:

$$I(x) = \log_2(1 + x) \tag{5.12}$$

which represents the normalized Shannon capacity formula, according to the Hartley-Shannon bound. Then, the generalized expression for effective $SINR_{eff}$ using CESM is:

$$SINR_{eff} = \beta \left[2^{\left(\frac{1}{N} \sum_{n=1}^{N} \log_2 \left(1 + \frac{SINR_n}{\beta}\right)\right)} - 1 \right] \tag{5.13}$$

For CESM model the parameters to be tuned by using Eq. 5.3 can be assumed as $\alpha_1 = \alpha_2 = \beta$ [107].

5.2.5 Mutual Information Effective SINR Mapping (MIESM)

One of the main disadvantages of the aforementioned ESM approaches is that the optimised parameters α_1^* and α_2^* must be computed for each different scenario. Then it is not possible to find general values for those parameters, to be applied to a

broader variety of systems and scenarios. Furthermore L2S mapping applications like Hybrid Automatic Repeat reQuest (HARQ) require the combination of codewords with different MCS across the different transmission/retransmissions. In addition to the reasons previously listed, it is difficult to extend these methods to Maximum Likelihood (ML) detection in the Multiple Input Multiple Output (MIMO) case because it is not easy to compute directly the required post-processing SINR values. These problems can be overcome in the case of the Mutual Information (MI) based ESM, where the mapping function I is derived from the modulation constrained capacity (*i.e.* constrained by the input symbols from a complex set) [104], [114].

The MI describes intuitively the information that two RVs share: it measures how much knowing one of these variables reduces the uncertainty about the other. In telecommunications, the channel capacity is equal to the MI, maximized over all input distributions. Generally, the MI for two RV x and y can be defined as [115]:

$$\mathrm{MI}(x,y) = E_{x,y}\left[\log_2\left(\frac{p_{y|x}(y|x)}{p_y(y)}\right)\right] \tag{5.14}$$

where $E_{x,y}(\cdot)$ is the expectation over x, y, $p_{y|x}(y|x)$ is the conditional probability density function (pdf) of y given x and $p_y(y)$ is the pdf, *i.e.*, marginal distribution of y. Usually y must be intended as the continuous decision variable received at the demodulator after the propagation through the channel. If x is taken to have M discrete different realizations, *i.e.*, symbol alphabet size of M, with equal probabilities $1/M$, the MI can be written:

$$\mathrm{MI}(x,y) = \frac{1}{M}\sum_{i=1}^{M} E_{x_i,y}\left[\log_2\left(\frac{p_{y|x_i}(y|x_i)}{p_y(y)}\right)\right] \tag{5.15}$$

It is possible to define the Log-Likelihood Ratio (LLR) as a statistical test used to compare the fit of two models, one of which (the null model) is a special case of the other (the alternative model). The LLR of i-th realization of x given y can be defined as [115]:

$$\mathrm{LLR}_{x_i}(y) = \ln\left[\frac{P(y|x_i)}{\sum_{k=1,k\neq i}^{M} P(y|x_k)}\right] \tag{5.16}$$

where $P(y|x_i)$ is the probability that x_i has been transmitted for a known received value of y. While $\sum_{k=1,k\neq i}^{M} P(y|x_k)$ represent the null model of transmitting any symbol of the alphabet but x_i. Using Bayes' theorem it is not difficult to show that:

$$\frac{p_{y|x_i}(y|x_i)}{p_y(y)} = \frac{M}{1+e^{-\mathrm{LLR}_{x_i}(y)}} \tag{5.17}$$

Therefore it is possible to write Eq. 5.15 as:

$$\mathrm{MI}(x,y) = \frac{1}{M}\sum_{i=1}^{M} E_{x_i,y}\Big[g\big(\mathrm{LLR}_{x_i}(y)\big)\Big] \tag{5.18}$$

with $g(\text{LLR}_{x_i}(y)) = \frac{M}{1+e^{-\text{LLR}_{x_i}(y)}}$. Depending on the selection of the variable x and decision y it is possible to define two different Mutual Information Effective SINR Mapping (MIESM) approaches, described in the following.

5.2.5.1 Received Bit Mutual Information Rate (RBIR) ESM

Considering x to be the transmitted M-QAM modulation symbol, then $\{x_i\}$ are the different values from the constellation composed of M different symbols. Hence, y is the received distorted M-QAM modulation symbol in this case. Therefore the normalized MI per received bit, to be used as mapping function I in Eq. 5.1, is computed from the symbol-level MI values, represented in Eq. 5.18, as follows:

$$I_{RBIR}(SINR_n) = \frac{\text{MI}_{symbol}(SINR_n)}{M} \tag{5.19}$$

RBIR assumes that the mean and the variance of the LLR distributions, from Eq. 5.18, directly depend on the SINR experienced at symbol-level. Even though symbol-level LLR distributions can be considered Gaussian, the expression for $g(\text{LLR}_{x_i}(y))$ and consequently the MI, can only be achieved through approximation [114], [116]. For that reason, the RBIR-SINR mapping tables for $I_{RBIR}(SINR_n)$ are computed and stored beforehand (*e.g.*, RBIR-SINR mapping tables in [117] and [106]).

5.2.5.2 Mean Mutual Information per Coded Bit (MMIB) ESM

For the RBIR method, the MI to be used as mapping function I in Eq. 5.1, is obtained in Eq. 5.19 from the symbol-level MI, by simply normalizing this constrained capacity, *i.e.*, by dividing it by the modulation order. However, it is worth highlighting that the symbol channel does not account for the constellation mapping, *i.e.*, the mapping of bits to symbols in the constellation. Thus it is invariable to different bit-to-symbol mappings.

An alternative method is to define the MI on the bit-level itself, which refers to Mutual Information per Coded Bit (MIB) or Mean MIB (MMIB), when the mean of multiple MIB is involved. In this case variable x in Eq. 5.15 can just take values 0 and 1, thus $M = 2$. The decision variable y is the soft bit at the receiver. The corresponding LLR distributions are more complex than in RBIR method, but they can be approximated as a mixture of Gaussian distributions depending on the order of QAM modulation [118]. Hence, the corresponding MMIB metric can be expressed as a function of the SINR of the QAM symbol as follows:

$$I_{MMIB}(SINR_n) = \frac{1}{M}\sum_{j=1}^{M} \text{MI}_{bit_j}^{M}(SINR_n) \simeq I_M(SINR_n) \tag{5.20}$$

where approximations $I_M(SINR_n)$ depend on the modulation order M and their analytical expressions can be found in [106]. A complete block diagram for the

MIESM approach is shown in Figure 5.4, where the use of Look Up Tables (LUTs) for the mapping functions MI-SINR is highlighted [119].

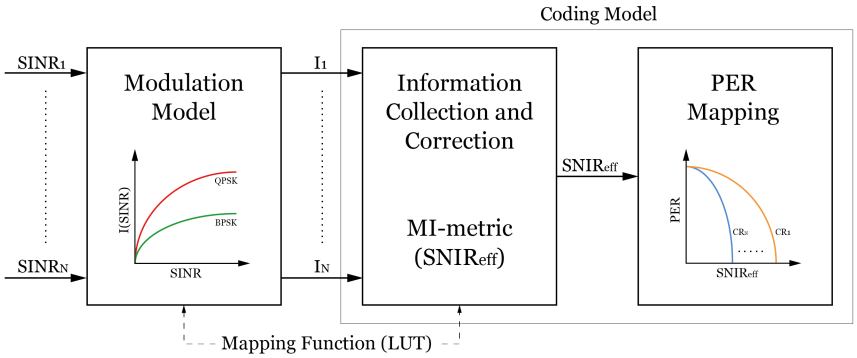

FIGURE 5.4: PHY abstraction and ESM procedure based on MI [119].

5.2.6 ESM methods Comparison

As already stated, to be effective, a PHY abstraction approach must be as versatile as possible to respond to the most diverse conditions of the system. However, the optimal model still needs to be found to best match the framework under analysis. In general, the greater accuracy of EESM and MIESM compared to the other aforementioned possibilities is discussed in [107] and [105]. In particular, it is highlighted that EESM presents some criticalities compared to the MIESM solution [104]. Firstly the parameter β must be recalculated for the different considered scenarios and it is difficult to extend this method to the case of ML detection. Moreover, in a multi-carrier system, EESM requires that the same β must be used for each of them, a limitation that requires the use of the same MCS for all sub-carriers [109]. On the other hand, MIESM methods apply to more general system conditions such as ACM and multiple antennas in transmission and reception. In any case, the fitting of parameters α_1 and α_2 leads to greater precision [119].

5.3 Non-ESM methods: Shannon Capacity Fitting

Similarly to the CESM method, this approach is based on the spectral efficiency concept and in its simplest variant it does not even utilize link-level results. It is possible to write normalized Shannon capacity formula for the theoretical Single Input Single Output (SISO) channel spectral efficiency as a function of SINR:

$$C^{ideal} = \log_2\left(1 + SINR\right) \tag{5.21}$$

with C expressed in terms of *bits/s/Hz*. Therefore, the ideal capacity in *bits/s* for a single carrier transmission, within a given portion of the packet with constant SINR, can be written as: $C_t^{ideal} = B\log_2\left(1 + SINR_n\right)$, where B is the bandwidth used for the transmission and $SINR_n$ is the SINR on a given portion of the packet of

duration t. The maximum amount of bits which could be delivered in an interval t is $L_t = C_t^{ideal}/D_t$, where D_t is the duration of the time interval with constant SINR. The total amount of bits delivered within that transmission is $\ddot{L} = \sum_{t=1}^{T} L_t$. This value is then compared with the actual packet size L. If $L > \ddot{L}$, the packet is considered to be erroneous due to insufficient SINR.

However, Eq. 5.21 is valid only for infinite delay and infinite packet size in AWGN channel and cannot be reached in practice. Therefore, in general, non idealities can be introduced in the following way [120]:

$$C = \rho\eta \log_2 \left(1 + SINR/\Gamma\right) \tag{5.22}$$

where ρ adjusts the system bandwidth efficiency, the SINR gap, Γ, takes into account the SINR implementation efficiency, and η is an additional correction factor. Reduction in bandwidth efficiency can be explained by such factors as adjacent channel leakage ratio, practical filter implementation, cyclic prefix utilization and pilot overhead; hence, ρ can be estimated theoretically. However, the nature of the SINR efficiency is more complicated; for that reason, Γ and η are extracted by using curve fitting to LLS results. This approach is also one of the options utilized in *ns-3* SLS for link adaptation [121], [122]. It is worth mentioning, that there is also a theoretical estimation of the SINR gap, $\Gamma = -\ln(5PER)/1.5$, where PER corresponds to the desired error rate threshold [104], [123].

5.4 PHY Abstraction Validation

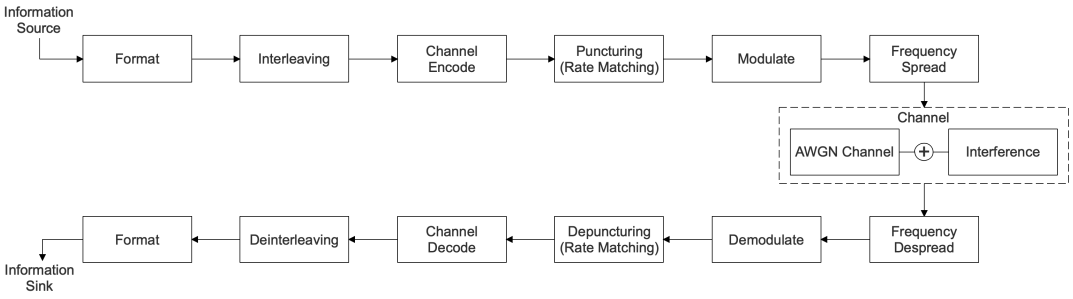

FIGURE 5.5: Block diagram for Transmitter and Receiver PHY Link Level Simulations.

The performance assessment of link performance models generally involves a comparison of the predicted PER, by means of the abstraction model, with the measured PERs derived from extensive LLSs. In the framework of the development of ESiM2M, different PHY abstraction methods have been tested. Aiming at finding the best fit for the simulation of the PHY layer of E-SSA[1] air interface, the analyses focused in particular on the aforementioned AESM methods, averaging on both

[1]The E-SSA air interface characteristics are described in Section 7.1.1.

SINR and interference, and on RBIR method. In order to properly test the performance of each ESM method, the PER over SINR curves for each of them have been derived. Then these curves have been directly compared with the PER over SINR curve of an actual PHY level simulation, *i.e.*, LLS.

For what concerns the PHY layer simulations, the Coded Modulation Library (CML) toolbox has been used [124]. The block diagram in Figure 5.5 shows all the main components of LLSs: i) the randomly generated source bits, forming information blocks of 100 and 304 bits, *i.e.*, the reference packet, are mapped onto symbols alphabet (*e.g.*, BPSK mapping); ii) interleaving is applied according to [125]; iii) the information blocks are then encoded according to [125], by means of Turbo Codes with rate $1/3$; iv) the puncturing matrix from [125] is applied to the information blocks; v) the information blocks are then modulated according to the UMTS Wideband Code Division Multiple Access (W-CDMA) scheme, as E-SSA is based on a modified version of the 3GPP W-CDMA; vi) finally, the modulated signal is spread by a Spreading Factor (SF) of 16 and 256. The same operations are performed at the receiver side, with the frequency de-spreading block, the demodulation, the de-puncturing, the channel decoding, the de-interleaving, and the recovery of the information bits.

For each SNR value at which the performance in terms of PER is tested, the decoding of the reference packet is attempted for up to 10^5 different realizations of noise, N, and interference, I, *i.e.*, until the convergence of the results for different N and I realizations. The simulation for a given SNR point is stopped before reaching 10^5 realizations if a maximum of 10^3 realizations incur in a wrongly decoded reference packet. Following this Monte Carlo approach, a different noise realization is generated at each iteration. The noise has to be intended as a complex Gaussian RV, with zero mean and variance $1/2SNR$ per component, *i.e.*, $\mathcal{CN}(0, 1/2SNR)$. As for the interference, 2, 32, 40, 64, and 128 overlapping interferers have been simulated, following three different approaches: i) interferers fully overlapped with the reference packet; ii) interferers randomly distributed (*e.g.*, random distribution) along the reference packet, *i.e.*, I starting/finishing on a random portion of the reference packet; iii) interferers overlapping only with a specific portion of the reference packet (*e.g.*, I only on $1/4$, $1/2$, or $3/4$ of the reference packet duration). As shown in the results, the number of interferers varies from a minimum of 2 up to 128, depending on the simulated scenario. It is worth highlighting that frequency/phase offset impairments are not taken into account, as well as problems related to a non-perfect sampling, thus, ideal synchronization parameters estimation at the receiver is assumed. Furthermore, interferers are considered aligned at symbol level with respect to reference packet, *i.e.*, no fractional delay.

From the LLSs, performed as shown in Figure 5.5, it is also possible to derive the SINR values for each received symbol to be used as input for the ESM methods chosen for this analysis. It should be stressed that for what concerns the tested AESM methods, SINR and interference are averaged over the whole packet duration for the

$SNIR_{eff}$ computation. The mapping function for the RBIR method, represented in Eq. 5.19, and used in Eq. 5.1, can be written expanding the equation for the LLR, as follows [114]:

$$I_{RBIR}(SINR_n) = \log_2 M - \frac{1}{M}\sum_{i=1}^{M} E\left\{\log_2\left(1+\sum_{\substack{k=1\\k\neq i}}^{M} e^{-\frac{|x_i-x_k+w|^2-|w|^2}{\sigma^2}}\right)\right\} \quad (5.23)$$

where the mean runs over the noise realizations and $\sigma^2 = 1/SINR_n$ is the overall variance of the complex Gaussian noise. It is worth highlighting that the LUT containing the mapping between SINR and I_{RBIR} values is computed beforehand for each MCS, by averaging through 10^6 noise realizations.

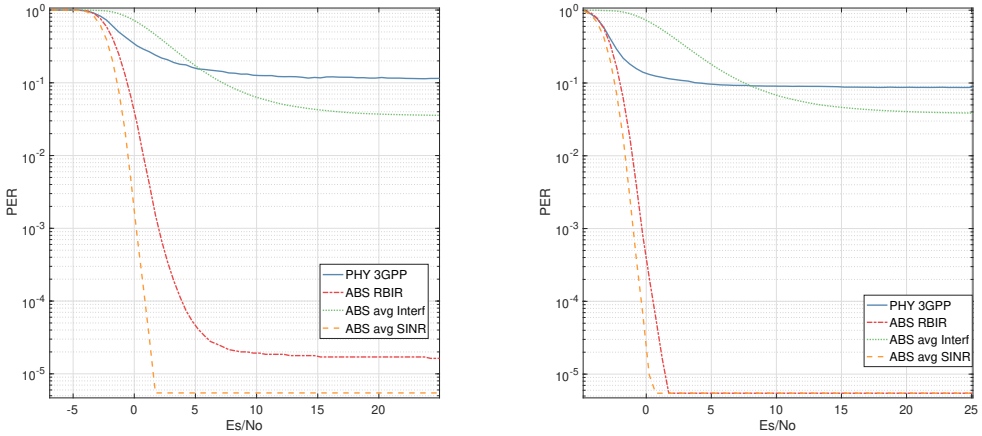

(A) I on $1/2$ of the packet (64 interferers) (B) I on $1/4$ of the packet (128 interferers)

FIGURE 5.6: ESM performance comparison with LLS (interference distributed on a portion of packet duration).

On the one hand, the AESM methods map a value of PER based on the average SINR over the whole packet, on the other hand, the RBIR method takes into account the actual amount of interferers over the different portions of the packet. Despite this characteristic, the latter doesn't give accurate results for some particular configurations of the interferers along the packet. In particular Figures 5.6a and 5.6b show that with the interference concentrated in a specific portion of the reference packet, $1/2$ and $1/4$ of the reference packet respectively, the performance of the PHY abstractions diverge from the results obtained from the actual PHY layer simulations. For what concerns the random distribution of interferers over the reference packet duration, and the full interferers overlap, the PHY abstraction performance are comparable to the ones of actual PHY layer simulations, as shown in Figures 5.7a and 5.7b, respectively.

Table 5.1 shows the Mean Square Error (MSE) computed between the PER estimated with the various PHY abstraction methods and the actual value of PER obtained from the LLSs. It is worth highlighting that the MSE is negligible when the

interferers fully overlap or are randomly distributed over the reference packet duration (*e.g.*, Full Overlap and Random Overlap). However, when the interference is limited to a specific portion of the reference packet (*e.g.*, Partial Overlap $1/2$ and $1/4$), the value of the MSE increases. This performance degradation of the ESM methods can be associated to the fact that the interference cannot be considered Gaussian. This result is particularly interesting because it can be associated to the interference distribution over a packet when the SIC is performed. Notably, when iterative SIC is performed, the component of interference are concentrated on a specific portion of the packet.

TABLE 5.1: Link Level PHY abstraction validation results (MSE).

PHY Abs / I Distribution	RBIR	AESM (SINR)	AESM (I)
Full Overlap	$5.73 \cdot 10^{-5}$	$5.61 \cdot 10^{-5}$	$5.61 \cdot 10^{-5}$
Random Overlap	$9.94 \cdot 10^{-5}$	$1.01 \cdot 10^{-5}$	$1.00 \cdot 10^{-4}$
Partial Overlap (1/2)	0.0223	0.0304	0.0197
Partial Overlap (1/4)	0.0093	0.0113	0.0669

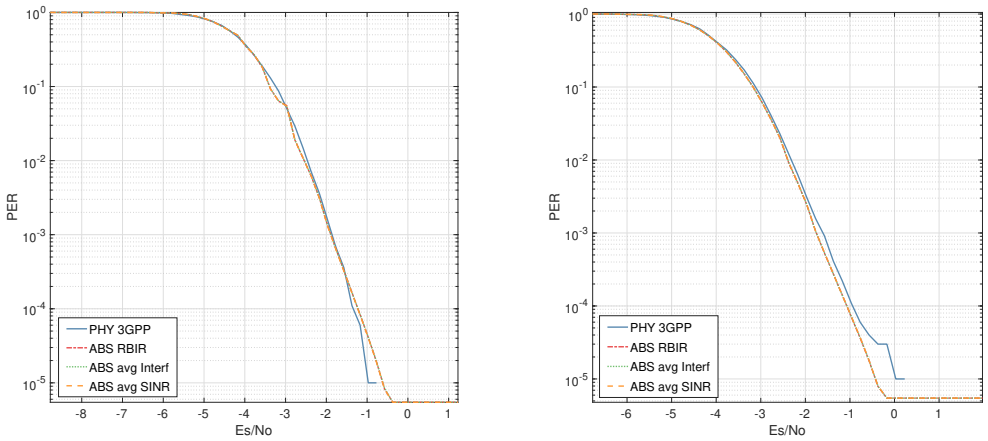

(A) Random distributed I (2 interferers) (B) Full packet I (2 interferers)

FIGURE 5.7: ESM performance comparison with LLS (interference distributed over the whole packet duration).

Besides the direct comparison of the ESM methods with the actual PHY level simulations performances, it if fundamental to derive the system-level performance, through SLSs, in terms of achieved PLR. For this purpose, the PHY abstraction implemented in ESiM2M, described in Chapter 2, has been used. Focusing on E-SSA air interface implementation, for which these performance test has been performed, the PHY abstraction can be summarized in the following steps:

1. The UTs in visibility of a specific beam are selected.
2. All the packets transmitted by the UTs are ordered by their arrival time at the satellite.

3. Due to the fact that E-SSA foresees an asynchronous RA, the packets are not aligned in time; thus, for each packet, different *interference zones* can be identified characterized by a different number of overlapping packets. It is worth highlighting that these zones could have random duration.

4. For each interference zone, the corresponding SINR after the de-spreading, is computed for each packet.

5. The PHY abstraction, exploiting the RBIR method, is executed as previously described.

6. Once the PER value for the packet has been derived, it is compared with a randomly generated threshold in order to establish whether the packet has been decoded or not.

7. If the packet has been decoded, SIC, with complete packet cancellation, is performed.

It is worth recalling that the PHY abstraction is run for each beam of each satellite, *i.e.*, a separate decoder has been considered for each beam. Collecting the statistics on the decoded packets from each beam-satellite pairs it is possible to derive the system-level performance in terms of PLR. Figure 5.8 compares the performance achieved by ESiM2M, with the semi-analytical performance of SSA systems derived in [126], while Figure 5.9 shows the same comparison for E-SSA systems. Both figures show the different behaviour of the RBIR PHY abstraction at different levels of power randomization at packet level (*e.g.*, 0, 1, 2, and 3 dB have been used as values for the variance, σ, of the power per packet) and different values of system normalized MAC load. Furthermore, Table 5.2 shows the MSE computed between the PLR curves estimated with the RBIR method and the semi-analytical value of PLR derived in [126].

TABLE 5.2: System-level PHY abstraction validation results (MSE).

PW rand / **Simulation**	**0**	**1**	**2**	**3**
SSA	0.0029	0.0015	$7.41 \cdot 10^{-4}$	$4.22 \cdot 10^{-4}$
E-SSA	-	0.1306	0.0795	0.0889

The results highlight that for SSA the performance of the PHY abstraction in SLS are comparable with the theoretical ones while there is a mismatch for what concern E-SSA. Furthermore, it can be noticed that an increment of the packet power randomization σ, corresponds to a closer match between estimated and theoretical curves. It is important to highlight that the main difference between SSA and E-SSA lies in the SIC process (*e.g.*, while in the former the SIC process is not implemented, in the latter 5 SIC iterations are performed),

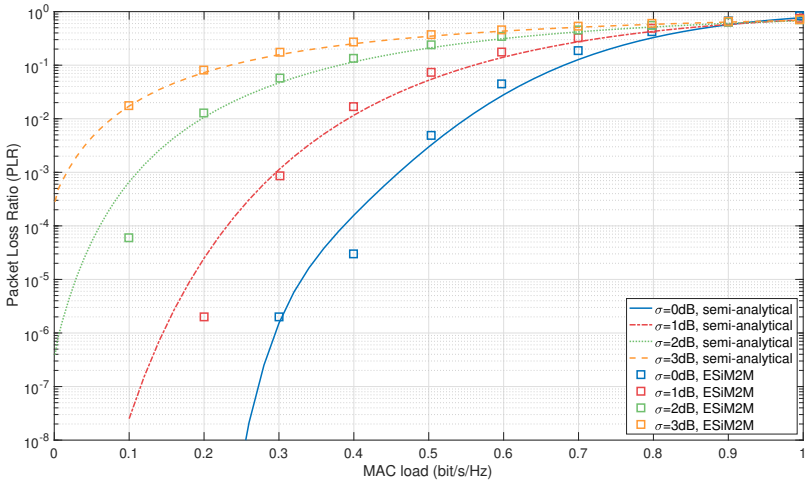

FIGURE 5.8: MIESM ESM performance, SLS PLR, SSA air-interface.

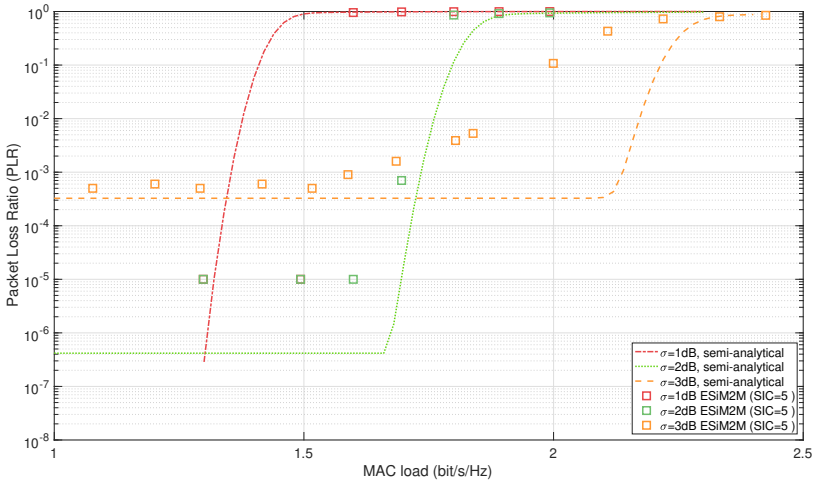

FIGURE 5.9: MIESM ESM performance, SLS PLR, E-SSA air-interface.

These results are in line with the ones previously showed in Figures 5.6 and 5.7 for PHY level simulations. Undoubtedly it is a fair assumption to assume Gaussian distributed interference over the reference packet [126], as far as the number of interferers is sufficiently large and SIC is not implemented. However, once SIC is used and the interfering power is canceled out, the interference will be concentrated in some specific parts of the packet, producing SINR zones with much lower SINR with respect to others, thus affecting the decoding process. As previously mentioned, it has been observed that these particular distributions of interference cause a degradation of the PHY abstraction accuracy. At this regard, alternative ESM methods, in order to overcome this problem, are currently under study. In particular a mathematical derivation for a mapping function I, which would take into account the actual interference distributions, and an innovative mapping method based on Neural Networks (NNs) are under development. However, the work is still in progress and

will not be part of this thesis.

Chapter 6

Channel Modelling and Link Budget

As previously described in Chapter 1 the performance for a SatCom system performance must be evaluated on: i) *DLs* from the satellites to the GSs and UTs; ii) *ULs* from GSs and UTs to the satellites; and iii) *ISL* between the satellites. The performance of the individual links that participate in the connection among the end terminals conditions the Quality of Service (QoS) for the connection among end-users, specified in terms of Bit Error Rate (BER) or PER for digital communications. In Chapter 5 it has been shown the impact that the different levels of SNR and SINR have in terms of achieved PER. In particular, it has been highlighted the paramount importance of a proper measure of those parameters to be used as inputs for the PHY abstraction model to properly evaluate the parameters for measuring the QoS of the system [1].

In the remainings of this chapter the main impairments characterising the satellite channel model will be thoroughly described and a mathematical framework necessary for their understanding will be derived. Finally, the mathematical framework for the LB computation, adopted for ESiM2M, will be described.

6.1 Channel Modelling

Notably, when compared to a terrestrial channel, satellite links pose challenging issues to the realization of a satellite-based networks, due to the large delays, Doppler shifts, and large path losses. In this section, the mathematical framework for the delay, differential delay, Doppler shift, differential Doppler shift, and Doppler rate will be discussed, such to make available the mathematical tools necessary for their understanding. Furthermore, the main impairments and contributions to the path loss are discussed. The framework described is then adopted in ESiM2M and it is the ground for the results presented in the following chapters.

6.1.1 Propagation Delay

Different types of delay are involved in satellite communications. Among them, the *propagation delay* is not only the predominant one, but it also reaches values much

larger than those of terrestrial networks. This could results in bottlenecks with harmful impacts on the protocols and procedures of the system, subject to the kind of air interface implemented.

Hence, considering the scenario depicted in Figure 6.1 with respect to the propagation delay, it must be taken into account: i) the propagation delay along the user link; ii) the propagation delay along the feeder link; and iii) the propagation delay along the ISL if present. Depending on the type of system implementation, only part of the latter could be considered, *i.e.*, whether the whole procedure or a specific step can be terminated at the satellite payload or it requires an interaction with the GS and the network. For example, in 5G NR the implementation of the gNB on board the regenerative satellite payload is foreseen for some architectures, making it possible to complete some of the procedures at the satellite, thus reducing the propagation delay impacts. Furthermore, both the one-way propagation delay and the RTT must be evaluated.

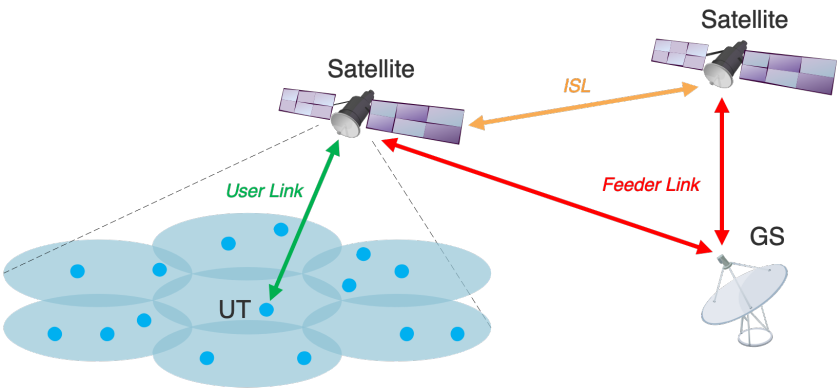

FIGURE 6.1: System Architecture.

In the following, the RTT is approximated by twice the propagation delay between the transmitter and the receiver, since the signal processing time in a SatCom context can be assumed negligible with respect to the propagation delay. In order to estimate the propagation delay, it has been considered a pessimistic scenario in which the transmitter and the receiver are not perfectly aligned and, thus, they have different elevation angles, θ. In the general case, the overall RTT can be computed as:

$$RTT \approx 2\,T_{OW} = 2\,\frac{d_{UT-Sat}(\theta_{UT}) + d_{Sat-Sat} + d_{Sat-GS}(\theta_{GS})}{c} \tag{6.1}$$

where T_{OW} is the one-way propagation delay, d_{UT-Sat} is the distance between the UT and the satellite on the user link as a function of its elevation angle θ_{UT}, $d_{Sat-Sat}$ is the distance among the satellites on the ISL, d_{Sat-GS} is the distance between the satellite and the GS on the feeder link as a function of its elevation angle θ_{GS}, and c the speed of light. The UT connected through the user link has to be intended as a generic user in the satellite coverage (*e.g.*, IoT device, data aggregator, relay node,

etc.). Furthermore, it is worth highlighting that there could be multiple ISL hops to be considered for the RTT computation. In Chapter 7 some examples for the values of RTT will be given for different scenarios. When taking into account the multi-path fading, the delay along the reflected path can be computed in a similar fashion. For the sake of simplicity, only the Line of Sight (LoS) component will be considered in the following discussion, while the reflections will be neglected.

6.1.1.1 Differential Delay

In a SatCom system, the propagation delay has to be assumed as the only contribution to the overall latency. It is now important to define the concept of *differential delay*, as the difference among the propagation delay experienced by two different UTs in the access area of the same satellite, *i.e.*, in the same beam in the case of multi-beam scenario. In general, for two or more UTs in the same beam, it is possible to split their one-way propagation delay, T_{OW} described in Eq. 6.1, into two distinct components:

$$T_{OW} = \Delta\tau + T_{com} = \Delta\tau + (T_{user} + T_{isl} + T_{feed}) \tag{6.2}$$

where T_{com} represents the delay component common for all the UTs in the same coverage, and $\Delta\tau$ is the differential component of the delay, represented by the difference in propagation delay of a UT with respect to a reference one in the same coverage, *i.e.*, the UT experiencing the minimum delay. The T_{com} can be further split into: the delay experienced by the reference UT in the user link, T_{user}, the delay caused by the ISL, T_{isl}, and the delay due to the propagation in the feeder link, T_{feed}.

Depending on the applications, as will be presented in Chapter 7, procedures can be heavily impacted by the differential delays (the maximum, in particular) of users belonging to the same beam. On the other hand, all sources of common delay can be pre-compensated, [6], [7]. Thus the remainder of this section will be focused on the computation of the differential delay. Referring to the generic UTs positions, P and Q, inside the beam coverage depicted in Figure 6.2, the differential delay is:

$$\Delta\tau = \tau_P - \tau_Q \tag{6.3}$$

where:

$$\tau_i = \frac{D_i}{c} = R_E \frac{\sqrt{\left(\frac{R_E + h_{sat}}{R_E}\right)^2 - \cos^2\varepsilon} - \sin\varepsilon}{c} \tag{6.4}$$

with $i = P, Q$, R_E being the Earth's radius, and h_{sat} being the satellite altitude. τ_i represents the delay on the user link as a function of the elevation angle ε, and is the only variable component on the delay budget for the users in the same beam, as described in Eq. 6.2.

The value of delay τ_i is directly related to the slant range between UT and satellite. As thoroughly explained in Chapter 3, under the hypothesis of spherical Earth, the geometrical relationship between the satellite FOV and the access area can be

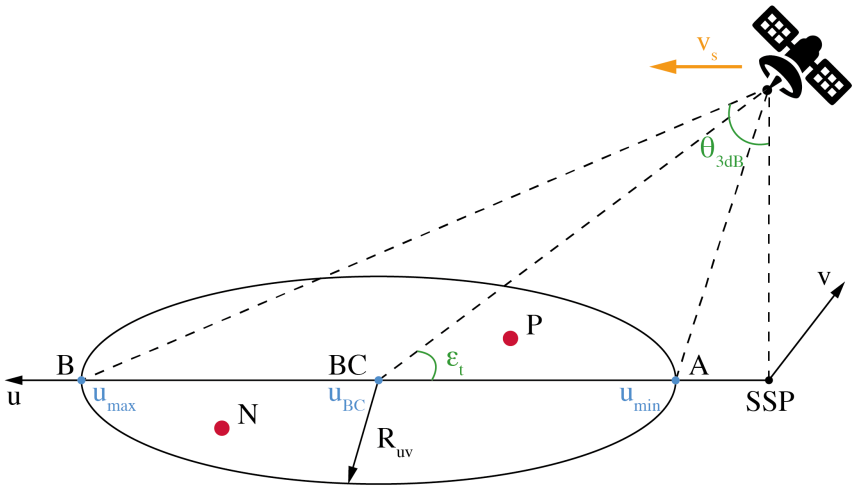

FIGURE 6.2: The *u-v* coordinates reference system for delay and Doppler.

completely described by means of spherical geometry. Thus, it is now trivial to compute the differential delay between two users, by using Eq. 3.26 to find the differential slant range between the two UTs, thus the value of $\Delta\tau$ as:

$$\Delta\tau = \frac{\Delta D}{c} = \frac{D_P - D_Q}{c} \tag{6.5}$$

where D_P and D_Q are the slant range of the two users computed by means of Eq. 3.26.

It is now important to focus on the evaluation of the maximum possible value for the differential delay, which corresponds to the maximum value of differential slant range, ΔD_{max}, too. The latter is achieved by considering the users at the maximum reciprocal distance along the longitudinal beam's dimension with respect to the satellite motion, as it is depicted in Figure 6.2 by points A and B. In fact, those are the points at the maximum elevation angle separation, thus at the maximum difference of experienced delay, being the latter a function of the elevation angle as it is shown in Eq. 6.4.

For many of the computations regarding the users in the access area, it is useful to refer to spacecraft coordinates centered on nadir (*e.g.*, for the LB computations as shown in Section 6.2). Defining the satellite antenna's pattern as a single- or multi-beam pattern with circular beams in *u-v* coordinates (*e.g.*, with radius R_{uv}), it is interesting to look at an approximation for the computation of differential delay for the satellite FOV. Although the following mathematical formulation is an approximation, due to the fact it does not take into account the Earth's curvature in the satellite access area, it is an interesting analytical derivation especially for LEO and VLEO scenarios. In these two scenarios, being the satellite altitude very low, the Earth curvature in the access area is negligible. This formulation is particularly useful for a simulation environment where all the measures (*e.g.*, users positions) are referred to *u-v* or θ-ϕ coordinates.

Referring to Figure 6.2, by means of orbital and geometrical considerations, it is known that the maximum difference in slant range between any two beam users is obtained when: i) the beam center is located on the satellite ground track, *i.e.*, $v_{BC} = 0$; and ii) the two users are located at the intersections between the ground track and the beam edge, *i.e.*, $v_{min} = v_{max} = 0$, with min and max denoting the users located closest and farthest from the satellite, points A and B respectively. In a given time instant, t, along its orbit, the satellite is positioned at an elevation angle ε_t from the beam center. Thus, from Eq. 3.70, 3.71, and 3.24, it is possible to write:

$$u_{BC} = \sin\theta_{BC} = \frac{R_E}{R_E + h_{sat}} \cos\varepsilon_t \tag{6.6}$$

Since the beam radius in *u-v* coordinates, R_{uv}, is known, the coordinates of the two users can be obtained as follows:

$$\begin{cases} u_{min} = u_{BC} - R_{uv} = \frac{R_E}{R_E + h_{sat}} \cos\varepsilon_t - R_{uv} \\ u_{max} = u_{BC} + R_{uv} = \frac{R_E}{R_E + h_{sat}} \cos\varepsilon_t + R_{uv} \end{cases} \tag{6.7}$$

However, the following aspects must be taken into account: i) when the SSP is inside the beam, the minimum slant range location is given by the SSP itself; and ii) when the maximum slant range point is over the satellite's FOV, the maximum slant range location is on the FOV. From these observations, it is possible to write:

$$u_{min} = \begin{cases} \frac{R_E}{R_E + h_{sat}} \cos\varepsilon_t - R_{uv}, & u_{BC} > R_{uv} \\ 0, & u_{BC} \leq R_{uv} \end{cases} \tag{6.8}$$

and

$$u_{max} = \begin{cases} \frac{R_E}{R_E + h_{sat}} \cos\varepsilon_t + R_{uv}, & u_{BC} + R_{uv} \leq \frac{R_E}{R_E + h_{sat}} \\ \frac{R_E}{R_E + h_{sat}}, & u_{BC} + R_{uv} > \frac{R_E}{R_E + h_{sat}} \end{cases} \tag{6.9}$$

Recalling Eq. 3.23, from the u-axis coordinates, the corresponding elevation angles can be obtained as follows:

$$\varepsilon_i = \cos^{-1}\left(\frac{R_E + h_{sat}}{R_E} u_i\right) \tag{6.10}$$

with $i = min, max$. Knowing the elevation angle ε_i and the nadir angle $\theta_i = \sin^{-1} u_i$, the Earth central angle as λ_i can be obtained from Eq. 3.25. This allows to obtain the slant range from Eq. 3.26 as:

$$D_i = R_E \frac{\sin\lambda_i}{\sin\theta_i} \tag{6.11}$$

Thus, the maximum differential slant range, ΔD_{max}, is given by:

$$\Delta D_{max} = R_E \left(\frac{\sin\lambda_{max}}{\sin\theta_{max}} - \frac{\sin\lambda_{min}}{\sin\theta_{min}}\right) \tag{6.12}$$

From the above, the maximum differential delay can be obtained as follows:

$$\Delta\tau_{max}\left(\varepsilon_t, h_{sat}, R_{uv}\right) = \frac{R_E}{c}\left(\frac{\sin\lambda_{max}}{\sin\theta_{max}} - \frac{\sin\lambda_{min}}{\sin\theta_{min}}\right) \tag{6.13}$$

where it is also explicitly highlighted that the maximum differential delay is a function of the elevation angle at beam center, the beam radius, and the satellite altitude, since both the nadir and Earth central angles depend on these parameters from Eq. 6.8, 6.9, and 6.10. To summarize: i) the maximum delay is experienced by the beam user at maximum slant range on the u-axis; ii) the minimum delay is experienced by the beam user at minimum slant range on the u-axis; iii) all other users are located at slant ranges between these two values.

6.1.2 Doppler Shift

The Doppler shift consists in the change in the carrier frequency due to the relative motion between the satellite and the user terminal. When considering satellite communications, the Doppler shift can be caused by the satellite movement in its orbit and the users' mobility on ground. It shall be noticed that considering GEO systems serving fixed on-ground nodes, the Doppler shift can be assumed to be negligible. On the other hand, when UTs mobility and in general LEO and VLEO satellite systems are considered, the Doppler shift can introduce significant frequency shifts with respect to those expected in terrestrial systems. This could deeply impact the frequency synchronization of the resources used to transmit through the designated air interface, as discussed in the following chapter.

In classical physics, if the speeds of source and receiver, relatively to the medium, are lower than the velocity of waves in the medium, the relationship between observed frequency, f, and emitted frequency, f_0, is given by [127]:

$$f = \left(\frac{c \pm v_r(t)}{c \pm v_s(t)}\right) f_0 \tag{6.14}$$

where c is the propagation speed of waves in the medium (*e.g.*, the speed of light); $v_r(t)$, is the speed of the receiver relative to the medium at the time instant t, added to c if the receiver is moving towards the source, subtracted if the receiver is moving away from the source; $v_s(t)$, is the speed of the source relative to the medium at the time instant t, added to c if the source is moving away from the receiver, subtracted if the source is moving towards the receiver. It is important to highlight that $v_s(t)$, and $v_r(t)$ are the radial velocities, thus the velocity vectors of source and receiver projected onto the unit vector connecting source and receiver. If the speeds $v_s(t)$, and $v_r(t)$, are small compared to the speed of the wave, the relationship between observed frequency $f(t)$ and emitted frequency f_0 is approximately [127]:

$$f(t) = \left(1 + \frac{-(v_r(t) - v_s(t))}{c}\right) f_0 = \left(1 + \frac{\Delta v}{c}\right) f_0 \tag{6.15}$$

where Δv is the opposite of the velocity of the receiver relative to the source and it is positive when the source and the receiver are moving towards each other. The actual Doppler shift, *i.e.*, frequency shift, caused by the source and receiver relative motion can be then written as:

$$f_D(t) = \frac{\Delta v}{c} f_0 = \frac{-(v_r(t) - v_s(t))}{\lambda} \tag{6.16}$$

with λ being the transmitted signal wavelength. Although the satellite speed in LEO and VLEO scenarios are very high with respect to the speeds usually achievable in mobility scenarios on terrestrial networks (*e.g.*, 4-7 km/s for the altitude in the range 600-1200 km), Eq. 6.15 still holds, being the value of c five orders of magnitude bigger than the satellite speed.

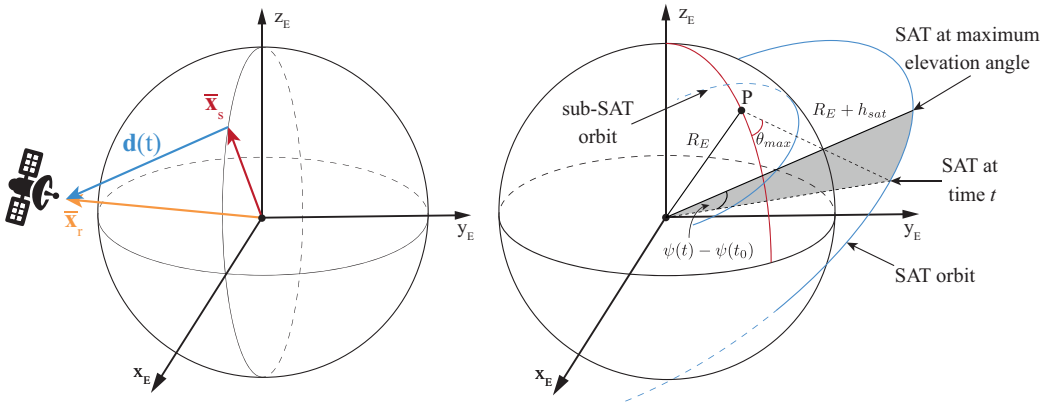

(A) Vector Doppler representation (B) Geometric LEO orbit representation

FIGURE 6.3: Doppler geometrical representations.

In order to better understand the Doppler shift formulation in Eq. 6.16, it is useful to describe the latter with a vector mathematical formalism. Referring to Figure 6.3a it is possible to write:

$$f_D(t) = -\left(\frac{\mathbf{d}(t)}{|\mathbf{d}(t)|} \cdot \frac{\partial \mathbf{x}_r}{\partial t} - \frac{\mathbf{d}(t)}{|\mathbf{d}(t)|} \cdot \frac{\partial \mathbf{x}_s}{\partial t} \right) \cdot \frac{f_0}{c} \tag{6.17}$$

where the vectors are written in boldface. In particular, i) $\mathbf{x}_s(t)$ is the vector of source position, thus $\partial \mathbf{x}_s / \partial t$ is its velocity; ii) $\mathbf{x}_r(t)$ is the vector of receiver position, thus $\partial \mathbf{x}_r / \partial t$ is its velocity; iii) $\mathbf{d}(t)$ represents the distance vector between the source and the receiver, pointing towards the receiver, thus $\mathbf{x}_r(t) - \mathbf{x}_s(t)$, and $\mathbf{d}(t)/|\mathbf{d}(t)|$ its unit vector. Thus the radial components of the source and receiver velocities, $v_s(t)$ and $v_r(t)$, to be plugged in Eq. 6.16, are obtained from the dot product between the partial derivative with respect to time of source and receiver positions, *i.e.*, velocity vectors, and the unit vector of the distance between source and receiver. Position vectors could be represented generically as $[X_{ECEF}, Y_{ECEF}, Z_{ECEF}]^T$ in a ECEF cartesian reference system, because it is common to have measures of positions and velocities, for both UTs and satellites, conveyed in this reference system.

When dealing with Doppler shifts in SatCom, it is convenient to find a mathematical formulation for the latter as a function of the satellite orbit parameters, and the satellite access area geometry. At this purpose, [128] proposed an analytical expression of the Doppler shift for a generic observation point P on Earth's surface. Referring to Figure 6.3b for the geometrical model, Eq. 6.17 can be written as:

$$f_D(t)(t) = -\frac{f_0}{c} \cdot \frac{R_E(R_E + h_{sat}) \sin\big(\psi(t) - \psi(t_0)\big)\Gamma(\theta_{max}) \cdot \omega_F(t)}{\sqrt{R_E^2 + (R_E + h_{sat})^2 - 2R_E(R_E + h_{sat}) \cos\big(\psi(t) - \psi(t_0)\big)\Gamma(\theta_{max})}} \tag{6.18}$$

with

$$\Gamma(\theta_{max}) = \cos\left(\cos^{-1}\left(\frac{R_E}{(R_E + h_{sat})}\cos\theta_{max}\right) - \theta_{max}\right) \tag{6.19}$$

where θ_{max} is the maximum elevation angle of the satellite that the generic point P will experience, and $\psi(t) - \psi(t_0)$ is the angular difference between satellite location at time t and satellite location at maximum elevation angle θ_{max} seen from P. Furthermore, $\omega_F(t)$ is the angular velocity of the satellite in the ECEF frame which can be approximated as a constant by the following expression:

$$\omega_F \approx \omega_s - \omega_E \cos(i) \overset{(a)}{\approx} \omega_s \tag{6.20}$$

where ω_s is the angular velocity of the satellite in the ECI frame, ω_E is the angular velocity of the Earth and i is the satellite orbit inclination, as it has been described in Chapter 4. Approximation *(a)* can be done in order to simplify the computation if the satellite orbit is sufficiently low that ω_E is negligible with respect to ω_s. The angular velocity of the satellite can be written as, [88]:

$$\omega_s = \sqrt{\frac{\mu}{(R_E + h_{sat})^3}} \tag{6.21}$$

where μ is the *standard gravitational parameter* of Earth, as defined in Chapter 4. As a simplified model for the Doppler shift computation, it is furthermore possible to write the latter as a function of the only elevation angle. For this purpose the authors in [23] derived the following formulation from Eq. 6.17:

$$f_D(\varepsilon_i) = f_0 \frac{\omega_s R_E \cos(\varepsilon_i)}{c} \tag{6.22}$$

where ε_i is the elevation angle at which the satellite is seen from the on-ground user. It is worth highlighting that the latter equation is a simplified formula for the Doppler shift experienced at locations on the satellite orbit projection on the ground, then with users who will see the satellite at a maximum elevation of 90 deg during its flight over the coverage. Thus, Eq. 6.22 is consistent for the users located on the segment $\overline{AB}$ in Figure 6.2, while it is an approximation not accounting for the azimuthal angle for the other locations in the beam.

Finally, it is worth mentioning that both the user- and the feeder-link are affected

by the Doppler shift, thus both contributions of Doppler should be taken into account, subordinated to the possibility of Doppler compensation at the satellite payload. Considering a consistent sign for the Doppler contributions, the mathematical formulation previously presented is valid for both the links. For the sake of clarity and without losing generality in the following section only the Doppler component on the user link will be taken into account. Moreover when taking into account the multi-path fading, the Doppler shift along the reflected path can be computed in a similar fashion. For the sake of simplicity, only the LoS component will be considered in the following discussion while the reflections will be neglected.

6.1.2.1 Differential Doppler Shift

It is now important to define the concept of *differential Doppler shift*, as the difference among the Doppler shift experienced by two different UTs in the access are of the same satellite, *i.e.*, in the same beam in the case of multi-beam scenario. In general, for two or more UTs in the same beam, it is possible to split their Doppler shift, $f_D(t)$, previously defined into two distinct components:

$$f_D(t) = \Delta f_D(t) + f_D^{com}(t) = \Delta f_D(t) + \left(f_D^{user}(t) \pm f_D^{isl}(t) \pm f_D^{feed}(t) \right) \tag{6.23}$$

For the sake of clarity, the time dependency in the formulation will be neglected in the following. Then f_D^{com} represents the Doppler shift component common for all the UTs in the same coverage, and Δf_D is the differential component of the Doppler shift, represented by the difference in Doppler shift of a UT with respect to a reference one in same coverage, *i.e.*, the UT experiencing the minimum Doppler shift. f_D^{com} can be further split into: the Doppler shift experienced by the reference UT in the user link, f_D^{user}, the Doppler shift caused by the ISL, f_D^{isl}, and the Doppler shift due to the propagation in the feeder link, f_D^{feed}.

Similarly to the above analyses for the propagation delay, as it will be presented in Chapter 7, procedures can be heavily impacted by the differential Doppler shift (the maximum, in particular). The remainder of the chapter will focus on the differential Doppler shift (the maximum, in particular) because all terms introducing a common shift can be pre-compensated assuming that: i) the terminals are equipped with GNSS capabilities (*e.g.*, as per 3GPP current analyses); and ii) the satellite ephemeris are known. Referring to the generic UTs positions, P and Q, inside the beam coverage depicted in Figure 6.2, the differential Doppler shift is:

$$\Delta f_D(t) = f_D^P(t) - f_D^Q(t) \tag{6.24}$$

By means of orbital and geometric considerations, it is known that the worst case scenario (in terms of maximum differential shift between any two users) arises when the beam major semi-axis lies on the satellite ground track, [128]. For a terminal not located at the beam center, but located on the beam major semi-axis, the same

Doppler curve applies with a horizontal shift given by the time instant at which that UT will see the satellite at $\varepsilon = \pi/2$ elevation (see Figure 7.12a). At this purpose the simplified formulation presented in Eq. 6.22 can be used for the differential Doppler computation between any two users, by evaluating the Doppler shift at the corresponding elevation angles and computing the difference. As for the maximum differential Doppler, the maximum variability is obtained when the UTs are at the two beam edges on the beam major semi-axis. It is important to notice that in Eq. 6.22 the elevation angle at the user location, ε_i, can be considered as a function of the elevation angle at beam center ε_t, *i.e.*, $\cos\varepsilon_i(\varepsilon_t)$. This is a consequence of the dependency of the u axis coordinate from the beam center elevation angle, previously discussed in the delay formulation. In order to define the maximum differential Doppler shift, the elevation angles at the minimum and maximum Doppler shift locations must be computed. They are given by Equations 6.8 and 6.9, respectively. From these, and Eq. 6.10 it is possible to write:

$$\begin{aligned}\Delta f_{d,max} &= f_D\left(\varepsilon_{max}\right) - f_D\left(\varepsilon_{min}\right) = \frac{f_0}{c}(R_E + h_{sat})\omega_s(u_{max} - u_{min}) \\ &= 2f_0\frac{R_E + h_{sat}}{c}\omega_s R_{uv}\end{aligned} \tag{6.25}$$

which is a function of the satellite altitude and the beam radius only, and not of the elevation angle at beam center, *i.e.*, in the considered system, the maximum differential delay within a beam does not depend on the satellite's location on its orbit, but only from its altitude. As it has been done for the delay, also Eq. 6.25 represents an approximation of differential Doppler computation with respect to the FOV of the satellite. Similarly it is possible to write Eq. 6.18 as a function of the satellite FOV, as an approximation in *u-v* coordinates. Referring to Figure 6.2, let us consider for the generic point P: i) the current SSP location fixed in $(u, v) = (0, 0)$; ii) the SSP location corresponding to the maximum elevation angle for P located on the u axis on the projection of P which can be written as:

$$\begin{aligned}u_{SSP}^{(curr)} = 0,\ v_{SSP}^{(curr)} = 0 \\ u_{SSP}^{(max,P)} = 0,\ v_{SSP}^{(max,P)} = 0\end{aligned} \tag{6.26}$$

from Eq. 6.10, the maximum elevation angle seen by the generic point P is thus:

$$\varepsilon_{max}(v_P) = \cos^{-1}\left(|v_P|\frac{R_E + h_{sat}}{R_E}\right) \tag{6.27}$$

The minimum value of the above maximum elevation is obtained for P location at beam edge:

$$\min_{v_P}\varepsilon_{max}(v_P) = \cos^{-1}\left(R_{uv}\frac{R_E + h_{sat}}{R_E}\right) \tag{6.28}$$

As for the angular distance, by means of geometrical observations it can be computed as the differential Earth central angle between the SSP locations at the current

instant and at the maximum elevation angle from Eq. 3.25:

$$\lambda = \frac{\pi}{2} - \varepsilon - \eta = \frac{\pi}{2} - \cos^{-1}\left(u\frac{R_E + h_{sat}}{R_E}\right) - \sin^{-1}(u) \tag{6.29}$$

Then the value for angles λ at the current and maximum elevation angle SSP locations, Eq. 6.26, will be:

$$\begin{aligned} \lambda_{curr} &= \frac{\pi}{2} - \cos^{-1}(0) - \sin^{-1}(0) = 0 \\ \lambda_{max} &= \frac{\pi}{2} - \cos^{-1}\left(u_P\frac{R_E + h_{sat}}{R_E}\right) - \sin^{-1}(u_P) \end{aligned} \tag{6.30}$$

Now it is possible to obtain the value of $\Delta\psi = \psi(t) - \psi(t_0)$ to be plugged in Eq. 6.18, which was the only value not represented in terms of *u-v* coordinates:

$$\Delta\psi(u_P) = \psi(t) - \psi(t_0) = \frac{\pi}{2} - \cos^{-1}\left(u_P\frac{R_E + h_{sat}}{R_E}\right) - \sin^{-1}(u_P) \tag{6.31}$$

6.1.2.2 Doppler Rate

Besides the Doppler shift problem, another impairment arises particularly in LEO and VLEO scenarios. The satellite orbital velocity is in fact in the order of 4-7 km/s for altitude in the range 600–1200 km, and induce strong Doppler shift, thus Doppler rate effects. The mathematical formulation for the Doppler rate is the following:

$$\dot{f_D}(t) = \frac{\partial f_D(t)}{\partial t} \tag{6.32}$$

Then the Doppler rate is the partial derivative with respect time of the Doppler shift. Steeper Doppler shift curves bring to harsher Doppler rate effects; thus, as previously said, greater elevation angles cause more abrupt changes in Doppler shift then higher Doppler rates. Being a variation of the frequency in time, it is important to emphasize that as the length of the packet increases, it is necessary to take countermeasures for the Doppler rate.

6.1.3 Losses

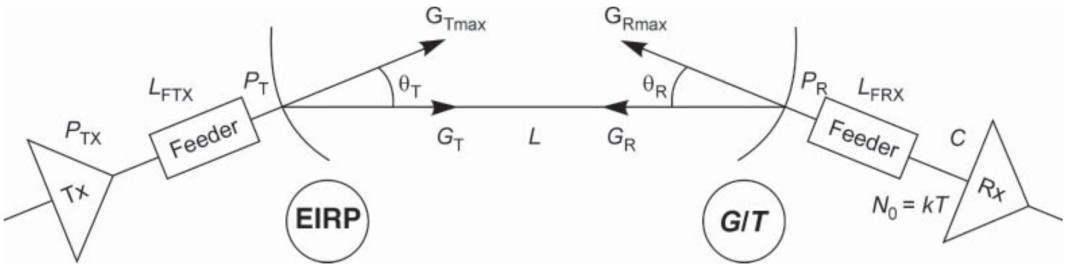

FIGURE 6.4: Link Configuration [1].

For a satellite communication link between a UT on ground and the satellite, depicted in Figure 6.4, the overall losses, L, can be computed as:

$$L = PL + L_E = \underbrace{L_B + L_A + L_{POL}}_{PL} + \underbrace{L_F + L_D}_{L_E} \tag{6.33}$$

where PL represents losses due to the channel impairments while L_E are the losses related to the equipment configuration. In details: *i*) L_B is the basic path loss, which combines free space, clutter, and shadowing losses; *ii*) L_A represents the losses due to atmosphere; *iii*) L_{POL} is the polarisation mismatch loss; *iv*) L_F represents the losses in the equipments; and *v*) L_D represents the depointing losses.

The *basic path loss* is the combination of FSL, L_{fs}, clutter loss, L_{cl}, and log-normal shadowing, L_σ:

$$L_B = L_{cl} + L_{fs} + L_\sigma \tag{6.34}$$

The clutter loss models the attenuation of signal power caused by surrounding buildings and objects on the ground. It depends on the elevation angle, ε, computed in Eq. 3.23, the system operating frequency, f_c[1], and the environment. Typical values for this parameter can be found in [12] for different scenarios and it can be always assumed null in LoS conditions. For a generic user located at slant range d from the satellite, the FSL is given by:

$$L_{fs} = 20 \log_{10} \left(\frac{4\pi d f_c}{c} \right) \tag{6.35}$$

where c is the speed of light. As for the shadowing loss, L_σ is modelled as a log-normal random variable with zero mean and a variance related to the harshness of the shadowing environment, *i.e.*, $L_\sigma \sim (0, \sigma_s^2)$, and the values of, σ_s^2 are provided by 3GPP for dense urban, urban, and rural scenarios as a function of the elevation angle in [12].

Atmospheric losses take into account the atmospheric gases absorption, L_{gas}, the rain/snow fall and cloud attenuation, L_{rain}, and the scintillation losses, L_s:

$$L_A = L_{gas} + L_{rain} + L_s \tag{6.36}$$

Atmospheric gases absorption depends mainly on frequency, elevation angle, altitude above sea level, and water vapour density (absolute humidity). In particular, in order to be compliant with 3GPP standardisation, losses is computed as provided in Annex 2 of ITU-R P.676 for slant paths. The atmosphere is modelled with temperature 288.15 K, pressure 1013.25 hPa, and water vapour density 7.5 g/m^3 [129]. Rain and cloud attenuation are dependent on the geographical location of the ground terminal. Section 2.2 of ITU-R P.618-13 describes a method to estimate the long-term

[1]The system operating frequency will be considered to be either at Ka or S band, in order to be compliant with the 3GPP NTN standardisation procedure.

statistics of attenuation due to rain [130]. For 3GPP SLS, the baseline is to consider clear sky conditions only and in any case rain attenuation is considered as negligible for frequencies below 6 GHz [12]. Scintillation is a variation of the amplitude of received carriers caused by variations of the refractive index of the troposphere and the ionosphere. The tropospheric scintillations, impacting signals in Ka-band, are modelled as a fixed term depending on the user elevation angle [12]. These values are obtained by means of the procedure described in ITU-R P.618 [130]. The ionospheric scintillations, impacting signals in S-band, are modelled as a fixed term of 2.2 dB as from [12], and described in ITU-R P.531-13 [131].

It is also necessary to consider the *polarisation mismatch loss* observed when the receiving antenna is not oriented with the polarisation of the received wave, because propagation through the atmosphere can also affect the polarisation. In fact the ionosphere introduces a rotation of the plane of polarisation of an angle, $\Delta\psi$ which is inversely proportional to the square of the frequency. This rotation is particularly dangerous for linear polarisations. Furthermore, with linear polarisation, the receiving antenna may not have its plane of polarisation aligned with that of the incident wave. In general the polarisation mismatch loss can be defined as [1]:

$$L_{POL} = -20\log_{10}(\cos\Delta\psi) \tag{6.37}$$

The *equipment losses* represents the losses in the transmitting and receiving equipment respectively, in the feeder between the power amplifier and the antenna:

$$L_F = L_{FTX} + L_{FRX} \tag{6.38}$$

In particular L_{FTX} is the feeder loss between the transmitter and the antenna, while L_{FRX} is the feeder loss between the antenna and the receiver.

Finally, the *depointing losses* are function of the transmission and reception angles misalignment, θ_T and θ_R respectively, with respect to the antenna boresight. The result is a fallout of antenna gain with respect to the maximum gain on transmission and on reception, which can be formulated as a function of the θ_{3dB}, later explained in this chapter:

$$L_D = L_T + L_R = 12\left(\frac{\theta_T}{\theta_{3dB}}\right) + 12\left(\frac{\theta_R}{\theta_{3dB}}\right) \tag{6.39}$$

6.2 Link Budget Characterization

In this section, the individual link performance are considered, providing the tools to evaluate the signal-power budget and the noise-contribution budget, thus the SNR level. Furthermore, multiple links are taken into account in order to consider the interference contributions and discuss the SINR computation. The link budget evaluation approach described in the following will thoroughly consider all the main aspects characterizing the satellite communication channel, still being compliant with the 3GPP methodologies [11], [12]. The formulation is considered for DL

and UL, while ISL is left out of the discussion because it is outside of the scope of this work and not yet implemented in the ESiM2M. In the remainings, if not otherwise specified, all the values are expressed in logarithmic units.

6.2.1 Antenna Pattern

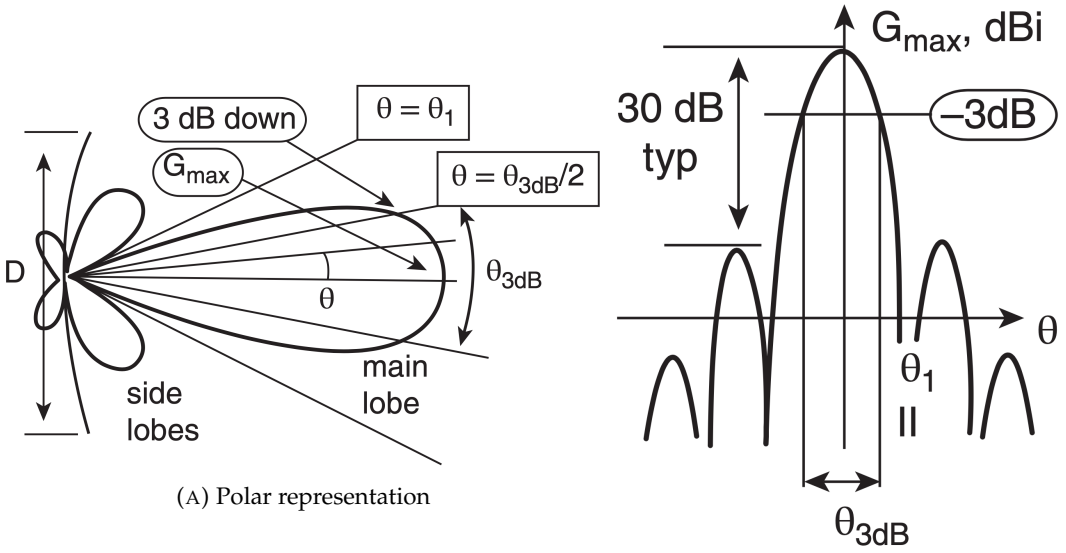

(A) Polar representation

(B) Cartesian representation

FIGURE 6.5: Antenna radiation pattern [1].

It is important to understand the main characteristics of an antenna pattern in order to properly define a link budget. the following discussion will be focused on aperture antennas characteristics. The radiation pattern indicates the variations of gain with direction, and is related to the antenna characteristics. Firstly, is necessary to define the *antenna gain* as the ratio of the power radiated (or received) per unit solid angle by the antenna in a given direction to the power radiated (or received) per unit solid angle by an isotropic antenna fed with the same power. The gain is maximum in the *boresight* direction and has a value given by:

$$G_{MAX} = 10 \log_{10} \left[\eta \left(\frac{\pi D f_c}{c} \right)^2 \right] \tag{6.40}$$

where D is the antenna diameter, and η is the efficiency of the antenna, which directly affects the effective aperture area of the antenna $A_{eff} = \eta(\pi D^2/4)$. The efficiency η of the antenna is the product of several factors that take into account the illumination law, spill-over loss, surface impairments, ohmic and impedance mismatch losses, and so on [1].

As previously described in Section 3.5, the antenna characteristics can be completely defined in θ-ϕ coordinates. In order to avoid bulky notation, in the following

formulation the antenna pattern is considered with rotational symmetry, *i.e.*, the antenna pattern is only function of the angle θ regardless the ϕ direction of the transmitted/received signal. It is then possible to completely represent an antenna beam as it is shown in Figure 6.5.

The angular beamwidth is the angle defined by the directions corresponding to a given gain fallout with respect to the maximum value. The 3 dB beamwidth, indicated in Figure 6.5a by θ_{3dB}, is often used; it corresponds to the angle between the directions in which the gain falls to half its maximum value. In general it is possible to define the antenna gain towards a certain direction ϑ, for both transmission, G_T, or reception, G_R, as:

$$G(\vartheta) = G_{MAX} + 10\log_{10}\Omega(\vartheta) \tag{6.41}$$

where $\Omega(\vartheta)$ represents the antenna pattern function value on the ϑ direction. According to the antenna design, different functions can be achieved. Gaussian and Bessel beam model are two examples of analytical functions used for the beam modelling. Gaussian beam model is implemented in SATSOFT antenna pattern design software by TICRA [132], and have been used for an application described in Chapter 7. As for the Bessel radiation pattern, it can be defined as:

$$\Omega(\vartheta) = \begin{cases} 1, & \vartheta = 0 \\ 4\left|\frac{J_1(ka\sin\vartheta)}{ka\sin\vartheta}\right|^2, & \vartheta \neq 0 \end{cases} \tag{6.42}$$

where: *i*) a is the antenna aperture radius; *ii*) $k = 2\pi f_c/c$ is the wave number; *iii*) $J_1(\cdot)$ is the Bessel function of the first order; and *iv*) ϑ is the angle measured from the boresight of the antenna. This antenna model is the one adopted in 3GPP specifications for NTN, to describe the satellite antenna pattern [11], [12]. Even if the antenna models previously mentioned could be adopted for any device, an omnidirectional antenna pattern has been considered for the UTs, as it will be highlighted in the applications described in Chapter 7. The equation for Ω is valid in both transmission and reception directions. It is important to stress the fact that when the antenna pattern symmetry is not circular, the antenna pattern Ω is defined as a function of both θ and ϕ. Once the antenna gain is defined and recalling the losses depending on the equipment in Equations 6.39 and 6.38, it is possible to characterize the transmitted antenna EIRP as:

$$EIRP(\vartheta) = G_T(\vartheta) + P_T - (L_T + L_{FTX}) \tag{6.43}$$

where P_T is the transmitted power.

The wave radiated by an antenna consists of an electric field component and a magnetic field component. These two components are orthogonal and perpendicular to the direction of propagation of the wave and they vary at the frequency of the wave. By convention, the polarisation of the wave is defined by the direction of the electric field which in general is not fixed. The direction of the polarisation become particularly important in multi-beam antenna patterns; it is, indeed, common

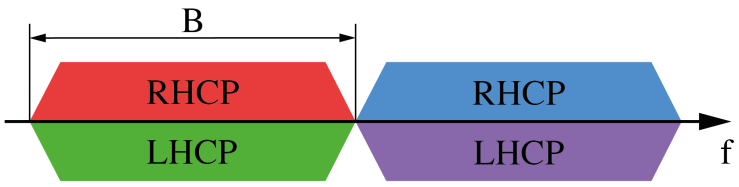

FIGURE 6.6: Frequency Reuse scheme.

using frequency coloring schemes where two beams work on the same frequency band but using opposite polarisations, as it is depicted in Figure 6.6, optimising bandwidth usage. It is worth highlighting that two beams sharing the same bandwidth with opposite polarisation, interfere with each other depending on the value of Cross Polarisation Discrimination (XPD)[2]. In this case, in the computation of the interference, it is important to take into account also the *cross-polar* gain component besides the *co-polar co-channel* ones. The cross-polarisation gain is strictly related to the co-polarisation gain, indeed it depends from the co-polarisation gain and the XPD, which is related to the antenna design [1].

6.2.2 Downlink

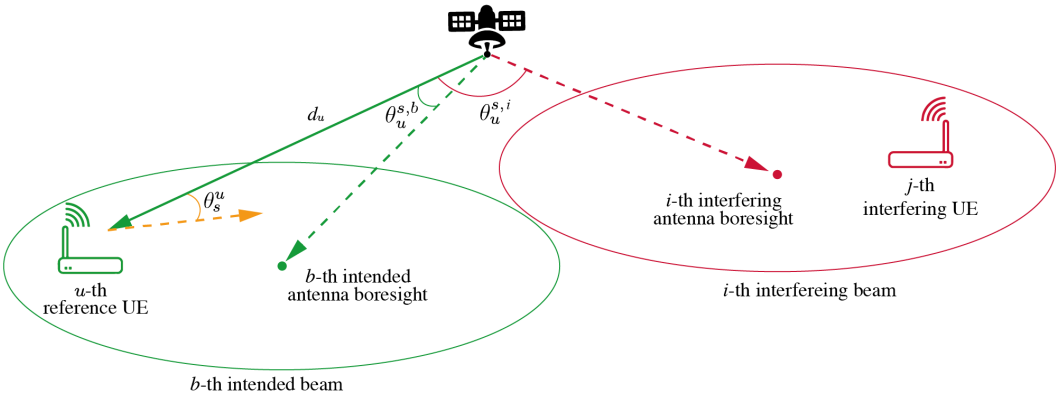

FIGURE 6.7: Geometry for LB computation (Downlink).

Now that the main elements contributing to the LB have been addressed, it is possible to focus on the SNR and SINR computations.

For the sake of clarity, only one satellite and two beams are represented in the reference model, but this assumption does not impact the generality of the proposed mathematical framework. In fact, when assessing the procedure for the LB computation, it shall be noticed that such procedures is considered for each beam and satellite. Although the numerical simulations will be performed in a multi-satellite and multi-beam environment, the mathematical framework can be simplified. For what concern the DL computation, the reference scheme is shown in Figure 6.7, where:

[2]The XPD is defined as a ratio of the co-polar component of the specified polarisation compared to the orthogonal cross-polar component over the beamwidth angle.

i) the intended u-th user (*e.g.*, a UT or a GS) is randomly located inside the intended b-th beam; *ii*) an interfering signal is transmitted from the i-th antenna towards the j-th user of the i-th beam; *iii*) d_u is the slant range of the u-th user in the b-th beam; *iv*) $\theta_u^{s,i}$ denotes the angle between the i-th antenna boresight of the s-th satellite, and the direction of the u-th user in the b-th beam (when $i = b$, this is the angle from the intended antenna boresight); *v*) θ_s^u denotes the angle between the antenna pointing of the u-th user and the s-th satellite, which does not depend on the satellite antenna index since they are assumed to be colocated. The intended power received by the u-th user in the b-th beam is given by:

$$S_u^{(DL)} = EIRP^{(DL)}\left(\theta_u^{s,b}\right) + G_{RX}\left(\theta_s^u\right) - L_u^s \tag{6.44}$$

where $G_{RX}(\theta_s^u)$ is the receiving UE antenna gain as a function of the angle between the UE antenna pointing and the s-th satellite direction. The transmitted EIRP from the intended b-th antenna, of the s-th intended satellite, towards the u-th user is $EIRP(\theta_u^{s,b})$. While L_u^s is the overall loss for the u-th intended user with respect to the intended s-th satellite computed as in Eq. 6.33.

The transmitted EIRP is computed with respect to the transmission direction $\theta_u^{s,b}$, while the receiving gain, G_{RX}, with respect to the incoming signal direction θ_s^u. This values depend on the antenna pattern chosen for the satellite and UT, as it is described in Section 6.2.1.

The noise power at the receiver can be computed as follows [1], [12]:

$$\begin{aligned} N = 10\log_{10}\Bigg(&\frac{T_a}{10^{0.1L_{FRX}}} + T_0\left(1 - \frac{1}{10^{0.1L_{FRX}}}\right) \\ &+ T_0(10^{0.1N_f} - 1)\Bigg) + 10\log_{10}\left(\kappa B\right) \end{aligned} \tag{6.45}$$

where N_f is the receiver noise figure, T_a is the receiver antenna temperature, κ is the Boltzmann constant, and $T_0 = 290$ K is the reference noise temperature.

The SNR, $SNR_u^{(DL)}$, can be then obtained by subtracting Eq. 6.45 from Eq. 6.44:

$$SNR_u^{(DL)} = S_u^{(DL)} - N = EIRP^{(DL)}\left(\theta_u^{s,b}\right) + 10\log_{10}(G/T)_u - L_u^s \tag{6.46}$$

where G/T is a typical figure of merit in SatCom systems, describing the receiver characteristics by means of the ratio of the antenna receiving gain, G, in the considered direction and the system noise temperature, T at the input of the receiver[3]. It can be written in general as:

$$G/T = G_{RX} - N_f - 10\log_{10}(T_0 + (T_a - T_0)10^{-0.1N_f}) \tag{6.47}$$

[3]The system noise temperature can be written in linear units as follows:

$$T = T_a + T_{eRX} = T_a + T_0(N_f - 1) = N_f T_0 + T_a - T_0 = N_f\left(T_0 + \frac{Ta - T_0}{N_f}\right)$$

The last thing that needs to be considered is the interference. The interference from the i-th interfering beam of the k-th satellite is computed as:

$$I_{k,i,u}^{(DL)} = EIRP^{(DL)}\left(\theta_u^{k,i}\right) + G_{RX}\left(\theta_k^u\right) - L_u^k \tag{6.48}$$

while the overall interference at the u-th user in the b-th beam is given by:

$$I_u^{(DL)} = 10\log_{10}\left(\sum_{k=1}^{N_{sat}}\sum_{i=1}^{N_{int}} 10^{0.1 I_{k,i,u}^{(DL)}}\right) \tag{6.49}$$

with N_{int} being the number of co-channel, co-polarized and cross-polarized beams, and N_{sat} the number of satellite in the constellation. It shall be noticed that, in the i-th interference term, the satellite EIRP is now computed based on the angle between the i-th interfering antenna boresight and the direction of the u-th intended user in the b-th beam. Similarly to the SNR, from Eq. 6.49, it is straightforward to obtain the Signal-to-Interference Ratio (SIR), $SIR_u^{(DL)}$, by subtracting Eq. 6.49 from Eq. 6.44. Finally the overall SINR is given by:

$$SINR_u^{(DL)} = -10\log_{10}\left(10^{-0.1 SNR_u^{(DL)}} + 10^{-0.1 SIR_u^{(DL)}}\right) \tag{6.50}$$

It is worthwhile highlighting that the above formulation for the DL performance can be applied to any SatCom system for either the user- or the feeder-link, and can be used also for analyses on all the systems foreseen for NTN [11], [12].

6.2.3 Uplink

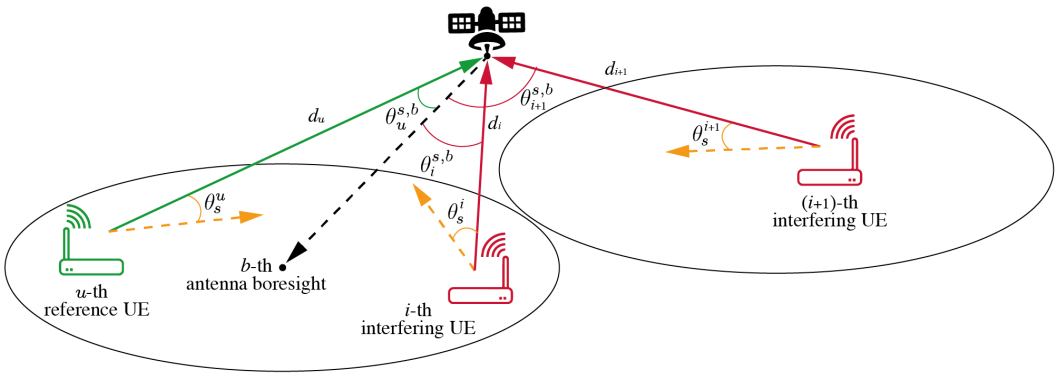

FIGURE 6.8: Geometry for LB computation (Uplink).

For the sake of clarity and without losing generality, as it has been done for the DL, the mathematical framework for the UL LB computation is presented considering one satellite and two beams. However all the assumptions hold for all the satellites and beams considered in a multi-satellite, multi-beam system. The reference scheme adopted is shown in Figure 6.8, where: *i*) the u-th reference user for the LB computation is randomly located inside the b-th reference beam; *ii*) d_s^u is the

slant range of the u-th user in the b-th beam, with respect to the s-th satellite; *iii*) the interfering i-th users are randomly located in both the reference b-th beam and the interfering i-th beams; *iv*) d_s^i is the slant range of the interfering i-th user towards the s-th satellite; *v*) $\theta_u^{s,b}$ denotes the angle between the boresight of the b-th reference antenna on the s-th satellite and the u-th user; *vi*) θ_s^u denotes the angle between the boresight of the u-th user's antenna and the s-th satellite; *vii*) $\theta_i^{s,b}$ denotes the angle between the boresight of the b-th receiving antenna on the s-th satellite and the i-th interferer; *viii*) θ_s^i denotes the angle between the boresight of the i-th interferer's antenna and the s-th satellite.

As in the DL, the intended power received by the b-th satellite antenna from the u-th user can be derived as:

$$S_{u,s,b}^{(UL)} = EIRP^{(UL)}\left(\theta_s^u\right) + G_{RX}\left(\theta_u^{s,b}\right) - L_s^u \tag{6.51}$$

where differently from Eq. 6.44 in the DL, the EIRP is a function of the UE antenna radiation pattern with respect to the angle between the UE antenna pointing and the s-th satellite direction, θ_s^u. While the receiving gain of the b-th antenna of the s-th satellite, is a function of the angle $\theta_u^{s,b}$ and depends form the satellite antenna pattern, as it is described in Section 6.2.1. The path loss L_s^u corresponds to the one in Eq. 6.44.

The noise power in the UL can be computed by using Eq. 6.45, but differently from the DL, N_f is the satellite payload noise figure, and T_a is satellite antenna equivalent noise temperature. The UL SNR is then obtained as:

$$SNR_u^{(UL)} = S_u^{(UL)} - N = EIRP^{(UL)}\left(\theta_s^u\right) + 10\log_{10}(G/T)_s - L_s^u \tag{6.52}$$

where G/T is the same fo Eq. 6.47, but it is now referring to the satellite payload characteristics.

The interference from the i-th interfering UT, towards the b-th beam of the s-th satellite, is computed as:

$$I_{k,i,u}^{(UL)} = EIRP^{(UL)}\left(\theta_s^i\right) + G_{RX}\left(\theta_i^{s,b}\right) - L_k^u \tag{6.53}$$

where the parameters are the same as in Eq.6.51, however it is worth highlighting that $EIRP^{(UL)}$, and L are related to the position of the i-th interferer with respect to the s-th satellite. Finally the overall interference towards the reference b-th beam of the s-th satellite is given by:

$$I_{s,b}^{(UL)} = 10\log_{10}\left(\sum_{i=1}^{N_{int}} 10^{0.1 I_{i,s,b}^{(UL)}}\right) \tag{6.54}$$

with $i = 1, \ldots, N_{int}$, being N_{int} is the number of interfering UT. It shall be noticed that the i-th interference term, is represented by either *i*) a UT served by the reference b-th beam of the reference s-th satellite; *ii*) a UT served by another beam of the

same s-th satellite; *iii*) or a UT served by another beam-satellite pair of the constellation. Moreover the interference should be considered coming from UT transmitting towards co-polarized beams and cross-polarized beams. From Eq. 6.54, it is straightforward to obtain the SIR from the u-th UT transmitting towards the b-th antenna of the s-th satellite, $SIR^{(UL)}_{u,s,b}$, by subtracting Eq. 6.54 from Eq. 6.51; then the overall SINR is given by:

$$SINR^{(UL)}_{u,s,b} = -10\log_{10}\left(10^{-0.1SNR^{(UL)}_{u,s,b}} + 10^{-0.1SIR^{(UL)}_{u,s,b}}\right) \tag{6.55}$$

As discussed for the DL, the above formulation for the UL performance can be applied to any SatCom system for either the user- or the feeder-link, and can be used also for analyses on all the systems foreseen for NTN [11], [12].

Chapter 7

Analyses and Results

In the previous chapters the ESiM2M simulator has been described and a thorough description of the mathematical framework behind its main modules has been given. The main goal of ESiM2M is to serve as a tool for deriving analyses regarding the S-IoT scenario described in Chapter 1. In the remainings of this chapter an introduction to the main Air Interfaces, study case of the author's publications, will be given; focusing in particular on the RA aspects of E-SSA and NB-IoT. Then the results derived from the delay, Doppler, and link budget analyses for NB-IoT in the framework of NTN standardisation in 5G will be given. Finally a side study IoT services over Galileo satellite constellation will be introduced.

7.1 Air Interfaces

7.1.1 E-SSA

Demand Assignment Multiple Access (DAMA) techniques, like the DVB, are widely used for connection-oriented satellite networks supporting voice and bulky data transmission applications. Such systems typically combine DAMA with an initial RA procedure for capacity request purposes, requiring longer setup time and unnecessary signalling overhead with respect to a pure RA approach. As opposed to the latter, IoT communications are characterized by: *i*) low packet size; *ii*) low data rate; *iii*) low duty cycle; *iv*) very large number of communicating terminals. Then for these kind of services the synchronization overhead of reservation-based approaches, like DAMA, greatly reduces the system efficiency, thus a pure RA solution is preferred for the return link. Classical RA schemes have been widely investigated in the literature and are known not to perform well in the satellite environment [133], [134], however in the recent past some appealing alternatives have been proposed [126].

E-SSA is a high efficiency transmission protocol for IoT to be used in hybrid satellite-terrestrial networks. It aims at solving the weaknesses identified for the legacy SSA scheme, providing remarkable enhancements in terms of robustness and absolute throughput over the latter, thanks to a more advanced digital signal processing at the GW. For what concern the multiple access technique, E-SSA is based on a modified version of the 3GPP W-CDMA. Instead of using standard Direct Sequence Spread Spectrum (DS-SS) where every UT is given a spreading sequence,

E-SSA uses the same pseudo-random sequence for all the UTs, relying on the asynchronous nature of the system to differentiate between different UTs and mitigate the effect of interference [135]. Being CDMA based, E-SSA structure is not organised into frames, thus messages are sent by UTs whenever they are ready. There are no replicas in E-SSA as spreading is used to increase the probability of decoding a packet instead of time diversity.

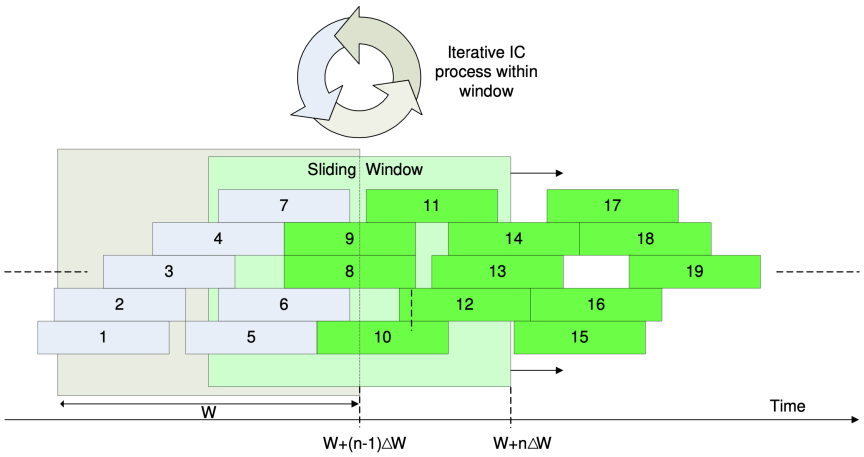

FIGURE 7.1: Enhanced Spread Spectrum ALOHA algorithm description from [126].

The E-SSA demodulator is the heart of the system and provide reliable detection of the incoming packets, even under heavy MAC channel load, exploiting Iterative SIC (iSIC) approach, shown in Figure 7.1, which transforms SSA biggest problem, *i.e.*, multiple access carrier power unbalance, in an advantage. The received signal, containing the superimposition of many asynchronously generated packets, is band-pass filtered, sampled, digitally down-converted to baseband with I-Q components and stored in a digital memory. Then packets are decoded through a sliding-window process. The memory window size, W, on which the iSIC is performed has a length of around 3 times the packet duration. The window is shifted in time after N_{iter} iSIC iteration by a discrete amount, ΔW, which is between $1/3$ and $1/2$ of W [126], [136]. At each window step, the following functions are implemented, [137]:

1. Store in the detector memory the new baseband signal samples corresponding to the current window step.

2. Perform packets preamble detection and select the packet with highest SINR value.

3. Perform data-aided channel estimation for the selected packet over the preamble.

4. Perform FEC decoding of the selected packet.

5. If the decoded FEC frame is considered correct then:

a) perform enhanced data-aided channel estimation over the whole recovered packet;

b) reconstruct at baseband the detected packet for the subsequent cancellation step;

c) perform interference cancellation.

6. Repeat from step 2 until the maximum number of SIC iterations are performed, when the limit is reached, advance the observation window by ΔW.

The key steps for a good E-SSA detector performance are the packet preamble detection and the SIC process.

7.1.2 NB-IoT

The 3GPP recognizing the importance of IoT has introduced a number of key features for supporting the latter since Release 13, providing progressively improved support for Low Power Wide Area Network (LPWAN). In fact, Release 13 EC-GSM-IoT [138] and LTE-eMTC [138] aim to enhance existing GSM and LTE networks, for better serving IoT use cases. A third technology, the so called NB-IoT [139], shares this objective as well. While it is designed to achieve excellent coexistence with legacy GSM and LTE technologies, NB-IoT is actually a new technology and, as a consequence, not fully backward compatible with existing 3GPP devices [140]. According to 3GPP, NB-IoT aims at offering [141]: i) ultra-low complexity devices to support IoT applications; ii) improved indoor coverage of 20 dB compared to legacy GPRS, corresponding to a Maximum Coupling Loss (MCL) of 164 dB while supporting a data rate of at least 160 bps for both uplink and downlink; iii) support of massive number of low-throughput devices (at least 52547 devices within a cell-site sector); iv) improved power efficiency (battery life of 10 years) with battery capacity of 5 Wh and transmission power depending on the terminal power class (*e.g.*, 23 dBm for Power Class 3, 20 dBm for Power Class 5 and 14 dBm for Power Class 6); and v) exception report latency of 10 s or less for 99% of the devices.

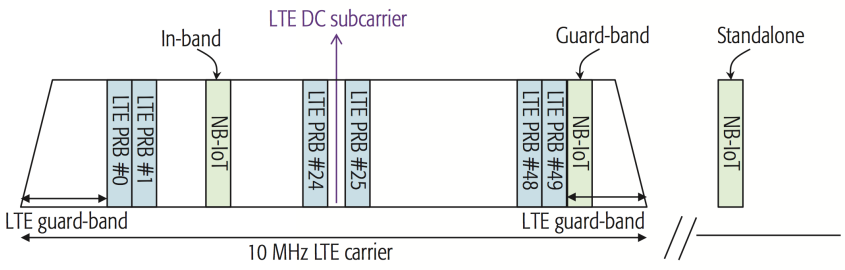

FIGURE 7.2: NB-IoT deployment, [140].

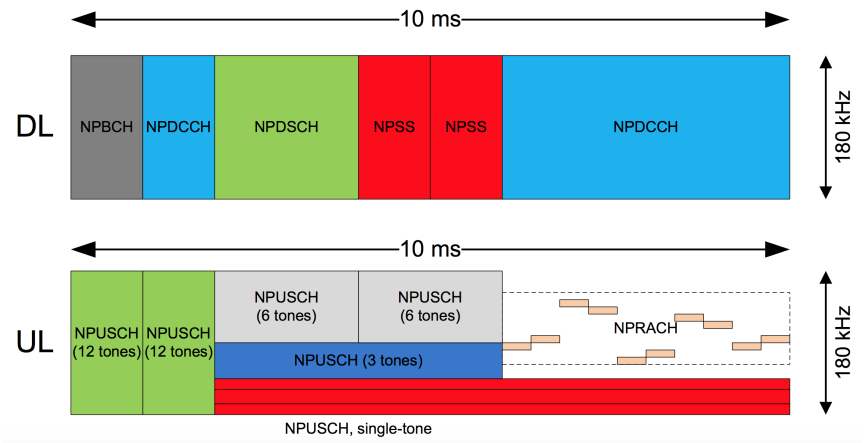

FIGURE 7.3: Example NB-IoT design, [142].

An operator can deploy NB-IoT inside an LTE carrier by allocating one of the Physical Resource Blocks (PRBs) of 180 kHz to NB-IoT, or in GSM spectrum, reducing the deployment costs. Three different modes of operation, depicted in Figure 7.2, have been defined [143]:

- *In-Band:* NB-IoT deployed inside an LTE carrier, with a carrier consisting of one 180 kHz resource block. In this case, LTE and NB-IoT share transmit power at the Base Station (BS).
- *Guard-Band:* the NB-IoT channel is placed in a guard band of an LTE channel. The NB-IoT downlink can share the same power amplifier as the LTE channel.
- *Stand-Alone:* NB-IoT is standalone with at least 180 kHz of the GSM spectrum. All the transmit power at the BS can be used for NB-IoT, which thus significantly enhances the coverage.

Similar to existing LTE UEs, an NB-IoT UE is only required to search for a carrier on a 100 kHz raster, referred as anchor carrier [140], intended for facilitating UE initial synchronization. An anchor carrier can only be placed in certain PRBs. NB-IoT reuses the LTE design extensively, including the numerology, with Orthogonal Frequency Division Multiplexing (OFDM) for the Downlink, Single-Carrier Frequency Division Multiple Access (SC-FDMA) for the Uplink, channel coding, rate matching, interleaving, *etc*. Although in the DL, NB-IoT fully inherits numerology from LTE, in the UL, besides the Sub-Carrier Spacing (SCS) of 15 kHz inherited from LTE, a 3.75, and 1.25 kHz SCS are also supported and single tone assignment could be used for the UL transmissions [140], [144]–[146].

In order to satisfy the stringent battery consumption requirement for IoT applications, NB-IoT adopts some protocol enhancement like: i) extend Discontinuous Reception (eDRX); and ii) Power Saving Mode (PSM). NB-IoT adopts different procedures for the optimisation of small data transmissions: i) Control Plane CIoT Evolved Packet System (EPS) optimisation (CP); ii) User Plane CIoT EPS optimisation (UP). Finally to ensure an improved coverage a high number of repetitions is

used for initial network access and data transmission[138], [141], [147], [148]. A wide range of IoT services are being embraced and NB-IoT deployment is going to satisfy most of the requirements for these services, from smart metering, smart cities and buildings, environmental and agriculture monitoring, up to animal/people tracking. However there are many application scenarios for IoT for which terrestrial network deployment is unfeasible or not economically profitable, here SatCom have the potential to play an important role, as previously mentioned. In this framework the recently approved 3GPP study item on NB-IoT over NTN is of paramount importance for the development of this technology.

7.1.2.1 Random Access

The RA procedure for NB-IoT has been studied with particular emphasis in the author's work, and will be the pivotal point of the analyses presented in the following sections. The RA procedure is a very crucial step of the NB-IoT network since it allows the NB-IoT UEs to achieve uplink synchronization, obtain a permanent ID, and initiate uplink data transmission. From an high-level point of view the RA procedure for NB-IoT follows the same message flow of LTE, with the main difference of using repeated transmission for each message in the RA procedure.

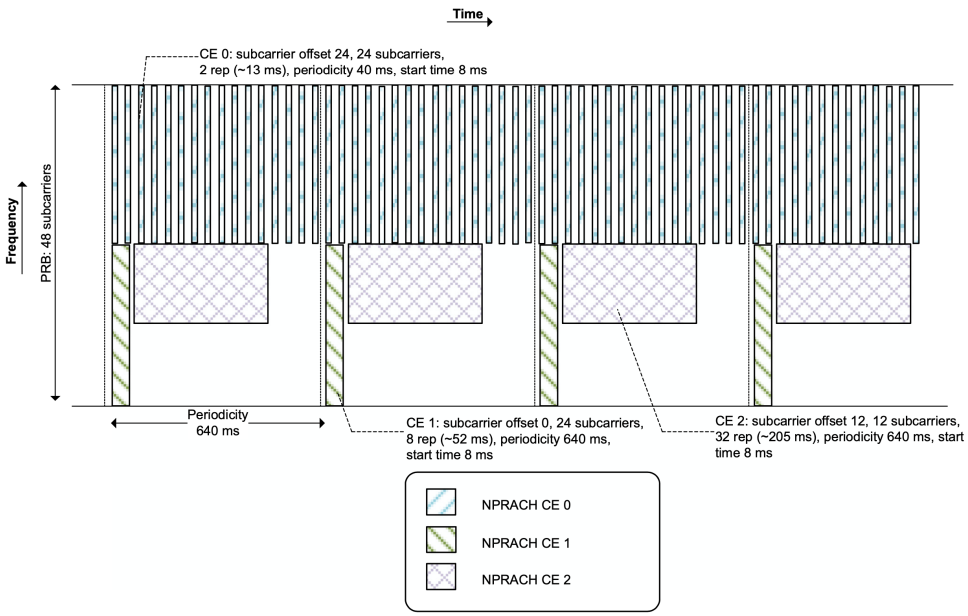

FIGURE 7.4: Example of NPRACH resources allocation [148].

Firstly the UE needs to synchronize in time and frequency with BS, then the UE uses the information broadcasted by the BS to retrieve the necessary parameters to access the network. In order to serve UEs in different *coverage classes*, who experience different ranges of path loss, the network can configure up to three Narrowband Physical Random Access Channel (NPRACH) resource configurations in a cell, as shown in Figure 7.4. Each UE measures its downlink received signal power to

estimate which of the three coverage levels it belongs to. In each configuration, a repetition value is specified for repeating the messages in the RA procedure as well as the level of transmission power. Furthermore NB-IoT allows flexible configuration of NPRACH resources in a time-frequency resource grid[144]. Once the coverage class has been determined, the actual RA procedure can start. NB-IoT supports both *contention-based* and *contention-free* RA procedures. The message exchange occurring between the UE and the BS is depicted in Figure 7.5 for the contention-based RA procedure.

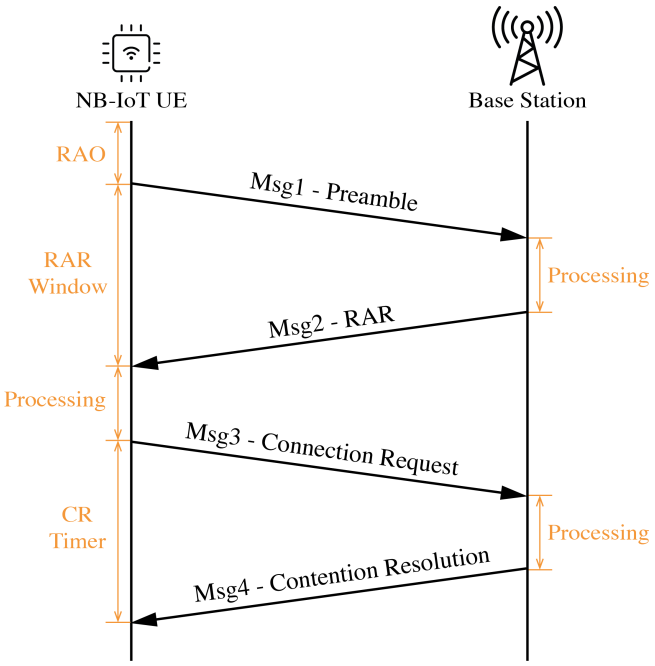

FIGURE 7.5: Contention-based Random Access.

TABLE 7.1: Preamble formats

Format	P	N	T_{CP}	SCS
0	4	5	66 μs	3.75 KHz
1	4	5	266.7 μs	3.75 KHz
2	6	3	800 μs	1.25 KHz

Message 1: The UE chooses a preamble among the 48 (or 144 according to the preamble format) and transmits it to the serving BS over the NPRACH. It is worth highlighting that UEs will compete for the same NPRACH resources, hence collisions will occur if the same preamble is chosen by more than one UE. As shown in Table 7.1, there are three different NB-IoT preamble formats. As a baseline, a preamble consists of P symbol groups, with each symbol group comprising the Cyclic Prefix (CP) and N identical symbols, the sequence. Each symbol group is transmitted on a different subcarrier, then the tone frequency index changes from one symbol group to another, resulting on a frequency hopping applied on symbol group granularity. This *inner frequency hopping* is

restricted to 12 (or 36) contiguous subcarriers and follows the same pattern for each repetition of the preamble. Up to 128 repetitions of preamble are allowed for each RA attempt, based on the coverage level of the UE, [149]. The starting subcarrier define both the inner hopping and the *outer frequency hopping* among the preamble repetitions.

Message 2: If the BS detects an NPRACH preamble, it responds to the request, on the Narrowband Physical Downlink Control Channel (NPDCCH), with the Random Access Response (RAR) message. The latter should be received by the UE within a RAR window, starting after the transmission of the last preamble repetition. The maximum duration of the RAR time window is extended, compared to the one of LTE, up to 10.24 s, [149]. After the timer expiration, the UE could attempt a new RA procedure. Then if the maximum number of attempts is reached without success, the UE proceeds to the next coverage level, if this level is configured, and try the procedure again. If the total number of access attempts is reached, an associated failure is reported to the RRC. The NPDCCH is addressed by the RA-RNTI, allowing the UE to know if the RAR is meant for him. With the RAR message the UE gets a Temporary C-RNTI, the Timing Advance (TA) command for time synchronization, as well as scheduling information pointing to the radio resources that the UE has to use to transmit the subsequent messages. Basically, from this step on, the transmission of the data, either in DL or UL, is orchestrated by the BS. This means that the BS guarantees that different resources (time/frequency) are assigned to various UEs in order to avoid packet collision.

Message 3: The device will include its identity, as well as a scheduling request [141], [145], [150]. Furthermore, it will also report its data volume status and power headroom, to facilitate the base station scheduling and power allocation decision for subsequent transmissions. At this step, the HARQ protocol is used by both, the UE and the BS, for the message exchange. Basically, after each packet transmission, the UE has to wait for an ACK or NACK by the BS, or vice versa, to know whether the packet was correctly received. If not, the same packet is retransmitted.

Message 4: Upon reception of the Contention Resolution indicating that the random access procedure is successfully finalized, the network assigns a permanent ID to the UEs which had a successful RA procedure, *i.e.*, the Temporary C-RNTI become permanent. At this point, the UE make the transition from RRC Idle to RRC Connected Mode. Likewise RAR time window, also the MAC contention resolution timer is extended up to 10.24 s. If the contention resolution message is not received before this timer expires, the UE could retry the RA procedure from Msg1 [140], [141], [144], [145], [147], [149]–[153].

7.1.2.2 Main Challenges for NTN integration

In this section, the main challenges to be faced concerning the integration of NB-IoT over satellite links, are highlighted. In particular, the focus is on LEO satellites due to the latency and link budget constraints for the mMTC-NB-IoT scenario. While the following item list is not completely exhaustive of all the possible issues to be tacked in the whole study, it includes the most important parameters:

Latency: even if the latency constraints in NB-IoT are relaxed [141], some timers coming from LTE architecture have to be taken into account into the investigation. In particular the study on the 3GPP standards highlighted the presence of timers in the RA procedure, shown in Figure 7.5, and RRC procedures that might be incompatible with SatCom channel RTT delays, which are: i) CP length; ii) RAR time window size; iii) TA; iv) Contention Resolution window size; v) RRC Timers procedure; and vi) HARQ.

Doppler effect and phase shift: due to the NB-IoT frame structure, with really narrow and close subcarriers, the characteristics Doppler and phase impairments of a satellite communication channel, in particular when LEO or MEO satellites are considered, could prevent a successful transmission.

Battery life: NB-IoT requirements suggest a battery life around 10 years. The larger RTT, typical for satellite communications, will imply longer wake up period for devices in order to perform access procedures and data transmission. Furthermore, higher power, with respect to the terrestrial case, could be needed in order to close the link. These issues could prevent the long duration of batteries.

Link budget: power constraints of Satellite, BS, and NarrowBand UE must be considered for the feasibility of GEO and LEO feeder and user links, on both forward and return paths.

7.2 Link Budget related Analysis

The following section is directly derived from the outcomes of the author's publication *"NB-IoT over Non-Terrestrial Networks: Link Budget Analysis"*, [70], in the framework of the 3GPP study item on NTN standardisation process. Although many different aspects have been studied in the recent past in order to better understand the requirements for NB-IoT integration over NTN, a complete link budget analysis taking into account the parameters approved in 3GPP study items is not available. An initial interesting analysis of the *link budget* is presented in [69], where the case of a single satellite, in LEO at a given elevation angle, is addressed to shed light on the trade-offs between the link parameters and the payload characteristics. However, to fully support the system design of future NB-IoT over NTN, the link budget analyses shall consider the NTN architecture in its entire complexity, in particular it shall

address the effect of moving non-geostationary satellites, *i.e.*, different elevation angles, actual propagation conditions, and multi-beam and multi-user interference.

In the following, this analysis is presented, providing the link budget evaluation for an NB-IoT systems by considering fixed IoT device on Earth and moving LEO satellites in different constellations, accounting for the multi-beam interference, in the down-link, and the multi-user interference, in the up-link. It is important highlighting that the results presented in the following sections rely on the mathematical framework for Link Budget computation presented in Section 6.2. In doing this analysis, the NTN system architecture options currently considered within 3GPP and the system assumptions are discussed, and a link budget calibration in both the down-link and the up-link according to [11], [12] is performed, by extending to NB-IoT the work reported in [39].

7.2.1 System Architecture

With reference to Figure 7.6, the main elements of the high-level system architecture [12] are: *i*) a UE, which is a NB-IoT device, fixed or mobile; *ii*) a regenerative payload satellite or Unmanned Aircraft System (UAS), providing connectivity to the UE through the user link; *iii*) a gNB implemented on the satellite; *iv*) a ground segment GW interconnected to the flying platform through the feeder link; *v*) the NGC.

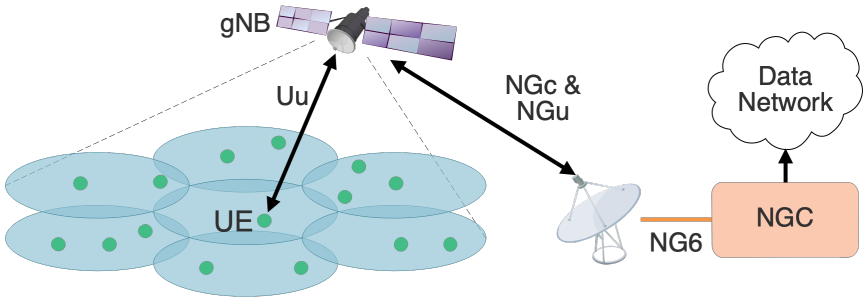

FIGURE 7.6: High-level system architecture: access based on regenerative payload.

The aforementioned architecture can be declined into different scenarios, [11], depending on the orbit and altitude of the flying platforms. In the first stage of standardisation for NTN, the focus is on GEO platforms and LEO platforms at 600 and 1200 km of altitude. For LEO platforms, the coverage can be achieved with *fixed* or *moving* beams. In the former case, the on-board antenna keeps serving the same on-ground area while the satellite moves on its orbit (steerable antennas). In the latter case, the served on-ground area is moving together with the satellite. Later in this analysis, if not otherwise specified, the following system configuration is assumed: direct access, regenerative payload, LEO or GEO multi-beam platform operating in S-band, with moving beams for LEO constellations. This configuration refers to scenario *B* and scenario *D2* in [11], as shown in Table 1.1.

7.2.1.1 Single- and Multi-Satellite Scenarios

For the Single-Satellite (S-S) scenario, the coverage area of the satellite, thus the multi-beam layout, are defined in *u-v* coordinates. Assuming θ_{3dB} as the antenna 3 dB angle, the beam radius on the *u-v* plane is defined as $R_{3dB} = \sin(\theta_{3dB})$. The hexagonal tessellation on the *u-v* plane is then obtained by locating the adjacent beam centers at a distance corresponding to the Adjacent Beam Spacing, $ABS = R_{3dB}\sqrt{3} = \sqrt{3}\sin(\theta_{3dB})$, as it is explained in [11], [39]. An example of satellite antenna pattern, with hexagonal tessellation is represented in Figure 7.7. In [11], the values of ABS for LEO and GEO systems, are provided assuming for the satellite antennas the Bessel radiation pattern of [12], and described in Eq. 6.42. On the other hand, for the UE an omnidirectional antenna has been considered, thus regardless the angle of departure and arrival defined in Section 6.2 the maximum gain has been considered for the UE antenna. For what concern the UE, it is worth mentioning that the noise power at the receiver is considered independent of the UE, *i.e.*, it is the same for every UE and satellite's beam pairs. It is worth highlighting that the antenna pattern described in [12] is defined regular with respect to θ-ϕ coordinates, while the beam spacing is defined regular with respect to *u-v* coordinates, *i.e.*, circular beams with radius R_{3dB} are considered in [11]. This choice leads to a mismatch, in fact a regular grid in θ-ϕ plane cannot be regular on the *u-v* plane and vice versa, as specified in Chapter 3. Therefore moving away from the central beam of the coverage, the surrounding beams begin to deform from the circular shape, leading to an imperfect coverage. However in this work a perfect coverage, as initially intended from 3GPP documentation, has been used.

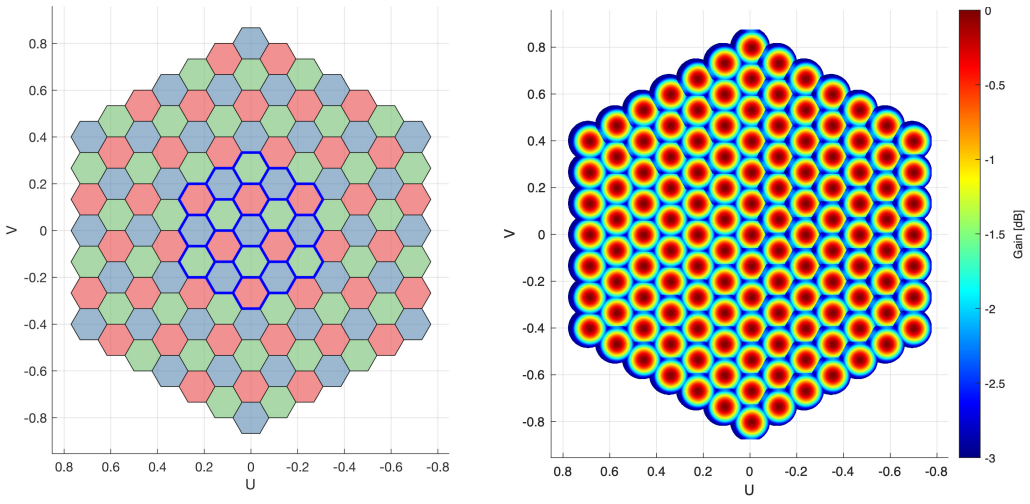

(A) Hexagonal beam layout (B) Antenna radiation pattern

FIGURE 7.7: Example of coverage (*u-v* coordinates): LEO system in S-band; h_{sat} = 1200 km; FR3; 6 tiers (127 beams).

For the Multi-Satellite (M-S) scenario, the methodologies proposed in [11] and [99] have been taken into account. In particular this work focuses on the *Option-1* described in Chapter 4, for simulation based on a reference constellation, defining the

parameters, *e.g.*, number of orbits/satellites, number of beams. The detailed parameters can be determined jointly with consideration on the RF characteristic of beams together with design principle for constellation, *e.g.*, how to achieve global coverage. Considering a specific satellite, with a specific altitude and position, and referring to the beam layout previously defined, it is possible to derive the coverage on the Earth's surface for that flying platform, thus the coverage for the entire constellation. This computation relies on the geometrical relationships between satellite FOV and access area defined in Chapter 3. The antenna pattern for each satellite in the constellation is derived with the same procedure detailed for the S-S scenario, however a different number of beams per satellite have been used, as shown in Table 7.4. It is worth highlighting that for this purpose, in the satellite coordinate reference system, the u-axis is pointing towards West and consequently the v-axis is pointing towards North, because of the convention adopted by the 3GPP for the NTN standardisation process, [11].

7.2.2 Numerical Results

The link budget analyses for single- and multi-satellite scenarios, is performed by means of Monte Carlo simulations, based on the configurations reported in Tables from 7.2 to 7.4 which are derived from [11], [154], [144], and [99]. The results detailed in this section are derived following the mathematical framework described in Section 6.2. The reference satellite-UE geometry, for the LB computations, in both S-S and M-S scenarios, is the one depicted in Figures 6.7 and 6.8.

Although [11] does not explicitly consider the NB-IoT case, the selection of these parameters is based on the observation that the smaller antenna size at the satellite, as it is in Set-2, is adequate also to the NB-IoT case. As a matter of fact in an S-IoT scenario, not only the IoT devices must be low-cost and low-energy, but it is equally important to have small, low-complexity equipment also in the space segment to reduce the cost of the infrastructure and thus the need of a small low cost antenna at the satellite. Although the parameters chosen for the constellations allow to achieve a global coverage, the actual antenna implementation that allows to obtain such a massive number of beams, could be impractical, in particular on small and cheap LEO platform. It is a fair assumption that a lower number of beams will be considered for actual implementations. Furthermore constellations with partial coverage will be probably considered for IoT services in the near future, and therefore these aspects will be subject of future studies.

Also, since NB-IoT terminals are not defined in the same 3GPP simulation set, the system bandwidth has been modified in line with the NB-IoT system, by choosing 180 kHz for the DL and 3.75, 15, 45, 90, 180 kHz for the UL, regardless to the adopted Frequency Reuse (FR) scheme, *i.e.*, Full Frequency Reuse (FFR) and Frequency Reuse 3 (FR3). For the sake of synthesis, only the results for the case with $B = 45$ kHz will be shown for the UL scenario, *i.e.*, the Narrowband Physical Uplink Shared Channel

TABLE 7.2: Satellite parameters for S-band (Set-2 [11]).

Parameter	GEO	LEO	
		600 km	1200 km
a: equivalent antenna radius [m]	6	0.5	0.5
δ_{EIRP}: EIRP density [dBW/MHz]	53.5	28	34
$G_{TX,max}$: max TX gain [dBi]	45.5	24	24
$G_{RX,max}$: max RX gain [dBi]	45.5	24	24
G/T [dB/K]	14	-4.9	-4.9
N. beams	61-FFR; 127-FR3; 19-retained		

TABLE 7.3: NB-IoT terminal parameters for S-band [144], [154].

Parameter	Value
P_{TX}: transmission power [dBm]	23
$G_{TX,max}$: max TX gain [dBi]	0
$G_{RX,max}$: max RX gain [dBi]	0
T_a: antenna temperature [K]	290
N_f: noise figure [dB]	9
Polarisation	linear
B_{DL}: DL bandwidth [kHz]	180
B_{UL}: UL bandwidth [kHz]	3.75, 15, 45, 90, 180

(NPUSCH) Format 1 configuration, with 3 tones allocation [144]. The UE parameters refer to [154] and [155], considering NB-IoT Class 3 terminals.

7.2.2.1 Single-Satellite Scenario

For S-S scenario the beams are located on the u-v plane so as to have equivalent elevation of the satellite at $45°$ (GEO) or at $90°$ (LEO) [11] from the coverage center. A variable number of tiers is considered depending on the FR scheme so as to ensure that the same number of interfering beams is considered for all scenarios; in order to properly model the overall interference experienced by each UE, the numerical results are gathered from the 19 internal beams only, which are highlighted by the thick blue line in the example in Figure 7.7a. The UEs are deployed in the coverage on a regular grid in u-v coordinates. It shall then be noticed that, in the DL, the interference towards any UE is generated by the co-channel transmitting antennas on the satellite; thus, interference is defined by geometry, *i.e.*, it is fixed given the receiving UE location and the beam layout configuration. The only stochastic aspect to be taken into account is the shadow fading, modelled as a log-normal random variable $L_\sigma \sim (0, \sigma^2)$ with the values of σ^2 depending on the UE's elevation angle [12]. As for the UL, interference is clearly depending on the specific interfering UE locations. In this case then, both the stochastic shadow fading and the interference source location vary through Monte Carlo iterations. Furthermore the interference is not defined by geometry as in the DL, but it is impacted by the scheduling algorithm,

TABLE 7.4: Constellation parameters for S-band [99].

Parameter	GEO	LEO	
		600 km	1200 km
Orbit type	GEO	LEO, circular	
Orbit inclination	0°	87.5°	
N_o: N. orbits	1	17	10
N_s: N. satellites (per orbit)	4	30	17
Beam diameter (at nadir) [km]	450	190	90
N_b: N. beams (per satellite)	547	127	91

which is assumed to be random, with one UE per beam transmitting at each iteration as it is in [11].

Figures from 7.8a to 7.8c, show the Carrier-to-Noise Ratio (CNR)[1], CIR and CINR Cumulative Distribution Function (CDF) for the DL, while figures from 7.9a to 7.9c for the UL. Table 7.5 provides the mean and standard deviation of the CINR for all cases. As can be seen from the results, the CINR with FFR is quite low for all scenarios; this is related to the severe interfering environment since no interference management technique is implemented. An improvement of the performance can be seen for FR3. The difference in the standard deviation between the DL and the UL scenarios is motivated by the fact that, in the DL, interference is defined by geometry, *i.e.*, the beam layout is fixed and the interfering satellite antennas are always transmitting towards their beam centers; while in the UL, a random scheduling algorithm is implemented to identify the interfering users at each time frame and, thus, an increased variability arises.

7.2.2.2 Multi-Satellite Scenario

The simulations for the M-S scenario are time-driven, *i.e.*, at each time instant the geometry of the constellation changes, thus the link budget and interference components change. Then both the satellite constellation geometry, and the stochastic shadow fading previously described, vary through Monte Carlo iterations. The UEs are deployed on a regular *lat-lon* grid and the statistics are gathered from all the points of the grid. The performance analysis is then computed for the whole evolution in time of the satellite constellation, considering a uniform user deployment. For each constellation geometry, the UE are assigned to the best satellite/beam pair according to the link budget fixed terms, *i.e.*, the antenna pattern for the constellation is projected in *lat-lon* coordinates, as previously described, then the highest value of $G - L_{fs}$ is chosen for each UE such to identify the best serving satellite/beam pair. An example of global coverage, showing the link budget fixed terms, is depicted in

[1]The 3GPP documentation refers to CNR, Carrier-to-Interference Ratio (CIR), and Carrier-to-Interference plus Noise Ratio (CINR), thus in this chapter the same nomenclature has been adopted, in order to be compliant with the specifications. However it is important to highlight that those values corresponds to SNR, SIR, and SINR computations presented in Section 6.2.

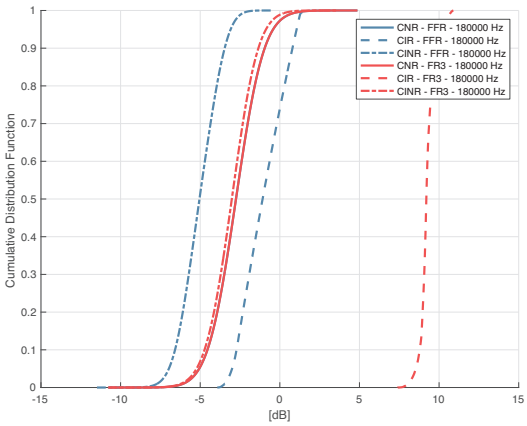

(A) Downlink link budget for GEO satellite

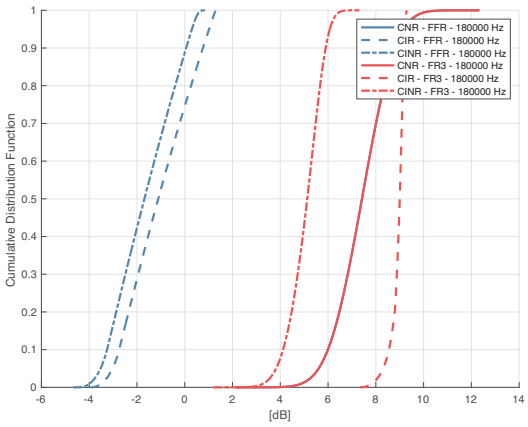

(B) Downlink link budget for LEO satellite at 1200 km

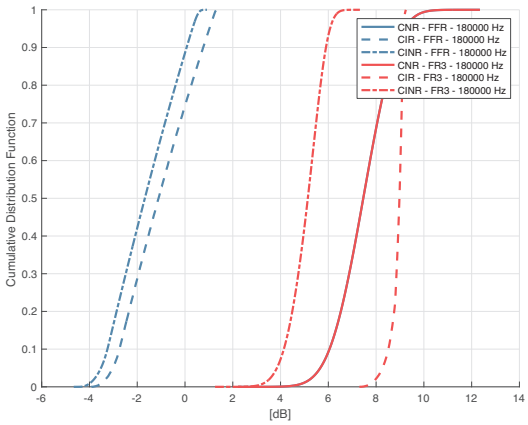

(C) Downlink link budget for LEO satellite at 600 km.

FIGURE 7.8: Downlink Link Budget.

Figure 7.10. The minimum elevation angle considered for the UE is 10°. In the DL, the useful received signal, C (Eq. 6.44), is computed with respect to the best serving satellite/beam pair while the interference, I (Eq. 6.49), is considered from all the satellite/beam pairs visible to the UE. As opposed to the S-S scenario here the interference toward any UE is not only dependent by the beam layout geometry, but also from the satellite-UE relative positions, *i.e.*, slant range and elevation angle with respect all the constellation satellites. As for the UL, a random scheduling is performed in the same fashion of S-S scenario, such to select only one transmitting UE for each beam of every satellite. Then the interference towards all the satellite/beam pairs visible from the UE are computed, as previously described, accounting for the satellite-UE relative geometry. In this case then the interference is also impacted by the scheduling algorithm.

For the sake of synthesis, CDF graphs are not shown but a summary of the results, with mean and standard deviation of the CINR for all cases, is shown in Table 7.5. As it is expected the mean values of all cases are lower with respect to the link budget calibration results shown previously, while the standard deviation is higher.

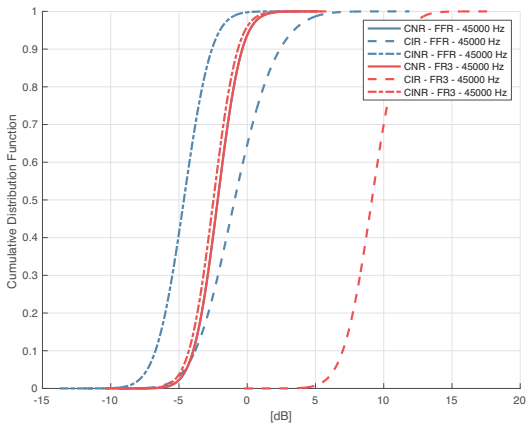

(A) Uplink link budget for GEO satellite

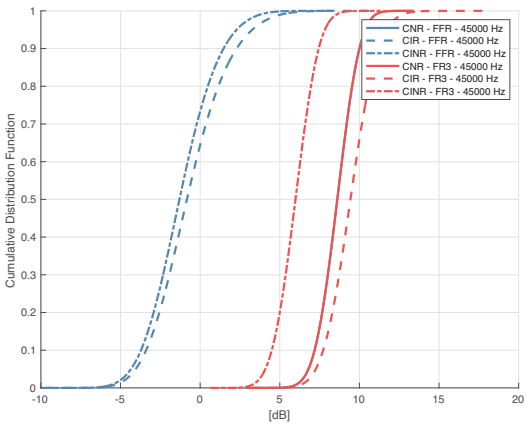

(B) Uplink link budget for LEO satellite at 1200 km

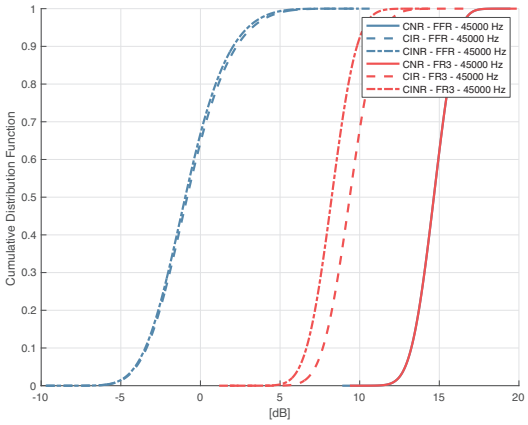

(C) Uplink link budget for LEO satellite at 600 km.

FIGURE 7.9: Uplink Link Budget.

These results are motivated by the fact that, the coverage is much bigger with respect to the S-S scenario; focusing on the LEO at 600 km for example, the coverage is composed from $N_{beams} = 127$ beams, opposed to the 19 retained beams for the statistics for the S-S scenario.

Numerical results show that FFR schemes require the implementation of interference management techniques, while for multi-color FR schemes the link budget already provides a good performance. It is worthwhile highlighting that the study on NB-IoT integration in NTN is on-going within 3GPP, so future works will target the evolution of this standardisation process.

7.3 Doppler related Analysis

The following section is directly derived from the result of the author's publication *"Doppler Impact Analysis for NB-IoT and Satellite Systems Integration"*, [67]. Few scientific works have been already published on the topic of Doppler impacts for NB-IoT integration on SatCom systems: [30], [66] study the effects of the high Doppler induced by non-geostationary satellites and the possible countermeasures; while [68]

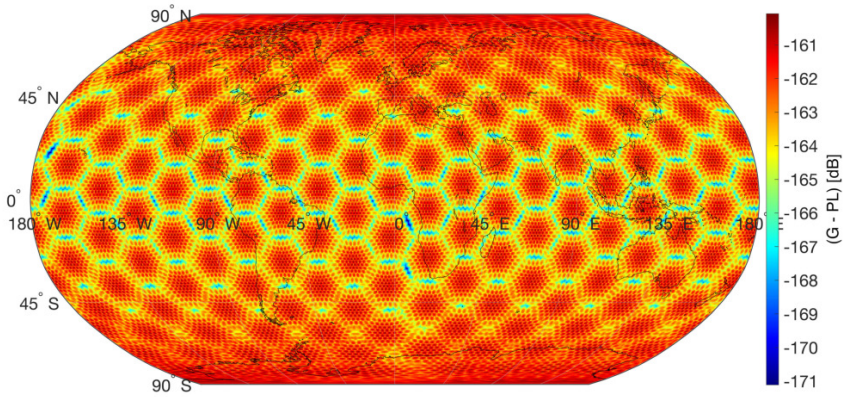

FIGURE 7.10: Example of satellite constellation coverage (1200 km).

TABLE 7.5: Single- and Multi-Satellite results: CINR μ and σ in dB.

Case		GEO		LEO1200		LEO600	
		μ	σ	μ	σ	μ	σ
DL (S-S)	FFR	-5.04	1.20	-1.65	1.22	-1.65	1.22
	FR3	-3.03	1.33	5.06	0.69	5.07	0.68
DL (M-S)	FFR	-9.24	6.09	-8.13	2.81	-8.37	2.59
	FR3	-8.50	6.42	-1.20	3.16	-1.34	3.35
UL (S-S)	FFR	-4.65	1.62	-1.20	2.01	-0.82	2.15
	FR3	-2.48	1.42	5.98	1.14	8.24	1.23
UL (M-S)	FFR	-6.45	6.40	-3.81	3.56	-3.50	3.20
	FR3	-5.26	3.85	0.21	3.34	3.55	4.53

addresses the design of a NB-IoT receiver in the presence of Doppler effects, at the GW side. In the remainings of the section an analysis for the Doppler shift and Carrier Frequency Offset (CFO) compensation will be given, with a particular attention on the satellite user link (UE-to-Sat). While the following analysis is not completely exhaustive for all the possible issues to be tackled in the whole study, it includes the most important challenges to be faced.

7.3.1 System Architecture

For the purpose of this Doppler analysis it has been assumed satellite constellations operating in S-band, deployed at altitudes of 300, 800 and 1200 km from Earth. For each altitude the same satellite constellation has been considered, with 66 satellites distributed on 6 polar orbits spaced 30° apart, with 11 satellites on each orbital plane. A minimum elevation angle of 10° is considered. In terms of system architecture, the following assumptions are made for the considered system: *i*) the terrestrial users are assumed to be uniformly distributed in the area covered by the satellite; *ii*) the terrestrial users are directly connected to the satellite; *iii*) the satellites are assumed to be transparent and to provide backhaul connection between the satellite gateway (GW) and terrestrial terminals; *iv*) the GW is connected to the satellites through ideal

feeder links, providing access to the terrestrial core network. Keeping in mind the aforementioned assumptions, the physical channel experienced by each end user varies instantaneously and can be modelled as:

$$h'_k(t) = h_k(t)e^{j2\pi f_{d_k} t} + n_k(t) \tag{7.1}$$

where $h_k(t) \in \mathbb{C}$ is the channel coefficient at time instant t with $k = 1, ..., N_u$, N_u is the number of users in the coverage area, f_{d_k} and $n_k(t)$ represent the instantaneous Doppler and the noise respectively, experienced from the k-th terrestrial user at instant t.

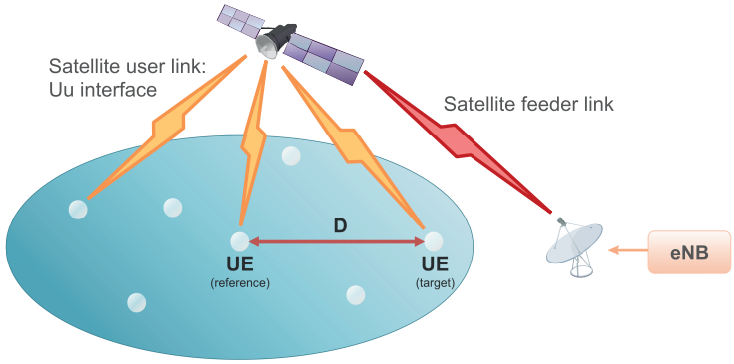

FIGURE 7.11: Reference Scenario.

The reference scenario is shown in Figure 7.11; it is based on the architecture for a NTN featuring an access network serving terrestrial UEs and based on a satellite with transparent payload, proposed in [12]. The terrestrial terminals are assumed to be NB-IoT UEs, directly connected to the BS through the satellite link by means of Uu LTE radio interface. The BS is conceptually located at the gateway, which interacts with the LTE EPC. Thus, for both the backhaul and access links, the system adopts OFDM in the downlink and SC-FDMA in the uplink, according to the aforementioned physical channel characteristics of NB-IoT. For the sake of simplicity and without losing generality, in the reference scenario two terrestrial users, in visibility with the same satellite and in LoS conditions, have been considered. The discussion in the following sections is made considering variable inter-UE distances between the two users, D, with different satellite altitudes.

7.3.2 Numerical Results

LEO and VLEO satellites describe low orbits, ranging from 200 to 2000 km, therefore their relative speed with respect to the ground is much higher compared to GEO. This translates on a stronger Doppler effect experienced by the terrestrial users. Due to the NB-IoT PRB deployment (in in-band operation mode), the UE must be able to search the carrier of NB-PRB with a CFO up to ± 7.5 kHz during the synchronization procedures, according to [141] and [140]. Furthermore the slotted structure of the NB-IoT physical channel is characterized by a narrow SCS (*i.e.*, down to 1.25, and

3.75 kHz for the UL), thus it is really susceptible to the Doppler effect as well as to the CFO.

In the reference scenario, the Doppler experienced by the i-th user in the DL channel and, vice versa, on the satellite with respect to the i-th user in the UL channel can be described as $f_{di} = f_{d_{common}} + \Delta f_{di}$, as described in Section 6.1, where $f_{d_{common}}$ is the common part of the Doppler experienced by every user in the same footprint while Δf_{di}, the differential part, depends on the relative positions of users in the footprint [7]. For the sake of simplicity in the rest of the discussion the feeder link is considered ideal, then does not introduce Doppler impairments, but the mathematical formulation could be extended to a non-ideal feeder link.

Since each UE has to compensate its own experienced Doppler f_{di} and CFO impairments, the differential Doppler is not an issue on the DL user link (Sat $\rightarrow$ UE). Indeed the whole bandwidth of 180 kHz will be received by each UE under the same Doppler condition, with negligible effects on the single subcarriers. In the UL user link (UE $\rightarrow$ Sat), on the contrary, each UE generates its own SC-FDMA signal then the differential Doppler must be compensated such that the frame structure seen by the satellite does not contain overlapping information among subcarriers[7].

As discussed in [152] and [156], LTE physical layer is specifically designed to tolerate a Doppler up to 950 Hz. This value is related to SCS of 15 kHz used in LTE, and correspond approximately to the 6.3 % of the SCS. Therefore it is possible to assume that a value of Δf_{di} up to ≈ 950 Hz could be tolerated for a SCS of 15 kHz while for a SCS of 3.75 kHz the value of Δf_{di} should be lower than ≈ 240 Hz (3.75 kHz $\times 6.3\%$), in order to fulfill the constraints on Doppler for NB-IoT.

7.3.2.1 Analysis on Carrier Frequency Offset and Doppler

This section is focused on the user link in both UL and DL directions. The effects of CFO and Doppler on the signals received by both, target UE in the footprint and BS, are evaluated. For the sake of clarity, it is worth mentioning that the index k refers to the k-th user. The parameters used in the following formulation are defined in Table 7.6.

It is assumed that the imperfections of the Local Oscillator (LO) on the UE_k introduce a frequency offset f_k. Moreover both, the BS and satellite LO (in case of frequency conversion), are perfectly centered in f_0, which is the carrier frequency of the system. Due to the nature of the SC-FDMA signal, a differential frequency offset among UEs in the UL channel can degrade or even destroy the quality of the link. In fact, each UE transmits its own signal affected by a CFO caused by the mismatch between its own carrier frequency (non perfect low cost LO) and the system carrier frequency (assuming perfect LO for BS). Furthermore the signal received by the satellite is affected by the differential Doppler among users. Due to the CFO and the differential Doppler among different UEs, the received baseband signal at the BS

TABLE 7.6: Nomenclature for CFO and Doppler analyses.

Definition	**Symbol**
Number of UE in the cell	N
Transmitted baseband signal BS $\rightarrow$ UE$_\text{k}$	x_T
Received baseband signal UE$_\text{k}\rightarrow$ BS	y_R
Transmitted baseband signal UE$_\text{k}\rightarrow$ BS	x_{UE_k}
Received baseband signals BS $\rightarrow$ UE$_\text{k}$	y_{UE_k}
Instantaneous channel coefficient for the k-th UE	h_k
Noise at the BS section	n_R
Noise at the k-th receiver section	n_k
System carrier frequency	f_0
Differential Frequency Offset of UEs (w.r.t. f_0)	$f_{\Delta k}$
Frequency offset added by UE$_\text{k}$ local oscillator	$f_k = f_0 + f_{\Delta k}$
Doppler at time instant t for the k-th user (Sat $\rightarrow$ UE$_\text{k}$)	$f_{d_k}(t)$
Doppler at time instant $t+\tau$ for the k-th user (UE$_\text{k}$ $\rightarrow$ Sat)	$f_{d_k}(t+\tau)$

is given by the superposition of each signal as follows:

$$y_R(t) = \sum_{k=1}^{N} x_{UE_k}(t) h_k(t) e^{-j2\pi f_{d_k}(t)t} \cos(2\pi f_k t) + n_R(t) \tag{7.2}$$

The multiple access of baseband signals associated to each UE is managed by means of SC-FDMA and the differential frequency offset and Doppler amongst UEs are sources of degradation which must be compensated at the UE. In order to accomplish this procedure, each UE must be aware of the instantaneous Doppler with respect to the satellite antenna. In this work a method based on the estimation of the Doppler based on the DL channel is proposed. The DL signal received by each UE is:

$$y_{UE_k}(t) = x_T(t) h_k(t) e^{-j2\pi f_{d_k}(t)t} \cos(2\pi f_0 t) + n_k(t) \tag{7.3}$$

Then after down-conversion and filtering out the higher order components:

$$\begin{aligned} y_{UE_k}(t) &= \left[x_T(t) h_k(t) e^{-j2\pi f_{d_k}(t)t} \cos(2\pi f_0 t) + n_k(t) \right] e^{j2\pi f_k t} \\ &\simeq x_T(t) h_k(t) e^{-j2\pi \left(f_{d_k}(t) - f_{\Delta k} \right) t} + n_k(t) \end{aligned} \tag{7.4}$$

In order to recover the data, the UE has to estimate the offset, $f_{0d_{kU}}(t) = f_{d_k}(t) - f_{\Delta k}$, then compensating as follows:

$$\begin{aligned} y_{UE_k}(t) &= \left[x_T(t) h_k(t) e^{-j2\pi f_{0d_{kU}}(t)t} + n_k(t) \right] e^{j2\pi \widehat{f}_{0d_{kU}}(t)t} \\ &\simeq x_T(t) h_k(t) + n_k(t) \end{aligned} \tag{7.5}$$

If the UE removes the estimated offset ($f_{0d_{kU}}(t)$) using frequency advance technique[157], [158], then the signal transmitted by each UE in the UL channel will be:

$$y(t) = x_{UE_k}(t) e^{-j2\pi \widehat{f}_{0d_{kU}}(t)t} cos(2\pi f_k t) \tag{7.6}$$

The offset compensation should be intended with respect to the BS reference frequency which is acquired by the UE at the switch on procedure every time the UE resumes from the RRC_IDLE state[152]. It is worth recalling that the feeder link is assumed ideal, then the BS will receive the superposition of all UEs signals as follows:

$$\begin{aligned} y_R(t) = \sum_{k=1}^{N} & x_{UE_k}(t) e^{-j2\pi \widehat{f}_{0d_{kU}}(t)t} h_k(t) \cdot \\ & e^{-j2\pi f_{d_k}(t+\tau_k)t} cos(2\pi f_k t) + n_R(t) \end{aligned} \tag{7.7}$$

Then after down-conversion and filtering out the higher order components:

$$\begin{aligned} y_R(t) &= \left[\sum_{k=1}^{N} x_{UE_k}(t) e^{-j2\pi \widehat{f}_{0d_{kU}}(t)t} h_k(t) \cdot \right. \\ &\quad \left. e^{-j2\pi f_{d_k}(t+\tau_k)t} cos(2\pi f_k t) + n_R(t) \right] e^{j2\pi f_0 t} \\ &\simeq \sum_{k=1}^{N} x_{UE_k}(t) h_k(t) e^{-j2\pi \widehat{f}_{0d_{kU}}(t)t} \cdot \\ &\quad e^{-j2\pi (f_{d_k}(t+\tau_k) + f_{\Delta k})t} + n_R(t) \end{aligned} \tag{7.8}$$

if the UL communication occurs within a sufficiently small time interval (τ_k) after the offset has been estimated on the DL signal, it is possible to assume that $\widehat{f}_{d_k}(t) \simeq f_{d_k}(t + \tau_k) = f_{d_k}$, so almost constant Doppler; then $\widehat{f}_{0d_{kU}}(t) = \widehat{(f_{d_k}(t) - f_{\Delta k})} \approx \widehat{(f_{d_k} - f_{\Delta k})}$. Eventually the BS will receive:

$$y_R(t) = \sum_{k=1}^{N} x_{UE_k}(t) h_k(t) e^{-j2\pi 2 f_{d_k} t} + n_R(t) \tag{7.9}$$

Therefore even if frequency advance technique is effective on removing CFO it cannot compensate the Doppler effect resulting on corrupted data.

On the other hand, the use of the proposed Doppler pre-compensation strategy

would mitigate the undesired differential Doppler if τ_k is sufficiently short to consider the Doppler almost constant. The main idea is to use the offset estimated on the DL channel with opposite sign, in order to compensate the UL signal. In this case, the superposition of all UE signals at the BS, after down-converting and filtering out the higher order components is:

$$\begin{aligned} y_R(t) = &\sum_{k=1}^{N} x_{UE_k}(t) h_k(t) e^{j2\pi \widehat{f}_{0d_kU}(t)t} \cdot \\ &e^{-j2\pi(f_{d_k}(t+\tau_k)+f_{\Delta k})t} + n_R(t) \\ = &\sum_{k=1}^{N} x_{UE_k}(t) h_k(t) e^{-2j2\pi f_{\Delta k} t} + n_R(t) \end{aligned} \tag{7.10}$$

if $\widehat{f}_{d_k}(t) \simeq f_{d_k}(t+\tau_k) = f_{d_k}$. It is worth noting that the pre-compensation is opposite to the frequency advance according to the formulation and, as a consequence, they should be treated separately. As a matter of fact it is not possible to simultaneously compensate both CFO and Doppler variation. Then, the most effective technique, in order to compensate the error which causes the greater signal degradation, should be chosen.

A further improvement of the aforementioned technique consists in the acquisition of two carriers at the UE terminal, exploiting them to recover both the frequency offset due to the non-perfect LO and the one caused by the Doppler shift. Avoiding the complete received signal notation, for the sake of notation simplicity, and focusing only on the frequencies, it is possible to describe the procedure as follow:

$$\begin{cases} f^{(c_1)} = f_k + f_{d_k}^{(c_1)} \\ f^{(c_2)} = (f_k + \Delta f^{(c)}) + f_{d_k}^{(c_2)} \end{cases} \tag{7.11}$$

then:

$$\begin{cases} f^{(c_1)} = f_k + f_0 \frac{\Delta v}{c} \\ f^{(c_2)} = (f_k + \Delta f^{(c)}) + (f_0 + \Delta f^{(c)}) \frac{\Delta v}{c} \end{cases} \tag{7.12}$$

where $f^{(c_1)}$ and $f^{(c_2)}$ represent the estimation of the two carriers, $f_{d_k}^{(c_1)}$ and $f_{d_k}^{(c_2)}$ represent the Doppler effect on the two different carriers and $\Delta f^{(c)}$ is the nominal frequency difference between the two carriers. As already mentioned before, f_k is the oscillator frequency at the terminal side while f_0 is the reference carrier frequency of the system. The only unknown in the equation system (7.12) are f_k and Δv, which can be computed unless an estimation error of the two carriers. After their computation it is possible to use the results in the previously analysed solution for the compensation of both the frequency offset, due to the LO imperfections, and the differential Doppler.

7.3.2.2 Residual Differential Doppler

In this paragraph, an evaluation of the differential Doppler over LEO satellites is shown. The assessment has been performed using an analytical characterization of the Doppler, which can be found in [128]. The aim of this paragraph is to quantify the differential Doppler in worst case conditions and compare the obtained results with the constraints given by NB-IoT. For the purpose of the analysis, the parameters in Table 7.7 were used.

TABLE 7.7: Simulation parameters.

Parameter	Value
Carrier Frequency	2.2 GHz
Satellite altitude range (h_{SAT})	$300, 800, 1200$ km
Orbits	6 circular-polar (30° apart)
Satellites per Orbit	11
Minimum elevation angle	10°
Reference UEs reciprocal distance	$20 - 200$ km

The mathematical formulation for the residual differential Doppler is:

$$\Delta f_{d_k}(t) = \Big(f_{d_k}(t) - f_{d_k}(t+\tau_k)\Big) - \Big(f_{d_1}(t) - f_{d_1}(t+\tau_k)\Big) \tag{7.13}$$

where the index k identifies the target UE while the index 1 is the reference UE for that coverage area. As already mentioned, the Doppler compensation method is efficient if and only if the value of τ_k is sufficiently small. Furthermore it is worth to recall that the common component of the Doppler, which is nothing but the Doppler seen by the reference user in the coverage area, can be compensated by means of a GNSS receiver, according to [23].

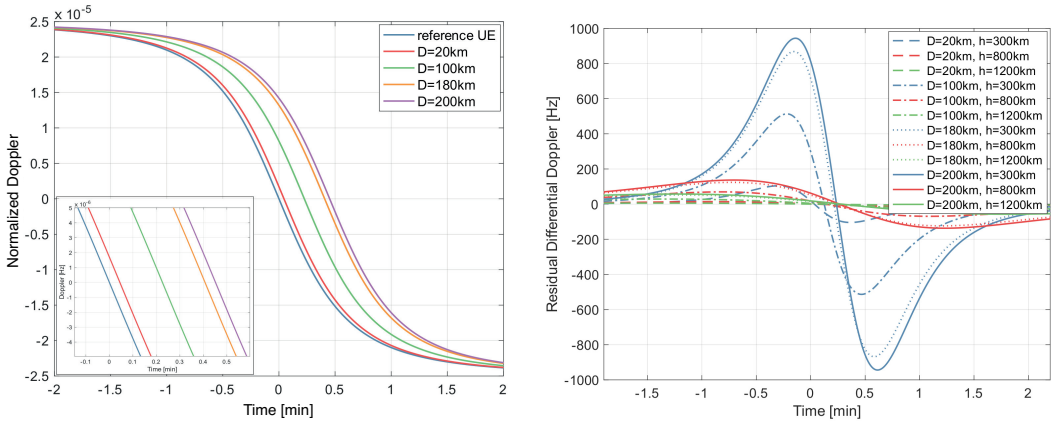

(A) Example of Doppler curves of reference UEs for $h_{SAT} = 300$ km

(B) Residual Differential Doppler

FIGURE 7.12: Doppler Shift and Residual Differential.

In Table 7.8 are reported the simulation results for the maximum allowed values of τ_k, for a satellite altitude value ranging of 300, 800 and 1200 km. The values of each row correspond to the worst case scenario for each value of h_{SAT}, i.e., the maximum inter-UEs distance among UEs in the same coverage area 200 km). Finally the maximum value of τ_k has been computed in order to achieve a residual Doppler lower than the maximum value of Doppler allowed for NB-IoT, as previously discussed. Figure 7.12a shows an example of the normalized Doppler[2] behaviour over time, for two UEs placed at different relative distances (D) within the coverage area, with a reference h_{SAT} of 300 km. The time origin (0 min) coincides with the UE position at the satellite's nadir, when the Doppler experienced by the UE is null. The difference between the curves of two users represents the differential Doppler which is seen by the satellite antenna at each timing instant. This helps to have a better understanding of the residual Doppler depicted in Figure 7.12b. As expected, the higher is the orbit the lower is the differential Doppler. Furthermore it can be noticed that the differential Doppler increases with the relative distance among UEs. Figure 7.12b shows the residual Doppler for a value of $\tau_k = 1337$ ms, which is the worst value acceptable for a subcarrier spacing $\Delta f_{sc} = 15$ kHz and a satellite altitude $h_{SAT} = 300$ km.

TABLE 7.8: Maximum values for τ_k.

h_{SAT}	τ_{MAX} $\Delta f_{sc} = 15$ kHz	τ_{MAX} $\Delta f_{sc} = 3.75$ kHz
300 km	1337 ms	303 ms
800 km	9378 ms	2356 ms
1200 km	22511 ms	5686 ms

Further simulations has been carried on in order to assess the typical value of τ_k for an hypothetic system. For the purpose of the analysis, the parameters in Table 7.7 were used. The three different satellite constellations, with transparent payloads, previously described have been used. Two different GW deployments on ground has been considered in order to analyse two different scenarios. In Scenario 1, $100\,\%$ GW availability is ensured for each satellite for the whole constellation revisit period, so each satellite is always visible from at least one GW. While in Scenario 2, $90\,\%$ GW availability is ensured. Figure 7.13a and 7.13b shows the CDF of τ_k, as the signal propagation delay from UE_k to the GW, for the first and second scenario respectively. It is worth noticing that in Scenario 1 the requirements on the maximum value of τ_k are met for all the UE served by the constellation, while it is not possible to meet the requirements in Scenario 2, where the satellites are not always visible at least from one GW, as shown in Figure 7.13b.

[2]Multiplying by the system frequency, it is possible to derive the value of Doppler shift for any carrier, for a satellite altitude of 300 km.

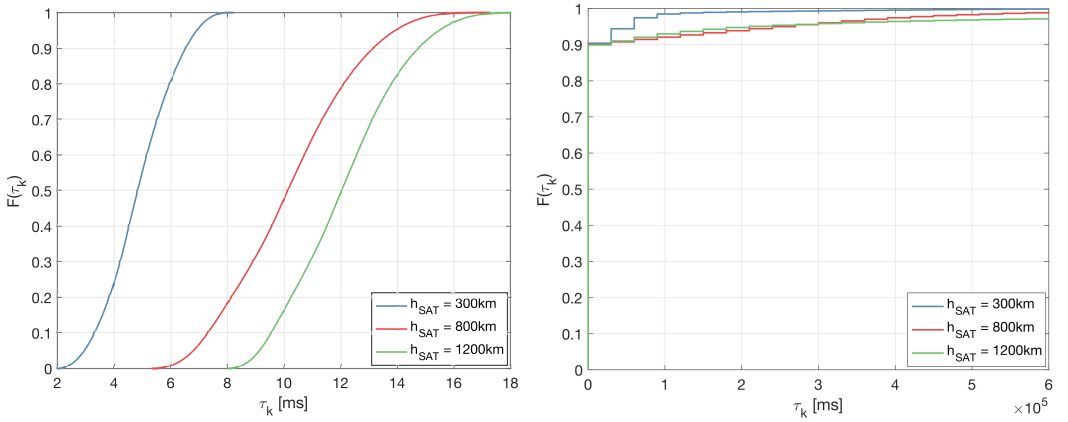

(A) *Scenario 1:* τ_k distribution for 100 % GW availability (B) *Scenario 2:* τ_k distribution for 90 % GW availability

FIGURE 7.13: τ_k distribution.

7.4 Delay related Analysis

The following section is directly derived from the analyses detailed in the author's publication *"Architectures and Key Technical Challenges for 5G Systems Incorporating Satellites"*, [7]. The remainder of the section will focus on delay aspects related the main PHY/MAC NB-IoT procedures.

7.4.1 Timing Advance

TA procedure is used to control uplink signal transmission timing, in order to maintain a perfect alignment among all the transmission from all the UEs served by the same BS. The TA in NB-IoT is performed from the UE assisted by the BS and follow the same steps as legacy LTE. Upon reception of a timing advance command, the UE shall adjust uplink transmission timing for NPUSCH based on the received timing advance command. Like in LTE, the timing advance command indicates the change of the uplink timing relative to the current uplink timing as multiples of $16\,T_s$, where $T_s = 1/(15000 \times 2048)\,s$ is the time unit for LTE. The transmission of the uplink radio frame from the UE shall start $(N_{TA} + N_{TA_{offset}}) \times T_s$ seconds before the start of the corresponding downlink radio frame at the UE. Where N_{TA} is the timing offset between uplink and downlink radio frames at the UE, expressed in T_s units, and it is define as $N_{TA} = T_A \times 16$. The timing advance command, T_A, is given by the BS to the UE in order to properly perform the time adjustment. If the timing advance command reception ends in the downlink subframe n the uplink transmission timing adjustment should be applied from the first available NB-IoT uplink slot following the end of $n + 12$ downlink subframe and the first available NB-IoT uplink slot for NPUSCH transmission. This leads to the conclusion that it is possible to compensate a time misalignment among UEs for the uplink transmission, up to a maximum of

0.67 ms for NB-IoT, which is also the maximum supported value for TA in legacy LTE[3], [144], [145], [150].

TABLE 7.9: Simulation parameters.

Parameter	Value
Carrier Frequency	2.2 GHz
Sat Altitude	$600 - 1500$ km
Elevation Angle	$90°$
Minimum Elevation Angle	$10°$
Reference UEs reciprocal distance	$40 - 200$ km

Let us consider the scenario depicted in Figure 7.11 but with different satellite altitudes and fixed relative distances among users in the satellite footprint, as described in Table 7.9. In the reference scenario, the maximum allowed TA must correspond to the maximum difference of the propagation delay of signals between UEs and Sat, *i.e.* in the worst case the propagation delay difference of the signals of the users at the edge of the footprint should be under the maximum allowed value for TA. In Section 6.1 it has been already defined the concept of differential propagation delay (ΔT_{pd}) as the difference between the propagation delay experienced by two different UEs in the footprint, with respect to the satellite. All the common components of the propagation delay could be in fact pre-compensated thus neglected, as far as the UE is equipped with a GNSS receiver and the ephemeris of the satellite. As a matter of fact, if $\Delta T_{pd} < 0.6667$ ms for the worst case scenario (*i.e*, one of the reference UEs in the edge of the footprint and the other one at the nadir of the satellite), no modifications to the TA are needed. Figure 7.14 shows the simulation results. The zero in the time axis corresponds to the maximum elevation angle (*e.g.*, $90°$). Specifically it has emerged that, according to the satellite altitude (h_{SAT}) and maximum UEs distance (D), there is a time window for which ΔT_{pd} is lower than the maximum TA allowed by the protocol. Performing the transmission inside this time window does not require modification to the standard. Adding a time offset which takes into account the propagation delay of the satellite channel, depending on geographical positions of UEs and Sat, could be an alternative solution to overcome the limitation of the TA command.

7.4.2 HARQ

The HARQ procedure for NB-IoT is similar to the one in LTE, however to enable low-complexity UE implementation, NB-IoT allows only up to 2 HARQ process, rather then 8 parallel process of LTE, in both DL and UL, and allows longer UE decoding time for both NPDCCH and Narrowband Physical Downlink Shared Channel

[3]This analysis is one of the outcome of the paper *"Architectures and Key Technical Challenges for 5G Systems Incorporating Satellites"*, [7], which did not take into account the new available Format 2 for NB-IoT. The latter bring the duration of the CP, thus the maximum value for the TA, up to 0.8 ms.

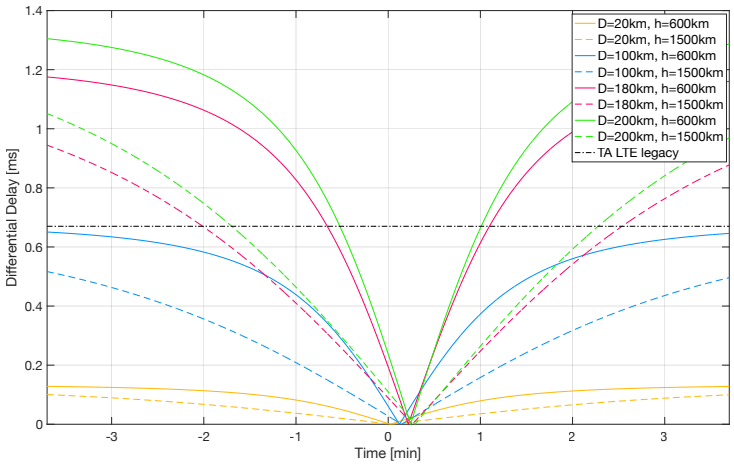

FIGURE 7.14: TA analyses.

(NPDSCH), [145]. An asynchronous, adaptive HARQ procedure is adopted to support scheduling flexibility. In order to schedule downlink data or uplink data the BS conveys a scheduling command through a Downlink Control Indicator (DCI), carried by NPDCCH. DCI could be repeated in order to achieve further coverage enhancement. Repetitions are sent in contiguous subframes and each repetition occupies one subframe. For what concern the downlink, in order to cope with the reduced computing capabilities of NB-IoT devices, the time offset between NPDCCH and the associated NPDSCH is at least 4 ms, instead to schedule the latter in the same Transmission Time Interval (TTI) as it is for legacy LTE [145]. After receiving NPDSCH, the UE needs to send back a HARQ acknowledgment using NPUSCH Format 2, which is scheduled at least 12 ms after receiving NPDSCH, for the sake of reduced complexity constraints. Similarly, for the uplink the time offset between the end of NPDCCH and the beginning of the associated NPUSCH is at least 8 ms [145]. After completing the NPUSCH transmission, the UE does not expect the reception of the associated HARQ acknowledgment before $3\,ms$ [145].

These relaxed time constraints allow ample decoding time for the UE. The resources to be allocated, as well as the precise time offsets are indicated in the DCI. In LTE a HARQ process is associated with a Transport Block (TB) in a given TTI. Due to the multiple retransmissions for the coverage enhancement, the HARQ entity in NB-IoT invokes the same HARQ process for each retransmission that is part of the same bundle. Within a bundle the retransmissions are non-adaptive and are triggered without waiting for feedback from previous transmissions according to the maximum number of repetitions established for that coverage level. A downlink assignment or an uplink grant, for downlink and uplink HARQ operations respectively, corresponding to a new transmission or a retransmission of the bundle, is received after the last repetition of the bundle. If a NACK is received and a retransmission is required, then the whole bundle is retransmitted [140], [145], [149], [150].

The HARQ protocol is used in message 3 and message 4 of the RA procedure previously described, and it is directly impacts the overall delay of the RA procedure,

since it doubles the number of messages exchanged by the UE and BS for the last two steps. Clearly, the higher the Round Trip Delay (RTD), the slower the RA procedure would be. Taking into account the characteristic delays for a satellite channel depicted in Table 7.10, it is immediate to understand that the rate in which the RA procedure slows down is much higher with respect to the terrestrial case. Thus alternative solutions should be considered, like disabling the HARQ protocol when the channel quality (*e.g.*, SINR) is sufficiently good to ensure a reliable communication even without HARQ.

TABLE 7.10: One-Way Propagation delay and RTT for the considered scenarios.

Scenario	One-Way [ms]	RTT [ms]
$h_{SAT} = 600$ km	≈ 14.2	≈ 28.4
$h_{SAT} = 1500$ km	≈ 25.83	≈ 51.66

7.4.3 CP Length and RA procedure Timers

For what concern the CP, an analysis similar to the one for the TA could be done. Notably if the misalignment among preambles sent in Msg1 is greater than the CP duration, T_{cp}, then the synchronization is lost because of the OFDM and SC-FDMA intrinsic properties. As a matter of fact, if $\Delta T_{pd} < T_{cp}$ no modifications to the CP are needed, as far as all the common components of the propagation delay are pre-compensated, thus negligible, by means of a GNSS receiver and the ephemeris knowledge at the UE side. Otherwise longer CPs are required for the RA procedure.

As for the RAR time windows and Contention Resolution timers, they have been extended up to 10.24 s, as previously mentioned, allowing to cope with the characteristic delay of the satellite channel; thus, no modifications are required.

7.5 IoT Services over GNSS

The following section is directly derived from the outcomes of the author's publication *"Galileo Second Generation: Two-Way Messaging for IoT"*, [76]. In the previous sections the analyses and results related to the the feasibility of NB-IoT implementation over SatCom systems have been shown. However, as already mentioned in Chapter 1, GNSS systems with their ubiquitous, continuous, and highly reliable coverage could represent an efficient integration to the satellite communication systems in serving the IoT use cases. On the basis of the previous considerations, in this section a Two-Way Messaging feature for the G2G satellite constellation is proposed. It can serve the IoT use cases by exploiting the full coverage provided by the Galileo infrastructure. To this aim, in the following the system model and the simulation

methodologies will be described, then the performance of the proposed service in terms of Goodput[4] and PLR, obtained by numerical simulation, are detailed.

7.5.1 System Architecture

With reference to Figure 7.15, the main elements of the high-level system architecture are: *i*) a UT, which is an IoT terminal, fixed or mobile; *ii*) a G2G payload satellite, providing connectivity to the UT through the user link; *iii*) a Ground Segment GW interconnected to the flying platform through the feeder link; *iv*) the Packet Core Network.

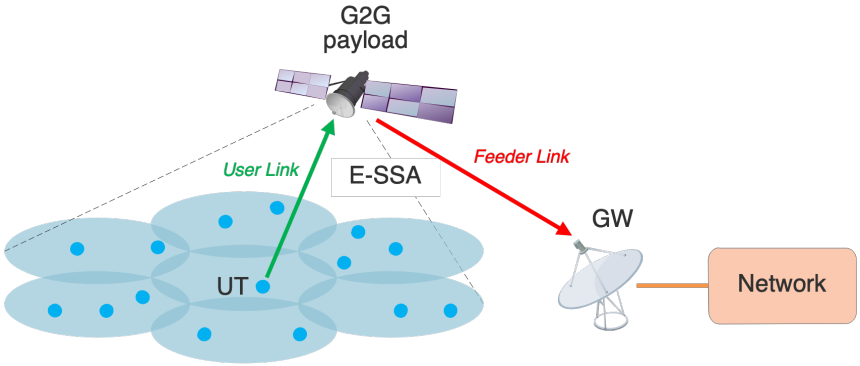

FIGURE 7.15: High-level system architecture.

The UTs are assumed to be low-complexity low-power machine-type devices, with small omnidirectional antennas, that can be deployed everywhere on ground and sea (*e.g.*, remote areas, forest, deserts, and oceans), enabling a wide range of applications characterized by the transmission of sporadic small data packets.

As for the satellite segment, Galileo comprises a total of 30 satellites placed in MEO which ensure continuous global coverage. The active constellation is composed of 24 satellites (Walker 24/3/1), including 6 spare ones, which can be moved to replace any failed satellite within the same plane, thereby reducing the impact of failures upon quality of service [159]. The detailed parameters considered for the satellite constellation are shown in Tab. 7.11. Concerning the payload characteristics, an additional on-board processor and dedicated antennas could be envisioned for the forthcoming G2G satellites, in order to fulfill the requirements for the two-way messaging services. A helix antenna with circular polarisation, common for GNSS applications [160], has been considered for this work. The numerical results are computed considering two different antenna patterns for the user link: *i*) a single-beam scenario, characterized by lower complexity and capacity; *ii*) a multi-beam scenario (7 beams per antenna), characterized by larger complexity and capacity. The antenna patterns have been designed by the means of SATSOFT software by Ticra [132]. A Gaussian beam model has been chosen for both single- and multi-beam antenna patterns.

[4]The term Goodput describes the achievable throughput of the system considering only the useful data bit transmitted, without considering any overhead.

TABLE 7.11: Satellite Constellation Parameters.

Parameter	Value
Constellation type	Walker 24/3/1
Altitude	23222 km (MEO)
Number of planes	3
Planes inclination	56°
Satellites per plane	10
Active satellites	24
N_{beam}: beams per satellite	1 (S-B), 7 (M-B)

Finally the Ground Segment is composed of GWs deployed such to guarantee uninterrupted connection to the core network to all the satellites in the constellation.

This work focuses on the return link, with particular attention on the RA performance for the user link, identifying E-SSA as a suitable Air Interface for serving the IoT scenario [60]. As for the forward link, it is used for the channel quality estimation purposes, *i.e.*, for a proper MCS and SF selection for the uplink transmissions, and for control messages transmission. However the analysis of the forward link is outside of the scope of this work and it is left for future studies.

7.5.1.1 Data Traffic

The UT is assumed to perform a purely asynchronous transmission. The packets generation process is modelled as a Poisson RV ($\mathcal{X}_i \sim Poisson(\lambda_i)$), with probability mass function (pmf):

$$\mathcal{P}_{\lambda_i}(x) = \frac{\lambda_i}{x!} e^{-\lambda_i} \tag{7.14}$$

where the rate parameter λ_i is the average number of packets generated in a time interval by the i-th UT. The values of λ_i for each UT are computed starting from the system design requirement on the *total requested traffic*, $\mathcal{A}_{sys}$, expressed in $kbps$. Given the number of UTs in the system, N_{ut}, and $\mathcal{A}_{sys}$, it is possible to derive the average *daily data volume* per UT as: $\mathcal{B}_{ut} = (\mathcal{A}_{sys}/N_{ut}) \cdot 3600 \cdot 24$. Then, given the packet size, P_{size}, (expressed in bit), it is possible to derive λ_i for Eq. 7.14 as: $\lambda_i = (\mathcal{B}_{ut} \cdot 10^3)/P_{size}$. It is worth recalling that the sum of independent Poisson RVs is still a Poisson RV ($\sum_{i=1}^{N_{ut}} \mathcal{X}_i \sim Poisson(\sum_{i=1}^{N_{ut}} \lambda_i)$), thus follows that: $\lambda_{sys} = \sum_{i=1}^{N_{ut}} \lambda_i$. Finally it is known that the sequence of inter-arrival times is described by the Exponential distribution, thus can be modelled as an exponential RV with pdf:

$$\mathcal{P}_{\mu}(x) = \begin{cases} \frac{1}{\mu} e^{-\frac{x}{\mu}}, & \text{if } x \geq 0 \\ 0, & \text{otherwise} \end{cases} \tag{7.15}$$

where μ is the reciprocal of the rate parameter λ previously described. Given $\mu = 1/\lambda_{sys}$, it is possible to compute the inter-arrival times for the packets generated in

TABLE 7.12: LB Parameters (Uplink: UT-to-SAT).

Parameter	Value
P_{TX}: transmission power [dBm]	27 (S-B), 17 (M-B)
G_{TX}: transmission gain (omni) [dBi]	5
G_{RX}^{max}: maximum receiving gain [dBi]	17.74 (S-B), 27.7 (M-B)
θ_{3dB}: HPBW [deg]	25 (S-B), 6 (M-B)
σ: shadowing variance [dB]	1
N_f: satellite noise figure [dB]	2
T_0: reference temperature [K]	290
T_A: antenna temperature [K]	400

the system by the means of Eq. 7.15, thus derive the timestamps of the actual traffic in the system.

7.5.2 Numerical Results

ESiM2M has been used in order to perform the KPI analyses. In particular in the time-driven simulation, the satellite constellation geometry, the LB, the stochastic shadow fading, as well as the interference due to the generated traffic conditions, vary at each simulation step. The value chosen for the simulation steps is 300 s, for a total simulation duration of 14 h, such to take into account for a complete satellite revisit period, *i.e.*, the period of time required such to have the satellite in the same position. Due to the slow changes in the satellite footprint on ground, because of the high altitude of satellites (MEO), a shorter simulation step is unnecessary. For what concern the users, 65 000 UTs have been uniformly distributed on a regular *lat-lon* grid.

After the computation of the satellite-UTs geometry, based on the mathematical formulation shown in Section 3.6, the UL LB has been computed, as described in Section 6.2.3, for all the UTs, using the parameters shown in Table 7.12. In particular, in order to perform the SNR and SINR computations, for each constellation geometry, the UTs are assigned to the best satellite/beam pair according to their LB, *i.e.*, the highest value of SNR is chosen for each UT such to identify the best serving satellite/beam pair for that simulation step. An example of global coverage, showing the SNR for single- and multi-beam patterns respectively, are depicted in Figures 7.16 and 7.17. Then the packets generation and transmission is performed as described in the previous section.

The last step is the most computationally demanding: collision detection, interference assessment, and decoding emulation for E-SSA are executed. An independent decoder is modelled for each beam in the system, then a packet is considered as a *useful* one only for the best serving satellite/beam pair, while it is considered as *interference* for all the other beams capturing it. Simulating the actual PHY links between multiple UTs and satellites, then the actual decoding process for each packet,

would be computationally prohibitive. Then the decoding process has been modelled using a PHY abstraction based on RBIR ESM abstraction method, described in Chapter 5.

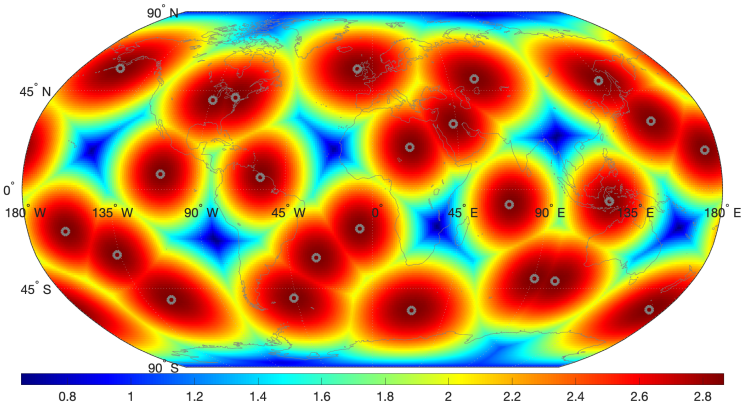

FIGURE 7.16: Constellation coverage (SNR in dB for the single-beam scenario).

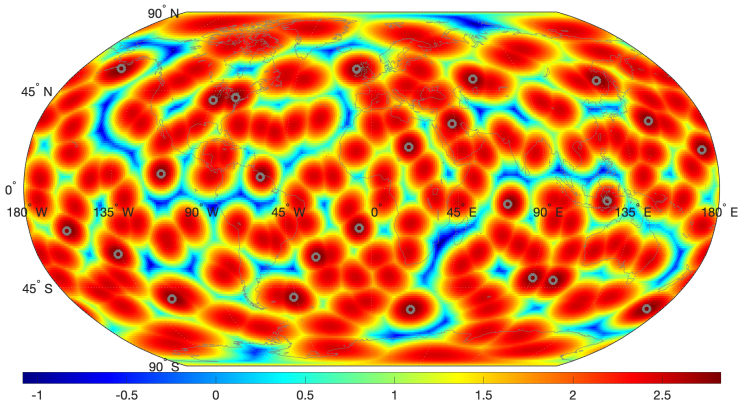

FIGURE 7.17: Constellation coverage (SNR in dB for the multi-beam scenario).

In both single- and multi-beam scenarios, each point on Earth sees at least one satellite at an elevation angle greater than $40°$. Therefore the satellite antenna has a small scan angle covering only within $\pm 9°$ of its FOV. The multi-beam pattern will be characterized by a smaller beam-width with respect to the single-beam pattern. It follows that the UT can have a small patch antenna covering only above $40°$ elevation.

For what concern the single-beam scenario, three different traffic profiles, with different systems loads have been chosen: *i*) *scenario 1* with 1 600 messages of 100 bits per day; *ii*) *scenario 2* with 2 400 messages of 100 bits per day; and *iii*) *scenario 3* with 3 200 messages of 100 bits per day. One million packets are simulated at each iteration, thus the traffic is generated computing the appropriate values of λ. The E-SSA packet duration depends on the bandwidth, SF, packet size, modulation, and coding rate. These parameters have been chosen according to the characteristics of

TABLE 7.13: Air Interface Parameters (E-SSA).

Parameter	Value
f_c: carrier frequency [MHz]	868
B: system bandwidth [kHz]	100
SF: spreading factor	16
Modulation	BPSK
Packet size	100 bit
r: coding rate	$1/3$

similar air interfaces adopted for IoT applications (*e.g.*, LoRa, and SigFox), using a small bandwidth and reduced packet size. All the values are shown in Tab. 7.13. It is worth highlighting that in this work, we consider the European Industrial, Scientific and Medical (ISM) frequency band at 868 MHz, however additional frequencies could be allocated for two-way messaging services in G2G.

The PHY abstraction is performed such to compute the actual effect of the interference over each transmitted packet. PLR and Goodput are then collected for every simulation step. While the PLR directly depends on the un-decoded packets, the Goodput is computed accounting for the amount of information bits of the decoded packets. It is worth highlighting that the number of users simulated is not representative of the actual number of users supported, but just of the total traffic volume. A population of only 65 000 UTs has been chosen in order to reduce the computational load of the simulations, thus the results are valid for instance for 1 million users (globally) sending between 100 and 200 messages per day, or 10 million users sending between 10 and 20 messages per day. Fig. 7.18a shows that a quasi error free transmission can be achieved in the single-beam scenario with a network load of 160 kbit/day per UT, enabling an almost constant Goodput $\geq$ 120 kbps per UT as shown in Fig. 7.18b.

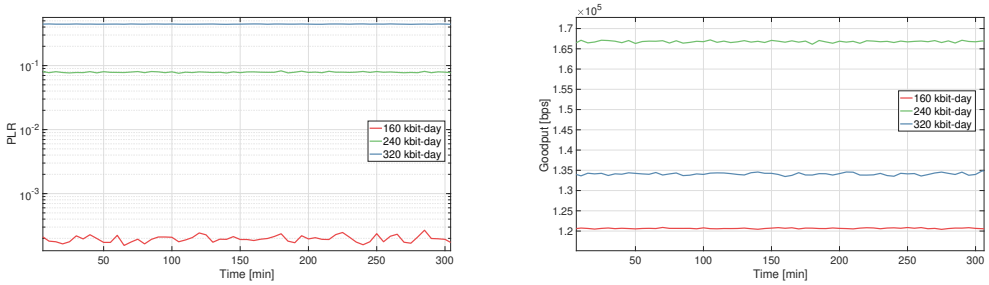

(A) System PLR (B) System Goodput

FIGURE 7.18: PLR and Goodput single-beam scenario.

The same analysis has been carried for the multi-beam scenario, but defining three different traffic profiles: *i*) *scenario 1* with 5 600 messages of 100 bits per day; *ii*) *scenario 2* with 11 200 messages of 100 bits per day; and *iii*) *scenario 3* with 22 400 messages of 100 bits per day. In this case, as shown in Fig. 7.19a, a quasi error free transmission can be achieved with a network load of 560 kbit/day per UT, enabling

an almost constant Goodput $\geq$ 400 kbps per UT as shown in Fig. 7.19b. As previously said, even if the simulations were carried for a population of 65 000 UTs having 100 kHz band available, the outcomes can be extended to a more general case. Notably due to the utilization of 7 beams, it is fair to say that the same performance can be achieved with a global traffic request of 10 messages a day from 7 million UTs on earth.

Figures 7.18, and 7.19, show only 2 of 14 hours of simulation, but due to the uniform distribution of UTs it is enough for the understanding of the behaviour of the system. It is worth mentioning that each simulation step represents a sufficient statistic for a specific satellite constellation geometry. Indeed simulating 1 million packets per iteration it is possible to have a complete understanding of the interference experienced by the packets.

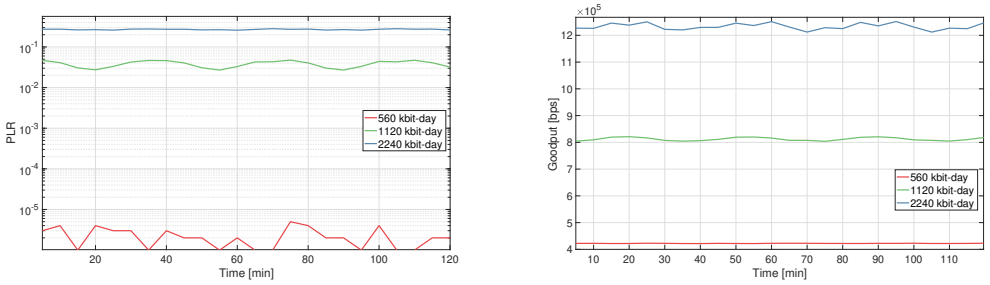

(A) System PLR (B) System Goodput

FIGURE 7.19: PLR and Goodput multi-beam scenario.

It has been shown that promising performance for IoT data transmission can be achieved in terms of PLR and Goodput, for both single- and multi-beam scenarios, making an IoT application a suitable service to be supported by the G2G satellite constellation. It is worth highlighting that the design of G2G satellite system is currently under study, so future works will target the evolution of this process, studying the performances with different payload architectures and different air interfaces.

Chapter 8

Conclusions

This thesis dealt with the feasibility and performance study of IoT applications over SatCom systems. After analysing all the pivotal aspects of a complex SatCom system, the main requirements for the realization of MTC/mMTC applications over satellite systems have beed thoroughly examined.

Given the lack of a software tool which allows to realize system-level performance evaluations for the aforementioned scenario, a complete MATLAB®based tool has been realized for this purpose. All the high-level characteristics of the ESiM2M tool have been highlighted and a deep analysis of the mathematical framework behind the main software modules have been discussed; focusing in particular on the link budget computation, on the Doppler and delay characterization, as well as on the PHY abstraction methodologies adopted.

Exploiting this tool manifold analyses have been performed:

- The effects of RTT on the NB-IoT timers and procedures have been analysed and possible solutions exploiting precompensation by means of GNSS and differential delay have been proposed.
- The problems arising in NB-IoT RA procedures due to the high Doppler effects in LEO applications have been identified and a solution for Doppler shift compensation, based on frequency advance technique, has been proposed.
- The high path loss characteristic for SatCom applications has been analysed proposing some interesting outcomes for the link budget analysis related to the 3GPP standardisation process for NB-IoT over NTN.
- Finally a two-way messaging side service for the G2G constellation, for serving the mMTC use case has been proposed.

Bibliography

[1] G. Maral, M. Bousquet, and Z. Sun, *Satellite Communications Systems: Systems, Techniques and Technology*, Sixth edition. Hoboken, N.J: John Wiley & Sons, 2020, 1 p., ISBN: 978-1-119-38212-6 978-1-119-38207-2.

[2] (). "SpaceX submits paperwork for 30,000 more Starlink satellites," SpaceNews, [Online]. Available: https://dev.spacenews.com/spacex-submits-paperwork-for-30000-more-starlink-satellites/ (visited on 11/16/2020).

[3] (). "SES and Thales Reach Record Speed and Enhanced Coverage via Integrated GEO/MEO Network, Raise Bar for Inflight Connectivity | Thales Group," [Online]. Available: https://www.thalesgroup.com/en/group/journalist/press-release/ses-and-thales-reach-record-speed-and-enhanced-coverage-integrated (visited on 11/16/2020).

[4] (). "European Data Relay Satellite System (EDRS) Overview | ESA's ARTES Programmes," [Online]. Available: https://artes.esa.int/edrs/overview (visited on 11/16/2020).

[5] O. Kodheli, E. Lagunas, N. Maturo, S. K. Sharma, B. Shankar, J. F. M. Montoya, J. C. M. Duncan, D. Spano, S. Chatzinotas, S. Kisseleff, J. Querol, L. Lei, T. X. Vu, and G. Goussetis. (Mar. 2, 2020). "Satellite Communications in the New Space Era: A Survey and Future Challenges." arXiv: 2002.08811 [eess], [Online]. Available: http://arxiv.org/abs/2002.08811 (visited on 11/16/2020).

[6] A. Guidotti, A. Vanelli-Coralli, M. Conti, S. Andrenacci, S. Chatzinotas, N. Maturo, B. Evans, A. Awoseyila, A. Ugolini, T. Foggi, L. Gaudio, N. Alagha, and S. Cioni, "Architectures and Key Technical Challenges for 5G Systems Incorporating Satellites," *IEEE Transactions on Vehicular Technology*, vol. 68, no. 3, pp. 2624–2639, Mar. 2019, ISSN: 0018-9545, 1939-9359. DOI: 10.1109/TVT.2019.2895263.

[7] A. Guidotti, S. Cioni, G. Colavolpe, M. Conti, T. Foggi, A. Mengali, G. Montorsi, A. Piemontese, and A. Vanelli-Coralli, "Architectures, standardisation, and procedures for 5G Satellite Communications: A survey," *Computer Networks*, vol. 183, p. 107 588, Dec. 2020, ISSN: 13891286. DOI: 10.1016/j.comnet.2020.107588. [Online]. Available: https://linkinghub.elsevier.com/retrieve/pii/S138912862031224X (visited on 11/29/2020).

[8] 5GPPP. (Mar. 2016). "5G innovations for new business opportunities," [Online]. Available: https://5g-ppp.eu/wp-content/uploads/2017/03/5GPPP-brochure-final-web-MWC.pdf (visited on 05/14/2020).

[9] ——, (Feb. 2016). "5G empowering vertical industries," [Online]. Available: https://5g-ppp.eu/wp-content/uploads/2016/02/5PPP-FLYER_BAT_PL-.pdf (visited on 05/14/2020).

[10] 3GPP, "TR38.913, Technical Specification Group Radio Access Network;Study on Scenarios and Requirements for Next Generation Access Technologies; (Release 15), V15.0.0," Technical Report, Jun. 2018.

[11] ——, "TR38.821, Technical Specification Group Radio Access Network; Solutions for NR to support non-terrestrial networks (NTN) (Release 16), V16.0.0," Technical Report, Dec. 2019.

[12] ——, "TR38.811, Technical Specification Group Radio Access Network; Study on New Radio (NR) to support non-terrestrial networks (Release 15), V15.3.0," Technical Report, Jul. 2020.

[13] (). "SaT5G Project," Sat 5G, [Online]. Available: https://www.sat5g-project.eu/ (visited on 12/21/2020).

[14] (). "SATis5 Demonstrator for Satellite-Terrestrial Integration in the 5G Context | ESA's ARTES Programmes," [Online]. Available: https://artes.esa.int/projects/satis5-0 (visited on 12/21/2020).

[15] (). "5G-VINNI – 5G Verticals Innovation Infrastructure," [Online]. Available: https://www.5g-vinni.eu/ (visited on 12/21/2020).

[16] (). "5GENESIS – 5th Generation End-to-end Network, Experimentation, System Integration, and Showcasing," [Online]. Available: https://5genesis.eu/ (visited on 12/21/2020).

[17] (). "CLOUDSAT Scenarios for integration of satellite components in future networks | ESA's ARTES Programmes," [Online]. Available: https://artes.esa.int/projects/cloudsat (visited on 12/21/2020).

[18] (). "VIrtualized hybrid satellite-TerrestriAl systems for resilient and fLexible future networks | VITAL Project | H2020 | CORDIS | European Commission," [Online]. Available: https://cordis.europa.eu/project/id/644843/it (visited on 12/21/2020).

[19] (). "Home - SANSA - Horizon 2020 Project 2016," [Online]. Available: https://sansa-h2020.eu/ (visited on 12/21/2020).

[20] F. Bastia, C. Bersani, E. A. Candreva, S. Cioni, G. E. Corazza, M. Neri, C. Palestini, M. Papaleo, S. Rosati, and A. Vanelli-Coralli, "LTE Adaptation for Mobile Broadband Satellite Networks," *J Wireless Com Network*, vol. 2009, no. 1,

p. 989 062, Dec. 2009, ISSN: 1687-1499. DOI: 10.1155/2009/989062. [Online]. Available: https://jwcn-eurasipjournals.springeropen.com/articles/10.1155/2009/989062 (visited on 12/21/2020).

[21] G. Araniti, M. Condoluci, and A. Petrolino, "Efficient resource allocation for multicast transmissions in Satellite-LTE networks," in *2013 IEEE Global Communications Conference (GLOBECOM)*, Atlanta, GA: IEEE, Dec. 2013, pp. 3023–3028, ISBN: 978-1-4799-1353-4. DOI: 10.1109/GLOCOM.2013.6831535. [Online]. Available: http://ieeexplore.ieee.org/document/6831535/ (visited on 12/21/2020).

[22] M. Amadeo, G. Araniti, A. Iera, and A. Molinaro, "A Satellite-LTE Network with Delay-Tolerant Capabilities: Design and Performance Evaluation," in *2011 IEEE Vehicular Technology Conference (VTC Fall)*, San Francisco, CA, USA: IEEE, Sep. 2011, pp. 1–5, ISBN: 978-1-4244-8327-3 978-1-4244-8328-0 978-1-4244-8325-9 978-1-4244-8326-6. DOI: 10.1109/VETECF.2011.6093140. [Online]. Available: http://ieeexplore.ieee.org/document/6093140/ (visited on 12/21/2020).

[23] A. Guidotti, A. Vanelli-Coralli, M. Caus, J. Bas, G. Colavolpe, T. Foggi, S. Cioni, A. Modenini, and D. Tarchi, "Satellite-enabled LTE systems in LEO constellations," in *2017 IEEE International Conference on Communications Workshops (ICC Workshops)*, Paris, France: IEEE, May 2017, pp. 876–881, ISBN: 978-1-5090-1525-2. DOI: 10.1109/ICCW.2017.7962769. [Online]. Available: http://ieeexplore.ieee.org/document/7962769/ (visited on 02/23/2020).

[24] A. Guidotti, A. Vanelli-Coralli, T. Foggi, G. Colavolpe, M. Caus, J. Bas, S. Cioni, and A. Modenini, "LTE based satellite communications in LEO mega constellations," *Int J Satell Commun Network*, vol. 37, no. 4, pp. 316–330, Jul. 2019, ISSN: 1542-0973, 1542-0981. DOI: 10.1002/sat.1258. [Online]. Available: https://onlinelibrary.wiley.com/doi/abs/10.1002/sat.1258 (visited on 02/23/2020).

[25] A. Guidotti, "Beam Size Design for New Radio Satellite Communications Systems," *IEEE Trans. Veh. Technol.*, vol. 68, no. 11, pp. 11 379–11 383, Nov. 2019, ISSN: 0018-9545, 1939-9359. DOI: 10.1109/TVT.2019.2944242. [Online]. Available: https://ieeexplore.ieee.org/document/8851287/ (visited on 05/20/2020).

[26] O. Kodheli, A. Guidotti, and A. Vanelli-Coralli, "Integration of Satellites in 5G through LEO Constellations," in *GLOBECOM 2017 - 2017 IEEE Global Communications Conference*, Singapore: IEEE, Dec. 2017, pp. 1–6, ISBN: 978-1-5090-5019-2. DOI: 10.1109/GLOCOM.2017.8255103. [Online]. Available: http://ieeexplore.ieee.org/document/8255103/ (visited on 05/20/2020).

[27] A. Jayaprakash, H. Chen, P. Xiao, B. G. Evans, Y. Zhang, J. Y. Li, and A. B. Awoseyila, "Analysis of Candidate Waveforms for Integrated Satellite-Terrestrial 5G Systems," in *2019 IEEE 2nd 5G World Forum (5GWF)*, Dresden, Germany: IEEE, Sep. 2019, pp. 636–641, ISBN: 978-1-72813-627-1. DOI: 10.1109/5GWF.2019.8911721. [Online]. Available: https://ieeexplore.ieee.org/document/8911721/ (visited on 12/21/2020).

[28] C. Ge, N. Wang, I. Selinis, J. Cahill, M. Kavanagh, K. Liolis, C. Politis, J. Nunes, B. Evans, Y. Rahulan, N. Nouvel, M. Boutin, J. Desmauts, F. Arnal, S. Watts, and G. Poziopoulou, "QoE-Assured Live Streaming via Satellite Backhaul in 5G Networks," *IEEE Trans. on Broadcast.*, vol. 65, no. 2, pp. 381–391, Jun. 2019, ISSN: 0018-9316, 1557-9611. DOI: 10.1109/TBC.2019.2901397. [Online]. Available: https://ieeexplore.ieee.org/document/8666159/ (visited on 12/21/2020).

[29] G. Araniti, I. Bisio, M. De Sanctis, A. Orsino, and J. Cosmas, "Multimedia Content Delivery for Emerging 5G-Satellite Networks," *IEEE Trans. on Broadcast.*, vol. 62, no. 1, pp. 10–23, Mar. 2016, ISSN: 0018-9316, 1557-9611. DOI: 10.1109/TBC.2015.2511625. [Online]. Available: http://ieeexplore.ieee.org/document/7383263/ (visited on 12/21/2020).

[30] O. Kodheli, S. Andrenacci, N. Maturo, S. Chatzinotas, and F. Zimmer, "An Uplink UE Group-Based Scheduling Technique for 5G mMTC Systems Over LEO Satellite," *IEEE Access*, vol. 7, pp. 67 413–67 427, 2019, ISSN: 2169-3536. DOI: 10.1109/ACCESS.2019.2918581.

[31] "Energy efficient hybrid satellite terrestrial 5G networks with software defined features," *J. Commun. Netw.*, vol. 19, no. 2, pp. 147–161, Apr. 2017, ISSN: 1229-2370, 1976-5541. DOI: 10.1109/JCN.2017.000024. [Online]. Available: https://ieeexplore.ieee.org/document/7919304/ (visited on 12/21/2020).

[32] E. Lagunas, C. G. Tsinos, S. K. Sharma, and S. Chatzinotas, "5G Cellular and Fixed Satellite Service Spectrum Coexistence in C-Band," *IEEE Access*, vol. 8, pp. 72 078–72 094, 2020, ISSN: 2169-3536. DOI: 10.1109/ACCESS.2020.2985012. [Online]. Available: https://ieeexplore.ieee.org/document/9052737/ (visited on 12/21/2020).

[33] F. Babich, M. Comisso, A. Cuttin, M. Marchese, and F. Patrone, "Nanosatellite-5G Integration in the Millimeter Wave Domain: A Full Top-Down Approach," *IEEE Trans. on Mobile Comput.*, vol. 19, no. 2, pp. 390–404, Feb. 1, 2020, ISSN: 1536-1233, 1558-0660, 2161-9875. DOI: 10.1109/TMC.2019.2897091. [Online]. Available: https://ieeexplore.ieee.org/document/8632762/ (visited on 12/21/2020).

[34] X. Yan, K. An, T. Liang, G. Zheng, Z. Ding, S. Chatzinotas, and Y. Liu, "The Application of Power-Domain Non-Orthogonal Multiple Access in Satellite

Communication Networks," *IEEE Access*, vol. 7, pp. 63 531–63 539, 2019, ISSN: 2169-3536. DOI: 10.1109/ACCESS.2019.2917060. [Online]. Available: https://ieeexplore.ieee.org/document/8715508/ (visited on 12/21/2020).

[35] F. Tang, L. Chen, X. Li, L. T. Yang, and L. Fu, "Intelligent Spectrum Assignment Based on Dynamical Cooperation for 5G-Satellite Integrated Networks," *IEEE Trans. Cogn. Commun. Netw.*, vol. 6, no. 2, pp. 523–533, Jun. 2020, ISSN: 2332-7731, 2372-2045. DOI: 10.1109/TCCN.2020.2988480. [Online]. Available: https://ieeexplore.ieee.org/document/9070215/ (visited on 12/21/2020).

[36] R. K. Saha, "Spectrum Sharing in Satellite-Mobile Multisystem Using 3D In-Building Small Cells for High Spectral and Energy Efficiencies in 5G and Beyond Era," *IEEE Access*, vol. 7, pp. 43 846–43 868, 2019, ISSN: 2169-3536. DOI: 10.1109/ACCESS.2019.2908203. [Online]. Available: https://ieeexplore.ieee.org/document/8676283/ (visited on 12/21/2020).

[37] L. Zhen, T. Sun, G. Lu, K. Yu, and R. Ding, "Preamble Design and Detection for 5G Enabled Satellite Random Access," *IEEE Access*, vol. 8, pp. 49 873–49 884, 2020, ISSN: 2169-3536. DOI: 10.1109/ACCESS.2020.2979871. [Online]. Available: https://ieeexplore.ieee.org/document/9031386/ (visited on 12/21/2020).

[38] M. Caus, A. I. Perez-Neira, J. Bas, and L. Blanco, "New Satellite Random Access Preamble Design Based on Pruned DFT-Spread FBMC," *IEEE Trans. Commun.*, vol. 68, no. 7, pp. 4592–4604, Jul. 2020, ISSN: 0090-6778, 1558-0857. DOI: 10.1109/TCOMM.2020.2985977. [Online]. Available: https://ieeexplore.ieee.org/document/9057636/ (visited on 12/21/2020).

[39] A. Guidotti, A. Vanelli-Coralli, A. Mengali, and S. Cioni, "Non-Terrestrial Networks: Link Budget Analysis," in *ICC 2020 - 2020 IEEE International Conference on Communications (ICC)*, Jun. 2020, pp. 1–7. DOI: 10.1109/ICC40277.2020.9149179.

[40] H.-L. Maattanen, B. Hofstrom, S. Euler, J. Sedin, X. Lin, O. Liberg, G. Masini, and M. Israelsson, "5G NR Communication over GEO or LEO Satellite Systems: 3GPP RAN Higher Layer Standardization Aspects," in *2019 IEEE Global Communications Conference (GLOBECOM)*, Waikoloa, HI, USA: IEEE, Dec. 2019, pp. 1–6, ISBN: 978-1-72810-962-6. DOI: 10.1109/GLOBECOM38437.2019.9014090. [Online]. Available: https://ieeexplore.ieee.org/document/9014090/ (visited on 12/21/2020).

[41] 3GPP, "TR38.801, Technical Specification Group Radio Access Network; Study on new radio access technology: Radio access architecture and interfaces (Release 14), V14.0.0," Technical Report, Mar. 2017.

[42] ——, "TS 38.410 Technical Specification Group Radio Access Network; NG-RAN; NG general aspects and principles, (Release 16), V16.3.0," Technical Report, Sep. 2020.

[43] "ETSI EN 302 307-1, V1.4.1, Digital Video Broadcasting (DVB); Second generation framing structure, channel coding and modulation systems for Broadcasting, Interactive Services, News Gathering and other broadband satellite applications; Part 1: DVB-S2," Jul. 2014.

[44] "ETSI EN 302 307-1, V1.1.1, Digital Video Broadcasting (DVB); Second generation framing structure, channel coding and modulation systems for Broadcasting, Interactive Services, News Gathering and other broadband satellite applications; Part 2: DVB-S2X," Oct. 2014.

[45] "ETSI EN 301 790, V1.5.1, Digital Video Broadcasting (DVB); Interaction channel for satellite distribution systems," May 2009.

[46] 3GPP, "TS 38.470, Technical Specification Group Radio Access Network; NG-RAN; F1 general aspects and principles (Release 16), V16.3.0," Technical Report, Sep. 2020.

[47] ——, "TS 38.420, Technical Specification Group Radio Access Network; NG-RAN; Xn general aspects and principles (Release 16), V16.0.0," Technical Report, Jul. 2020.

[48] Cisco, "Cisco Annual Internet Report (2018–2023)," Whitepaper. [Online]. Available: https://www.cisco.com/c/en/us/solutions/collateral/executive-perspectives/annual-internet-report/white-paper-c11-741490.pdf.

[49] (). "E2UT Energy Efficient User Terminals for Massive Uncoordinated Access via Satellite | ESA's ARTES Programmes," [Online]. Available: https://artes.esa.int/projects/e2ut (visited on 12/29/2020).

[50] (). "NB-IoT4Space - 3GPP Narrow-Band Internet-of-Things (NB-IoT) User Sensor Integration into Satellite | ESA's ARTES Programmes," [Online]. Available: https://artes.esa.int/projects/nbiot4space (visited on 12/29/2020).

[51] (). "Internet of Things Technology Demonstration | ESA's ARTES Programmes," [Online]. Available: https://artes.esa.int/projects/internet-things-technology-demonstration (visited on 12/29/2020).

[52] (). "IOT SATBACK - Satellite Backhauling Prototype for Future Narrow Band Internet of Things (NB-IoT) Networks | ESA's ARTES Programmes," [Online]. Available: https://artes.esa.int/projects/iot-satback (visited on 12/29/2020).

[53] (). "R3 Artes - R3 Artes – Industrial IoT via smart satellite backhaul | ESA's ARTES Programmes," [Online]. Available: https://artes.esa.int/projects/r3-artes (visited on 12/29/2020).

[54] (). "R3_homepage," R3-IoT, [Online]. Available: https://r3-iot.com/ (visited on 12/29/2020).

[55] (). "M2MSAT - Demonstrator of Light-Weight Application and Transport Protocols For Future M2M Applications | ESA's ARTES Programmes," [Online]. Available: https://artes.esa.int/projects/m2msat (visited on 12/29/2020).

[56] M. De Sanctis, E. Cianca, G. Araniti, I. Bisio, and R. Prasad, "Satellite Communications Supporting Internet of Remote Things," *IEEE Internet Things J.*, vol. 3, no. 1, pp. 113–123, Feb. 2016, ISSN: 2327-4662. DOI: 10.1109/JIOT.2015.2487046. [Online]. Available: http://ieeexplore.ieee.org/document/7289337/ (visited on 02/23/2020).

[57] Z. Qu, G. Zhang, H. Cao, and J. Xie, "LEO Satellite Constellation for Internet of Things," *IEEE Access*, vol. 5, pp. 18 391–18 401, 2017, ISSN: 2169-3536. DOI: 10.1109/ACCESS.2017.2735988. [Online]. Available: http://ieeexplore.ieee.org/document/8002583/ (visited on 11/29/2020).

[58] N. Alagha, "Satellite Air Interface Evolutions in the 5G and IoT Era," *SIGMETRICS Perform. Eval. Rev.*, vol. 46, no. 3, pp. 93–95, Jan. 25, 2019, ISSN: 0163-5999. DOI: 10.1145/3308897.3308941. [Online]. Available: https://doi.org/10.1145/3308897.3308941 (visited on 05/20/2020).

[59] T. Wu, D. Qu, and G. Zhang, "Research on LoRa Adaptability in the LEO Satellites Internet of Things," in *2019 15th International Wireless Communications & Mobile Computing Conference (IWCMC)*, Tangier, Morocco: IEEE, Jun. 2019, pp. 131–135, ISBN: 978-1-5386-7747-6. DOI: 10.1109/IWCMC.2019.8766462. [Online]. Available: https://ieeexplore.ieee.org/document/8766462/ (visited on 12/22/2020).

[60] S. Cioni, R. De Gaudenzi, O. Del Rio Herrero, and N. Girault, "On the Satellite Role in the Era of 5G Massive Machine Type Communications," *IEEE Network*, Sep. 2018.

[61] M. Inc., "RP-193235, Study on NB-IoT/eMTC support for Non-Terrestrial Network, RAN Meeting #86," Technical Report, Dec. 2019.

[62] G. Charbit, D. Lin, K. Medles, L. Li, and I.-K. Fu, "Space-Terrestrial Radio Network Integration for IoT," in *2020 2nd 6G Wireless Summit (6G SUMMIT)*, Mar. 2020, pp. 1–5. DOI: 10.1109/6GSUMMIT49458.2020.9083854.

[63] O. Liberg, S. E. Löwenmark, S. Euler, B. Hofström, T. Khan, X. Lin, and J. Sedin. (Oct. 10, 2020). "Narrowband Internet of Things for Non-terrestrial Networks." arXiv: 2010.04906 [cs, eess], [Online]. Available: http://arxiv.org/abs/2010.04906 (visited on 12/22/2020).

[64] R. Barbau, V. Deslandes, G. Jakllari, J. Tronc, J.-F. Chouteau, and A.-L. Beylot, "NB-IoT over GEO Satellite: Performance Analysis," in *2020 10th Advanced Satellite Multimedia Systems Conference and the 16th Signal Processing for Space Communications Workshop (ASMS/SPSC)*, Graz, Austria: IEEE, Oct. 20, 2020, pp. 1–8, ISBN: 978-1-72815-794-8. DOI: 10.1109/ASMS/SPSC48805.2020.9268829. [Online]. Available: https://ieeexplore.ieee.org/document/9268829/ (visited on 12/22/2020).

[65] M. Gineste, T. Deleu, M. Cohen, N. Chuberre, V. Saravanan, V. Frascolla, M. Mueck, E. C. Strinati, and E. Dutkiewicz, "Narrowband IoT Service Provision to 5G User Equipment via a Satellite Component," in *2017 IEEE Globecom Workshops (GC Wkshps)*, Dec. 2017, pp. 1–4. DOI: 10.1109/GLOCOMW.2017.8269209.

[66] O. Kodheli, S. Andrenacci, N. Maturo, S. Chatzinotas, and F. Zimmer, "Resource Allocation Approach for Differential Doppler Reduction in NB-IoT over LEO Satellite," in *2018 9th Advanced Satellite Multimedia Systems Conference and the 15th Signal Processing for Space Communications Workshop (ASMS/SPSC)*, Sep. 2018, pp. 1–8. DOI: 10.1109/ASMS-SPSC.2018.8510724.

[67] M. Conti, S. Andrenacci, N. Maturo, S. Chatzinotas, and A. Vanelli-Coralli, "Doppler Impact Analysis for NB-IoT and Satellite Systems Integration," in *IEEE ICC'20 - SAC-08 SSC*.

[68] S. Cluzel, L. Franck, J. Radzik, S. Cazalens, M. Dervin, C. Baudoin, and D. Dragomirescu, "3GPP NB-IOT Coverage Extension Using LEO Satellites," in *2018 IEEE 87th Vehicular Technology Conference (VTC Spring)*, Jun. 2018, pp. 1–5. DOI: 10.1109/VTCSpring.2018.8417723.

[69] O. Kodheli, N. Maturo, S. Andrenacci, S. Chatzinotas, and F. Zimmer, "Link Budget Analysis for Satellite-Based Narrowband IoT Systems," in *Ad-Hoc, Mobile, and Wireless Networks*, ser. Lecture Notes in Computer Science, M. R. Palattella, S. Scanzio, and S. Coleri Ergen, Eds., vol. 11803, Cham: Springer International Publishing, 2019, pp. 259–271, ISBN: 978-3-030-31830-7 978-3-030-31831-4. DOI: 10.1007/978-3-030-31831-4_18. [Online]. Available: http://link.springer.com/10.1007/978-3-030-31831-4_18 (visited on 05/14/2020).

[70] M. Conti, C. Amatetti, A. Guidotti, and A. Vanelli-Coralli, "NB-IoT over Non-Terrestrial Networks: Link Budget Analysis," in *2020 IEEE Global Communications Conference (GLOBECOM2020)*.

[71] Y. Gong, S. Fan, L. Luo, and X. Liu, "Research on the Online Monitoring Data Transmission Technology Based on Beidou Communication," presented at the 2018 IEEE 18th ICCT, Chongqing: IEEE, Oct. 2018.

[72] F. Xin, X. Bai, and Q. Liu, "Subscription Resource Transfer Protocol Based on Beidou Short Message in Satellite Distance Education System," presented at the 2019 IEEE 9th ICEIEC, Beijing, China: IEEE, Jul. 2019.

[73] Y. Huo, Z. Ao, Y. Zhao, H. Liu, and G. He, "A Novel Push-To-Talk Service over Beidou-3 Satellite Navigation System," presented at the 2019 IEEE ICSPCC, Dalian, China: IEEE, Sep. 2019, pp. 1–6.

[74] Y. Wei, H. Liu, J. Ma, Y. Zhao, H. Lu, and G. He, "Global voice chat over short message service of Beidou navigation system," presented at the 2019 14th IEEE ICIEA, Xi'an, China: IEEE, Jun. 2019.

[75] A. Lewandowski, B. Niehoefer, and C. Wietfeld, "Concept and Performance Evaluation of a Galileo-Based Emergency Short Message Service," presented at the 2009 IEEE 69th VTC, Apr. 2009.

[76] M. Conti and A. Vanelli-Coralli, "Galileo Second Generation: Two-Way Messaging for IoT," in *ICC 2021 - 2021 IEEE International Conference on Communications Workshops (ICC Workshops)*, Jan. 2021.

[77] G. A. Akpakwu, B. J. Silva, G. P. Hancke, and A. M. Abu-Mahfouz, "A Survey on 5G Networks for the Internet of Things: Communication Technologies and Challenges," *IEEE Access*, vol. 6, pp. 3619–3647, 2018, ISSN: 2169-3536. DOI: 10.1109/ACCESS.2017.2779844. [Online]. Available: http://ieeexplore.ieee.org/document/8141874/ (visited on 09/20/2020).

[78] K. Sparks, M. Sirbu, J. Nasielski, L. Merrill, K. Leddy, P. Krishnaswamy, W. Johnston, R. Gyurek, B. Daly, M. Bayliss, J. Barnhill, and K. Balachandran, "5G Network Slicing Whitepaper - FCC Technological Advisory Council – 5G IoT Working Group," p. 34,

[79] 3GPP, "TR36.763, Study on Narrow-Band Internet of Things (NB-IoT) / enhanced Machine Type Communication (eMTC) support for Non-Terrestrial Networks (NTN) (Release 17)," Technical Report, 2020.

[80] M. Conti, "Satcom Systems Simulation and Verification Tools - ESiM2M (ESA M2M Simulator)," Final Report of the ESA Contract Nr. 4000125588/18/NL/FE, Oct. 2019.

[81] E. Re, *LEOSIM: Mega Constellation Performance Simulation Tool*.

[82] S. E. Urban and P. K. Seidelmann, Eds., *Explanatory Supplement to the Astronomical Almanac*, 3rd ed. Mill Valley, Calif: University Science Books, 2013, 676 pp., ISBN: 978-1-891389-85-6.

[83] M. S. Grewal, L. R. Weill, and A. P. Andrews, *Global Positioning Systems, Inertial Navigation, and Integration*, 2nd ed. Hoboken, N.J: Wiley-Interscience, 2007, 525 pp., ISBN: 978-0-470-04190-1.

[84] (). "Reference Systems and Frames - Navipedia," [Online]. Available: https://gssc.esa.int/navipedia/index.php/Reference_Systems_and_Frames (visited on 12/02/2020).

[85] A. Leick, L. Rapoport, and D. Tatarnikov, *GPS Satellite Surveying*, fourth edition. Hoboken, NJ: Wiley, 2015, 807 pp., ISBN: 978-1-119-01826-1 978-1-118-67557-1 978-1-119-01828-5.

[86] C. Boucher and Z. Altamimi, "ITRS, PZ-90 and WGS 84: Current realizations and the related transformation parameters," *Journal of Geodesy*, vol. 75, no. 11, pp. 613–619, Nov. 1, 2001, ISSN: 0949-7714, 1432-1394. DOI: 10.1007/s001900100208. [Online]. Available: http://link.springer.com/10.1007/s001900100208 (visited on 12/02/2020).

[87] J. R. Smith, *Introduction to Geodesy: The History and Concepts of Modern Geodesy*, ser. Wiley Series in Surveying and Boundary Control. New York: Wiley, 1996, 224 pp., ISBN: 978-0-471-16660-3.

[88] J. R. Wertz, *Mission Geometry: Orbit and Constellation Design and Management: Spacecraft Orbit and Attitude Systems*, ser. Space Technology Library. Microcosm Press : Kluwer Academic Publishers, 2001.

[89] H. D. Curtis, *Orbital Mechanics for Engineering Students*, 1. ed., reprinted, ser. Elsevier Aerospace Engineering Series. Amsterdam: Elsevier/Butterworth-Heinemann, 2008, 673 pp., ISBN: 978-0-7506-6169-0.

[90] (). "GPS and Galileo Satellite Coordinates Computation - Navipedia," [Online]. Available: https://gssc.esa.int/navipedia/index.php/GPS_and_Galileo_Satellite_Coordinates_Computation (visited on 12/25/2020).

[91] C. A. Balanis, Ed., *Modern Antenna Handbook*. Hoboken, NJ: Wiley, 2008, 1680 pp., ISBN: 978-0-470-03634-1.

[92] H. Goldstein, C. P. Poole, and J. L. Safko, *Classical Mechanics*, 3. ed. San Francisco, NJ: Addison Wesley, 2002, 638 pp., ISBN: 978-0-201-65702-9 978-0-201-31611-7.

[93] E. W. Weisstein. (). "Alibi Transformation," [Online]. Available: https://mathworld.wolfram.com/AlibiTransformation.html (visited on 12/06/2020).

[94] A. S. Glassner, Ed., *Graphics Gems. 1: ...* Nachdr., ser. The Graphics Gems Series. San Diego: Kaufmann, 2005, 833 pp., ISBN: 978-0-12-286166-6.

[95] N. Capitaine, "Definition and realization of the celestial intermediate reference system," *Proc. IAU*, vol. 3, no. S248, pp. 367–373, Oct. 2007, ISSN: 1743-9213, 1743-9221. DOI: 10.1017/S1743921308019583. [Online]. Available: https://www.cambridge.org/core/product/identifier/S1743921308019583/type/journal_article (visited on 12/05/2020).

[96] (). "Transformations between ECEF and ENU coordinates - Navipedia," [Online]. Available: https://gssc.esa.int/navipedia/index.php/Transformations_between_ECEF_and_ENU_coordinates (visited on 12/07/2020).

[97] A. Tewari, *Atmospheric and Space Flight Dynamics: Modeling and Simulation with MATLAB and Simulink*, ser. MSSET - Modeling and Simulation in Science, Engineering & Technology. Boston, Mass.: Birkhäuser, 2007, 556 pp., ISBN: 978-0-8176-4438-3 978-0-8176-4437-6.

[98] M. Silver, "A short derivation of the sperling-Burdet equations," *Celestial Mechanics*, vol. 11, no. 1, pp. 39–41, Feb. 1, 1975, ISSN: 1572-9478. DOI: 10.1007/BF01228733. [Online]. Available: https://doi.org/10.1007/BF01228733 (visited on 12/23/2020).

[99] H. Huawei, "R1-1911858, Discussion on performance evaluation for NTN, RAN1#99," Technical Report, Nov. 2019.

[100] N. S. B. Nokia, "R2-1814877, Considerations on NTN deployment scenarios, RAN2#103bis," Technical Report, Oct. 2018.

[101] ZTE, "R1-1904765, Considerations on the simulation assumption and methodology for NTN, RAN1#96bis," Technical Report, Apr. 2019.

[102] ——, "R1-1912610, System simulation results and link budget for NTN, RAN1#99," Technical Report, Nov. 2019.

[103] N. S. B. Nokia, "R1-1909693, Simulation Assumptions for Multi-Satellite Evaluation, RAN1#98," Technical Report, Aug. 2019.

[104] D. Petrov, P. Gonchukov, and T. H. Stitz, "Link to System Mapping for FBMC Based Systems in SISO case," in *2013 IEEE ISWCS*, Aug. 2013.

[105] F. L. Aguilar, G. R. Cidre, and J. R. Paris, "Effective SNR mapping algorithms for link prediction model in 802.16e," presented at the 2009 IEEE ICUMT, IEEE, Oct. 2009.

[106] I. Corporation, "IEEE 802.16m Evaluation Methodology Document (EMD)."

[107] K. Brueninghaus, D. Astely, T. Salzer, S. Visuri, A. Alexiou, S. Karger, and G. Seraji, "Link Performance Models for System Level Simulations of Broadband Radio Access Systems," in *2005 IEEE 16th International Symposium on Personal, Indoor and Mobile Radio Communications*, vol. 4, Berlin, Germany: IEEE, 2005, pp. 2306–2311. DOI: 10.1109/PIMRC.2005.1651855. [Online]. Available: http://ieeexplore.ieee.org/document/1651855/ (visited on 06/12/2019).

[108] K.-H. Kim, H.-B. Lee, Y.-H. Lee, and S.-C. Kim, "PHY abstraction methodology for the performance evaluation of PLC channels," in *ISPLC2010*, Rio de Janeiro, Brazil: IEEE, 2010, pp. 28–32, ISBN: 978-1-4244-5009-1. DOI: 10.1109/ISPLC.2010.5479903. [Online]. Available: http://ieeexplore.ieee.org/document/5479903/ (visited on 11/21/2020).

[109] E. Tuomaala and Haiming Wang, "Effective SINR approach of link to system mapping in OFDM/multi-carrier mobile network," in *2005 2nd Asia Pacific Conference on Mobile Technology, Applications and Systems*, Nov. 2005, 5 pp.–5. DOI: 10.1109/MTAS.2005.243791.

[110] J. Olmos, A. Serra, S. Ruiz, M. Garcia-Lozano, and D. Gonzalez, "Exponential Effective SIR metric for LTE downlink," in *2009 IEEE 20th International Symposium on Personal, Indoor and Mobile Radio Communications*, Tokyo: IEEE, Sep. 2009, pp. 900–904, ISBN: 978-1-4244-5122-7 978-1-4244-5123-4. DOI: 10.1109/PIMRC.2009.5449772. [Online]. Available: http://ieeexplore.ieee.org/document/5449772/ (visited on 11/23/2020).

[111] M. Moisio and A. Oborina, "Comparison of Effective SINR Mapping with Traditional AVI Approach for Modeling Packet Error Rate in Multi–state Channel," in *Next Generation Teletraffic and Wired/Wireless Advanced Networking*, ser. Lecture Notes in Computer Science, Y. Koucheryavy, J. Harju, and V. B. Iversen, Eds., vol. 4003, Berlin, Heidelberg: Springer Berlin Heidelberg, 2006, pp. 461–473, ISBN: 978-3-540-34429-2 978-3-540-34430-8. DOI: 10.1007/11759355_42. [Online]. Available: http://link.springer.com/10.1007/11759355_42 (visited on 11/22/2020).

[112] W. Anwar, K. Kulkarni, T. R. Augustin, N. Franchi, and G. Fettweis, "PHY Abstraction Techniques for IEEE 802.11p and LTE-V2V: Applications and Analysis," in *2018 IEEE Globecom Workshops (GC Wkshps)*, Dec. 2018, pp. 1–7. DOI: 10.1109/GLOCOMW.2018.8644470.

[113] R. Sandanalakshmi, T. G. Palanivelu, and K. Manivannan, "Effective SNR mapping for link error prediction in OFDM based systems," in *2007 IET-UK International Conference on Information and Communication Technology in Electrical Sciences (ICTES 2007)*, Dec. 2007, pp. 684–687.

[114] I. Corporation, "IEEE 802.16 Broadband Wireless Access Working Group - Link Performance Abstraction for ML Receivers based on RBIR Metrics."

[115] T. M. Cover and J. A. Thomas, *Elements of Information Theory*, 2nd ed. Hoboken, N.J: Wiley-Interscience, 2006, 748 pp., ISBN: 978-0-471-24195-9.

[116] B. Louay Jalloul, "IEEE 802.16 Broadband Wireless Access Working Group - On the Expected Value of the Received Information Bit Rate," Sep. 18, 2007.

[117] H. Zheng, W. Mav, Y.-s. Choi, and S. Zhang, "Link Performance Abstraction for ML Receivers based on RBIR Metrics," U.S. Patent 20100064185A1, Mar. 11, 2010. [Online]. Available: https://patents.google.com/patent/US20100064185A1/en (visited on 10/03/2020).

[118] K. Sayana, K. Stewart, J. Zhuang, and M. Inc., "IEEE 802.16 Broadband Wireless Access Working Group - Link Performance Abstraction based on Mean Mutual Information per Bit (MMIB) of the LLR Channel," Mar. 5, 2007.

[119] F. L. Aguilar, G. R. Cidre, J. M. L. López, and J. R. Paris, "Mutual Information Effective SNR Mapping Algorithm for Fast Link Adaptation Model in 802.16e," in *Mobile Lightweight Wireless Systems*, P. Chatzimisios, C. Verikoukis, I. Santamaría, M. Laddomada, and O. Hoffmann, Eds., 2010.

[120] P. Mogensen, W. Na, I. Z. Kovacs, F. Frederiksen, A. Pokhariyal, K. I. Pedersen, T. Kolding, K. Hugl, and M. Kuusela, "LTE Capacity Compared to the Shannon Bound," in *2007 IEEE 65th Vehicular Technology Conference - VTC2007-Spring*, Dublin, Ireland: IEEE, Apr. 2007, pp. 1234–1238, ISBN: 978-1-4244-0266-3. DOI: 10.1109/VETECS.2007.260. [Online]. Available: http://ieeexplore.ieee.org/document/4212688/ (visited on 11/23/2020).

[121] M. Mezzavilla, M. Miozzo, M. Rossi, N. Baldo, and M. Zorzi, "A lightweight and accurate link abstraction model for the simulation of LTE networks in ns-3," in *Proceedings of the 15th ACM International Conference on Modeling, Analysis and Simulation of Wireless and Mobile Systems - MSWiM '12*, Paphos, Cyprus: ACM Press, 2012, p. 55, ISBN: 978-1-4503-1628-6. DOI: 10.1145/2387238.2387250. [Online]. Available: http://dl.acm.org/citation.cfm?doid=2387238.2387250 (visited on 11/23/2020).

[122] nsnam. (). "Ns-3," ns-3, [Online]. Available: https://www.nsnam.org/ (visited on 11/23/2020).

[123] A. Goldsmith and Soon-Ghee Chua, "Variable-rate variable-power MQAM for fading channels," *IEEE Trans. Commun.*, vol. 45, no. 10, pp. 1218–1230, Oct./1997, ISSN: 00906778. DOI: 10.1109/26.634685. [Online]. Available: http://ieeexplore.ieee.org/document/634685/ (visited on 11/23/2020).

[124] (). "Coded Modulation Library," [Online]. Available: http://www.iterativesolutions.com/Matlab.htm (visited on 11/27/2020).

[125] 3GPP, "TS25.212 Technical Specification Group Radio Access Network; Multiplexing and channel coding (FDD) (Release 16) V16.0.0," Technical Report, Jul. 2020.

[126] O. Del Rio Herrero and R. De Gaudenzi, "High Efficiency Satellite Multiple Access Scheme for Machine-to-Machine Communications," *IEEE Transactions on Aerospace and Electronic Systems*, 2012.

[127] J. Rosen and L. Q. Gothard, *Encyclopedia of Physical Science*. New York: Facts On File, 2010, ISBN: 978-1-4381-1909-0.

[128] I. Ali, N. Al-Dhahir, and J. Hershey, "Doppler characterization for LEO satellites," *IEEE Transactions on Communications*, vol. 46, no. 3, pp. 309–313, Mar. 1998, ISSN: 00906778. DOI: 10.1109/26.662636. [Online]. Available: http://ieeexplore.ieee.org/document/662636/ (visited on 10/06/2017).

[129] ITU, "ITU-R P.676 : Attenuation by atmospheric gases and related effects," Aug. 2019.

[130] ——, "ITU-R P.618 : Propagation data and prediction methods required for the design of Earth-space telecommunication systems," Dec. 2017.

[131] ——, "ITU-R P.531 : Ionospheric propagation data and prediction methods required for the design of satellite networks and systems," Aug. 2019.

[132] TICRA, "SATSOFT User's Manual - SATSOFT Version 3.0.0," Jun. 2016.

[133] H. Peyravi, "Medium access control protocols performance in satellite communications," *IEEE Communications Magazine*, Mar. 1999.

[134] D. P. Bertsekas and R. G. Gallager, *Data Networks*, 2nd ed. Prentice Hall, 1992.

[135] N. Abramson, "Spread aloha CDMA data communications," U.S. Patent 5537397A, Jul. 16, 1996. [Online]. Available: https://patents.google.com/patent/US5537397/en (visited on 04/14/2021).

[136] R. De Gaudenzi, O. del Rio Herrero, and G. Gallinaro, "Enhanced spread Aloha physical layer design and performance: ENHANCED SPREAD ALOHA PHYSICAL LAYER DESIGN AND PERFORMANCE," *Int. J. Satell. Commun. Network.*, vol. 32, no. 6, pp. 457–473, Nov. 2014, ISSN: 15420973. DOI: 10.1002/sat.1078. [Online]. Available: http://doi.wiley.com/10.1002/sat.1078 (visited on 09/03/2020).

[137] M. Vaezi, Z. Ding, and H. V. Poor, *Multiple Access Techniques for 5G Wireless Networks and Beyond*. 2019.

[138] 3GPP, "TR45.820, Technical Specification Group GSM/EDGE Radio Access Network; Cellular system support for ultra-low complexity and low throughput Internet of Things (CIoT) (Release 13), V13.1.0," Technical Report, Nov. 2015.

[139] Q. Inc., "Narrowband IoT (NB-IoT), RP-151621, 3GPP TSG RAN Meeting #69," Technical Report, Sep. 2015.

[140] Y.-P. E. Wang, X. Lin, A. Adhikary, A. Grovlen, Y. Sui, Y. Blankenship, J. Bergman, and H. S. Razaghi, "A Primer on 3GPP Narrowband Internet of Things," *IEEE Commun. Mag.*, vol. 55, no. 3, pp. 117–123, Mar. 2017, ISSN: 0163-6804. DOI: 10.1109/MCOM.2017.1600510CM. [Online]. Available: http://ieeexplore.ieee.org/document/7876968/ (visited on 02/23/2020).

[141] R. Ratasuk, N. Mangalvedhe, Y. Zhang, M. Robert, and J.-P. Koskinen, "Overview of narrowband IoT in LTE Rel-13," in *2016 IEEE Conference on Standards for Communications and Networking (CSCN)*, Berlin, Germany: IEEE, Oct. 2016, pp. 1–7, ISBN: 978-1-5090-3862-6. DOI: 10.1109/CSCN.2016.7785170. [Online]. Available: http://ieeexplore.ieee.org/document/7785170/ (visited on 02/23/2020).

[142] N. Mangalvedhe, R. Ratasuk, and A. Ghosh, "NB-IoT deployment study for low power wide area cellular IoT," in *2016 IEEE 27th Annual International Symposium on Personal, Indoor, and Mobile Radio Communications (PIMRC)*, Valencia, Spain: IEEE, Sep. 2016, pp. 1–6, ISBN: 978-1-5090-3254-9. DOI: 10.1109/PIMRC.2016.7794567. [Online]. Available: http://ieeexplore.ieee.org/document/7794567/ (visited on 02/23/2020).

[143] C. Yu, L. Yu, Y. Wu, Y. He, and Q. Lu, "Uplink Scheduling and Link Adaptation for Narrowband Internet of Things Systems," *IEEE Access*, vol. 5, pp. 1724–1734, 2017, ISSN: 2169-3536. DOI: 10.1109/ACCESS.2017.2664418. [Online]. Available: http://ieeexplore.ieee.org/document/7842562/ (visited on 02/23/2020).

[144] 3GPP, "TS36.211, Evolved Universal Terrestrial Radio Access (E-UTRA) and Evolved Universal Terrestrial Radio Access Network (E-UTRAN); Physical Channels and Modulation, V16.1.0," Technical Report, Mar. 2020.

[145] ——, "TS36.213, Technical Specification Group Radio Access Network; Evolved Universal Terrestrial Radio Access (E-UTRA); Physical layer procedures (Release 16), V16.1.0," Technical Report, Apr. 2020.

[146] ——, "TS36.212, Technical Specification Group Radio Access Network; Evolved Universal Terrestrial Radio Access (E-UTRA); Multiplexing and channel coding (Release 14), V14.3.0," Technical Report, Jun. 2017.

[147] Rohde&Schwarz, "Narrowband Internet of Things," Whitepaper.

[148] O. Liberg, *Cellular Internet of Things: From Massive Deployments to Critical 5g Applications*, 1st ed. Cambridge: Elsevier Inc, 2019, ISBN: 978-0-08-102902-2.

[149] 3GPP, "TS36.331, Technical Specification Group Radio Access Network; Evolved Universal Terrestrial Radio Access (E-UTRA); Radio Resource Control (RRC); Protocol specification (Release 14), V14.2.2," Technical Report, Apr. 2017.

[150] ——, "TS36.321, Technical Specification Group Radio Access Network; Evolved Universal Terrestrial Radio Access (E-UTRA); Medium Access Control (MAC) protocol specification (Release 14), V14.3.0," Technical Report, Jun. 2017.

[151] ——, "TS36.101 Technical Specification Group Radio Access Network; Evolved Universal Terrestrial Radio Access (E-UTRA); User Equipment (UE) radio transmission and reception (Release 16), V16.5.0," Technical Report, Mar. 2020.

[152] ——, "TS36.304 Technical Specification Group Radio Access Network; Evolved Universal Terrestrial Radio Access (E-UTRA); User Equipment (UE) procedures in idle mode (Release 14) V14.3.0," Technical Report, Jun. 2017.

[153] H. Technologies, "NB-IoT Radio and Performance Basics Feature Parameter Description," Aug. 30, 2017.

[154] H. Huawei, "R1-1903998: Discussion on link budget for NTN," Technical Report, Apr. 2019.

[155] 3GPP, "TR36.888 Technical Specification Group Radio Access Network; Study on provision of low-cost Machine-Type Communications (MTC) User Equipments (UEs) based on LTE (Release 12), V12.0.0," Technical Report, Jun. 2013.

[156] ——, "TR25.913 TSG-RAN Requirements for Evolved UTRA (E-UTRA) and Evolved UTRAN (E-UTRAN) (Release 9), V9.0.0," Technical Report, Dec. 2009.

[157] V. Jungnickel, H. Gaebler, U. Krueger, K. Manolakis, and T. Haustein, "LTE trials in the return channel over satellite," in *2012 6th Advanced Satellite Multimedia Systems Conference (ASMS) and 12th Signal Processing for Space Communications Workshop (SPSC)*, Vigo, Spain: IEEE, Sep. 2012, pp. 238–245, ISBN: 978-1-4673-2676-6. DOI: 10.1109/ASMS-SPSC.2012.6333083. [Online]. Available: http://ieeexplore.ieee.org/document/6333083/ (visited on 02/23/2020).

[158] V. Jungnickel, M. Schellmann, A. Forck, H. Gäbler, S. Wahls, A. Ibing, K. Manolakis, T. Haustein, W. Zirwas, J. Eichinger, E. Schulz, C. Juchems, F. Luhn, and R. Zavrtak, "Demonstration of Virtual Mimo in the Uplink," in *Proc. IET Smart Antennas and Cooperative Communications Seminar*, 2007.

[159] ESA. (). "System | European GNSS Service Centre," [Online]. Available: https://www.gsc-europa.eu/galileo/system (visited on 09/08/2020).

[160] J. J. H. Wang, "Antennas for Global Navigation Satellite System (GNSS)," *Proc. IEEE*, vol. 100, no. 7, pp. 2349–2355, Jul. 2012, ISSN: 0018-9219, 1558-2256. DOI: 10.1109/JPROC.2011.2179630. [Online]. Available: http://ieeexplore.ieee.org/document/6130567/ (visited on 02/11/2021).

Acknowledgements

Questa tesi è il risultato di tre anni di lavoro. Vorrei ringraziare le molte persone che mi sono state vicine durante questo percorso e che mi hanno aiutato a crescere.

Ringrazio Alessandro V. che ha creduto in me e mi ha dato la possibilità di intraprendere questo percorso. E' stato un grande mentore e gli sono grato per tutto quello che ha fatto per me, ho appreso tanto da lui e spero di continuare a farlo nel prossimo futuro.

Ringrazio Alberto Ginesi per avermi accolto in ESTEC, è stata un'esperienza meravigliosa e una grande opportunità di crescita.

Thanks to the people I worked with while I was in ESTEC, for their incredible patience and willingness in teaching me.

Ringrazio Alessandro G. per tutto quello che mi ha insegnato e per le attività di ricerca in cui mi ha coinvolto e continua a coinvolgermi.

Ringrazio Carla e tutti i colleghi del laboratorio con cui ho condiviso questi anni.

Grazie a tutti gli amici di Bologna e del paesello per i tanti bei momenti passati insieme e per il supporto nei momenti più difficili.

Infine grazie ai miei genitori che mi hanno sempre supportato e sostenuto.